Supplementary Materials for

Universal and scalable synthesis of ultrahigh-density single-atom libraries on metal oxides

Rui-Ting Gao,[1,2] Chao Fan,[2] Zehua Gao,[2] Lei Wang[2]* & Limin Wu [1,2]*

[1] College of Smart Materials and Future Energy, Fudan University, Shanghai 200433, China

[2] College of Chemistry and Chemical Engineering, College of Energy Material and Chemistry, Inner Mongolia Key Laboratory of Low Carbon Catalysis, Inner Mongolia University, Hohhot 010021, China

*Corresponding author. E-mail: wanglei@imu.edu.cn. Lmw@fudan.edu.cn

The PDF file includes:

Supplementary Methods

Supplementary Figs. S1 to S60

Supplementary Tables S1 to S15

Supplementary References

1. Syntheses

1.1 Synthesis of 2D-Fe_2O_3

A piece of iron foil (1 cm^2, 0.25 mm thick, 99.99%, Alfa) was ultrasonically cleaned in acetone and ethanol for 10 min for degreasing, followed by dried under a nitrogen stream. To prepare α-Fe_2O_3 nanosheets grown on the iron substrate, the foil was thermally annealed at 430 °C for 2 h in air using a HF-Kejing furnace (Model KSL-1100X), with a heating rate of 10 °C min^{-1}. This thermal annealing process resulted in the formation of nano-leaf-like structures across the entire sample surface.

1.2 Synthesis of 1D-Cu_2O

The copper foil (1 cm^2, 0.1 mm thick, 99.99%, Alfa) was ultrasonically cleaned in acetone and ethanol for 10 min for degreasing, followed by dried under a nitrogen stream. The cleaned foil was then electrochemically anodized in a 3 M KOH solution at a current density of 10 mA cm^{-2} until the potential reached 2 V to form $Cu(OH)_2$ nanowires. Subsequently, the as-grown $Cu(OH)_2$ nanowires were converted into one-dimensional Cu_2O by annealing in an Ar atmosphere at 550 °C for 5 h with a heating rate of 10 °C min^{-1}.

1.3 Synthesis of 2D-$ZnIn_2S_4$

The precursor solution was prepared by dissolving $ZnCl_2$ (0.2045 g, 99.95%, Alfa), $InCl_3 \cdot 4H_2O$ (0.8795 g, 99.9%, Aladdin), and thiourea (0.4565 g, 99%, Aladdin) in 150 mL of ultrapure water. Subsequently, 20 mL of the solution and a clean FTO substrate (conductive side down) were loaded into a Teflon-lined autoclave, which was heated at 160 °C for 6 h. The resulting sample was collected, washed with water and ethanol, and vacuum-dried at 50 °C for 24 h.

1.4 Synthesis of 2D-C_3N_4

Bulk 2D-C_3N_4 was synthesized by directly annealing 10 g of urea (99.9%, Aladdin) in a crucible at 550 °C for 3 h under ambient air.

1.5 Synthesis of 3D-Fe_2O_3

Following the preparation of a precursor solution from $FeCl_3 \cdot 6H_2O$ (0.15 M, 99%, Aladdin), $NaNO_3$ (1 M, 99%, Aladdin), and concentrated HNO_3 (150 μL) in 100 mL of ultrapure water, a clean FTO substrate (conductive side down) was placed in a Teflon-lined autoclave with 20 mL of the solution. The autoclave was heated at 100 °C for 4 h. The obtained product was washed with ultrapure water/ethanol and dried.

Subsequently, the FeOOH sample was then subjected to annealing in argon at 600 °C for 1 h, followed by ramping to 750 °C at 2 °C min^{-1} and holding for 20 min before natural cooling.

1.6 Synthesis of 3D-TiO_2

Following the preparation of a precursor solution from tetrabutyl titanate (1 mL, 99%, Aladdin) and $NaNO_3$ (1 M, 99%, Aladdin) in a mixture of ultrapure water (30 mL) and concentrated HCl (30 mL), a clean FTO substrate (conductive side down) was subjected to a hydrothermal treatment with 20 mL of the solution at 150 °C for 12 h. The resulting product was washed with deionized water, and subsequently annealed at 450 °C for 1 h in air.

2. Characterizations

2.1 Structure and morphology

The crystal structure and composition were characterized by X-ray diffraction (XRD, Rigaku RINT-2000, Cu Kα radiation at 40 kV and 40 mA) and X-ray photoelectron spectroscopy (XPS, ESCALAB 250xi, Thermo Fisher Scientific). The morphology was examined using field-emission scanning electron microscopy (FE-SEM, Supra 55, Zeiss, Germany) and spherical aberration-corrected high-resolution scanning transmission electron microscopy (JEM GRAND ARM 300F, Japan). Electron paramagnetic resonance (EPR) measurements were recorded at a low temperature of -150 °C using a JES-FA200 spectrometer.

2.2 XAFS Measurements

X-ray absorption fine structure (XAFS) measurements were performed with Si (111) crystal monochromators at the BL14W Beam line at Shanghai Synchrotron Radiation Facility (SSRF) (Shanghai, China). Before the analysis at the beamline, samples were placed into aluminum sample holders and sealed using Kapton tape film. The obtained XAFS data was processed in Athena (version 0.9.26) for background, pre-edge line and post-edge line calibrations. Then Fourier transformed fitting was carried out in Artemis (version 0.9.26). The k^3 weighting, k-range of 3~11.5 $Å^{-1}$ and R range of 1-4 Å were used for the fitting of UHL-SACs/Fe_2O_3. For Wavelet Transform analysis, the χ(k) exported from Athena was imported into the Hama Fortran code. The parameters were listed as follow: R range, 0-4 Å. k range, 0-16 $Å^{-1}$. k weight, 2. and Morlet function with κ=10, σ=1 was used as the mother wavelet to provide the overall distribution.

2.3 Electrochemical performance measurements

The electrochemical OER and HER performances of the as-prepared W_{PM}/C_3N_4 and W_M/C_3N_4 samples were evaluated in a standard three-electrode system using a 0.5 M H_2SO_4 electrolyte. The measurements were conducted with a CHI 760E electrochemical workstation, and all recorded potentials were converted to the reversible hydrogen electrode (RHE) scale.

2.4 Density functional theory calculations

All density functional theory (DFT) calculations were performed using the Vienna Ab-initio Simulation Package (VASP).[1] The electron-ion interactions were described by the projector-augmented wave (PAW) potentials, which accurately describe the core-valence electron interactions.[2] The exchange-correlation energy was calculated within the generalized gradient approximation (GGA) using the Perdew-Burke-Ernzerhof (PBE) functional, which is widely adopted for solid-state calculations due to its reliable performance in describing the electronic structure and structural properties of many materials.[3] To account for the strong correlation effects of d electrons, the DFT+U correction was employed. The effective U value for the Fe elements was set to 4 eV, which was chosen based on previous literatures or calibration calculations.[4] Additionally, the DFT+D3 correction was incorporated to consider the long-range van der Waals (vdW) interactions, which is crucial for systems involving weak intermolecular or interfacial interactions.[5] For the calculation of density of states (DOS), hybrid density functional theory (HSE06) calculations were performed to improve the accuracy of electronic structure predictions.[6] The cutoff energy for the plane-wave basis set was set to 500 eV, which was tested to ensure the total energy convergence. For the k-point sampling in the first Brillouin zone, a Monkhorst-Pack grid of 3×3×1 was used for optimization, and the convergence of total energy with respect to k-point density was verified.[7]

The adsorption energy of the system is defined by:

$$E_{form} = E_{total} - E_{sub} - E_{bulk/n} \quad (1)$$

where E_{total} is the total energy of SAC on Fe_2O_3 (001), E_{sub} is the energy of Fe_2O_3 (001), E_{bulk} is the energy of metals in bulk, and n is the number of metal atoms in the bulk.

The cohesive energy of the system is defined by:

$$E_{coh} = (E_{bulk} - n^*E_{atom})/n \quad (2)$$

where E_{bulk} is the energy of bulk metal and E_{atom} is the energy of single metal in this system. The lower the cohesive energy, the easier it is for atoms to agglomerate.

The binding energy of the system is defined by:

$$E_{bind} = E_{total} - E_{substrate} - E_{SAC} \quad (3)$$

where $E_{substrate}$ is the energy of the substrate, and E_{total} is the total energy of the system.

The Gibbs free energy of the system is defined by:

$$\Delta G = \Delta H - T\Delta S \quad (4)$$

where ΔH is enthalpy, T is the temperature, and ΔS is the entropy of the system. Negative ΔG means that the reaction occurs spontaneously.

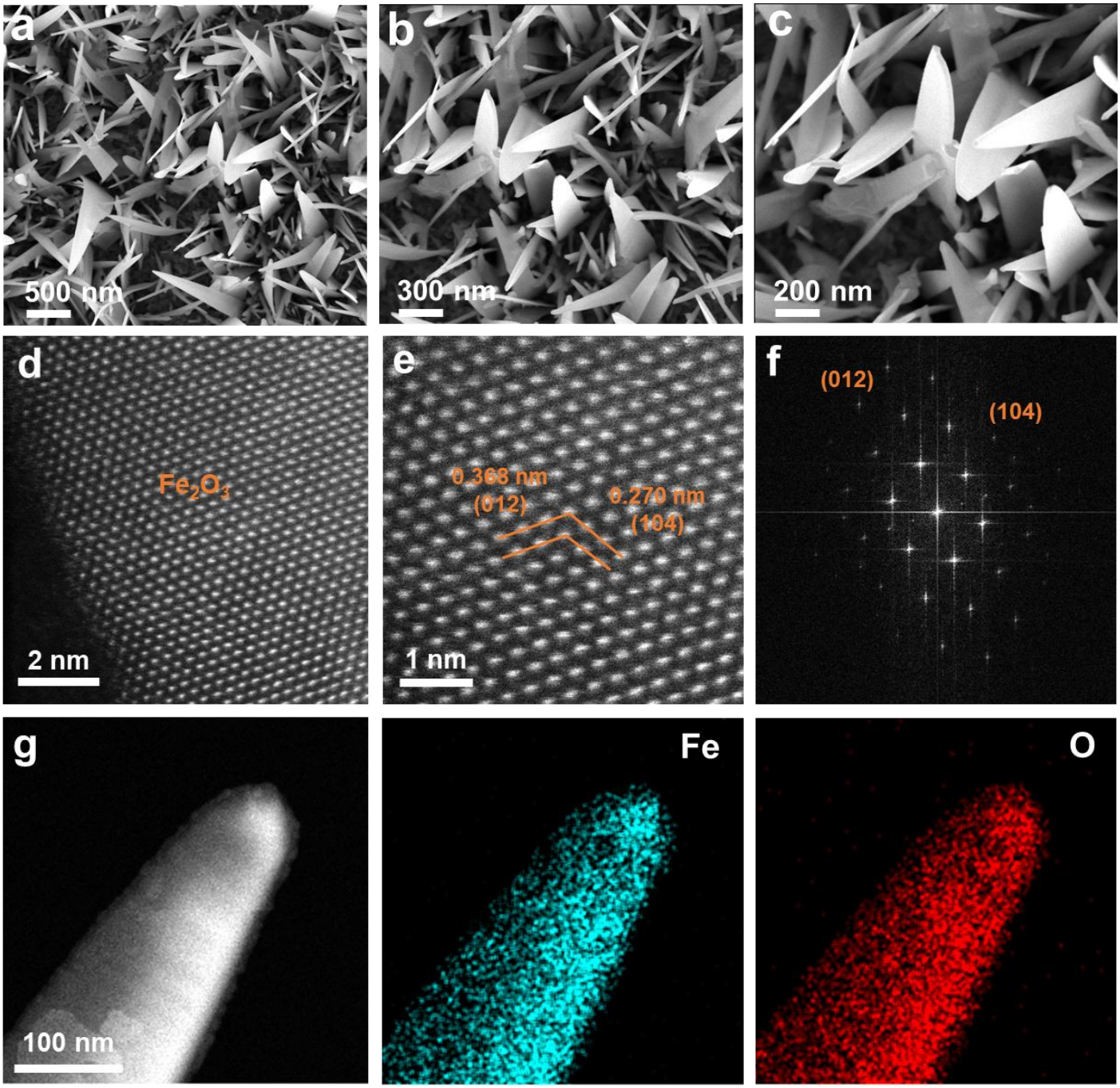

Supplementary Fig. 1 SEM, HAADF-STEM and EDS elemental mappings images of Fe_2O_3. a-c, SEM images of Fe_2O_3. **d, e,** high resolution HAADF-STEM images of Fe_2O_3. **f**, FFT pattern**. g,** elemental mappings of Fe_2O_3.

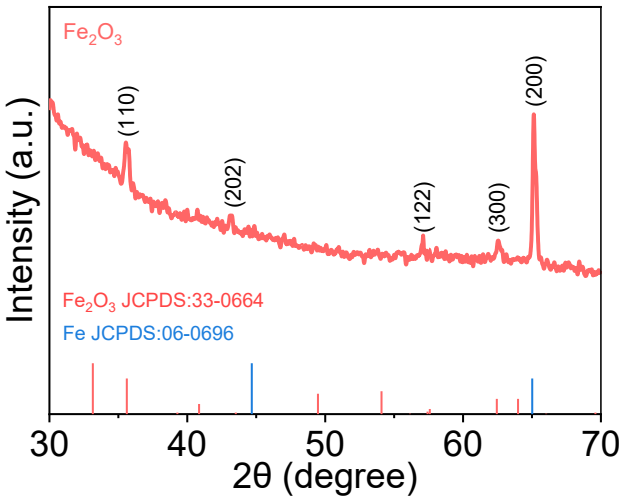

Supplementary Fig. 2 X-ray diffraction (XRD) pattern. XRD pattern of Fe_2O_3.

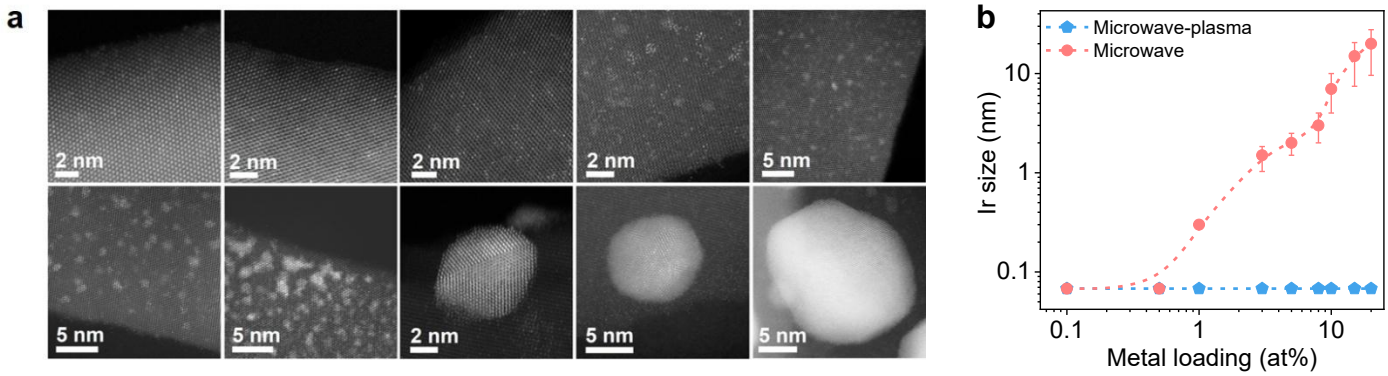

Supplementary Fig. 3 a,b, The HAADF-STEM images (**a**) and the size of Ir (**b**) on Fe_2O_3 with various Ir loadings (0.1-20 wt%).

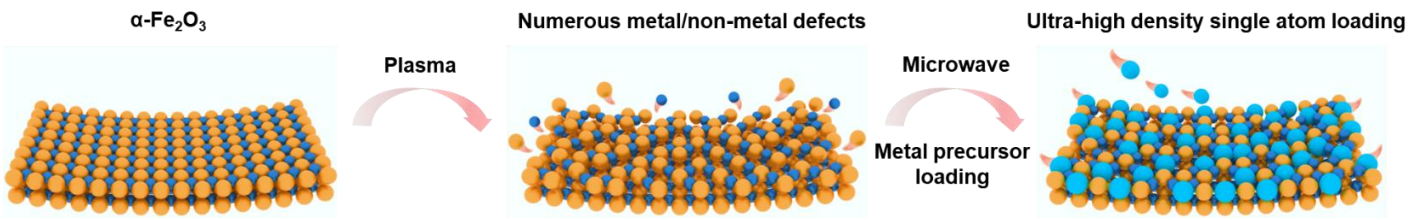

Supplementary Fig. 4 Illustration of the synthesis approach. Schematic illustration for the synthesis of UHL-SACs/Fe_2O_3.

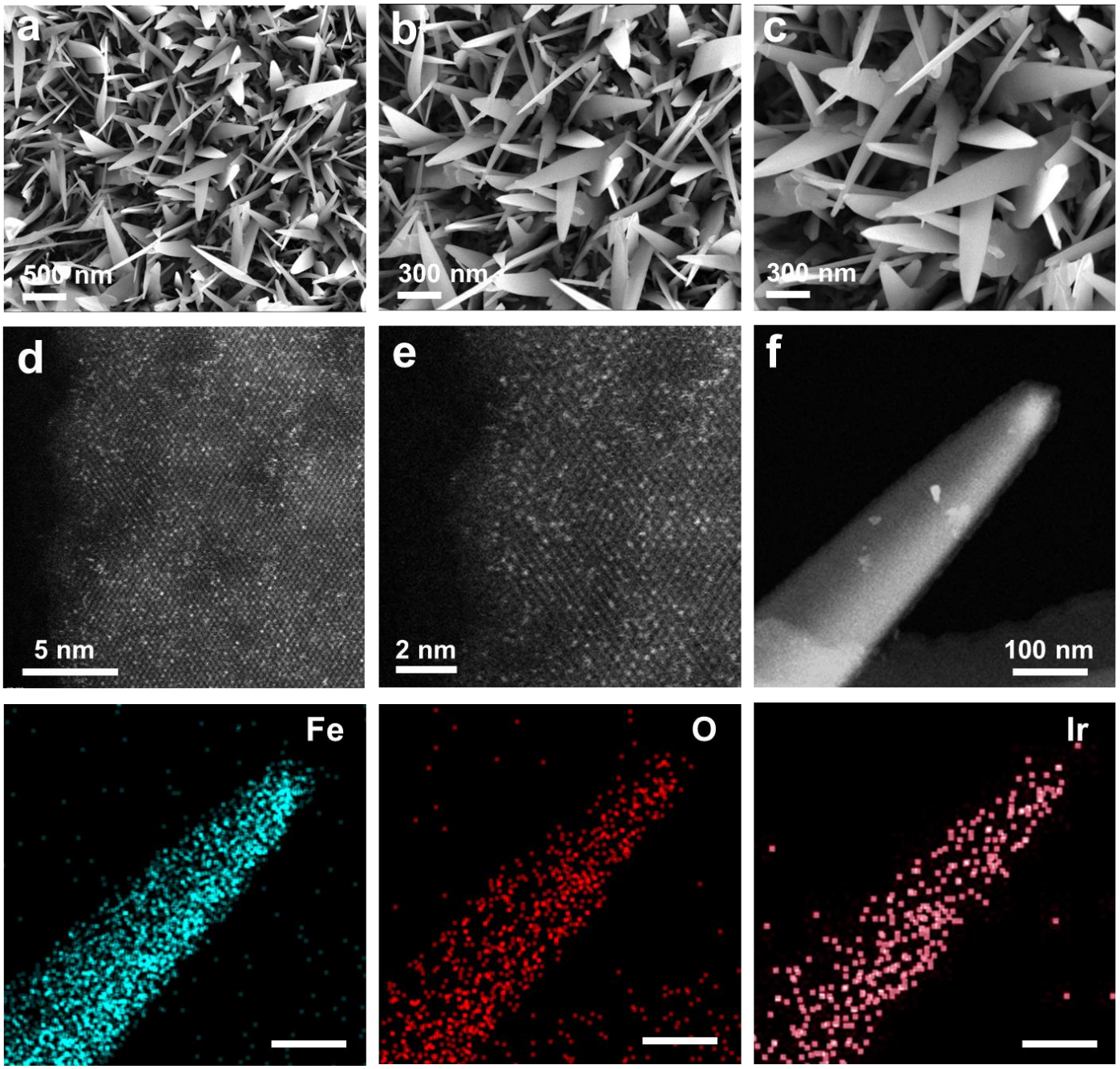

Supplementary Fig. 5 SEM, HAADF-STEM and EDS elemental mappings images of UHL-Ir/Fe_2O_3. a-c, SEM images of UHL-Ir/Fe_2O_3. **d, e,** high resolution HAADF-STEM images of UHL-Ir/Fe_2O_3. **f,** elemental mappings of UHL-Ir/Fe_2O_3.

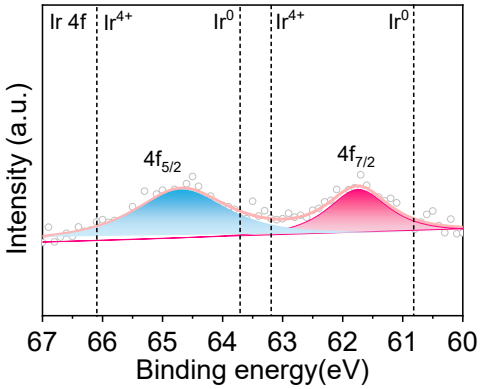

Supplementary Fig. 6 X-ray photoelectron spectroscopy (XPS) characterization. Ir *4f* XPS spectra for UHL-Ir/Fe_2O_3.

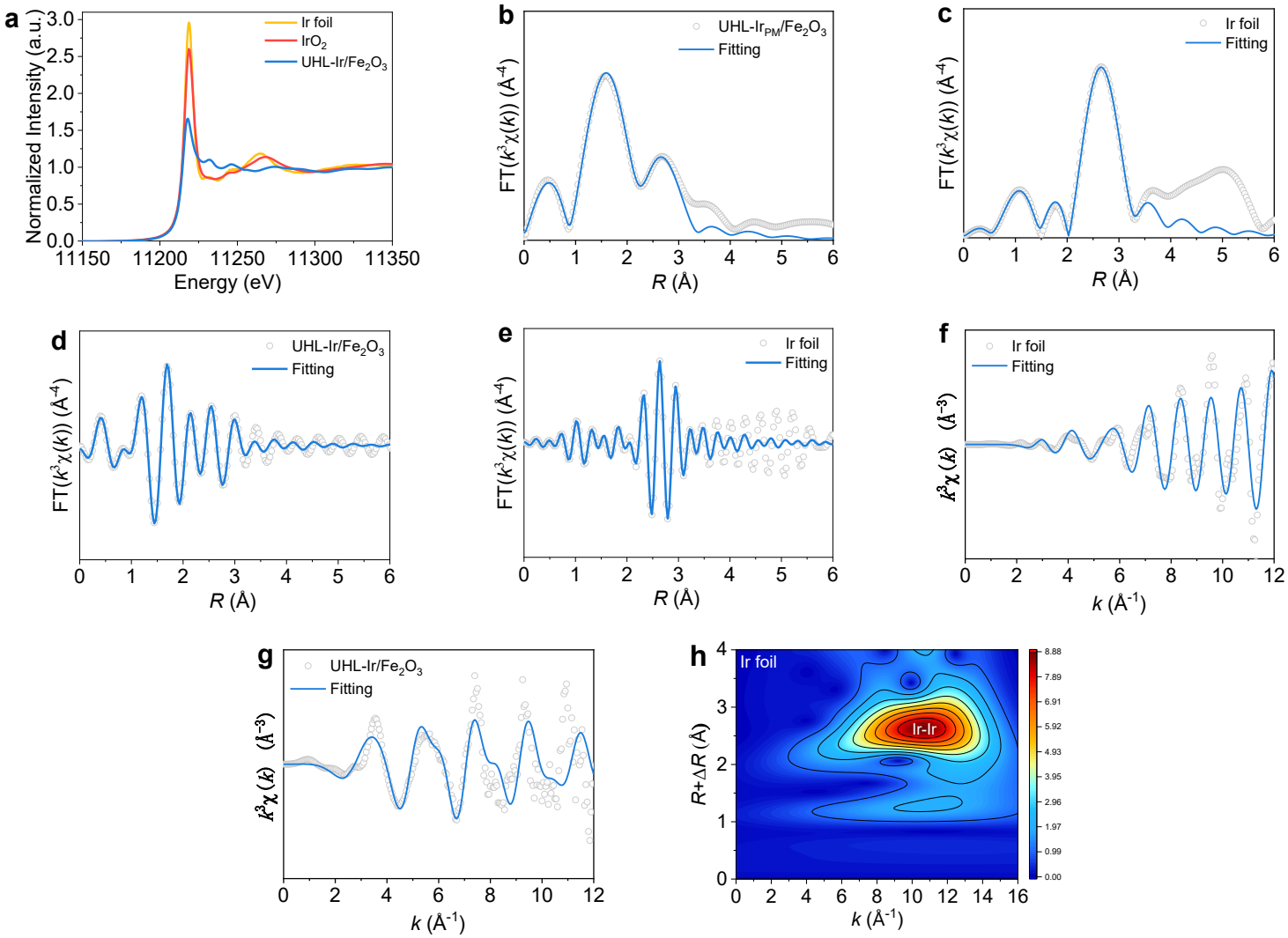

Supplementary Fig. 7 Atom structural characterization of UHL-Ir/Fe$_2$O$_3$. a, Ir L_3-edge XANES spectra of UHL-Ir/Fe$_2$O$_3$, Ir foil and IrO$_2$. **b-e,** Ir *K*-edge EXAFS data and fit for UHL-Ir/Fe$_2$O$_3$ in *R*-space and **f, g,** *k*-space. **h,** WT-EXAFS plot of UHL-Ir/Fe$_2$O$_3$.

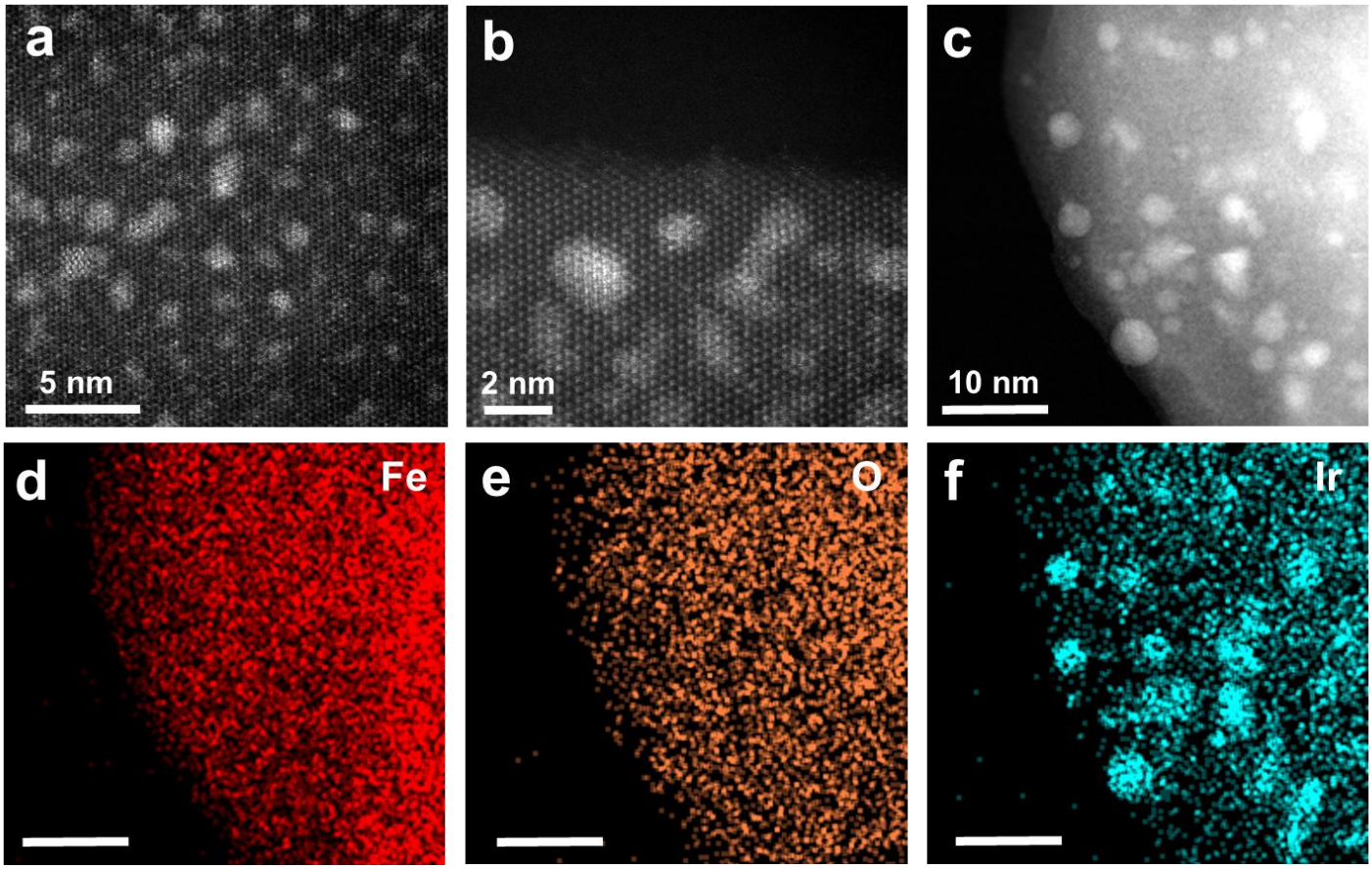

Supplementary Fig. 8 HAADF-STEM and EDS elemental mappings images of UHL-Ir/Fe_2O_3 without plasma pretreatment. a,b, HAADF-STEM images of UHL-Ir/Fe_2O_3 without plasma pretreatment. **c-f,** elemental mappings of UHL-Ir/Fe_2O_3 without plasma pretreatment.

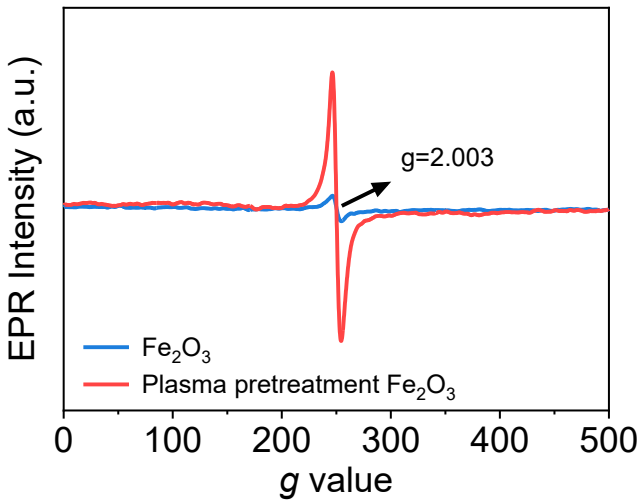

Supplementary Fig. 9 Electron paramagnetic resonance (EPR) spectroscopy. EPR spectra of Fe_2O_3 before and after plasma pretreatment.

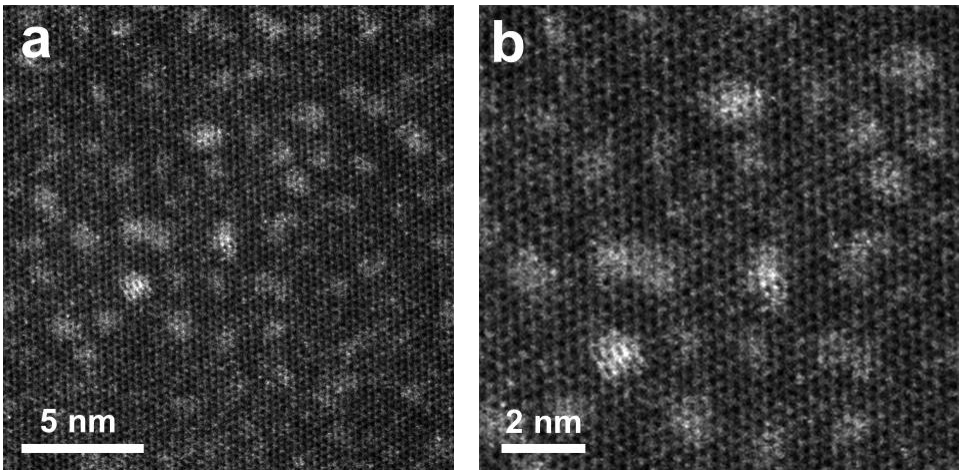

Supplementary Fig. 10 HAADF-STEM images. HAADF-STEM image of Ir precursor loaded onto Fe_2O_3 after plasma pretreatment, following conventional sluggish annealing.

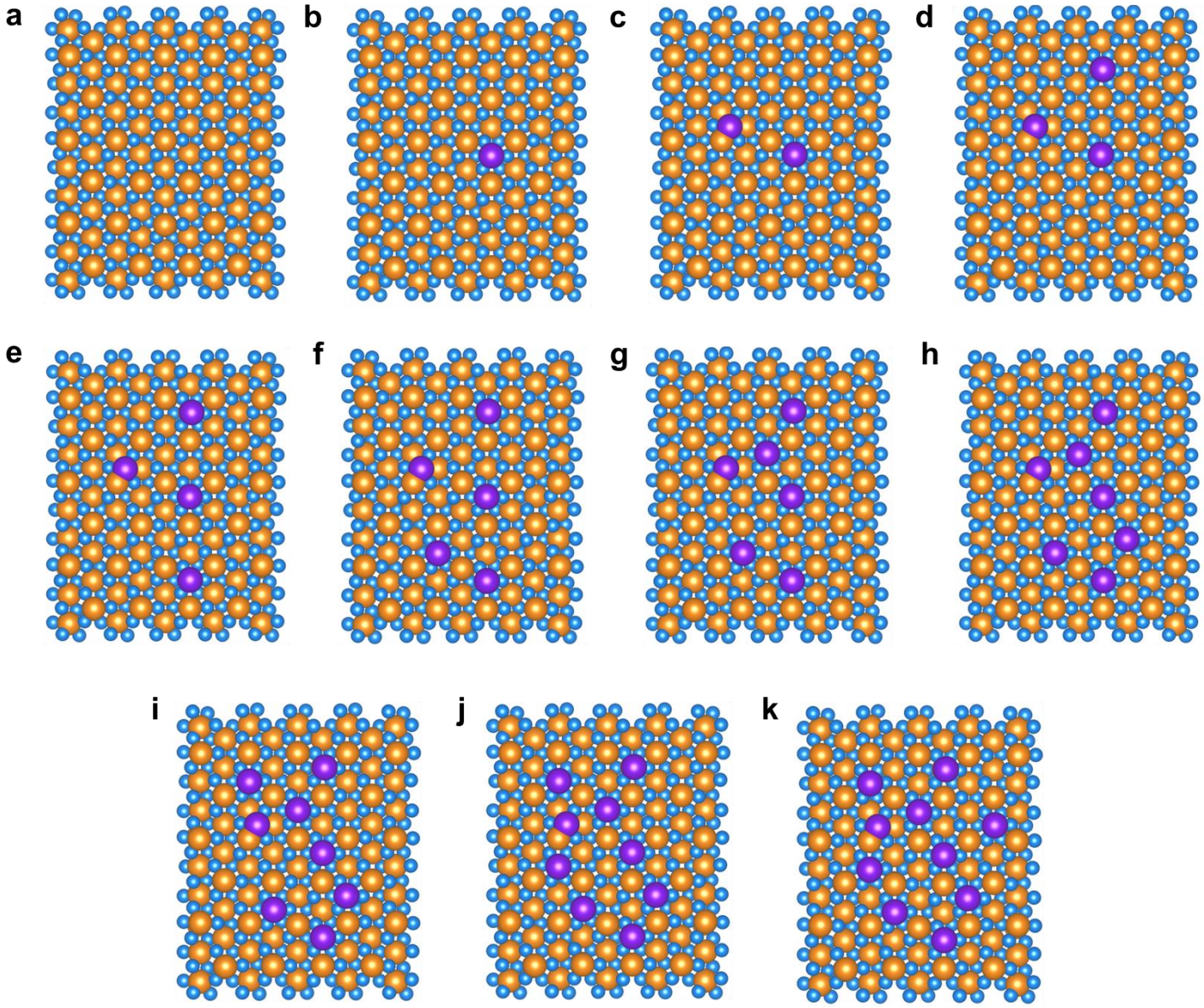

Supplementary Fig. 11 Structural modes. a-k, Structural modes of pristine Fe_2O_3 surfaces loaded with 1-10 dispersed Ir atoms.

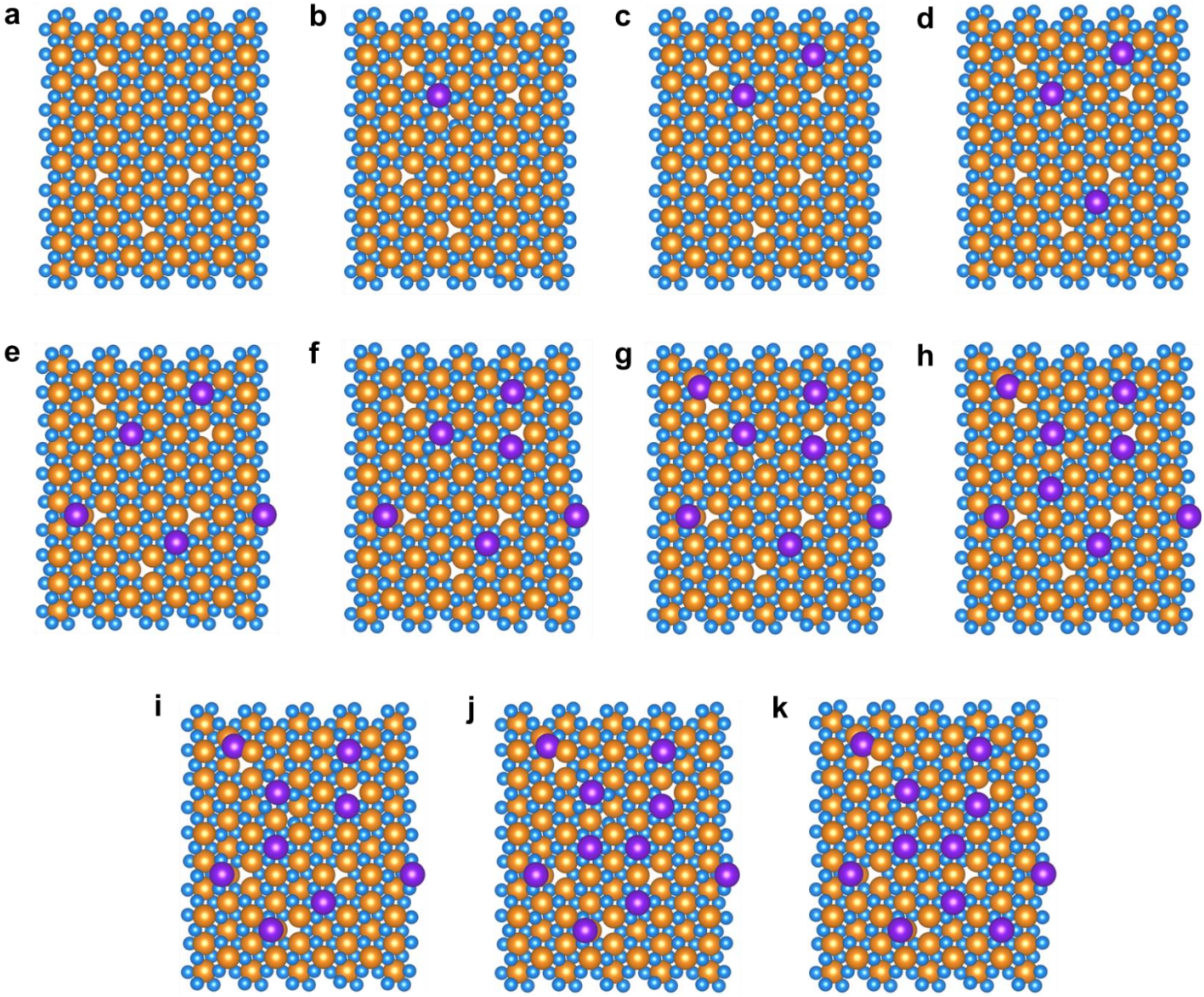

Supplementary Fig. 12 Structural modes. a-k, Structural modes of plasma-treated Fe_2O_3 surfaces loaded with 1-10 dispersed Ir atoms.

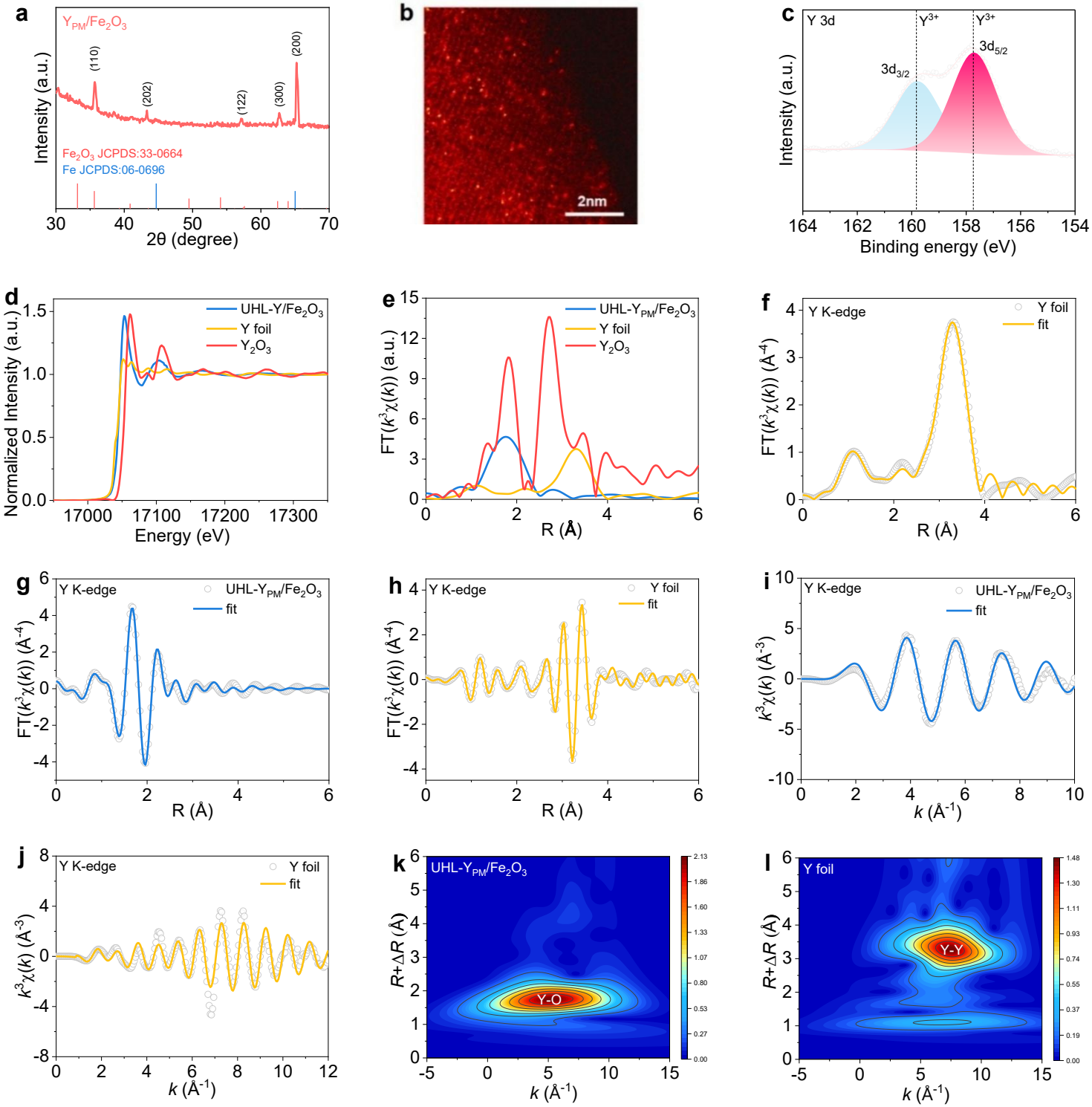

Supplementary Fig. 13 Structural characterization of Y_{PM}/Fe_2O_3. a, XRD patterns of Y_{PM}/Fe_2O_3. **b**, HAADF-STEM image of Y_{PM}/Fe_2O_3. **c**, Y 3d XPS spectra of Y_{PM}/Fe_2O_3. **d**, Normalized Y *K*-edge X-ray absorption near-edge structure (XANES) spectra. **e**, Fourier-transformed R-space of the experimental Y *K*-edge EXAFS signals. **f-h,** Y *K*-edge EXAFS data and fit for UHL-Y_{PM}/Fe_2O_3 in *R*-space and **i, j,** *k*-space. **k,l,** WT-EXAFS plots of UHL-Y_{PM}/Fe_2O_3 and Y foil.

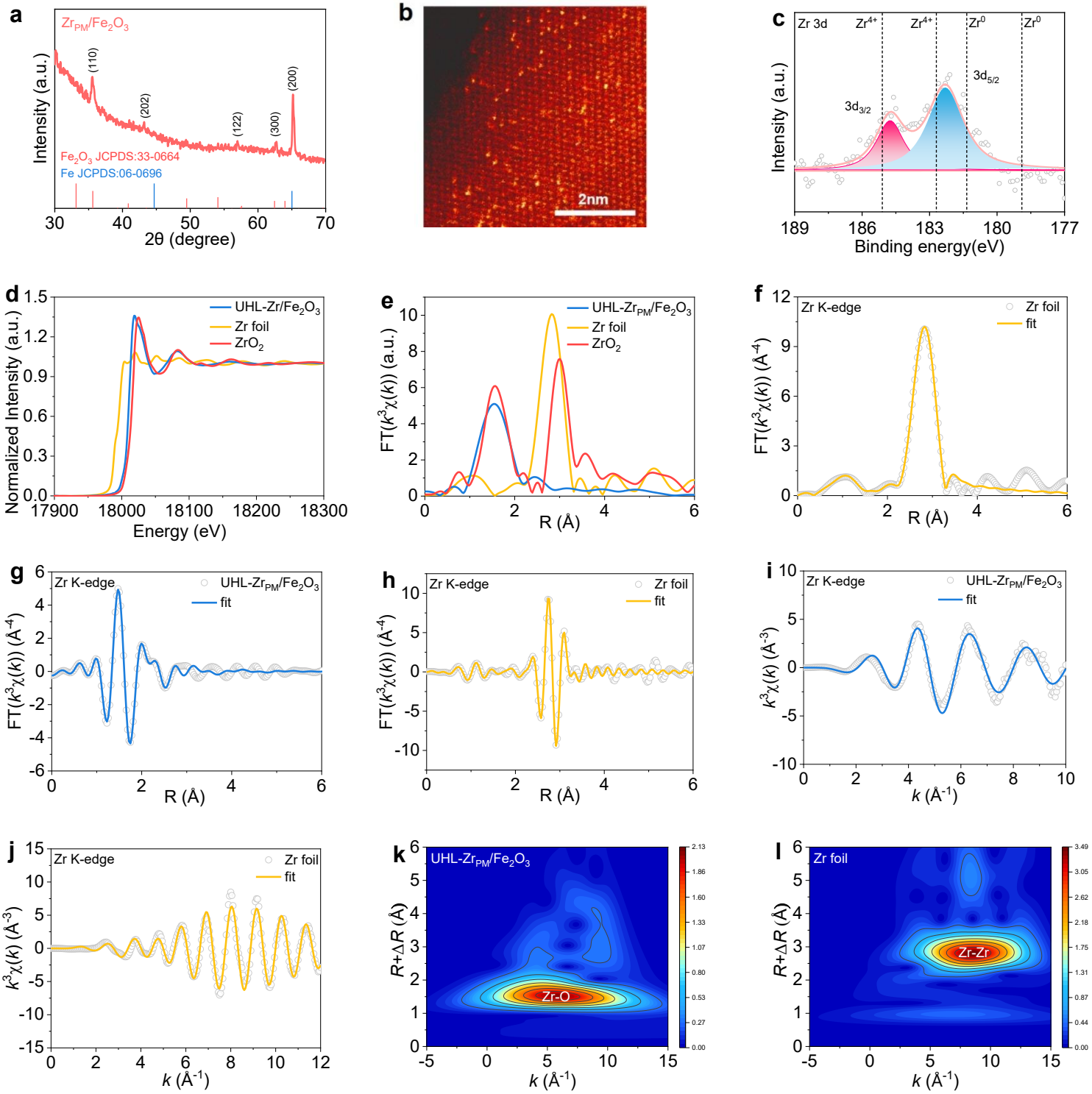

Supplementary Fig. 14 Structural characterization of Zr$_{PM}$/Fe$_2$O$_3$. a, XRD patterns of Zr$_{PM}$/Fe$_2$O$_3$. **b**, HAADF-STEM image of Zr$_{PM}$/Fe$_2$O$_3$. **c**, Zr 3d XPS spectra of Zr$_{PM}$/Fe$_2$O$_3$. **d**, Normalized Zr *K*-edge X-ray absorption near-edge structure (XANES) spectra. **e**, Fourier-transformed R-space of the experimental Zr *K*-edge EXAFS signals. **f-h,** Zr *K*-edge EXAFS data and fit for UHL-Zr$_{PM}$/Fe$_2$O$_3$ in *R*-space and **i, j,** *k*-space. **k,l,** WT-EXAFS plots of UHL-Zr$_{PM}$/Fe$_2$O$_3$ and Zr foil.

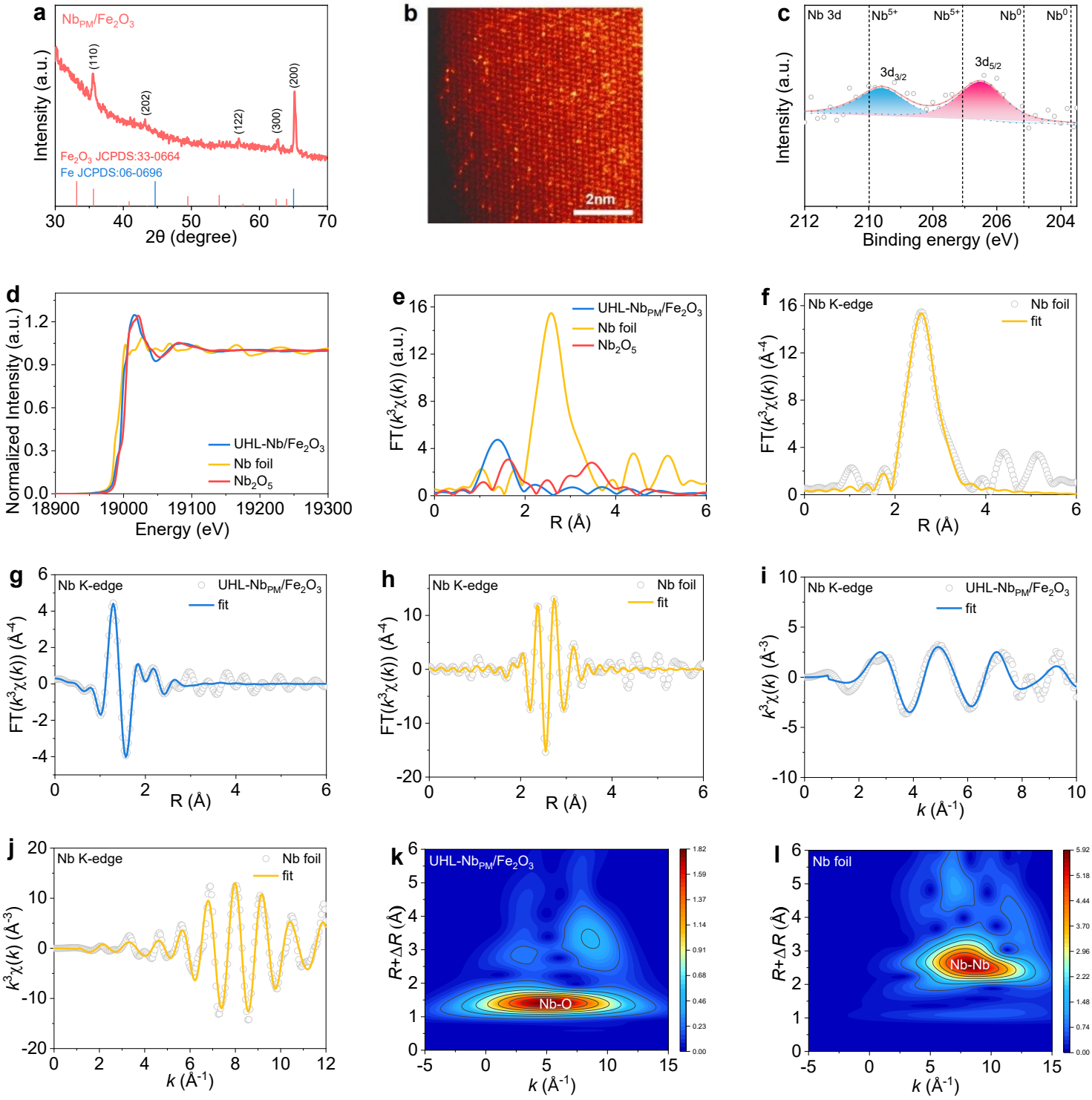

Supplementary Fig. 15 Structural characterization of Nb$_{PM}$/Fe$_2$O$_3$. a, XRD patterns of Nb$_{PM}$/Fe$_2$O$_3$. **b**, HAADF-STEM image of Nb$_{PM}$/Fe$_2$O$_3$. **c**, Nb 3d XPS spectra of Nb$_{PM}$/Fe$_2$O$_3$. **d**, Normalized Nb *K*-edge X-ray absorption near-edge structure (XANES) spectra. **e**, Fourier-transformed R-space of the experimental Nb *K*-edge EXAFS signals. **f-h,** Nb *K*-edge EXAFS data and fit for UHL-Nb$_{PM}$/Fe$_2$O$_3$ in *R*-space and **i, j,** *k*-space. **k,l,** WT-EXAFS plots of UHL-Nb$_{PM}$/Fe$_2$O$_3$ and Nb foil.

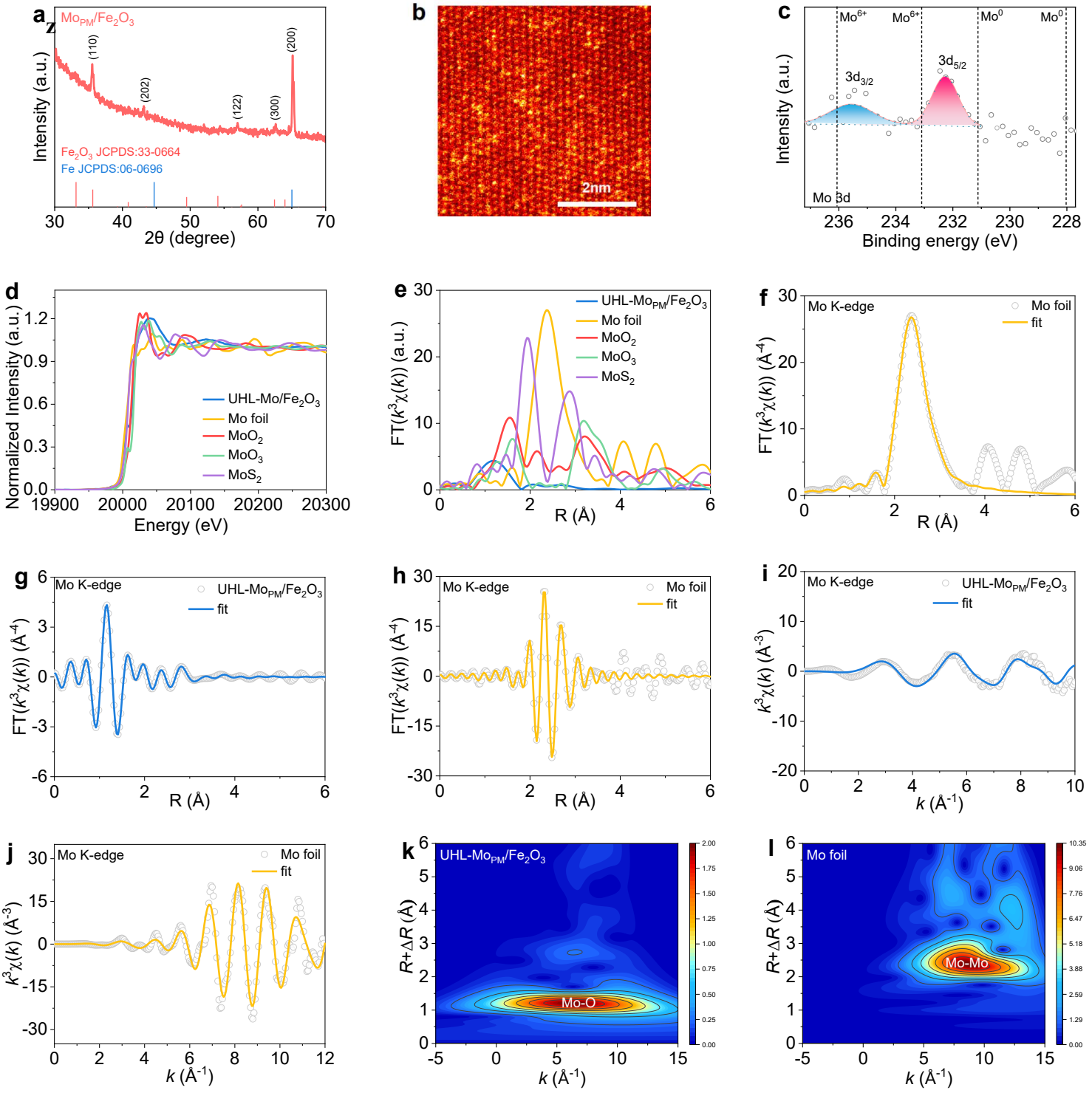

Supplementary Fig. 16 Structural characterization of Mo_{PM}/Fe_2O_3. a, XRD patterns of Mo_{PM}/Fe_2O_3. **b**, HAADF-STEM image of Mo_{PM}/Fe_2O_3. **c**, Mo 3d XPS spectra of Mo_{PM}/Fe_2O_3. **d**, Normalized Mo *K*-edge X-ray absorption near-edge structure (XANES) spectra. **e**, Fourier-transformed R-space of the experimental Mo *K*-edge EXAFS signals. **f-h,** Mo *K*-edge EXAFS data and fit for UHL-Mo_{PM}/Fe_2O_3 in *R*-space and **i, j,** *k*-space. **k,l,** WT-EXAFS plots of UHL-Mo_{PM}/Fe_2O_3 and Mo foil.

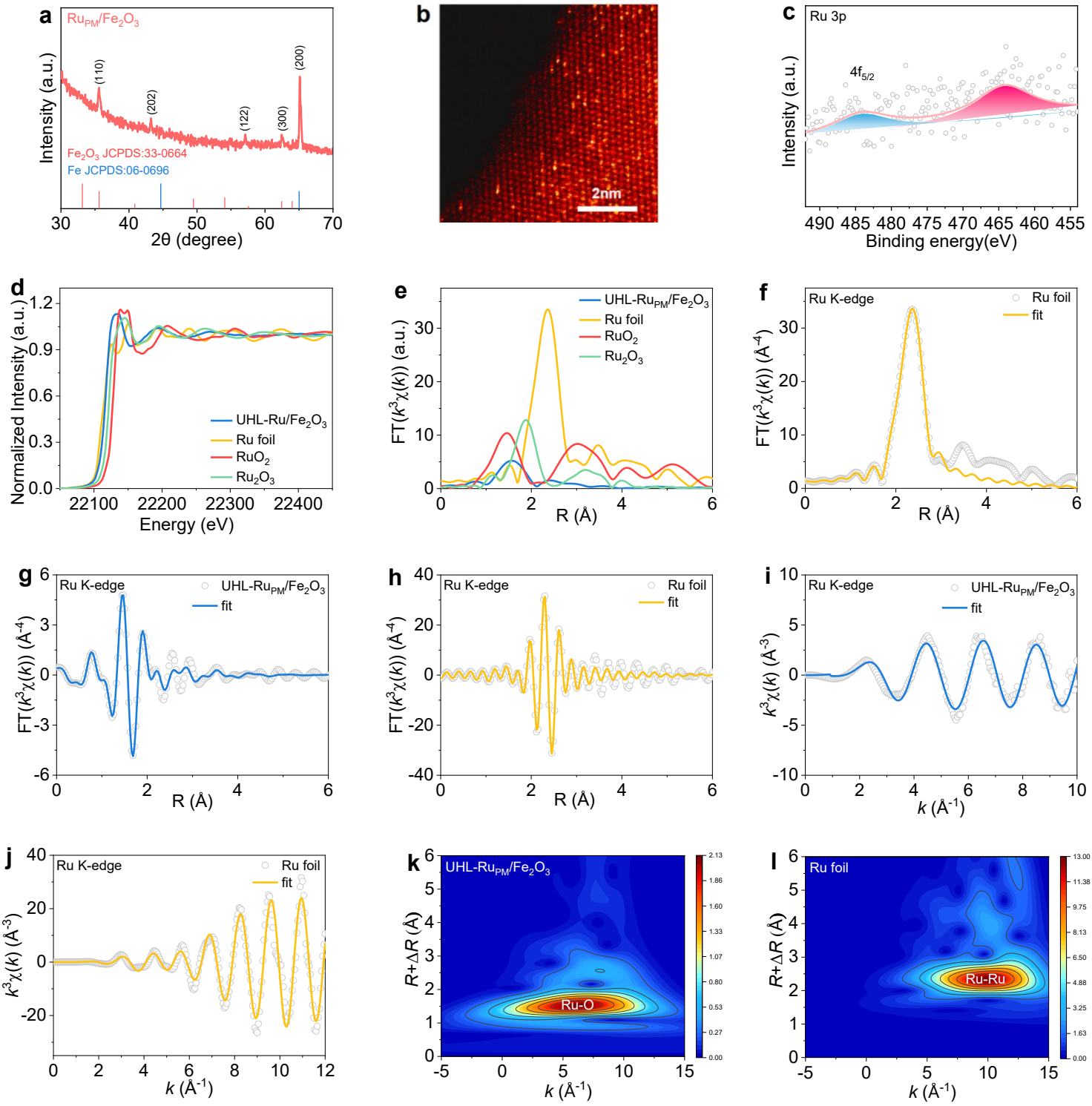

Supplementary Fig. 17 Structural characterization of Ru_{PM}/Fe_2O_3. a, XRD patterns of Ru_{PM}/Fe_2O_3. **b**, HAADF-STEM image of Ru_{PM}/Fe_2O_3. **c**, Ru 3p XPS spectra of Ru_{PM}/Fe_2O_3. **d**, Normalized Ru *K*-edge X-ray absorption near-edge structure (XANES) spectra. **e**, Fourier-transformed R-space of the experimental Ru *K*-edge EXAFS signals. **f-h,** Ru *K*-edge EXAFS data and fit for UHL-Ru_{PM}/Fe_2O_3 in *R*-space and **i, j,** *k*-space. **k,l,** WT-EXAFS plots of UHL-Ru_{PM}/Fe_2O_3 and Ru foil.

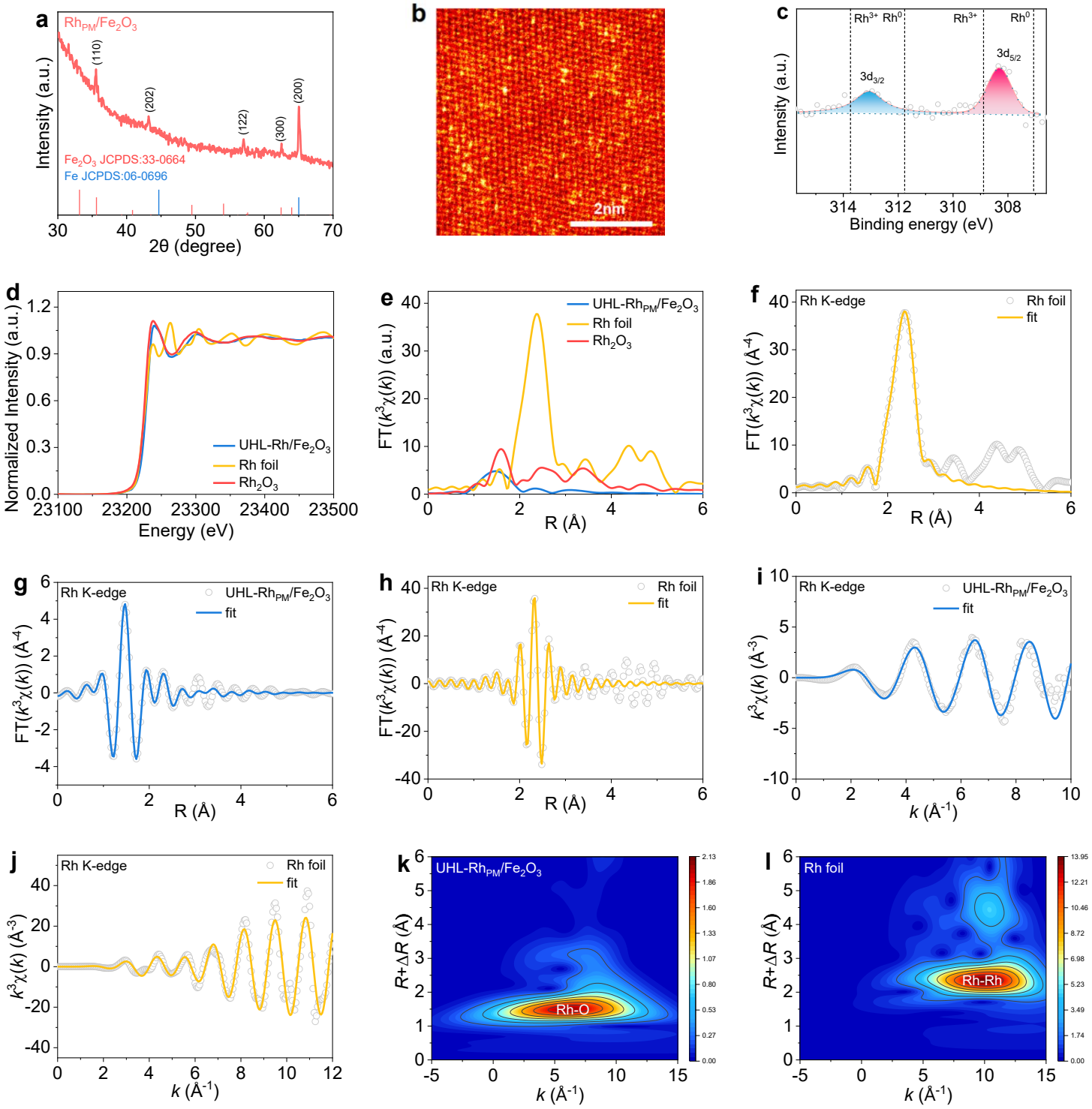

Supplementary Fig. 18 Structural characterization of Rh$_{PM}$/Fe$_2$O$_3$. a, XRD patterns of Rh$_{PM}$/Fe$_2$O$_3$. **b**, HAADF-STEM image of Rh$_{PM}$/Fe$_2$O$_3$. **c**, Rh 3d XPS spectra of Rh$_{PM}$/Fe$_2$O$_3$. **d**, Normalized Rh *K*-edge X-ray absorption near-edge structure (XANES) spectra. **e**, Fourier-transformed R-space of the experimental Rh *K*-edge EXAFS signals. **f-h,** Rh *K*-edge EXAFS data and fit for UHL-Rh$_{PM}$/Fe$_2$O$_3$ in *R*-space and **i, j,** *k*-space. **k,l,** WT-EXAFS plots of UHL-Rh$_{PM}$/Fe$_2$O$_3$ and Rh foil.

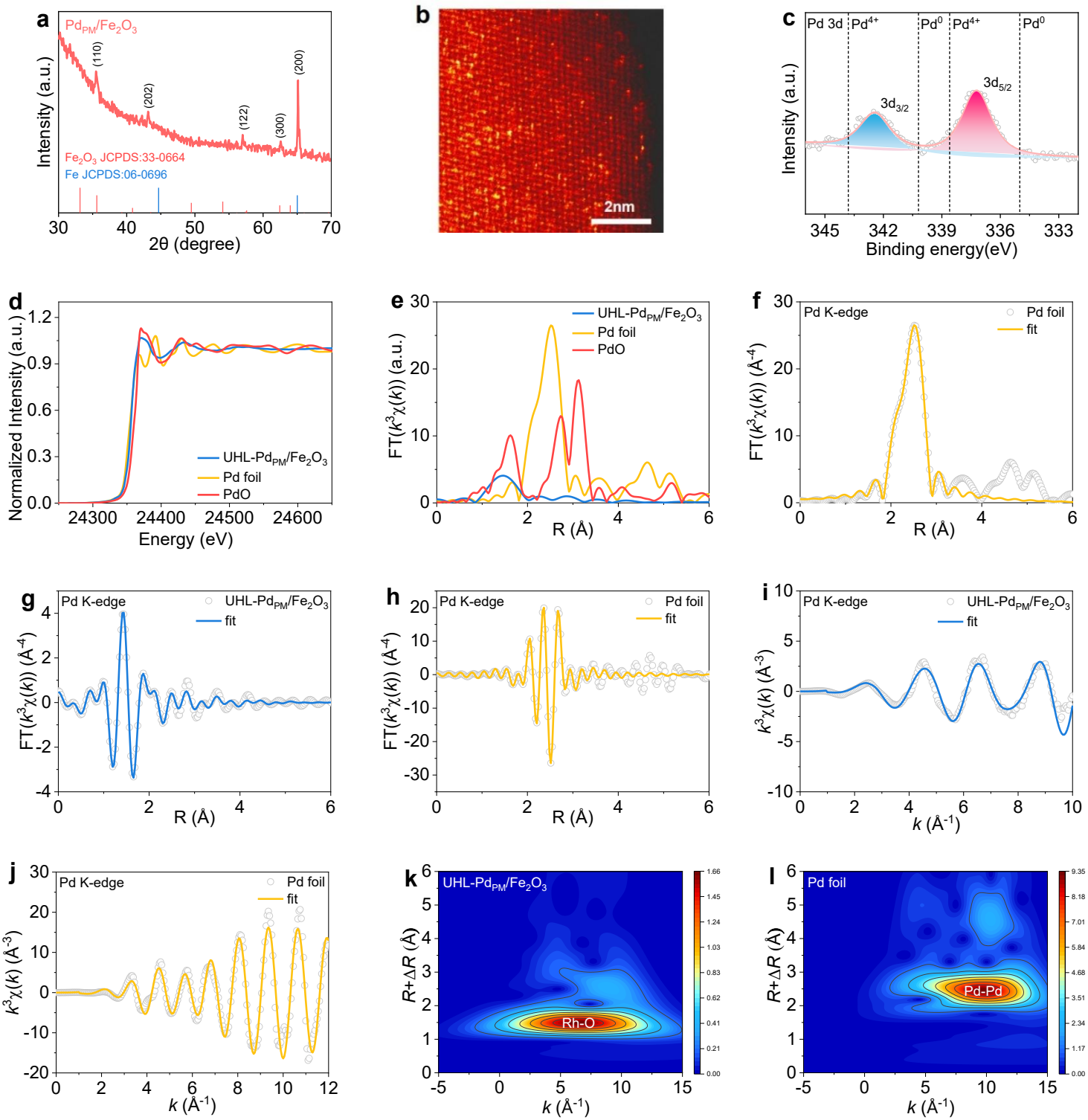

Supplementary Fig. 19 Structural characterization of Pd$_{PM}$/Fe$_2$O$_3$. a, XRD patterns of Pd$_{PM}$/Fe$_2$O$_3$. **b**, HAADF-STEM image of Pd$_{PM}$/Fe$_2$O$_3$. **c**, Pd 3d XPS spectra of Pd$_{PM}$/Fe$_2$O$_3$. **d**, Normalized Pd *K*-edge X-ray absorption near-edge structure (XANES) spectra. **e**, Fourier-transformed R-space of the experimental Pd *K*-edge EXAFS signals. **f-h,** Pd *K*-edge EXAFS data and fit for UHL-Pd$_{PM}$/Fe$_2$O$_3$ in *R*-space and **i, j,** *k*-space. **k,l,** WT-EXAFS plots of UHL-Pd$_{PM}$/Fe$_2$O$_3$ and Pd foil.

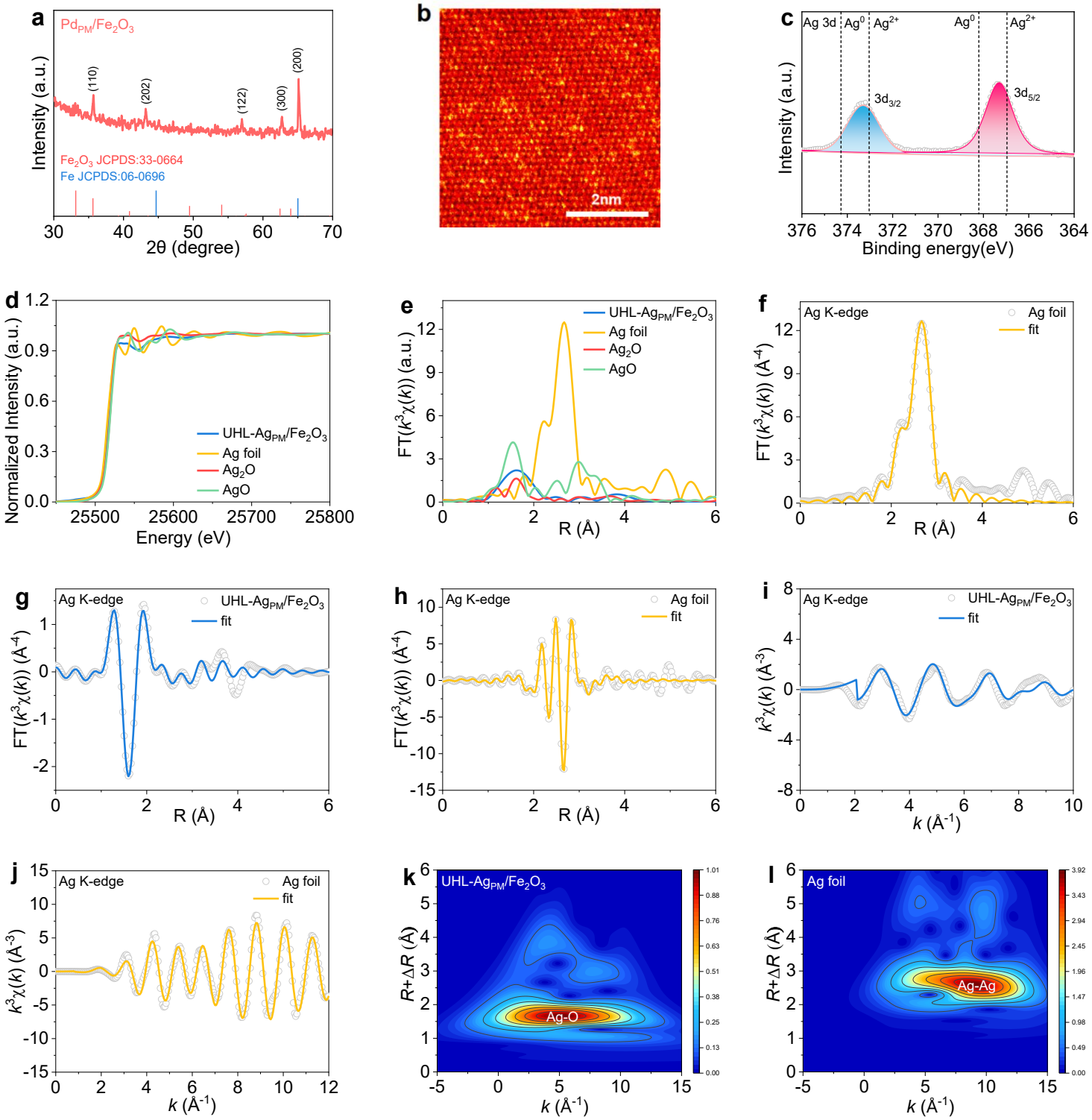

Supplementary Fig. 20 Structural characterization of Ag$_{PM}$/Fe$_2$O$_3$. **a**, XRD patterns of Ag$_{PM}$/Fe$_2$O$_3$. **b**, HAADF-STEM image of Ag$_{PM}$/Fe$_2$O$_3$. **c**, Ag 3d XPS spectra of Ag$_{PM}$/Fe$_2$O$_3$. **d**, Normalized Ag *K*-edge X-ray absorption near-edge structure (XANES) spectra. **e**, Fourier-transformed R-space of the experimental Ag *K*-edge EXAFS signals. **f-h,** Ag *K*-edge EXAFS data and fit for UHL-Ag$_{PM}$/Fe$_2$O$_3$ in *R*-space and **i, j,** *k*-space. **k,l,** WT-EXAFS plots of UHL-Ag$_{PM}$/Fe$_2$O$_3$ and Ag foil.

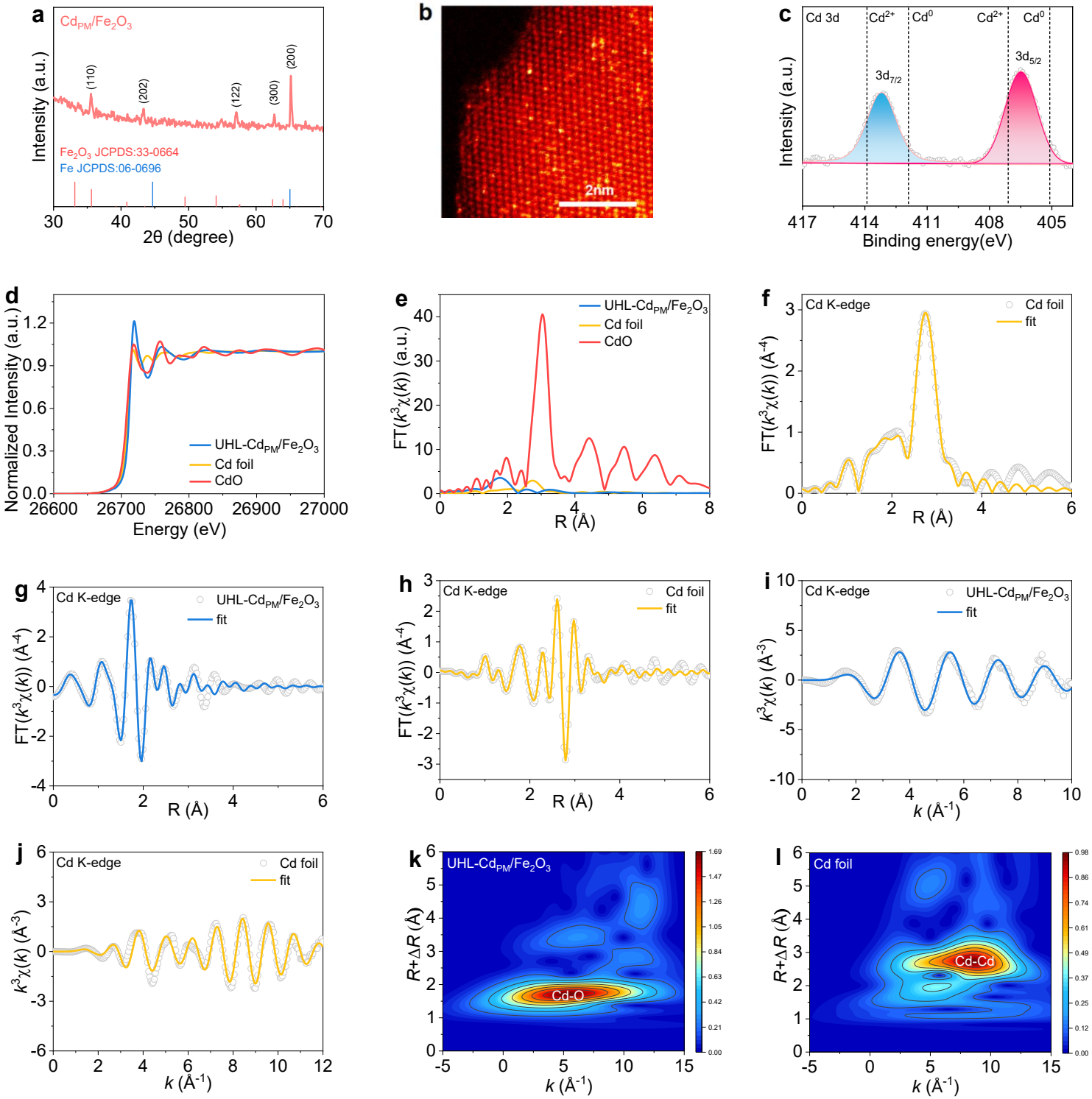

Supplementary Fig. 21 Structural characterization of Cd$_{PM}$/Fe$_2$O$_3$. a, XRD patterns of Cd$_{PM}$/Fe$_2$O$_3$. **b**, HAADF-STEM image of Cd$_{PM}$/Fe$_2$O$_3$. **c**, Cd 3d XPS spectra of Cd$_{PM}$/Fe$_2$O$_3$. **d**, Normalized Cd *K*-edge X-ray absorption near-edge structure (XANES) spectra. **e**, Fourier-transformed R-space of the experimental Cd *K*-edge EXAFS signals. **f-h,** Cd *K*-edge EXAFS data and fit for UHL-Cd$_{PM}$/Fe$_2$O$_3$ in *R*-space and **i, j,** *k*-space. **k,l,** WT-EXAFS plots of UHL-Cd$_{PM}$/Fe$_2$O$_3$ and Cd foil.

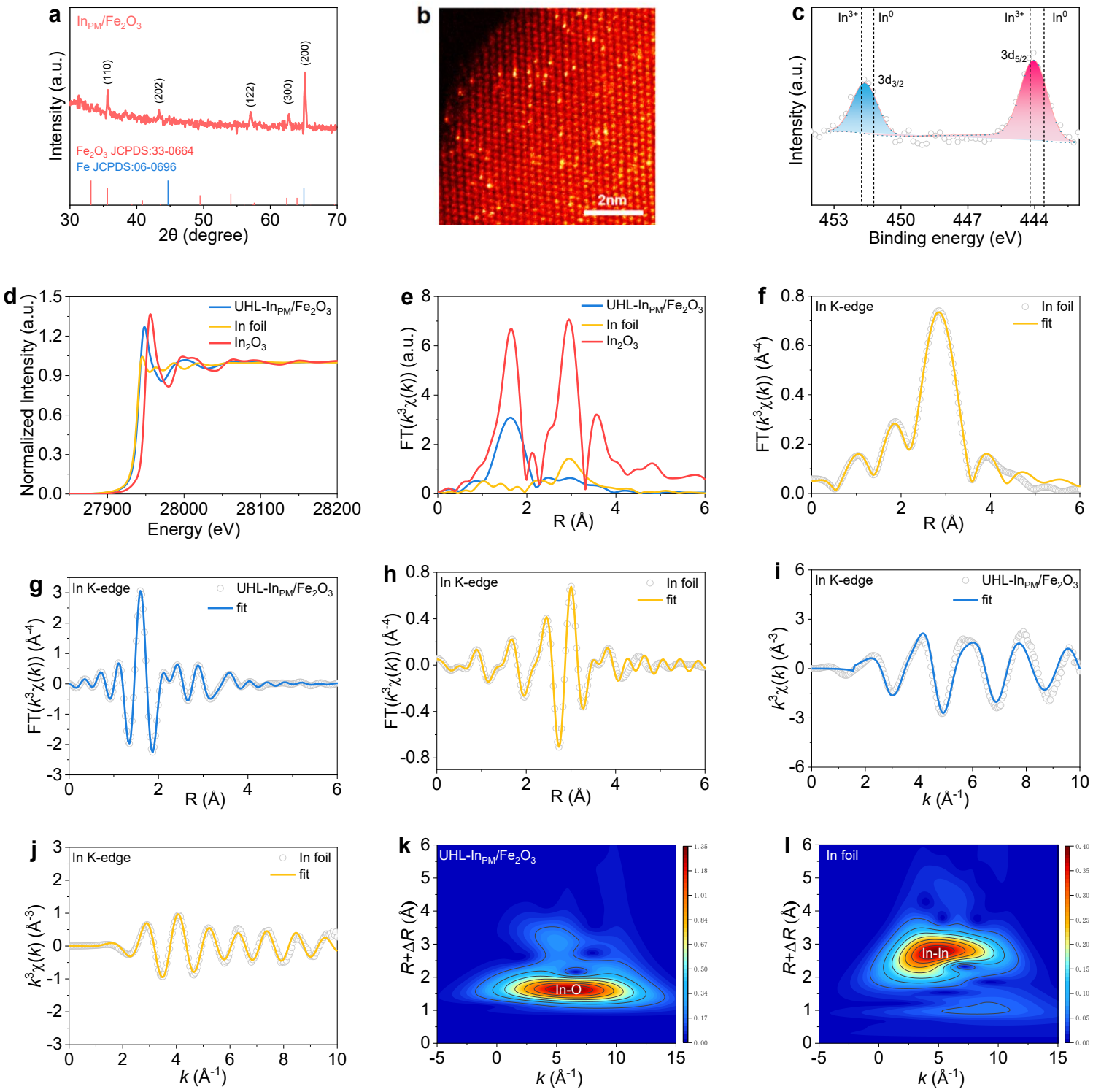

Supplementary Fig. 22 Structural characterization of In$_{PM}$/Fe$_2$O$_3$. **a**, XRD patterns of In$_{PM}$/Fe$_2$O$_3$. **b**, HAADF-STEM image of In$_{PM}$/Fe$_2$O$_3$. **c**, In 3d XPS spectra of In$_{PM}$/Fe$_2$O$_3$. **d**, Normalized In *K*-edge X-ray absorption near-edge structure (XANES) spectra. **e**, Fourier-transformed R-space of the experimental In *K*-edge EXAFS signals. **f-h,** In *K*-edge EXAFS data and fit for UHL-In$_{PM}$/Fe$_2$O$_3$ in *R*-space and **i, j,** *k*-space. **k,l,** WT-EXAFS plots of UHL-In$_{PM}$/Fe$_2$O$_3$ and In foil.

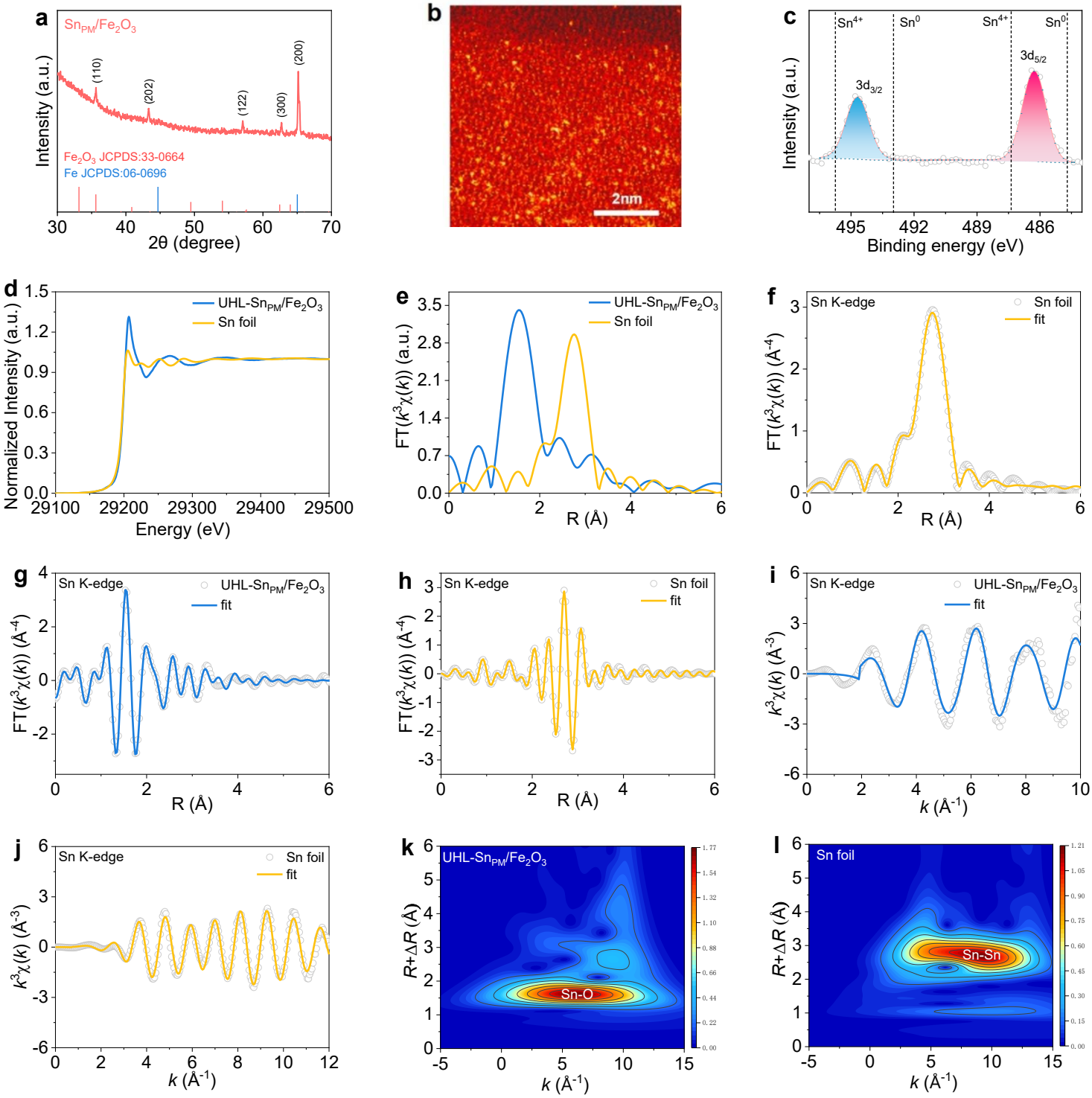

Supplementary Fig. 23 Structural characterization of Sn$_{PM}$/Fe$_2$O$_3$. a, XRD patterns of Sn$_{PM}$/Fe$_2$O$_3$. **b**, HAADF-STEM image of Sn$_{PM}$/Fe$_2$O$_3$. **c**, Sn 3d XPS spectra of Sn$_{PM}$/Fe$_2$O$_3$. **d**, Normalized Sn *K*-edge X-ray absorption near-edge structure (XANES) spectra. **e**, Fourier-transformed R-space of the experimental Sn *K*-edge EXAFS signals. **f-h,** Sn *K*-edge EXAFS data and fit for UHL-Sn$_{PM}$/Fe$_2$O$_3$ in *R*-space and **i, j,** *k*-space. **k,l,** WT-EXAFS plots of UHL-Sn$_{PM}$/Fe$_2$O$_3$ and Sn foil.

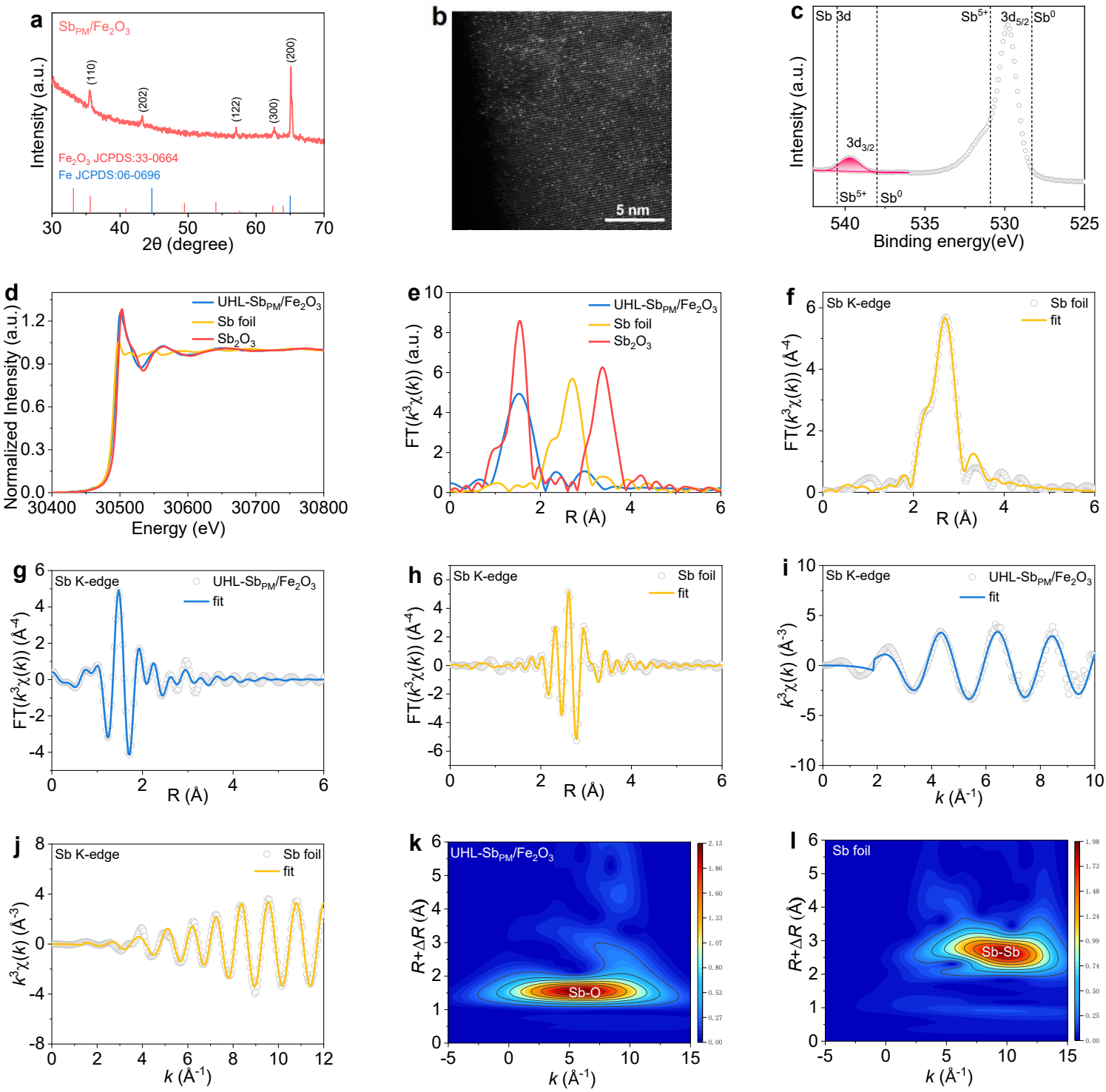

Supplementary Fig. 24 Structural characterization of Sb$_{PM}$/Fe$_2$O$_3$. a, XRD patterns of Sb$_{PM}$/Fe$_2$O$_3$. **b**, HAADF-STEM image of Sb$_{PM}$/Fe$_2$O$_3$. **c**, Sb 3d XPS spectra of Sb$_{PM}$/Fe$_2$O$_3$. **d**, Normalized Sd *K*-edge X-ray absorption near-edge structure (XANES) spectra. **e**, Fourier-transformed R-space of the experimental Sd *K*-edge EXAFS signals. **f-h,** Sd *K*-edge EXAFS data and fit for UHL-Sd$_{PM}$/Fe$_2$O$_3$ in *R*-space and **i, j,** *k*-space. **k,l,** WT-EXAFS plots of UHL-Sd$_{PM}$/Fe$_2$O$_3$ and Sd foil.

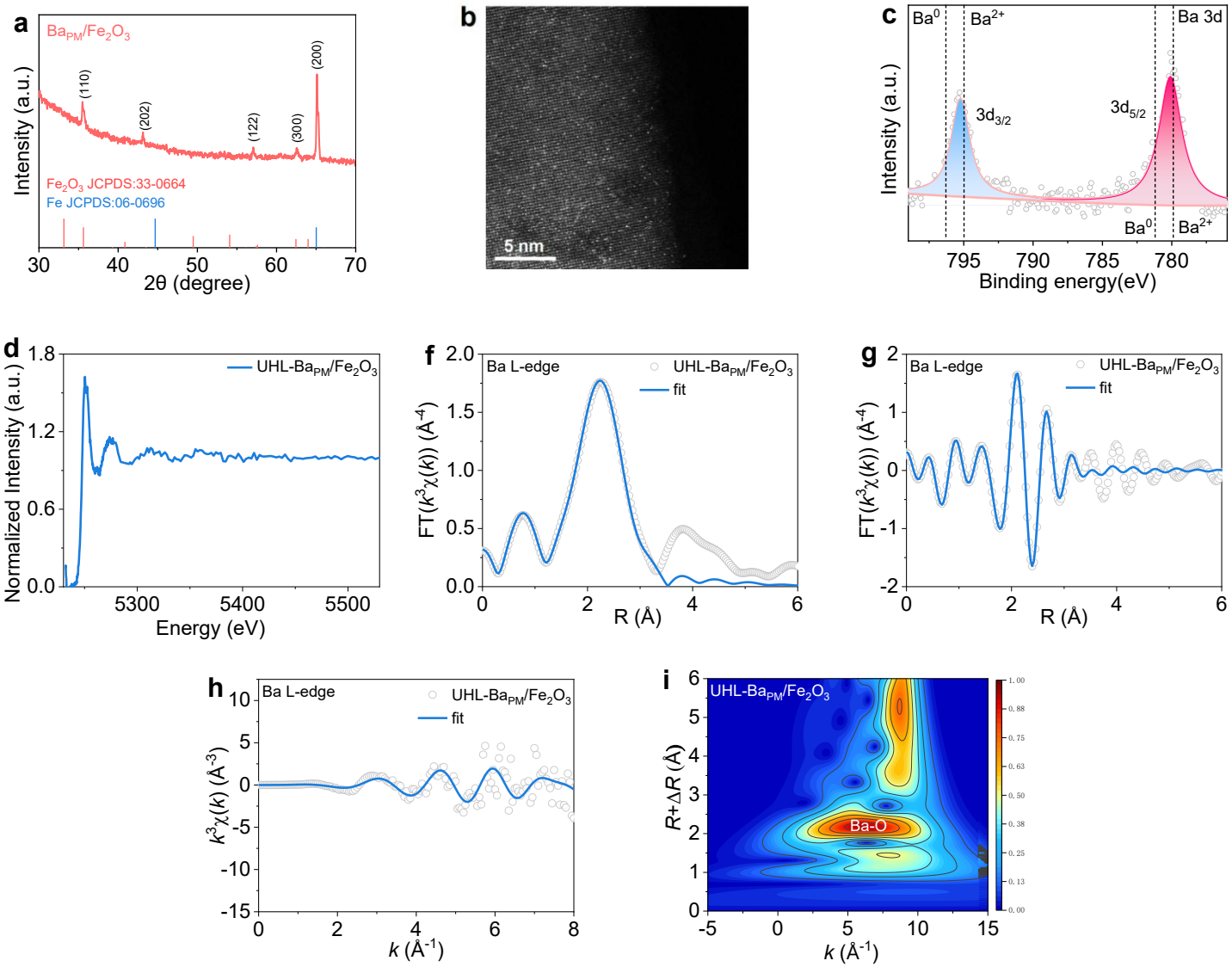

Supplementary Fig. 25 Structural characterization of Ba$_{PM}$/Fe$_2$O$_3$. a, XRD patterns of Ba$_{PM}$/Fe$_2$O$_3$. **b**, HAADF-STEM image of Ba$_{PM}$/Fe$_2$O$_3$. **c**, Ba 3d XPS spectra of Ba$_{PM}$/Fe$_2$O$_3$. **d**, Normalized Ba *L*-edge X-ray absorption near-edge structure (XANES) spectra. **e**, Fourier-transformed R-space of the experimental Ba *L*-edge EXAFS signals. **f-h,** Ba *L*-edge EXAFS data and fit for UHL-Ba$_{PM}$/Fe$_2$O$_3$ in *R*-space and **i, j,** *k*-space. **k,l,** WT-EXAFS plots of UHL-Ba$_{PM}$/Fe$_2$O$_3$ and Ba foil.

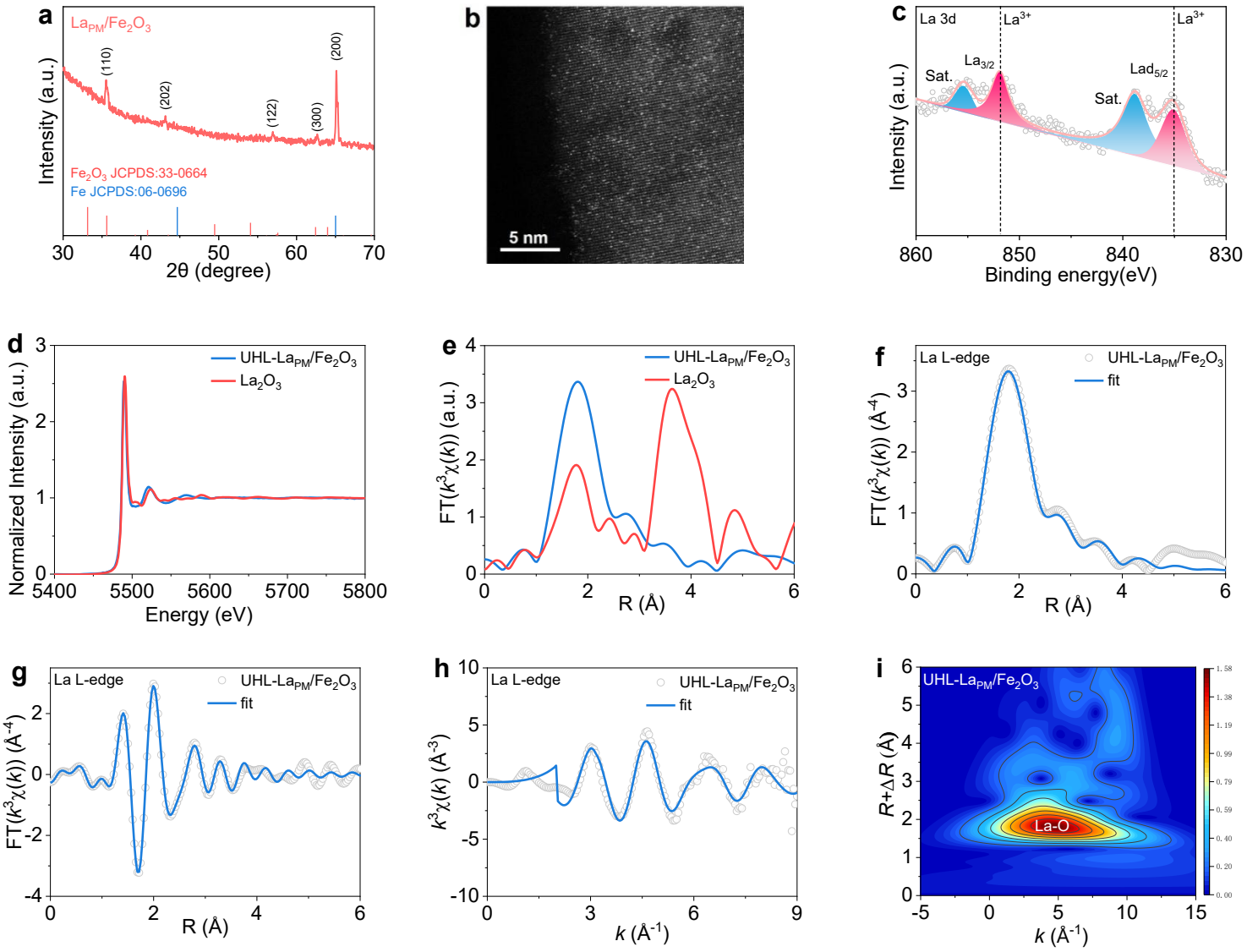

Supplementary Fig. 26 Structural characterization of La_{PM}/Fe_2O_3. **a**, XRD patterns of La_{PM}/Fe_2O_3. **b**, HAADF-STEM image of La_{PM}/Fe_2O_3. **c**, La 3d XPS spectra of La_{PM}/Fe_2O_3. **d**, Normalized La *L*-edge X-ray absorption near-edge structure (XANES) spectra. **e**, Fourier-transformed R-space of the experimental La *L*-edge EXAFS signals. **f-h,** La *L*-edge EXAFS data and fit for UHL-La_{PM}/Fe_2O_3 in *R*-space and **i, j,** *k*-space. **k,l,** WT-EXAFS plots of UHL-La_{PM}/Fe_2O_3 and La foil.

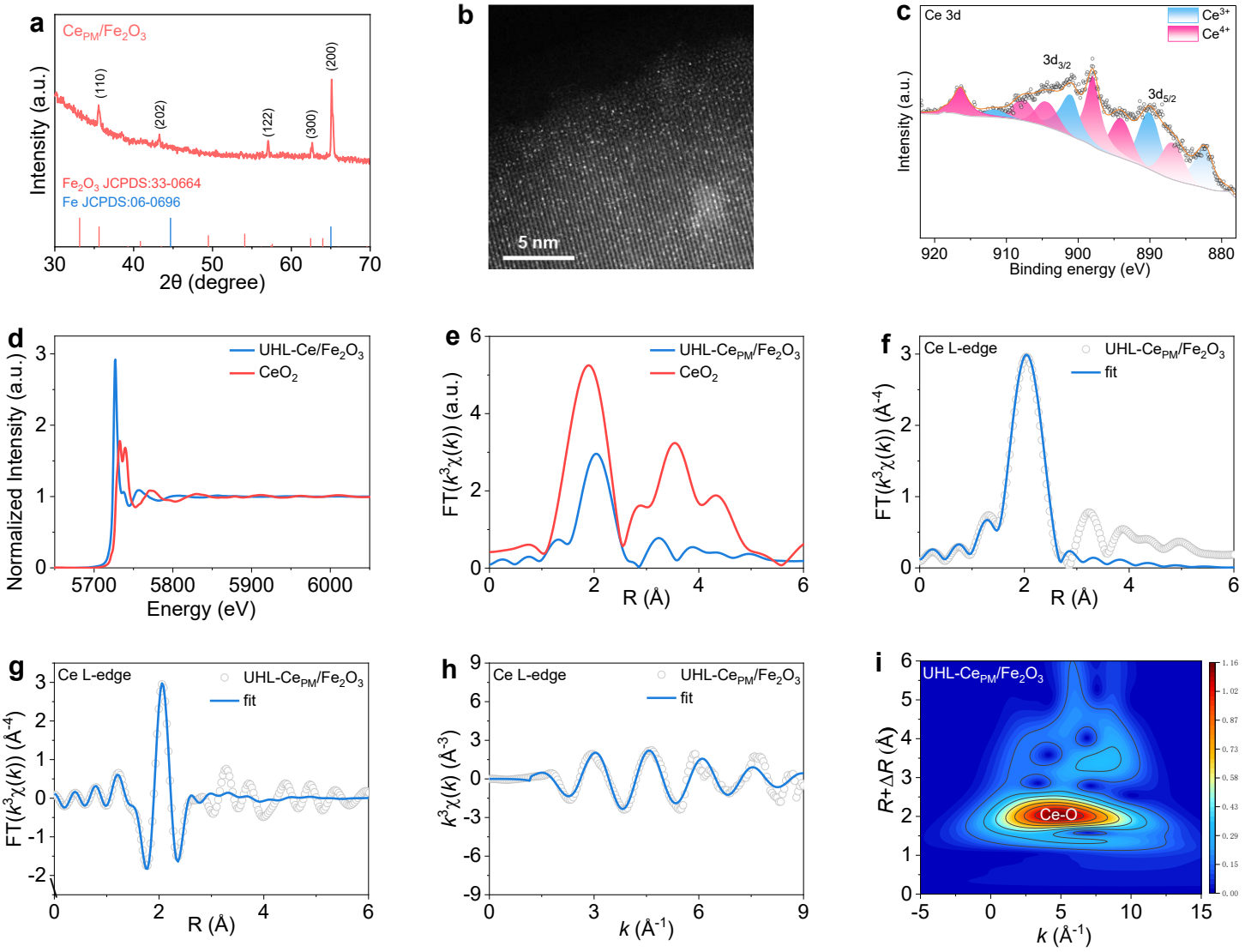

Supplementary Fig. 27 Structural characterization of Ce$_{PM}$/Fe$_2$O$_3$. **a**, XRD patterns of Ce$_{PM}$/Fe$_2$O$_3$. **b**, HAADF-STEM image of Ce$_{PM}$/Fe$_2$O$_3$. **c**, Ce 3d XPS spectra of Ce$_{PM}$/Fe$_2$O$_3$. **d**, Normalized Ce *L*-edge X-ray absorption near-edge structure (XANES) spectra. **e**, Fourier-transformed R-space of the experimental Ce *L*-edge EXAFS signals. **f-h,** Ce *L*-edge EXAFS data and fit for UHL-Ce$_{PM}$/Fe$_2$O$_3$ in *R*-space and **i, j,** *k*-space. **k,l,** WT-EXAFS plots of UHL-Ce$_{PM}$/Fe$_2$O$_3$ and Ce foil.

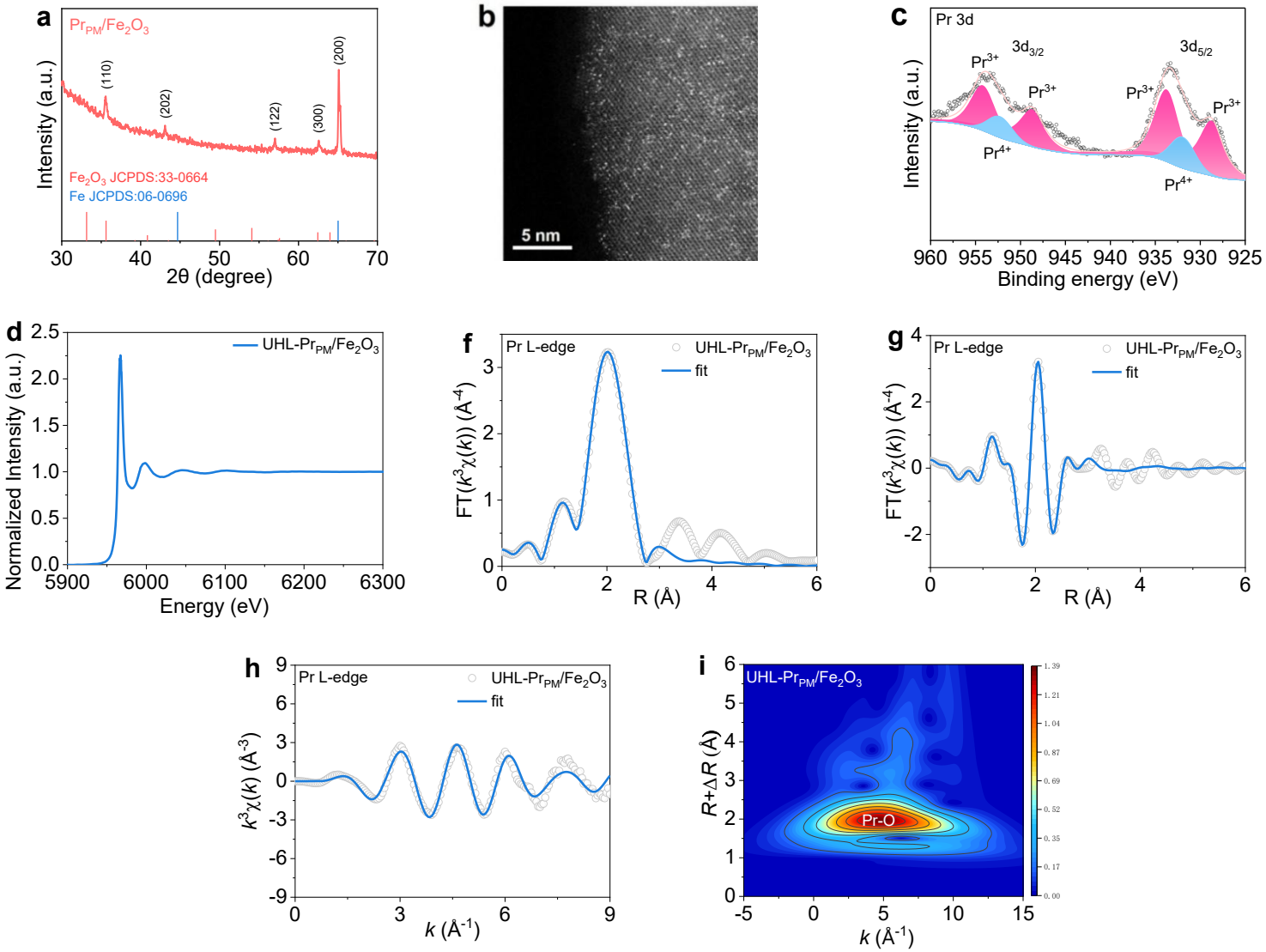

Supplementary Fig. 28 Structural characterization of Pr_{PM}/Fe_2O_3. **a**, XRD patterns of Pr_{PM}/Fe_2O_3. **b**, HAADF-STEM image of Pr_{PM}/Fe_2O_3. **c**, Pr 4f XPS spectra of Pr_{PM}/Fe_2O_3. **d**, Normalized Pr *K*-edge X-ray absorption near-edge structure (XANES) spectra. **e**, Fourier-transformed R-space of the experimental Pr *L*-edge EXAFS signals. **f-h,** Pr *L*-edge EXAFS data and fit for UHL-Pr_{PM}/Fe_2O_3 in *R*-space and **i, j,** *k*-space. **k,l,** WT-EXAFS plots of UHL-Pr_{PM}/Fe_2O_3 and Pr foil.

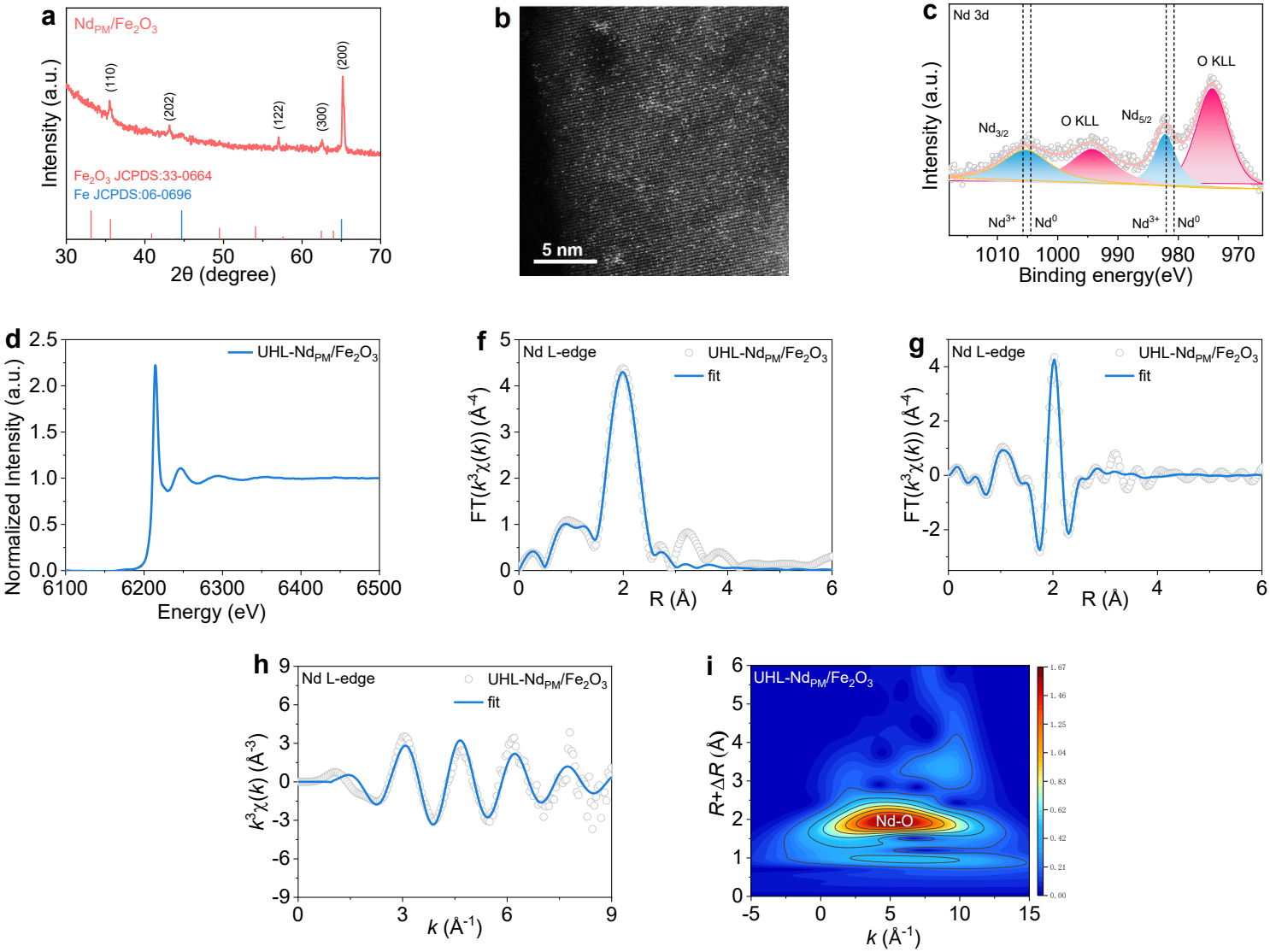

Supplementary Fig. 29 Structural characterization of Nd$_{PM}$/Fe$_2$O$_3$. **a**, XRD patterns of Nd$_{PM}$/Fe$_2$O$_3$. **b**, HAADF-STEM image of Nd$_{PM}$/Fe$_2$O$_3$. **c**, Nd 3d XPS spectra of Nd$_{PM}$/Fe$_2$O$_3$. **d**, Normalized Nd *L*-edge X-ray absorption near-edge structure (XANES) spectra. **e**, Fourier-transformed R-space of the experimental Nd *L*-edge EXAFS signals. **f-h,** Nd *L*-edge EXAFS data and fit for UHL-Nd$_{PM}$/Fe$_2$O$_3$ in *R*-space and **i, j,** *k*-space. **k,l,** WT-EXAFS plots of UHL-Nd$_{PM}$/Fe$_2$O$_3$ and Nd foil.

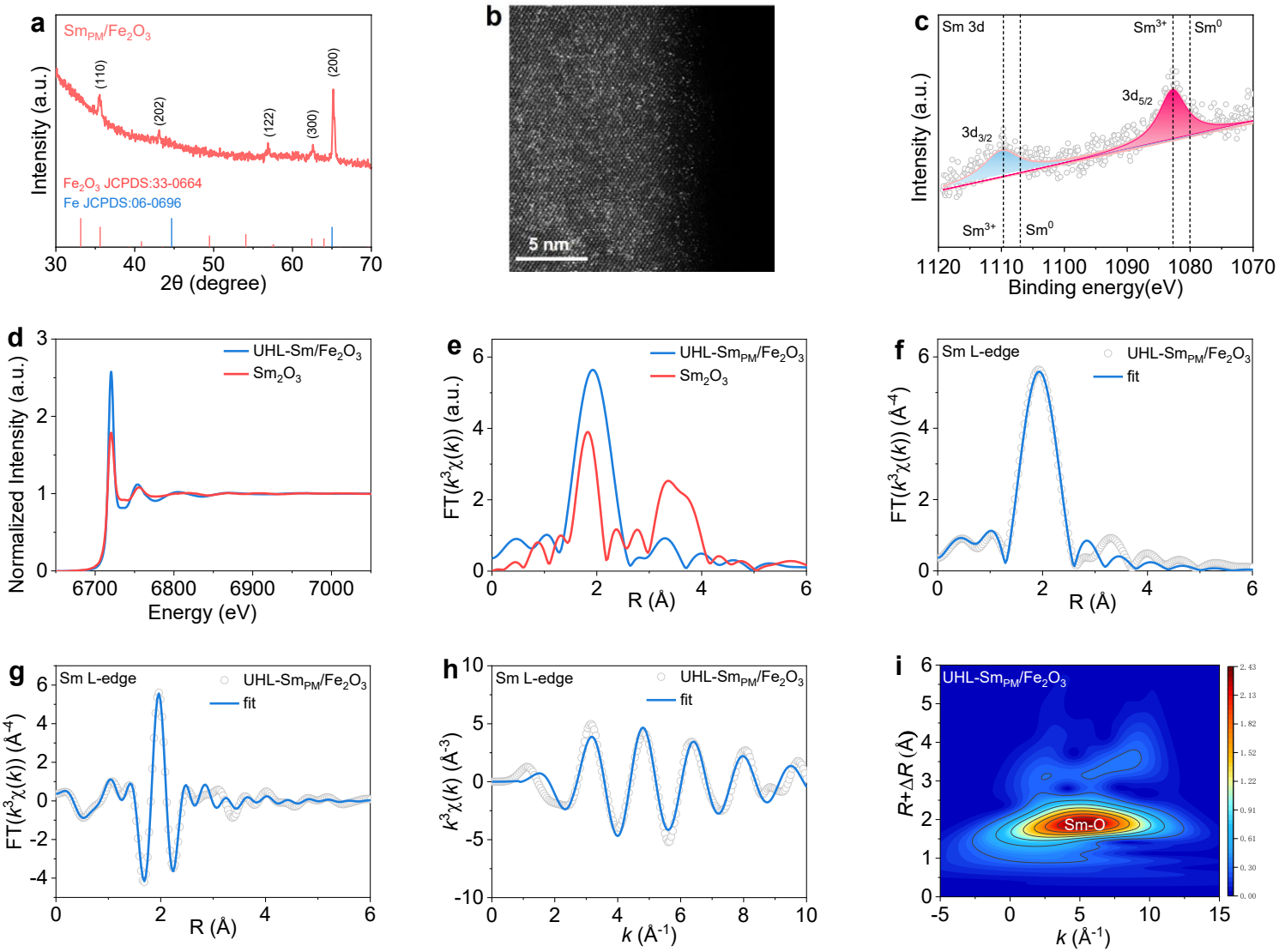

Supplementary Fig. 30 Structural characterization of Sm$_{PM}$/Fe$_2$O$_3$. **a**, XRD patterns of Sm$_{PM}$/Fe$_2$O$_3$. **b**, HAADF-STEM image of Sm$_{PM}$/Fe$_2$O$_3$. **c**, Sm 3d XPS spectra of Sm$_{PM}$/Fe$_2$O$_3$. **d**, Normalized Sm *L*-edge X-ray absorption near-edge structure (XANES) spectra. **e**, Fourier-transformed R-space of the experimental Sm *L*-edge EXAFS signals. **f-h,** Sm *L*-edge EXAFS data and fit for UHL-Sm$_{PM}$/Fe$_2$O$_3$ in *R*-space and **i, j,** *k*-space. **k,l,** WT-EXAFS plots of UHL-Sm$_{PM}$/Fe$_2$O$_3$ and Sm foil.

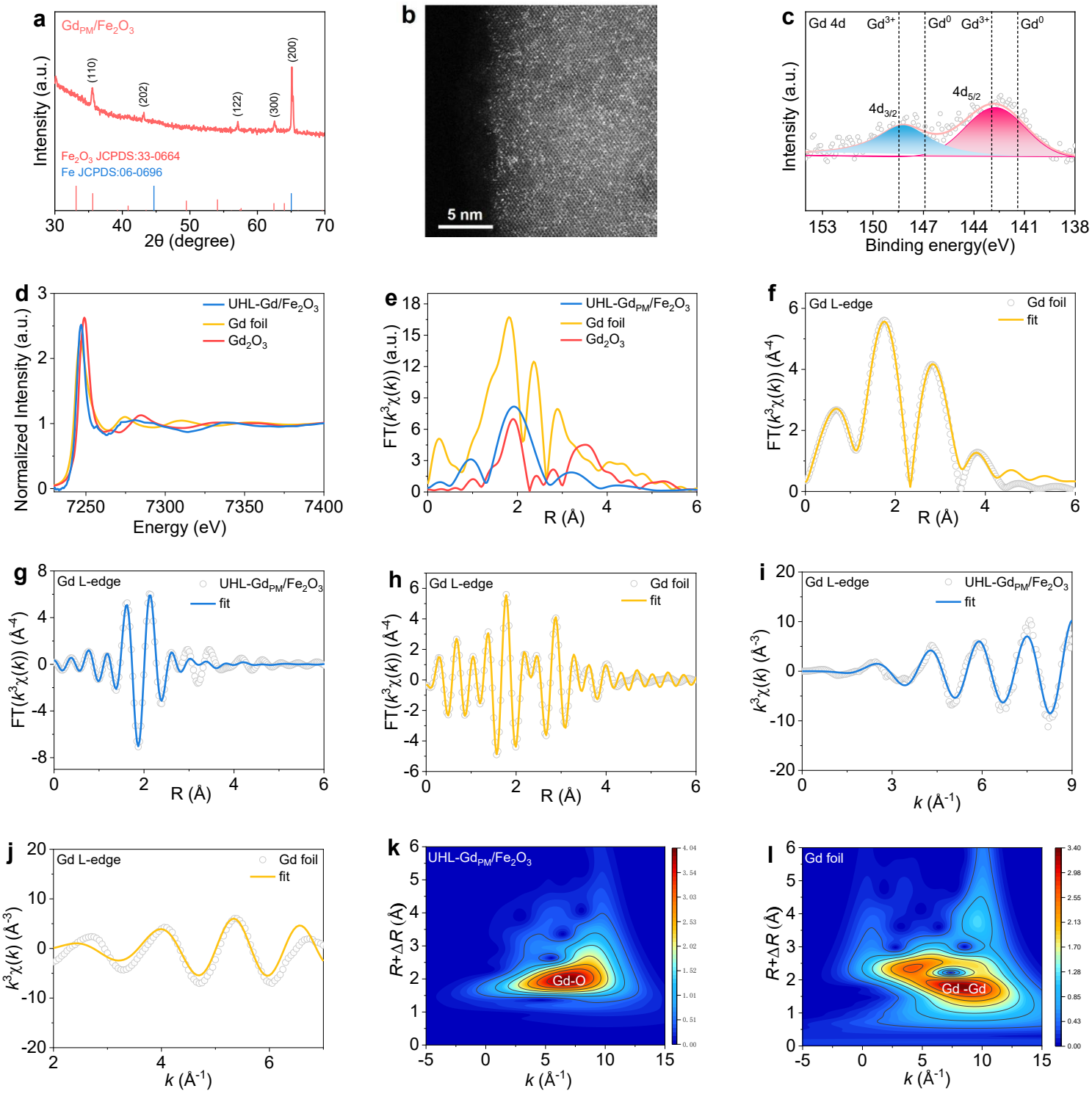

Supplementary Fig. 31 Structural characterization of Gd$_{PM}$/Fe$_2$O$_3$. a, XRD patterns of Gd$_{PM}$/Fe$_2$O$_3$. **b**, HAADF-STEM image of Gd$_{PM}$/Fe$_2$O$_3$. **c**, Gd 3d XPS spectra of Gd$_{PM}$/Fe$_2$O$_3$. **d**, Normalized Gd *L*-edge X-ray absorption near-edge structure (XANES) spectra. **e**, Fourier-transformed R-space of the experimental Gd *L*-edge EXAFS signals. **f-h,** Gd *L*-edge EXAFS data and fit for UHL-Gd$_{PM}$/Fe$_2$O$_3$ in *R*-space and **i, j,** *k*-space. **k,l,** WT-EXAFS plots of UHL-Gd$_{PM}$/Fe$_2$O$_3$ and Gd foil.

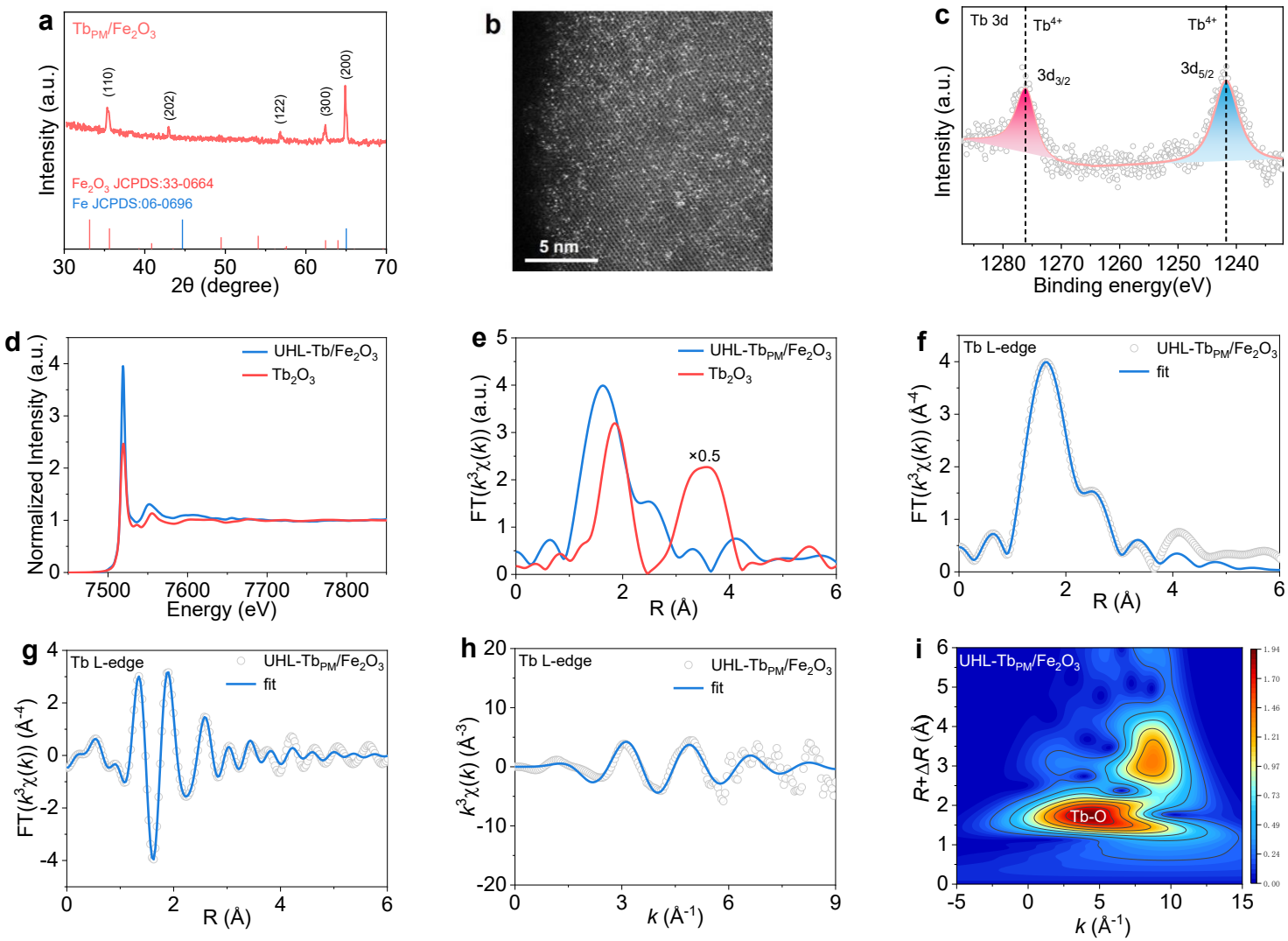

Supplementary Fig. 32 Structural characterization of Tb_{PM}/Fe_2O_3. a, XRD patterns of Tb_{PM}/Fe_2O_3. **b**, HAADF-STEM image of Tb_{PM}/Fe_2O_3. **c**, Tb 3d XPS spectra of Tb_{PM}/Fe_2O_3. **d**, Normalized Tb *L*-edge X-ray absorption near-edge structure (XANES) spectra. **e**, Fourier-transformed R-space of the experimental Tb *L*-edge EXAFS signals. **f-g,** Tb *L*-edge EXAFS data and fit for UHL-Tb_{PM}/Fe_2O_3 in *R*-space and **h,** *k*-space. **i,** WT-EXAFS plots of UHL-Tb_{PM}/Fe_2O_3 and Tb foil.

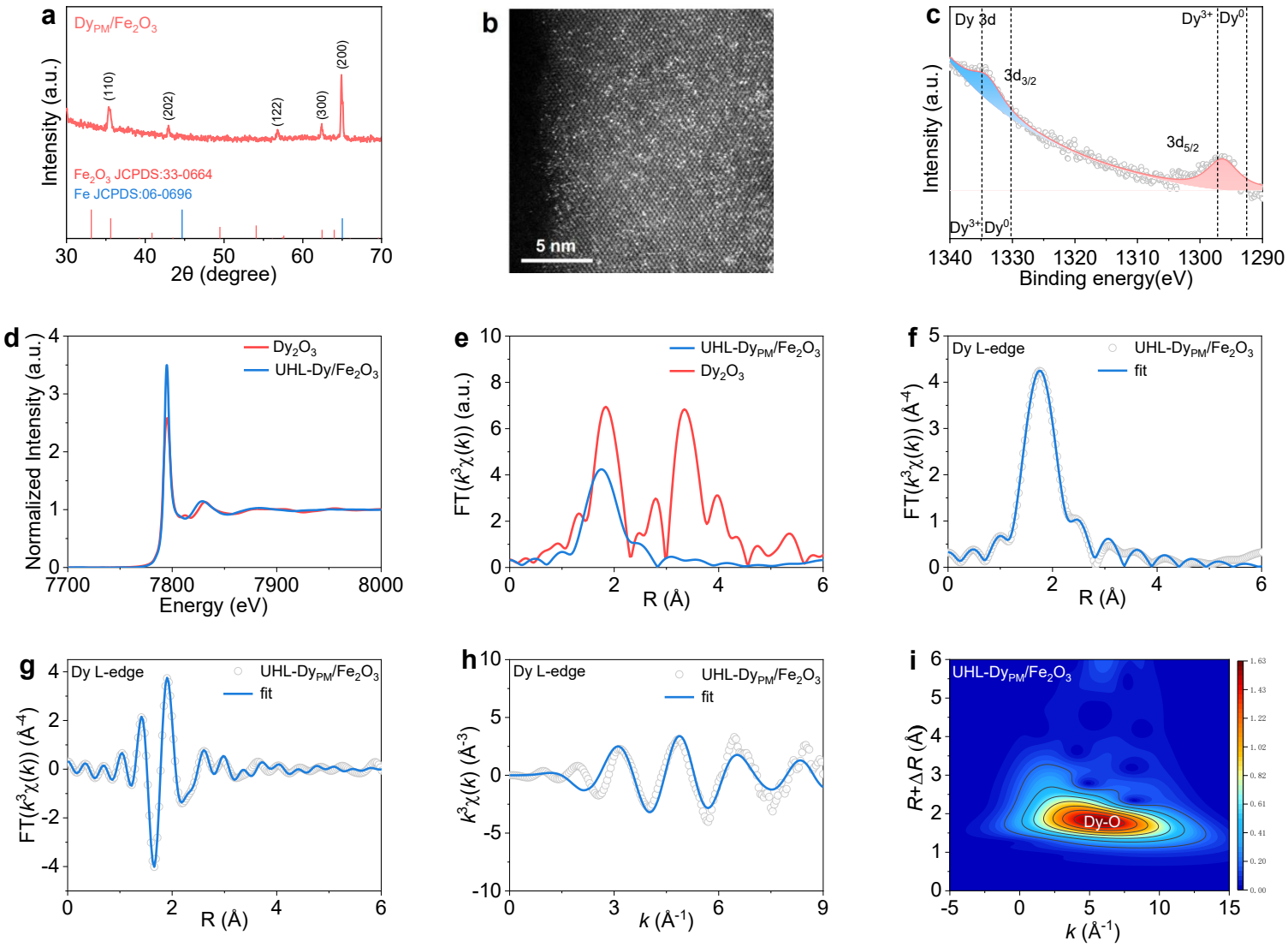

Supplementary Fig. 33 Structural characterization of Dy_{PM}/Fe_2O_3. **a**, XRD patterns of Dy_{PM}/Fe_2O_3. **b**, HAADF-STEM image of Dy_{PM}/Fe_2O_3. **c**, Dy 3d XPS spectra of Dy_{PM}/Fe_2O_3. **d**, Normalized Dy *L*-edge X-ray absorption near-edge structure (XANES) spectra. **e**, Fourier-transformed R-space of the experimental Dy *L*-edge EXAFS signals. **f-g,** Dy *L*-edge EXAFS data and fit for UHL-Dy_{PM}/Fe_2O_3 in *R*-space and **h,** *k*-space. **i,** WT-EXAFS plots of UHL-Dy_{PM}/Fe_2O_3 and Dy foil.

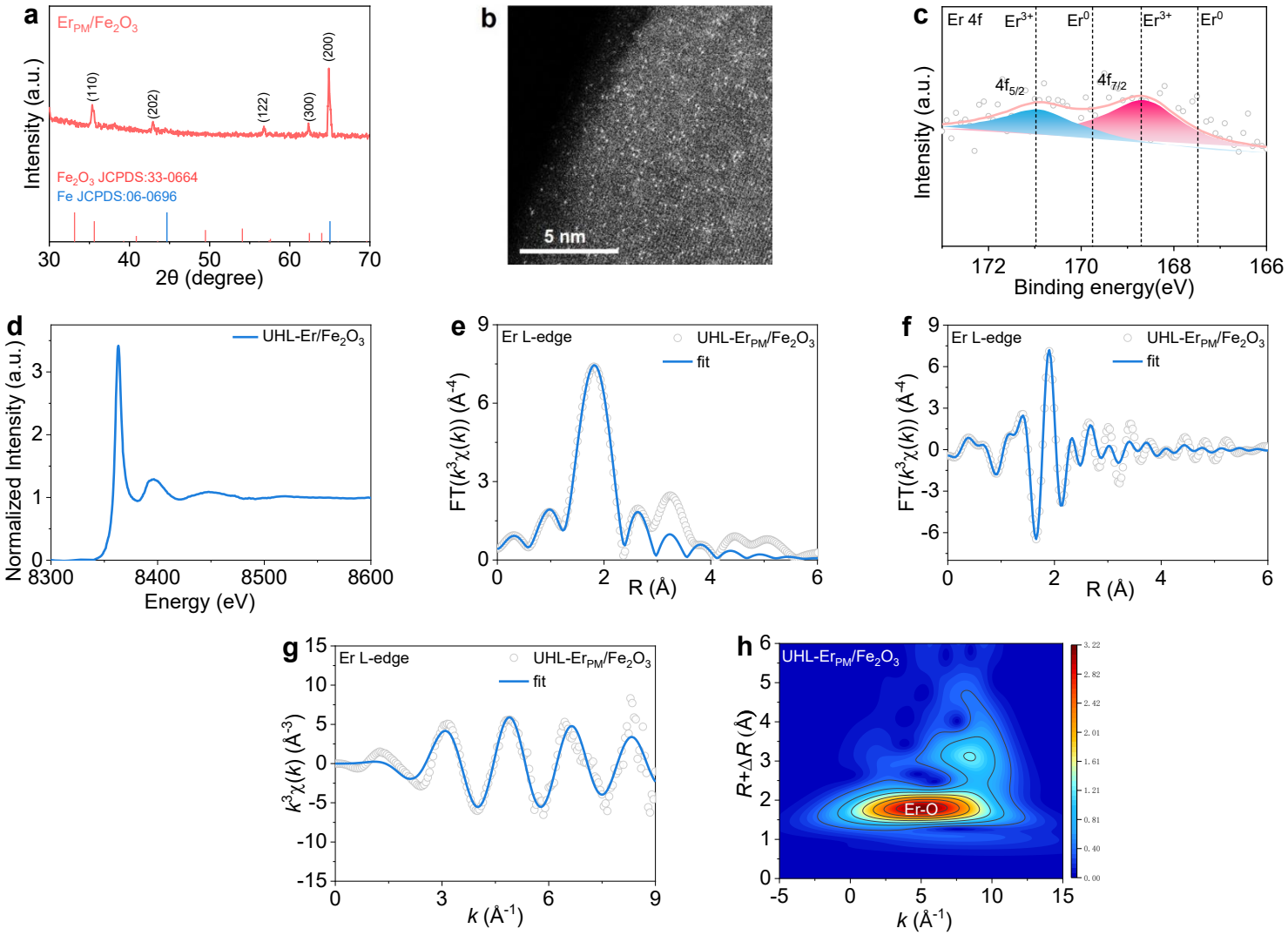

Supplementary Fig. 34 Structural characterization of Er$_{PM}$/Fe$_2$O$_3$. a, XRD patterns of Er$_{PM}$/Fe$_2$O$_3$. **b**, HAADF-STEM image of Er$_{PM}$/Fe$_2$O$_3$. **c**, Er 4f XPS spectra of Er$_{PM}$/Fe$_2$O$_3$. **d**, Normalized Er *L*-edge X-ray absorption near-edge structure (XANES) spectra. **e**, Fourier-transformed R-space of the experimental Er *L*-edge EXAFS signals. **f,** Er *L*-edge EXAFS data and fit for UHL-Er$_{PM}$/Fe$_2$O$_3$ in *R*-space and **g,** *k*-space. **h,** WT-EXAFS plot of UHL-Er$_{PM}$/Fe$_2$O$_3$.

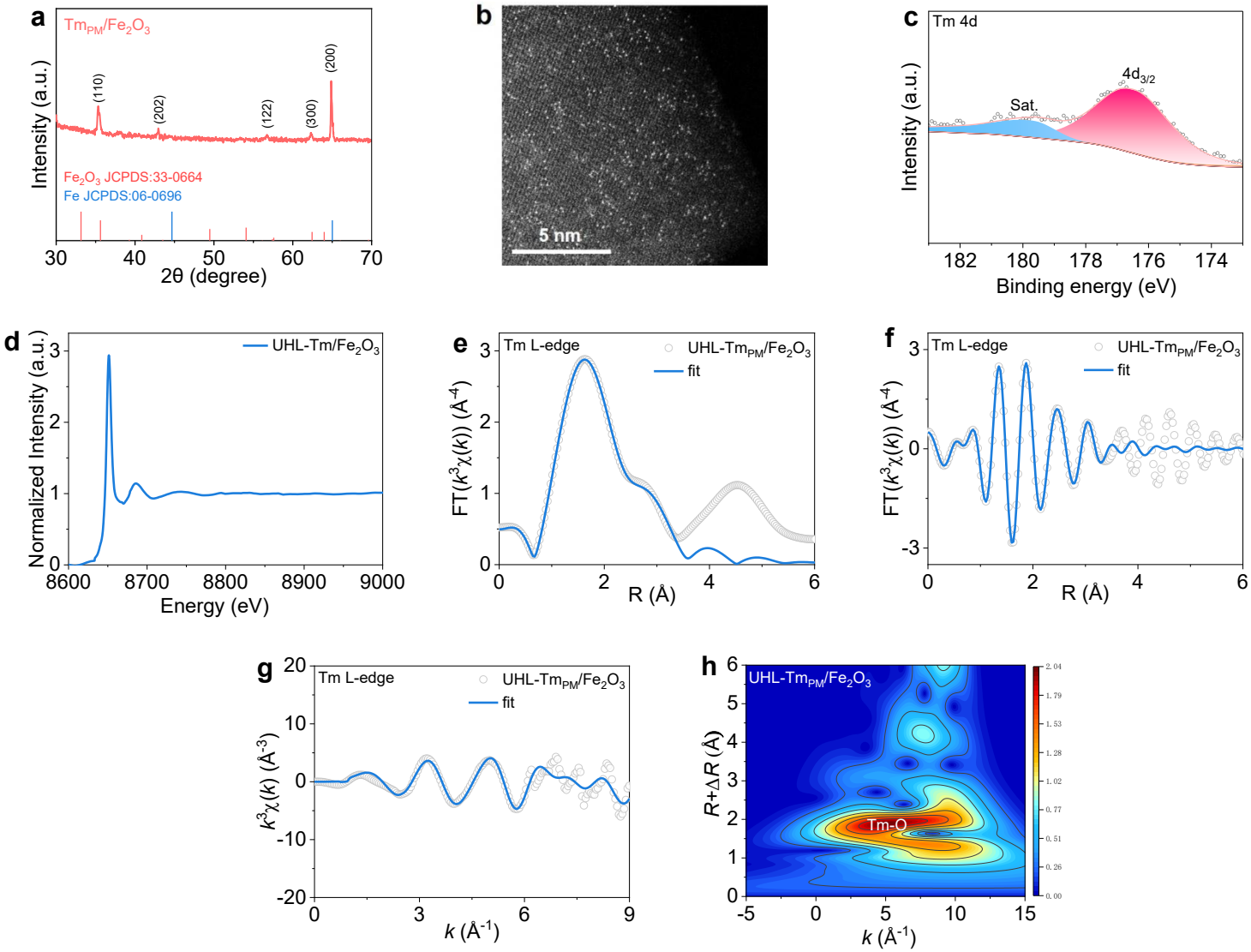

Supplementary Fig. 35 Structural characterization of Tm$_{PM}$/Fe$_2$O$_3$. **a**, XRD patterns of Tm$_{PM}$/Fe$_2$O$_3$. **b**, HAADF-STEM image of Tm$_{PM}$/Fe$_2$O$_3$. **c**, Tm 4d XPS spectra of Tm$_{PM}$/Fe$_2$O$_3$. **d**, Normalized Tm *L*-edge X-ray absorption near-edge structure (XANES) spectra. **e**, Fourier-transformed R-space of the experimental Tm *L*-edge EXAFS signals. **f,** Tm *L*-edge EXAFS data and fit for UHL-Tm$_{PM}$/Fe$_2$O$_3$ in *R*-space and **g,** *k*-space. **h,** WT-EXAFS plot of UHL-Tm$_{PM}$/Fe$_2$O$_3$.

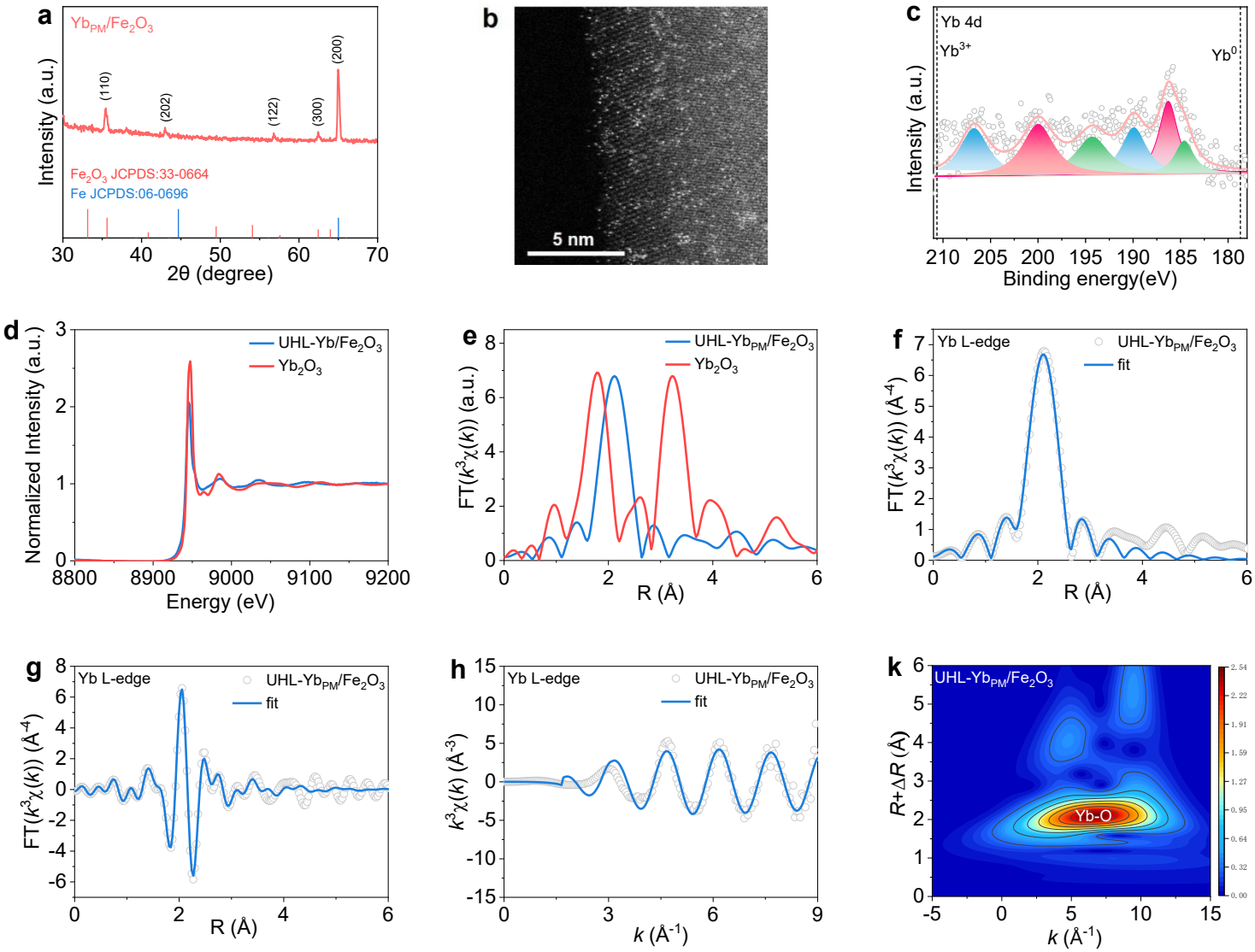

Supplementary Fig. 36 Structural characterization of Yb$_{PM}$/Fe$_2$O$_3$. a, XRD patterns of Yb$_{PM}$/Fe$_2$O$_3$. **b**, HAADF-STEM image of Yb$_{PM}$/Fe$_2$O$_3$. **c**, Yb 4d XPS spectra of Yb$_{PM}$/Fe$_2$O$_3$. **d**, Normalized Yb *L*-edge X-ray absorption near-edge structure (XANES) spectra. **e**, Fourier-transformed R-space of the experimental Yb *L*-edge EXAFS signals. **f,g,** Yb *L*-edge EXAFS data and fit for UHL-Yb$_{PM}$/Fe$_2$O$_3$ in *R*-space and **h,** *k*-space. **k,l,** WT-EXAFS plots of UHL-Yb$_{PM}$/Fe$_2$O$_3$ and Yb foil.

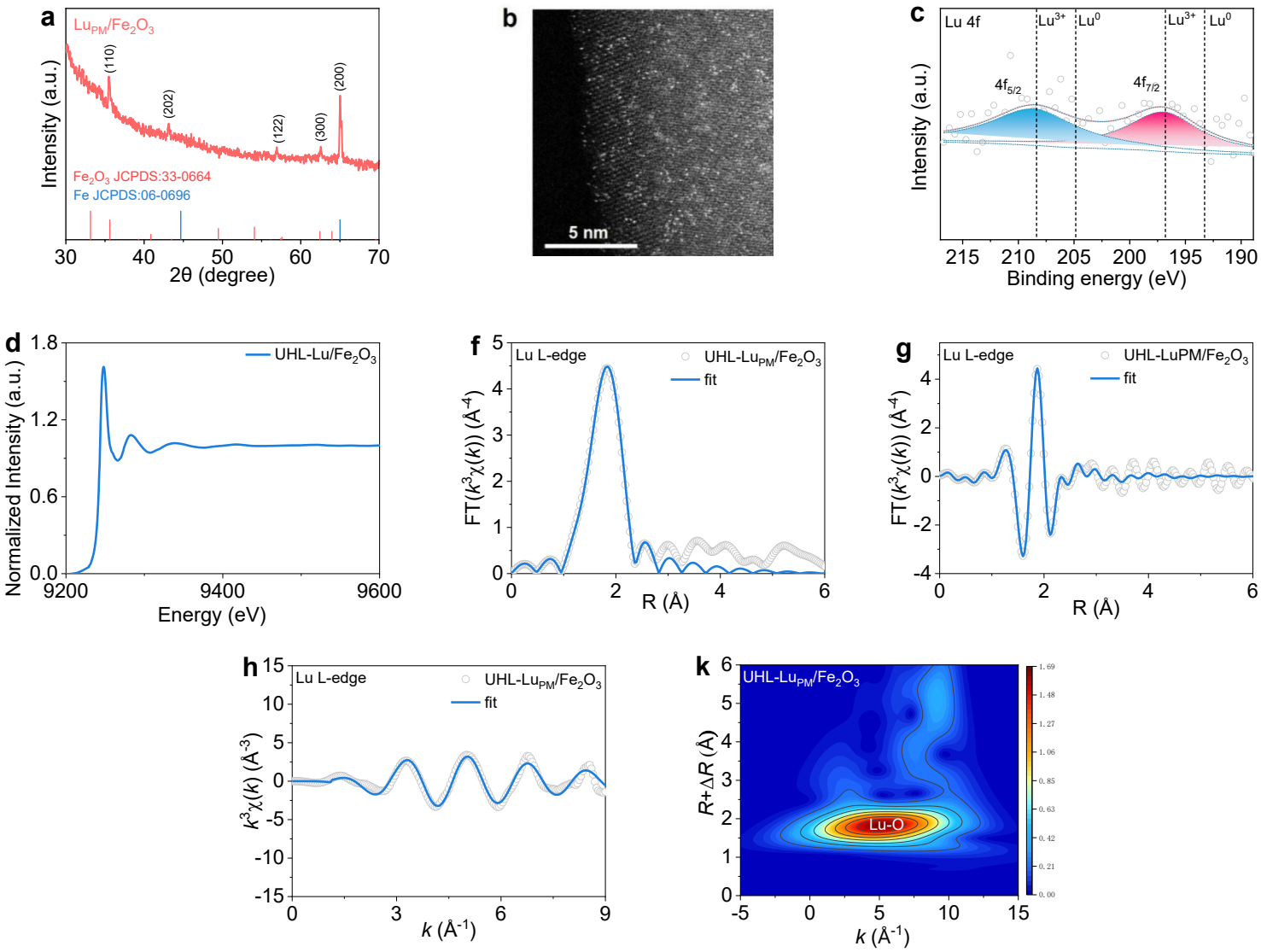

Supplementary Fig. 37 Structural characterization of Lu$_{PM}$/Fe$_2$O$_3$. **a**, XRD patterns of Lu$_{PM}$/Fe$_2$O$_3$. **b**, HAADF-STEM image of Lu$_{PM}$/Fe$_2$O$_3$. **c**, Lu 4f XPS spectra of Lu$_{PM}$/Fe$_2$O$_3$. **d**, Normalized Lu *L*-edge X-ray absorption near-edge structure (XANES) spectra. **e**, Fourier-transformed R-space of the experimental Lu *L*-edge EXAFS signals. **f,g,** Lu *L*-edge EXAFS data and fit for UHL-Lu$_{PM}$/Fe$_2$O$_3$ in *R*-space and **h,** *k*-space. **k,** WT-EXAFS plot of UHL-Lu$_{PM}$/Fe$_2$O$_3$.

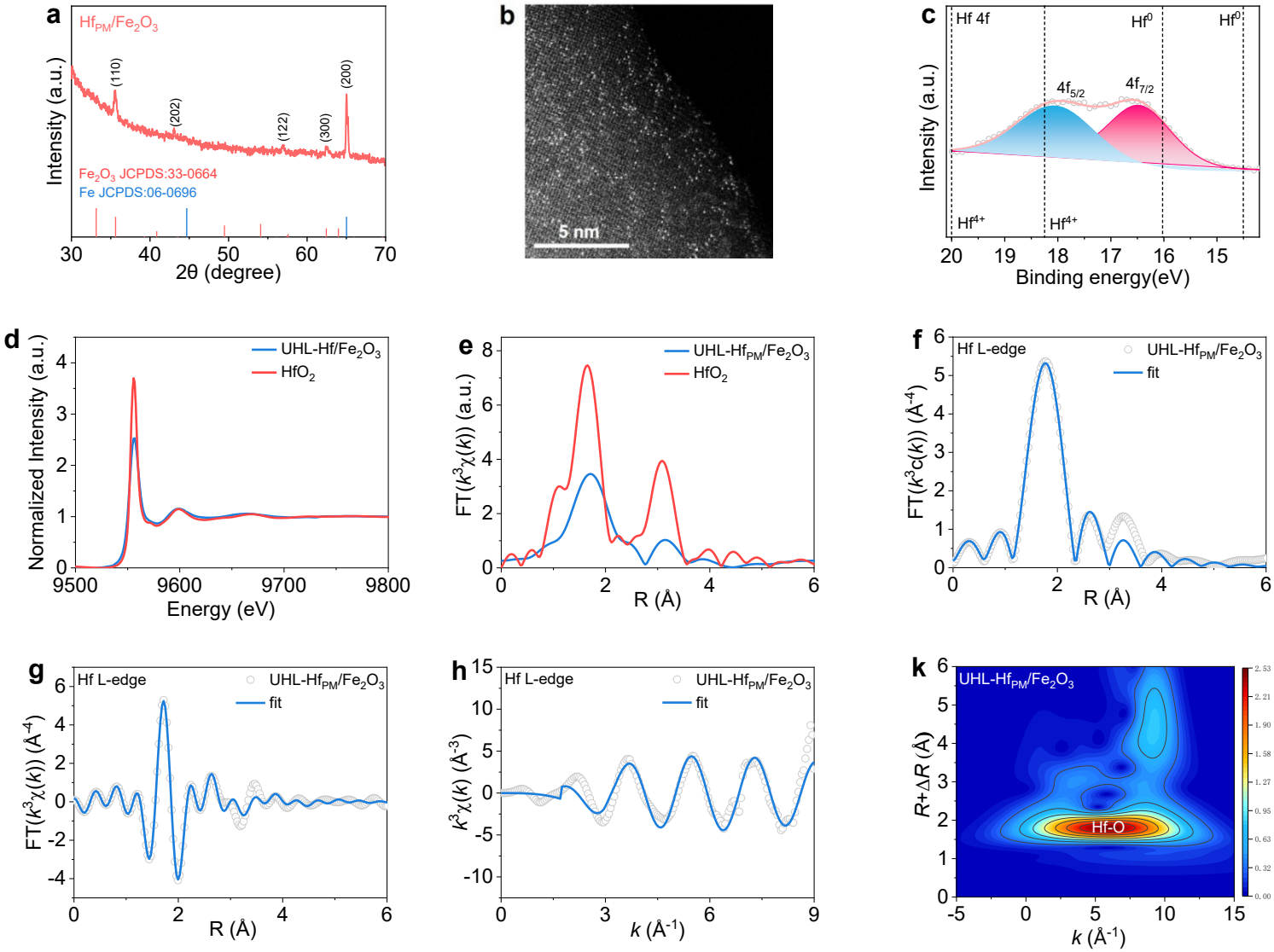

Supplementary Fig. 38 Structural characterization of Hf$_{PM}$/Fe$_2$O$_3$. a, XRD patterns of Hf$_{PM}$/Fe$_2$O$_3$. **b**, HAADF-STEM image of Hf$_{PM}$/Fe$_2$O$_3$. **c**, Hf 4f XPS spectra of Hf$_{PM}$/Fe$_2$O$_3$. **d**, Normalized Hf *L*-edge X-ray absorption near-edge structure (XANES) spectra. **e**, Fourier-transformed R-space of the experimental Hf *L*-edge EXAFS signals. **f,g,** Hf *L*-edge EXAFS data and fit for UHL-Hf$_{PM}$/Fe$_2$O$_3$ in *R*-space and **h,** *k*-space. **k,** WT-EXAFS plots of UHL-Hf$_{PM}$/Fe$_2$O$_3$.

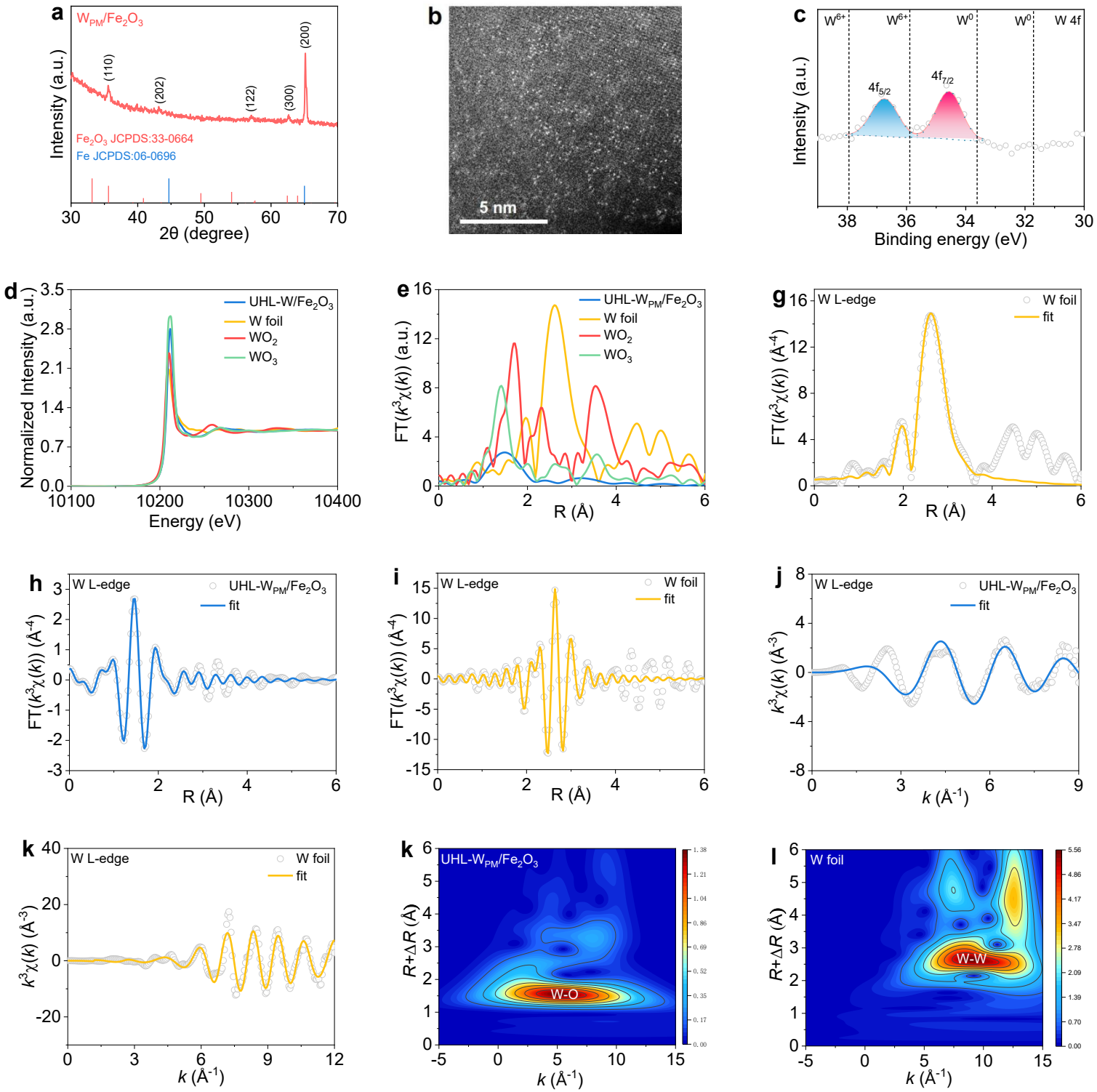

Supplementary Fig. 39 Structural characterization of W_{PM}/Fe_2O_3. **a**, XRD patterns of W_{PM}/Fe_2O_3. **b**, HAADF-STEM image of W_{PM}/Fe_2O_3. **c**, W 4F XPS spectra of W_{PM}/Fe_2O_3. **d**, Normalized W *L*-edge X-ray absorption near-edge structure (XANES) spectra. **e**, Fourier-transformed R-space of the experimental W *L*-edge EXAFS signals. **f-h,** W *L*-edge EXAFS data and fit for UHL-W_{PM}/Fe_2O_3 in *R*-space and **i, j,** *k*-space. **k,l,** WT-EXAFS plots of UHL-W_{PM}/Fe_2O_3 and W foil.

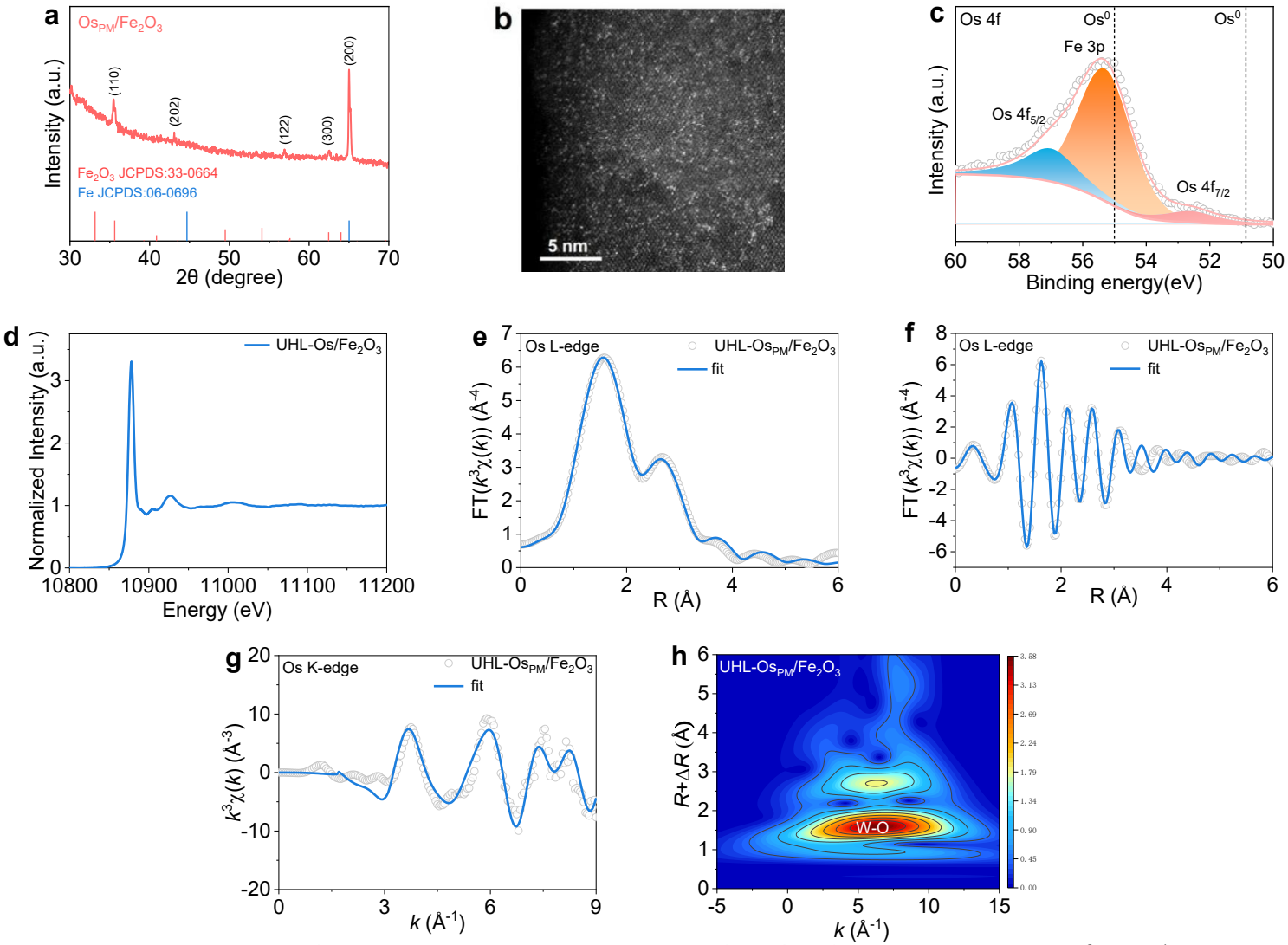

Supplementary Fig. 40 Structural characterization of Os$_{PM}$/Fe$_2$O$_3$. a, XRD patterns of Os$_{PM}$/Fe$_2$O$_3$. **b**, HAADF-STEM image of Os$_{PM}$/Fe$_2$O$_3$. **c**, Os 4f XPS spectra of Os$_{PM}$/Fe$_2$O$_3$. **d**, Normalized Os *L*-edge X-ray absorption near-edge structure (XANES) spectra. **e**, Fourier-transformed R-space of the experimental Os *L*-edge EXAFS signals. **f,** Os *L*-edge EXAFS data and fit for UHL-Os$_{PM}$/Fe$_2$O$_3$ in *R*-space and **g,** *k*-space. **h,** WT-EXAFS plots of UHL-Os$_{PM}$/Fe$_2$O$_3$.

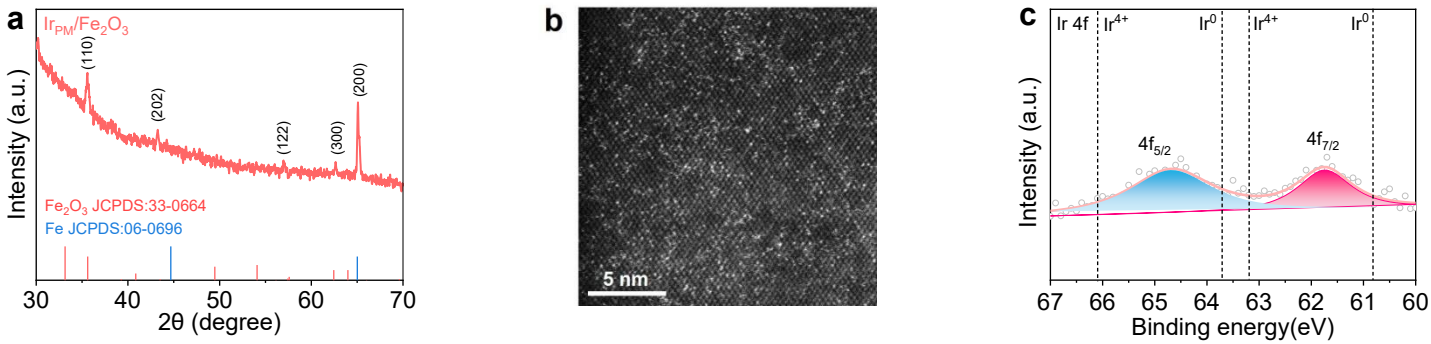

Supplementary Fig. 41 Structural characterization of Ir_{PM}/Fe_2O_3. a, XRD patterns of Ir_{PM}/Fe_2O_3. **b**, HAADF-STEM image of Ir_{PM}/Fe_2O_3. **c**, Ir 4f XPS spectra of Ir_{PM}/Fe_2O_3.

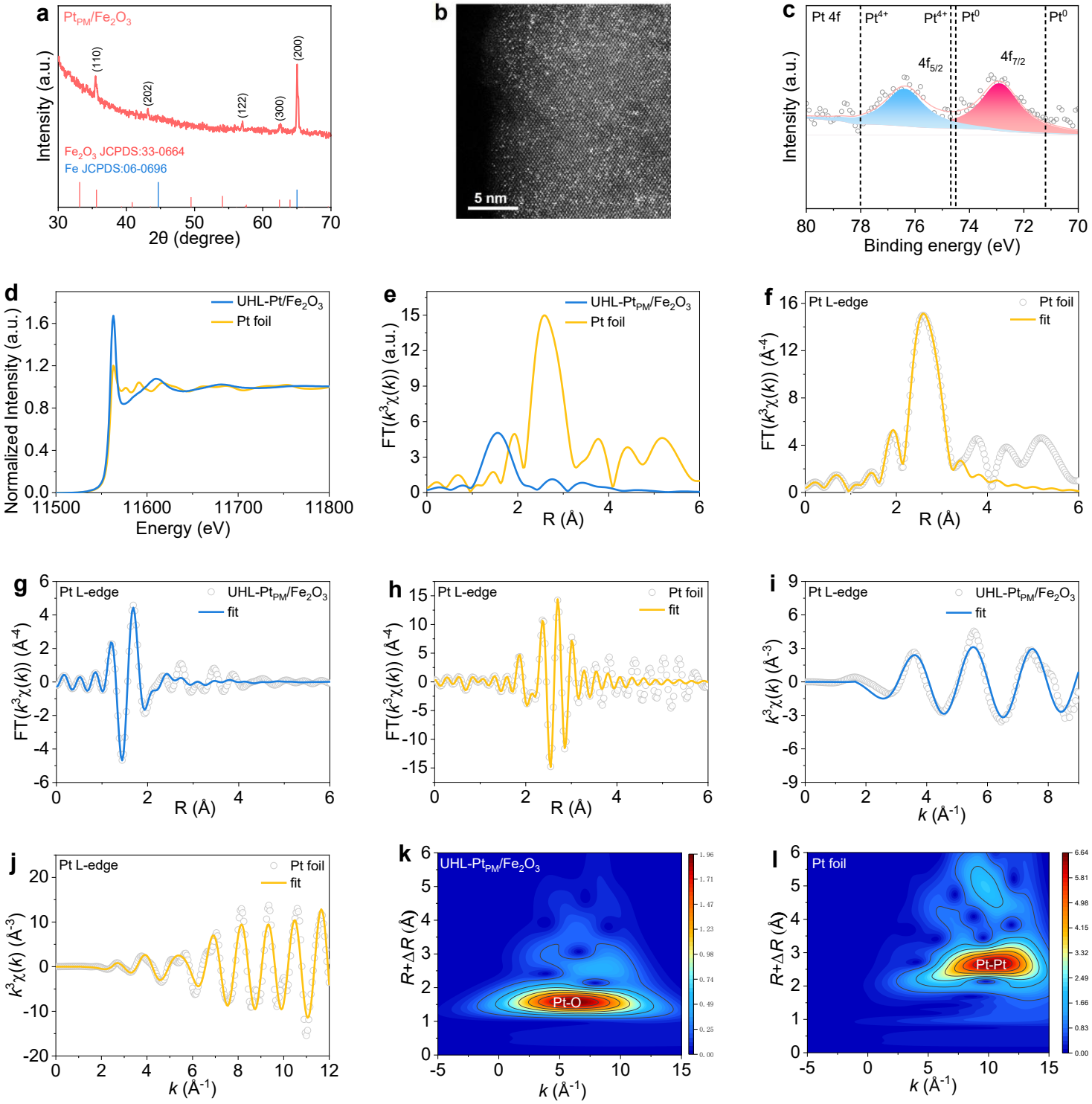

Supplementary Fig. 42 Structural characterization of Pt$_{PM}$/Fe$_2$O$_3$. a, XRD patterns of Pt$_{PM}$/Fe$_2$O$_3$. **b**, HAADF-STEM image of Pt$_{PM}$/Fe$_2$O$_3$. **c**, Pt 4f XPS spectra of Pt$_{PM}$/Fe$_2$O$_3$. **d**, Normalized Pt *L*-edge X-ray absorption near-edge structure (XANES) spectra. **e**, Fourier-transformed R-space of the experimental Pt *L*-edge EXAFS signals. **f-h,** Pt *L*-edge EXAFS data and fit for UHL-Pt$_{PM}$/Fe$_2$O$_3$ in *R*-space and **i, j,** *k*-space. **k,l,** WT-EXAFS plots of UHL-Pt$_{PM}$/Fe$_2$O$_3$ and Pt foil.

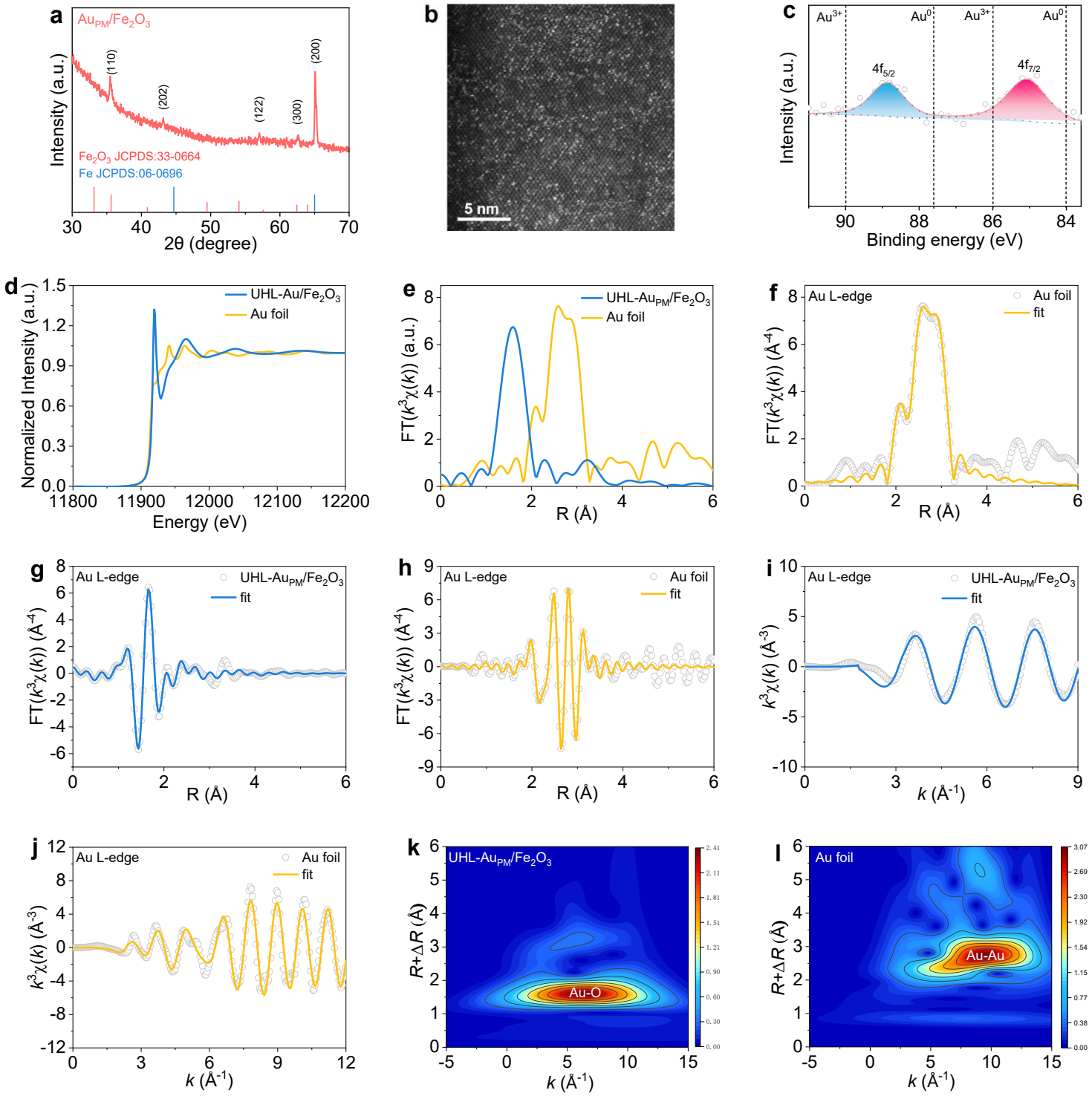

Supplementary Fig. 43 Structural characterization of Au$_{PM}$/Fe$_2$O$_3$. a, XRD patterns of Au$_{PM}$/Fe$_2$O$_3$. **b**, HAADF-STEM image of Au$_{PM}$/Fe$_2$O$_3$. **c**, Au 4f XPS spectra of Au$_{PM}$/Fe$_2$O$_3$. **d**, Normalized Au *L*-edge X-ray absorption near-edge structure (XANES) spectra. **e**, Fourier-transformed R-space of the experimental Au *L*-edge EXAFS signals. **f-h,** Au *L*-edge EXAFS data and fit for UHL-Au$_{PM}$/Fe$_2$O$_3$ in *R*-space and **i, j,** *k*-space. **k,l,** WT-EXAFS plots of UHL-Au$_{PM}$/Fe$_2$O$_3$ and Au foil.

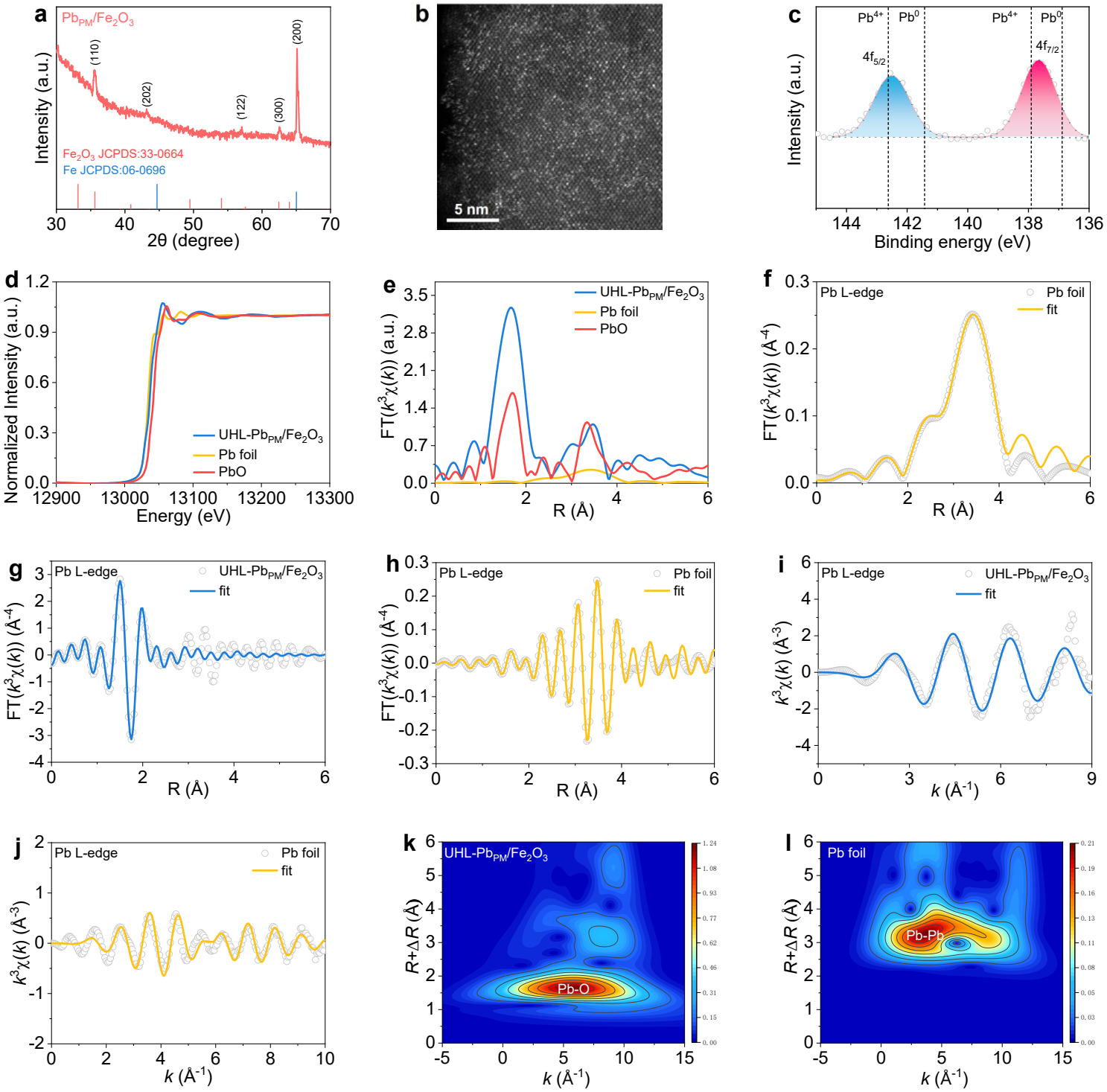

Supplementary Fig. 44 Structural characterization of Pb$_{PM}$/Fe$_2$O$_3$. a, XRD patterns of Pb$_{PM}$/Fe$_2$O$_3$. **b**, HAADF-STEM image of Pb$_{PM}$/Fe$_2$O$_3$. **c**, Pb 4f XPS spectra of Pb$_{PM}$/Fe$_2$O$_3$. **d**, Normalized Pb *L*-edge X-ray absorption near-edge structure (XANES) spectra. **e**, Fourier-transformed R-space of the experimental Pb *L*-edge EXAFS signals. **f-h,** Pb *L*-edge EXAFS data and fit for UHL-Pb$_{PM}$/Fe$_2$O$_3$ in *R*-space and **i, j,** *k*-space. **k,l,** WT-EXAFS plots of UHL-Pb$_{PM}$/Fe$_2$O$_3$ and Pb foil.

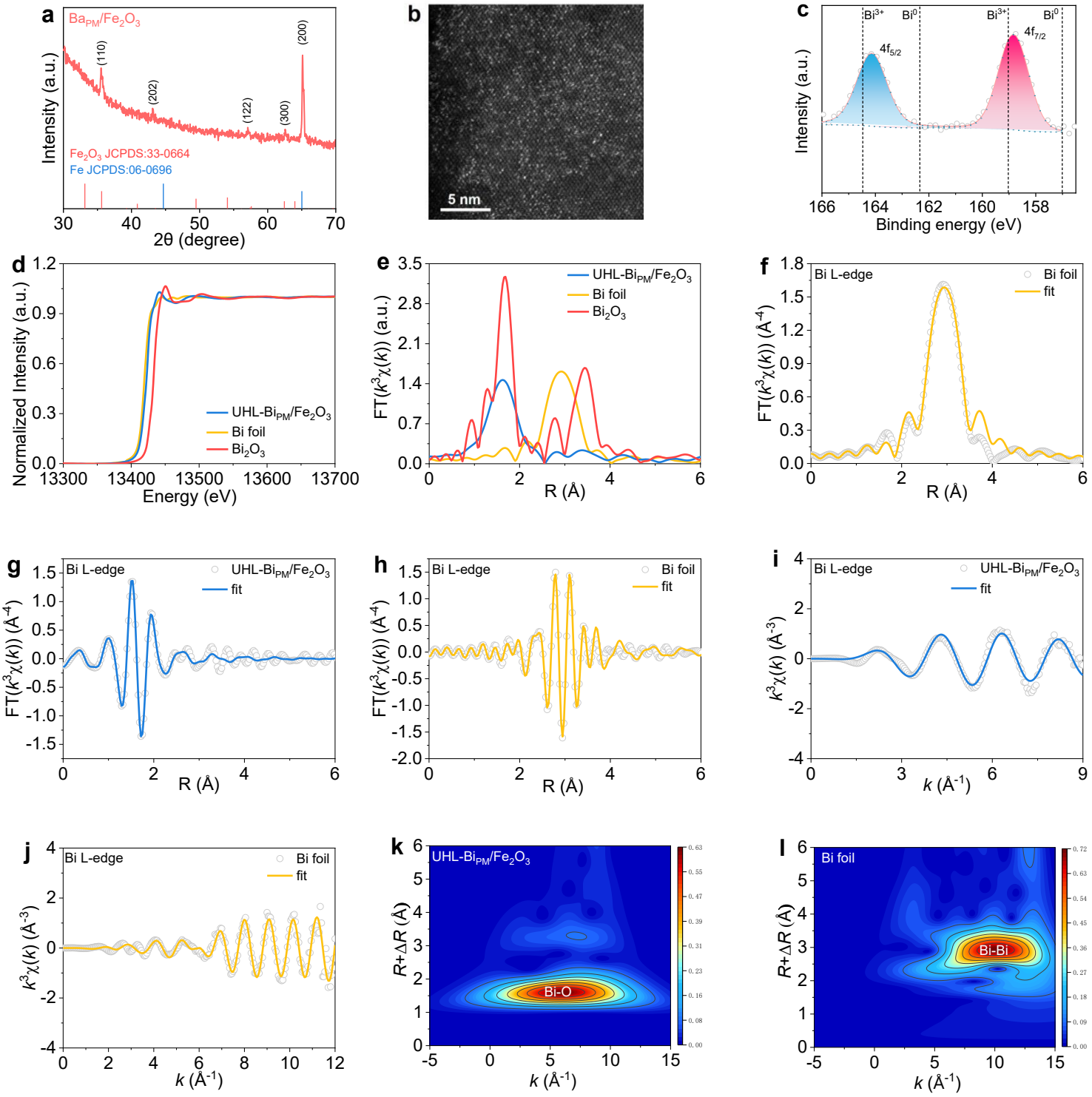

Supplementary Fig. 45 Structural characterization of Bi_{PM}/Fe_2O_3. a, XRD patterns of Bi_{PM}/Fe_2O_3. **b**, HAADF-STEM image of Bi_{PM}/Fe_2O_3. **c**, Bi 4f XPS spectra of Bi_{PM}/Fe_2O_3. **d**, Normalized Bi *L*-edge X-ray absorption near-edge structure (XANES) spectra. **e**, Fourier-transformed R-space of the experimental Bi *L*-edge EXAFS signals. **f-h,** Bi *L*-edge EXAFS data and fit for UHL-Bi_{PM}/Fe_2O_3 in *R*-space and **i, j,** *k*-space. **k,l,** WT-EXAFS plots of UHL-Bi_{PM}/Fe_2O_3 and Bi foil.

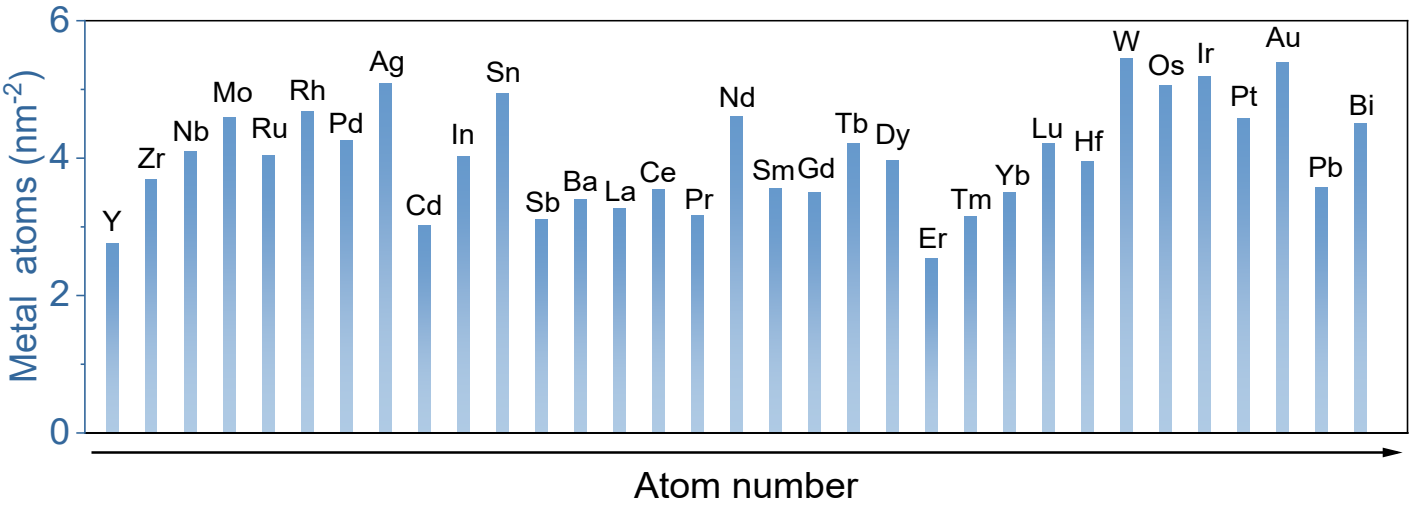

Supplementary Fig. 46 Surface concentration of metal atoms. Number of metal atoms per square nanometre on Fe_2O_3 carrier surface for UHL-SACs

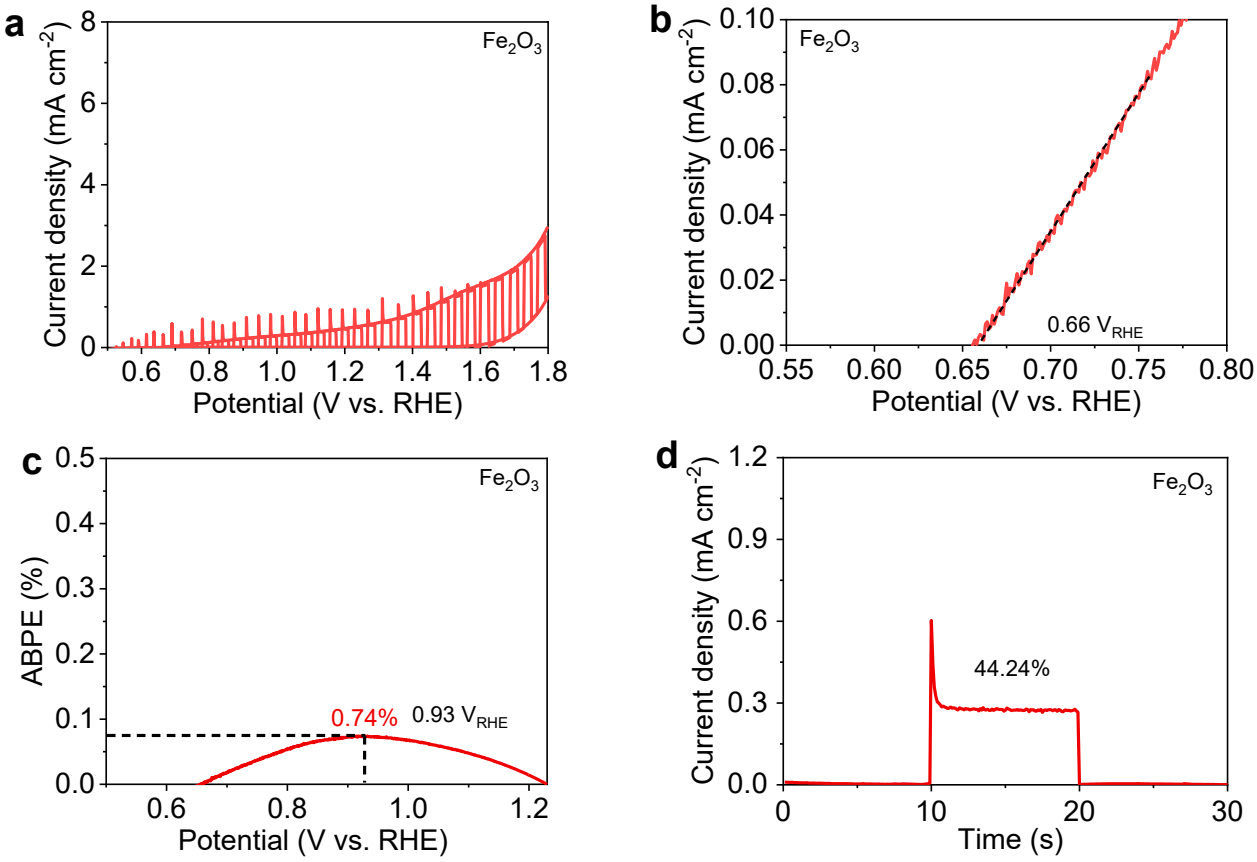

Supplementary Fig. 47 Photoelectrochemical performance measurement of Fe_2O_3. a, *J-V* and chopped curves of Fe_2O_3. **b,** Onset potential of Y_{PM}/Fe_2O_3. **c,** Applied bias photon-to current efficiency of Y_{PM}/Fe_2O_3. **d,** Transient photocurrent of Fe_2O_3. All measurements were performed in 1 M KOH under AM 1.5G illumination (100 mW cm^{-2}).

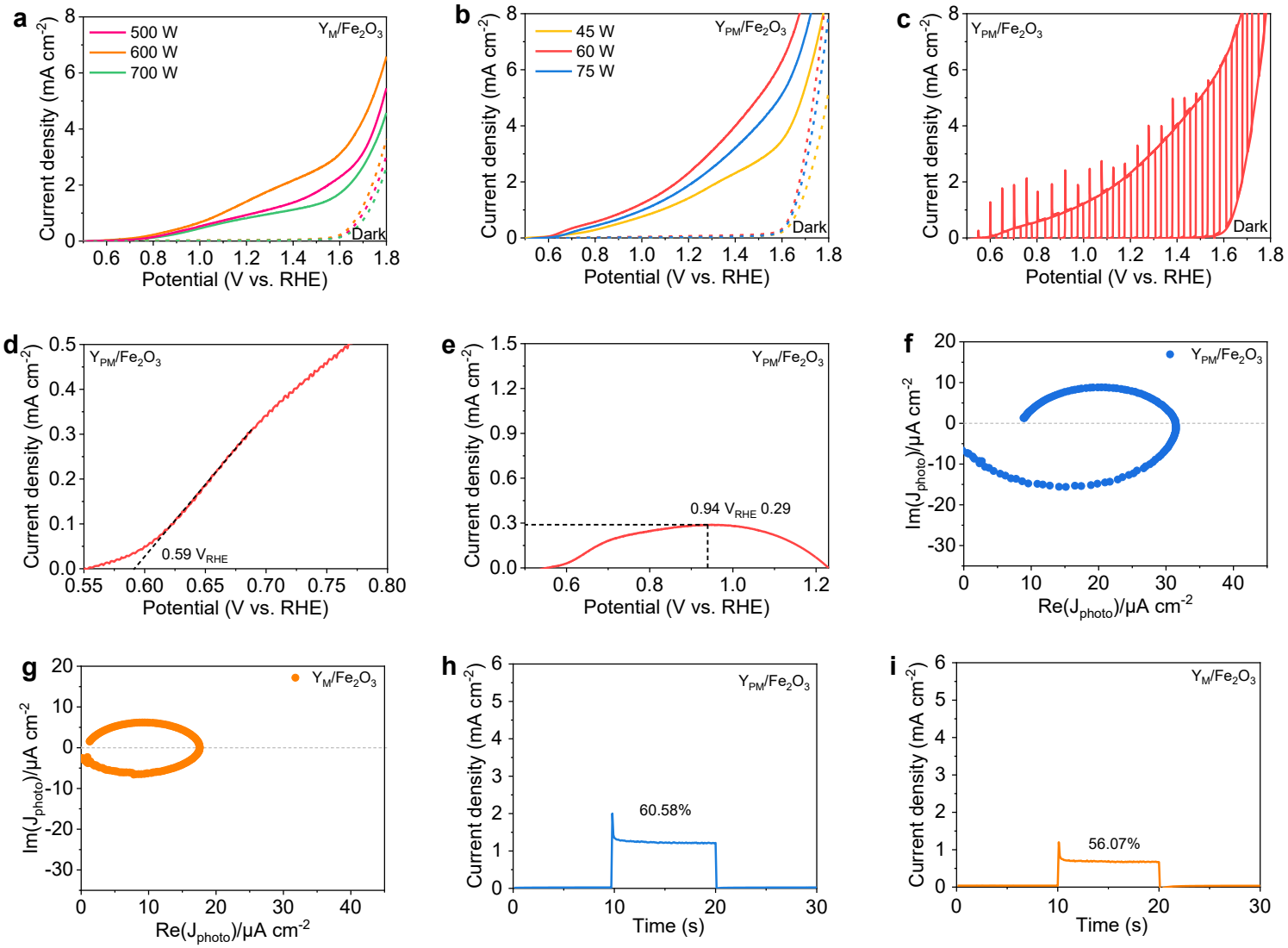

Supplementary Fig. 48 Photoelectrochemical performance measurement of $Y_{PM}Fe_2O_3$. a, *J-V* curves of Y-loaded Fe_2O_3 annealed directly by microwave at various power (800 W, 1000 W, and 1200 W) without plasma pretreatment, **b,** *J-V* curves of Y single atoms anchored on Fe_2O_3 via microwave annealing after plasma pretreatment at various powers (45, 60, and 75 W), **c,** Chopped *J-V* curve of Y_{PM}/Fe_2O_3. **d,** Onset potential of Y_{PM}/Fe_2O_3. **e,** Applied bias photon-to current efficiency of Y_{PM}/Fe_2O_3. **f, g,** IMPS responses of Y_{PM}/Fe_2O_3 and Y_M/Fe_2O_3 applied at 1 V_{RHE}. **h, I,** Transient photocurrent density of Y_{PM}/Fe_2O_3 and Y_M/Fe_2O_3. All measurements were performed in 1 M KOH under AM 1.5G illumination (100 mW cm^{-2}).

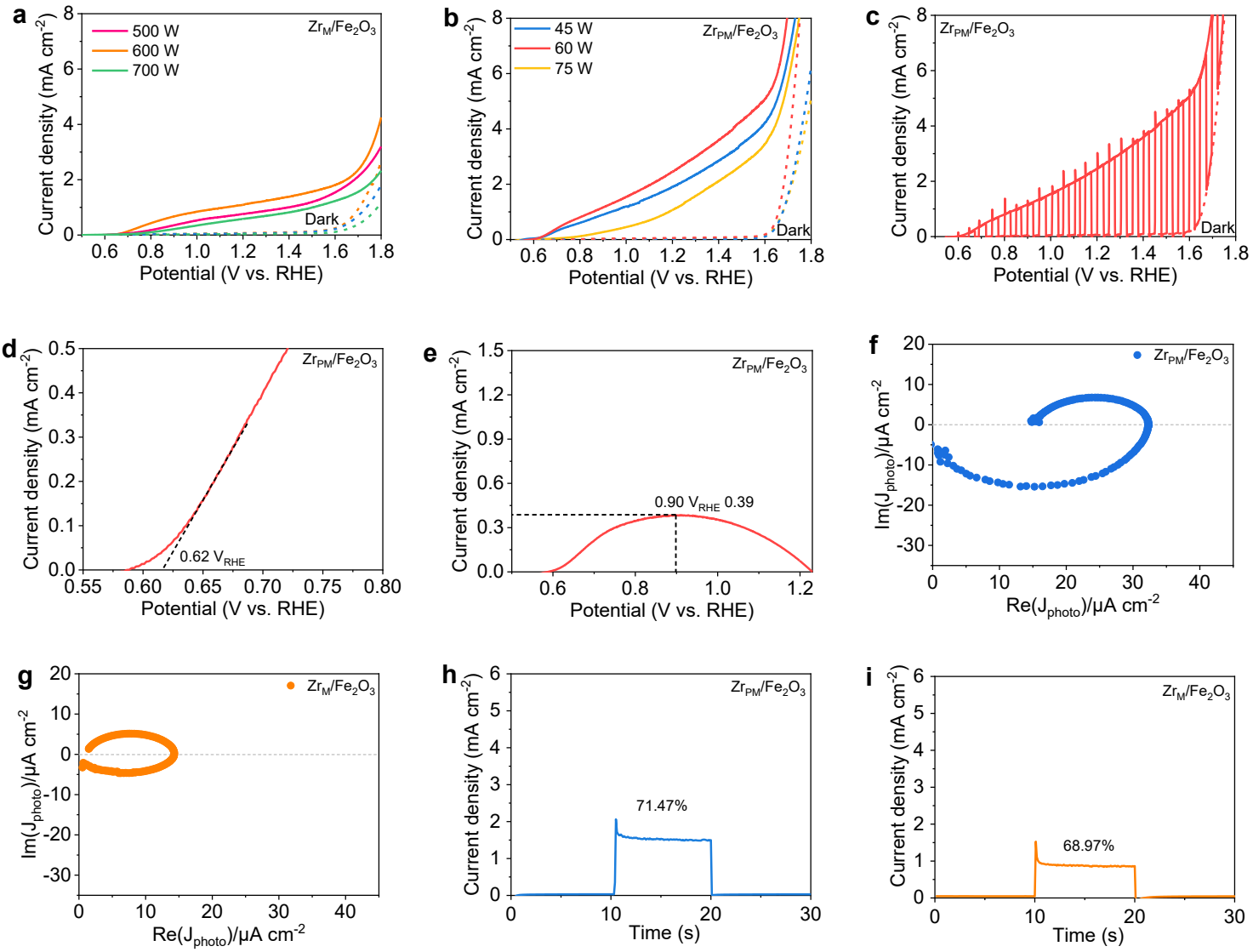

Supplementary Fig. 49 Photoelectrochemical performance measurement of Zr$_{PM}$/Fe$_2$O$_3$. A, *J-V* curves of Zr-loaded Fe_2O_3 annealed directly by microwave at various power (800 W, 1000 W, and 1200 W) without plasma pretreatment. **b,** *J-V* curves of Zr single atoms anchored on Fe_2O_3 via microwave annealing after plasma pretreatment at various powers (45, 60, and 75 W). **c,** Chopped *J-V* curve of Zr$_{PM}$/Fe$_2$O$_3$. **d,** Onset potential of Zr$_{PM}$/Fe$_2$O$_3$. **e,** Applied bias photon-to current efficiency of Zr$_{PM}$/Fe$_2$O$_3$. **f, g,** IMPS responses of Zr$_{PM}$/Fe$_2$O$_3$ and Zr$_M$/Fe$_2$O$_3$ applied at 1 V$_{RHE}$. **h, I,** Transient photocurrent density of Zr$_{PM}$/Fe$_2$O$_3$ and Zr$_M$/Fe$_2$O$_3$. All measurements were performed in 1 M KOH under AM 1.5G illumination (100 mW cm^{-2}).

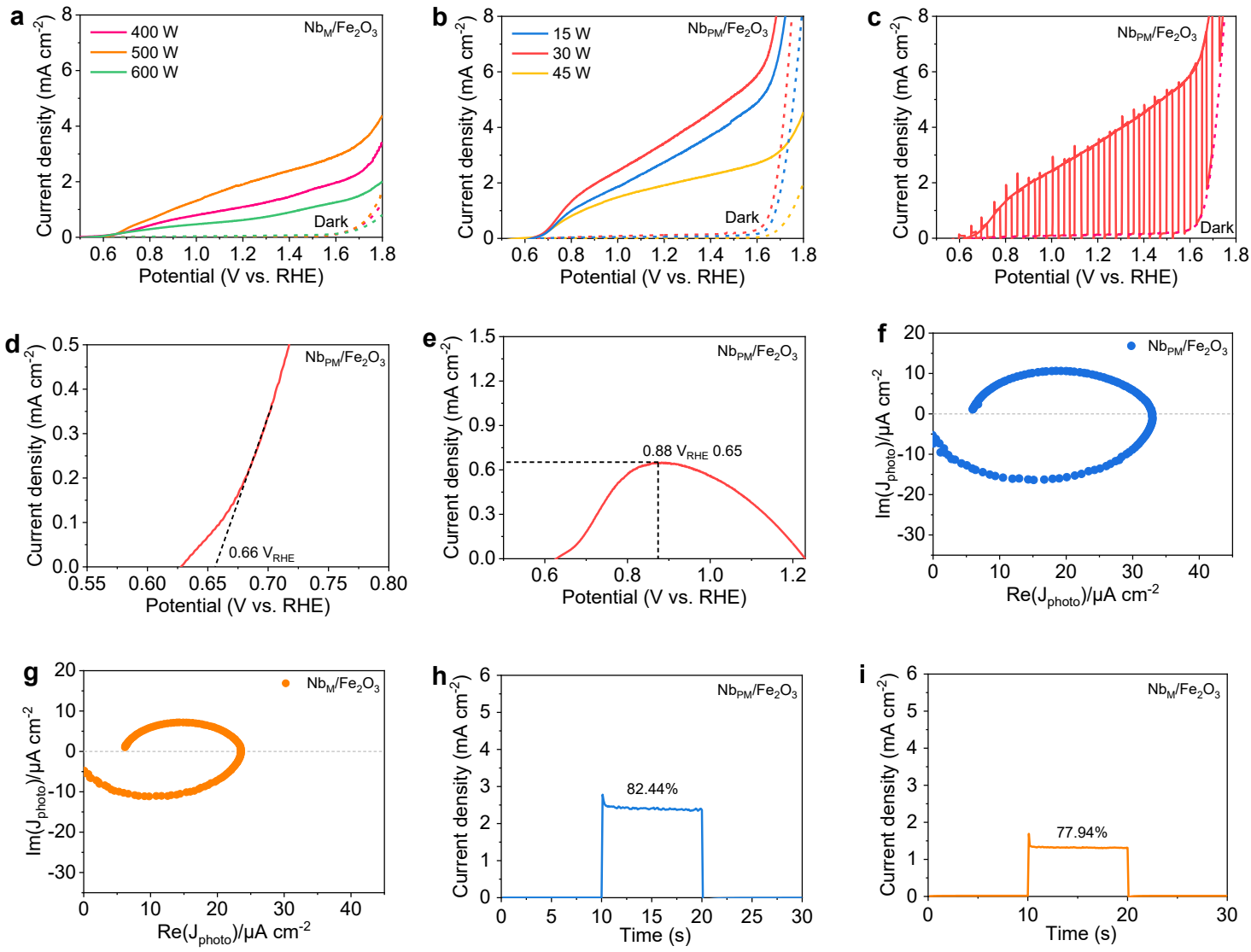

Supplementary Fig.50 Photoelectrochemical performance measurement of Nb$_{PM}$/Fe$_2$O$_3$. a, *J-V* curves of Nb-loaded Fe_2O_3 annealed directly by microwave at various power (600 W, 800 W, and 1000 W) without plasma pretreatment. **b,** *J-V* curves of Nb single atoms anchored on Fe_2O_3 via microwave annealing after plasma pretreatment at various powers (15, 30, and 45 W). **c,** Chopped *J-V* curve of Nb$_{PM}$/Fe$_2$O$_3$. **d,** Onset potential of Nb$_{PM}$/Fe$_2$O$_3$. **e,** Applied bias photon-to current efficiency of Nb$_{PM}$/Fe$_2$O$_3$. **f, g,** IMPS responses of Nb$_{PM}$/Fe$_2$O$_3$ and Nb$_M$/Fe$_2$O$_3$ applied at 1 V$_{RHE}$. **h, i,** Transient photocurrent density of Nb$_{PM}$/Fe$_2$O$_3$ and Nb$_M$/Fe$_2$O$_3$. All measurements were performed in 1 M KOH under AM 1.5G illumination (100 mW cm^{-2}).

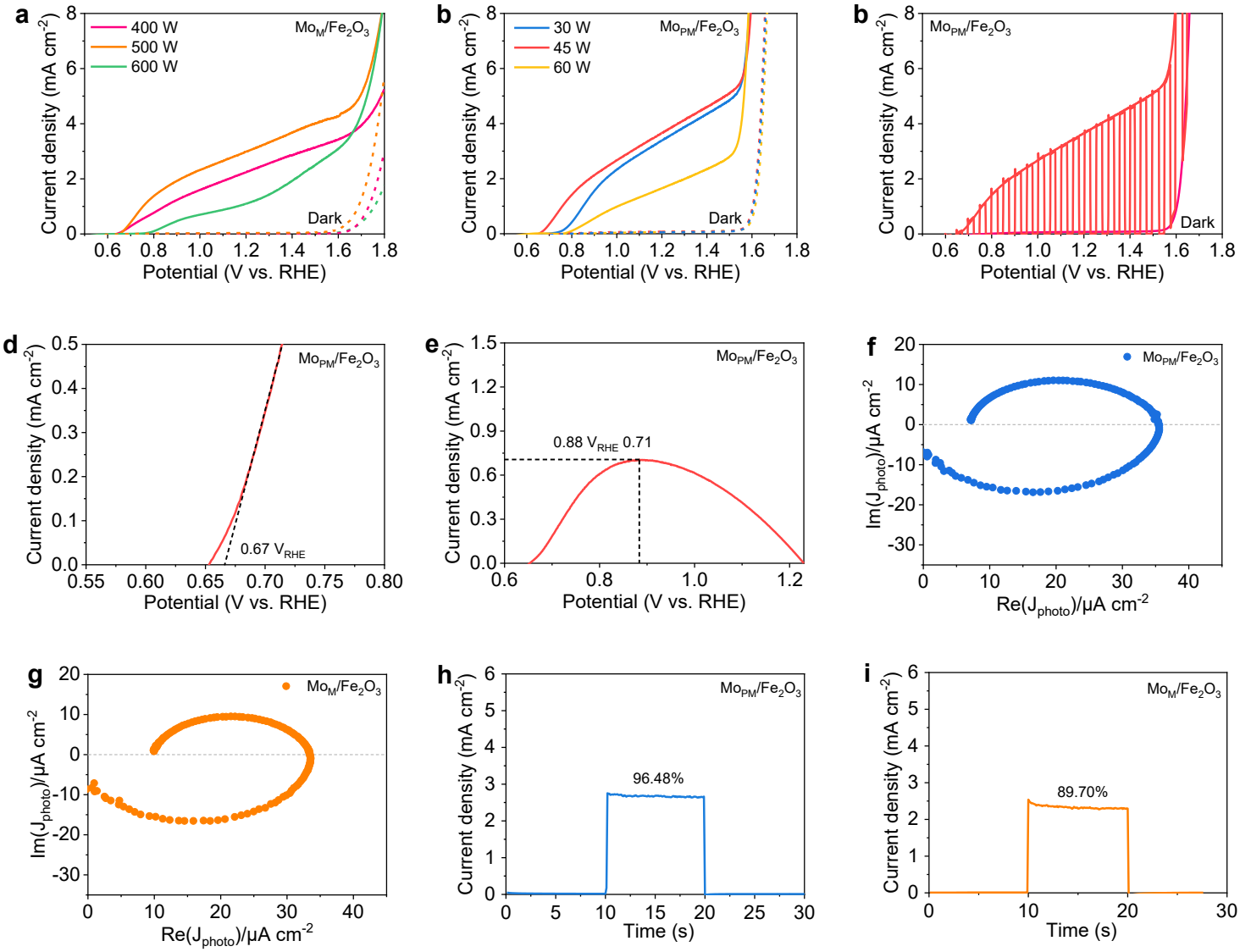

Supplementary Fig.51 Photoelectrochemical performance measurement of Mo$_{PM}$/Fe$_2$O$_3$. a, *J-V* curves of Mo-loaded Fe_2O_3 annealed directly by microwave at various power (400 W, 600 W, and 1000 W) without plasma pretreatment. **b,** *J-V* curves of Mo single atoms anchored on Fe_2O_3 via microwave annealing after plasma pretreatment at various powers (30, 45, and 60 W). **c,** Chopped *J-V* curve of Mo$_{PM}$/Fe$_2$O$_3$. **d,** Onset potential of Mo$_{PM}$/Fe$_2$O$_3$. **e** Applied bias photon-to current efficiency of Mo$_{PM}$/Fe$_2$O$_3$. **f, g,** IMPS responses of Mo$_{PM}$/Fe$_2$O$_3$ and Mo$_M$/Fe$_2$O$_3$ applied at 1 V$_{RHE}$. **h, i,** Transient photocurrent density of Mo$_{PM}$/Fe$_2$O$_3$ and Mo$_M$/Fe$_2$O$_3$. All measurements were performed in 1 M KOH under AM 1.5G illumination (100 mW cm^{-2}).

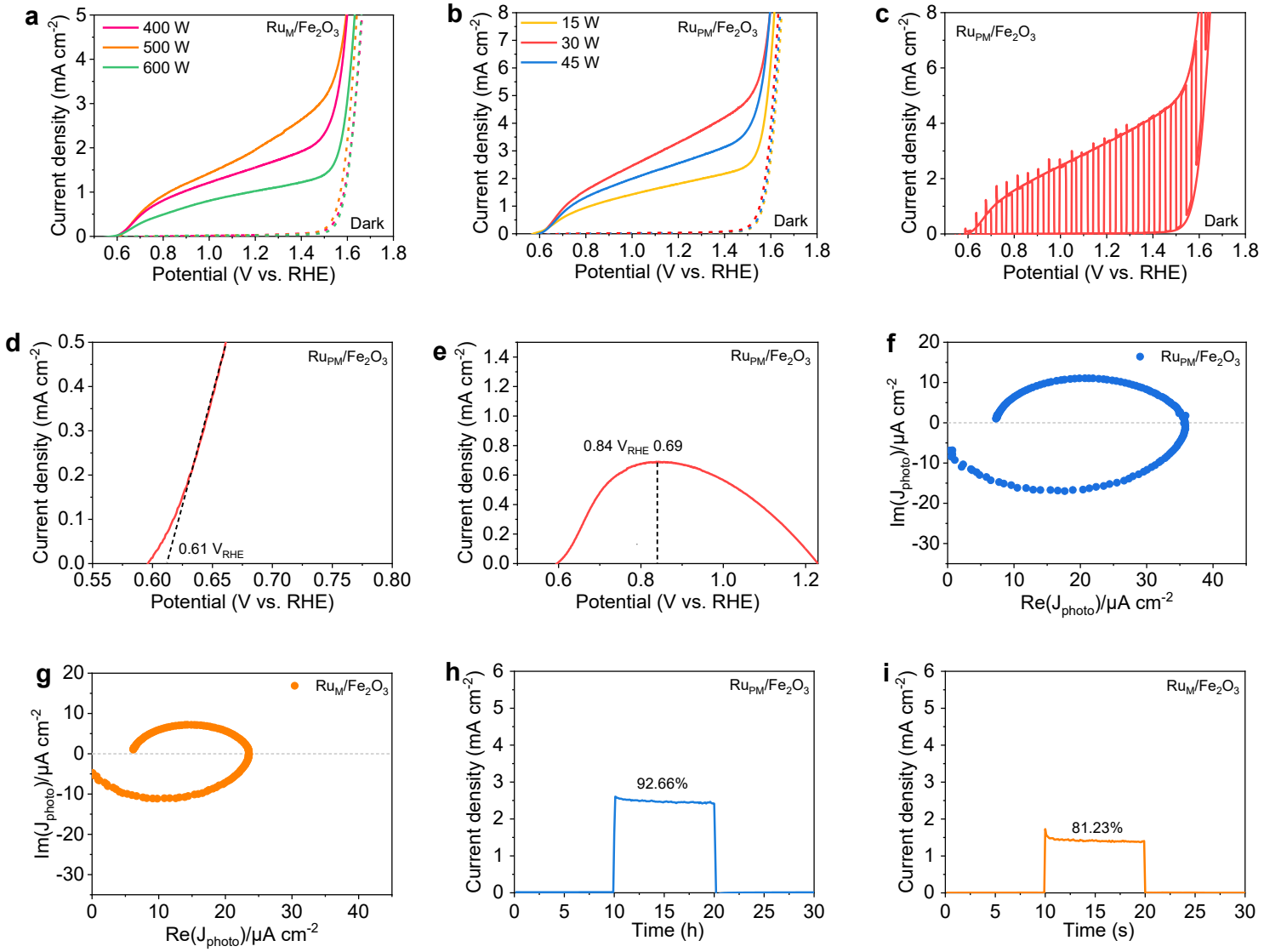

Supplementary Fig.52 Photoelectrochemical performance measurement of Ru_{PM}/Fe_2O_3. a, *J-V* curves of Ru-loaded Fe_2O_3 annealed directly by microwave at various power (600 W, 800 W, and 1000 W) without plasma pretreatment. **b,** *J-V* curves of Ru single atoms anchored on Fe_2O_3 via microwave annealing after plasma pretreatment at various powers (15, 30, and 45 W). **c,** Chopped *J-V* curve of Ru_{PM}/Fe_2O_3. **d,** Onset potential of Ru_{PM}/Fe_2O_3. **e** Applied bias photon-to current efficiency of Ru_{PM}/Fe_2O_3. **f, g,** IMPS responses of Ru_{PM}/Fe_2O_3 and Ru_M/Fe_2O_3 applied at 1 V_{RHE}. **h, i,** Transient photocurrent density of Ru_{PM}/Fe_2O_3 and Ru_M/Fe_2O_3. All measurements were performed in 1 M KOH under AM 1.5G illumination (100 mW cm^{-2}).

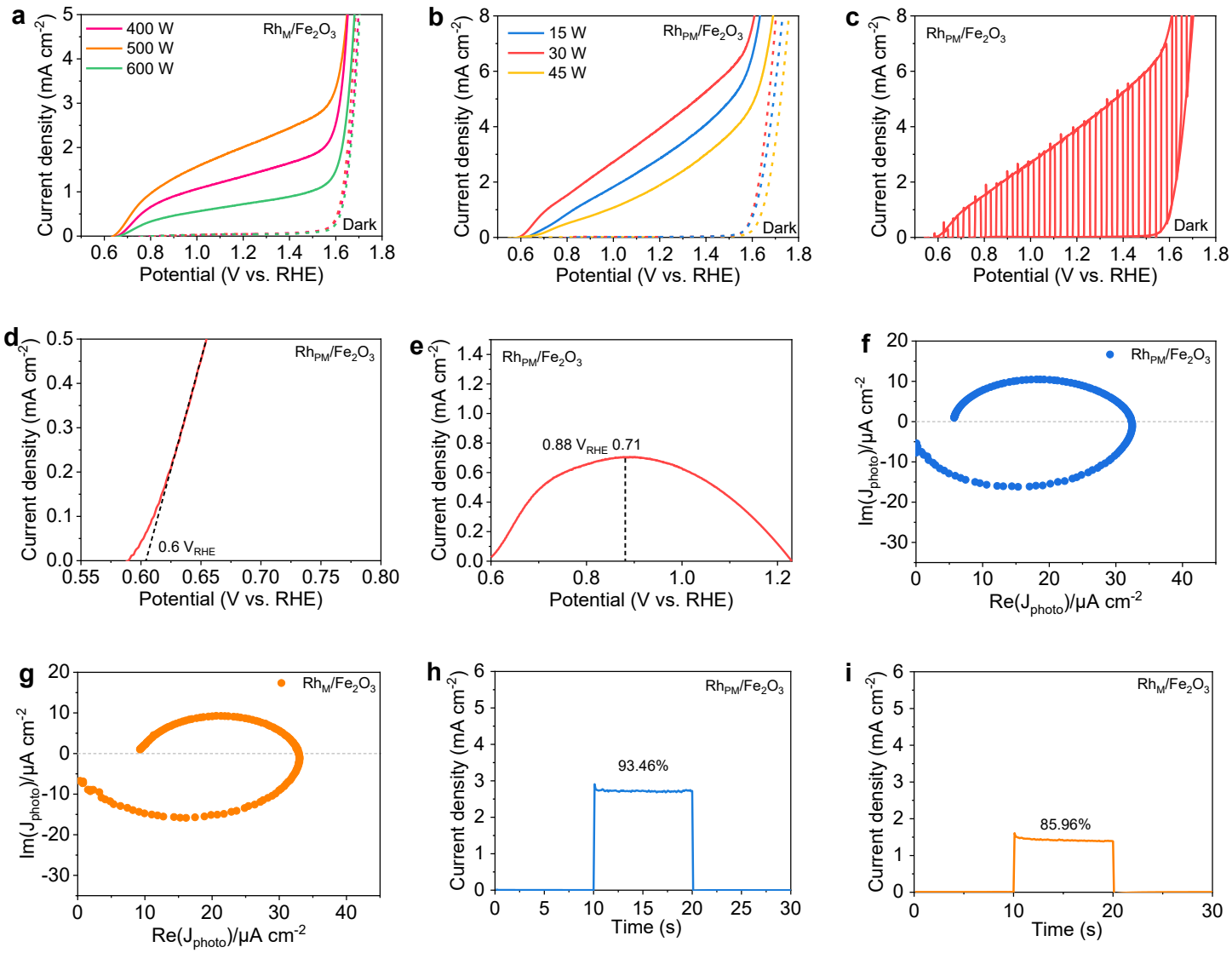

Supplementary Fig.53 Photoelectrochemical performance measurement of Rh$_{PM}$/Fe$_2$O$_3$. a, *J-V* curves of Rh-loaded Fe_2O_3 annealed directly by microwave at various power (600 W, 800 W, and 1000 W) without plasma pretreatment. **b,** *J-V* curves of Rh single atoms anchored on Fe_2O_3 via microwave annealing after plasma pretreatment at various powers (15, 30, and 45 W). **c,** Chopped *J-V* curve of Rh$_{PM}$/Fe$_2$O$_3$. **d,** Onset potential of Rh$_{PM}$/Fe$_2$O$_3$. **e** Applied bias photon-to current efficiency of Rh$_{PM}$/Fe$_2$O$_3$. **f, g,** IMPS responses of Rh$_{PM}$/Fe$_2$O$_3$ and Rh$_M$/Fe$_2$O$_3$ applied at 1 V$_{RHE}$. **h, i,** Transient photocurrent density of Rh$_{PM}$/Fe$_2$O$_3$ and Mo$_M$/Fe$_2$O$_3$. All measurements were performed in 1 M KOH under AM 1.5G illumination (100 mW cm^{-2}).

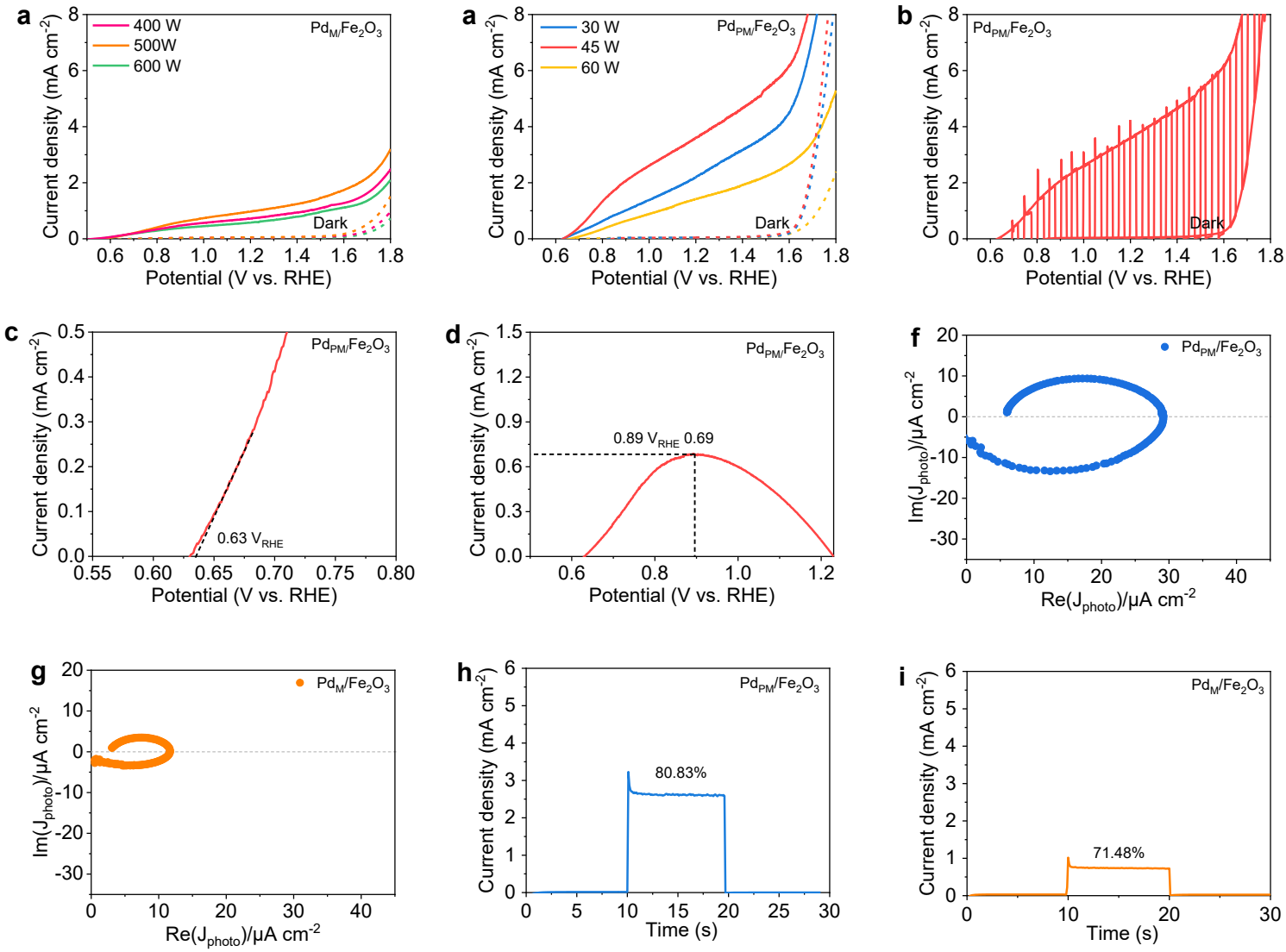

Supplementary Fig.54 Photoelectrochemical performance measurement of Pd_{PM}/Fe_2O_3. a, *J-V* curves of Pd-loaded Fe_2O_3 annealed directly by microwave at various power (600 W, 800 W, and 1000 W) without plasma pretreatment. **b,** *J-V* curves of Pd single atoms anchored on Fe_2O_3 via microwave annealing after plasma pretreatment at various powers (15, 30, and 45 W). **c,** Chopped *J-V* curve of Pd_{PM}/Fe_2O_3. **d,** Onset potential of Pd_{PM}/Fe_2O_3. **e,** Applied bias photon-to current efficiency of Pd_{PM}/Fe_2O_3. **f, g,** IMPS responses of Pd_{PM}/Fe_2O_3 and Pd_M/Fe_2O_3 applied at 1 V_{RHE}. **h, i,** Transient photocurrent density of Pd_{PM}/Fe_2O_3 and Mo_M/Fe_2O_3. All measurements were performed in 1 M KOH under AM 1.5G illumination (100 mW cm^{-2}).

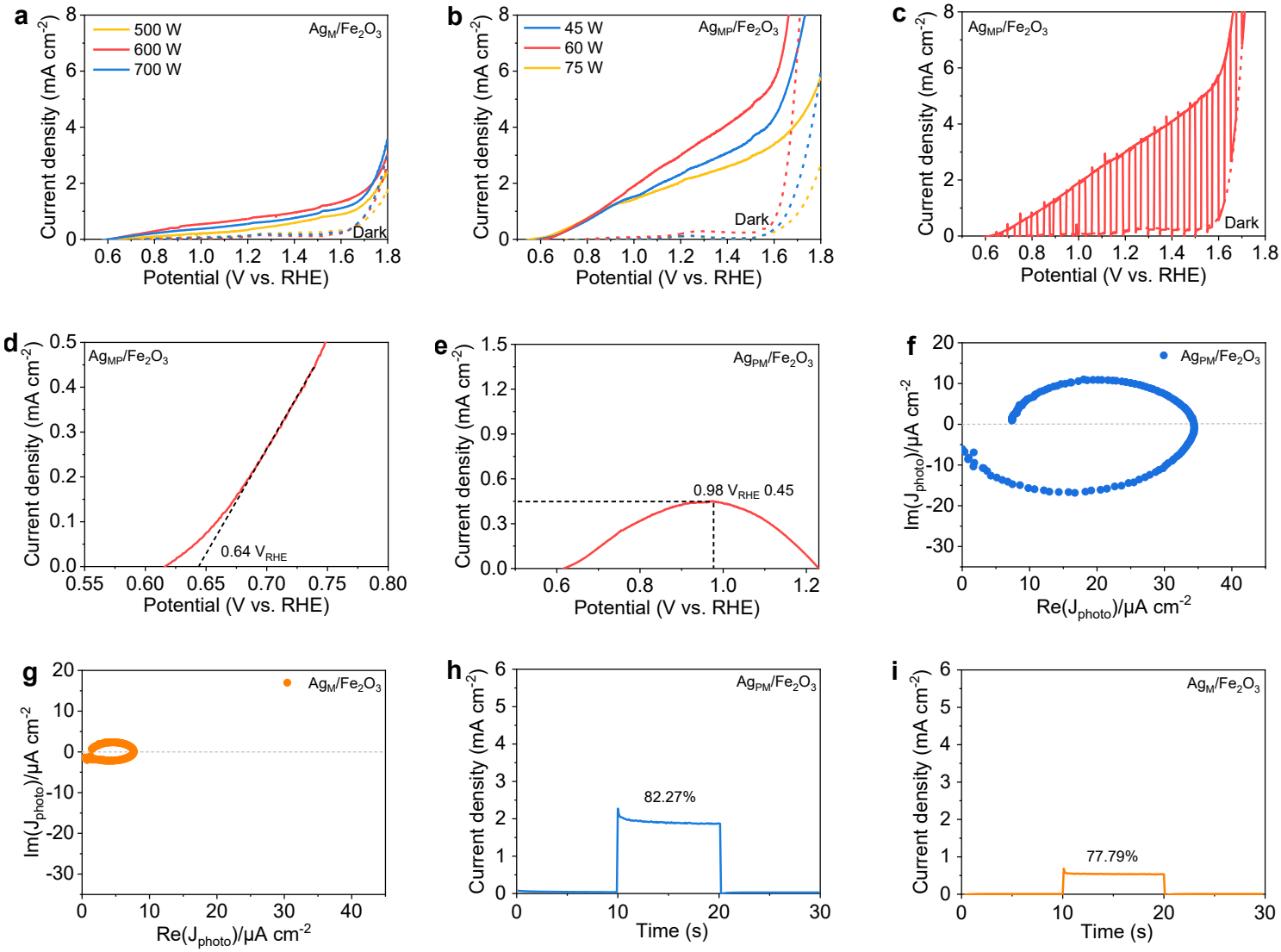

Supplementary Fig.55 Photoelectrochemical performance measurement of Ag$_{PM}$/Fe$_2$O$_3$. a, *J-V* curves of Ag-loaded Fe_2O_3 annealed directly by microwave at various power (600 W, 800 W, and 1000 W) without plasma pretreatment. **b,** *J-V* curves of Ag single atoms anchored on Fe_2O_3 via microwave annealing after plasma pretreatment at various powers (15, 30, and 45 W). **c,** Chopped *J-V* curve of Ag$_{PM}$/Fe$_2$O$_3$. **d,** Onset potential of Ag$_{PM}$/Fe$_2$O$_3$. **e,** Applied bias photon-to current efficiency of Ag$_{PM}$/Fe$_2$O$_3$. **f, g,** IMPS responses of Ag$_{PM}$/Fe$_2$O$_3$ and Ag$_M$/Fe$_2$O$_3$ applied at 1 V$_{RHE}$. **h, i,** Transient photocurrent density of Ag$_{PM}$/Fe$_2$O$_3$ and Ag$_M$/Fe$_2$O$_3$. All measurements were performed in 1 M KOH under AM 1.5G illumination (100 mW cm^{-2}).

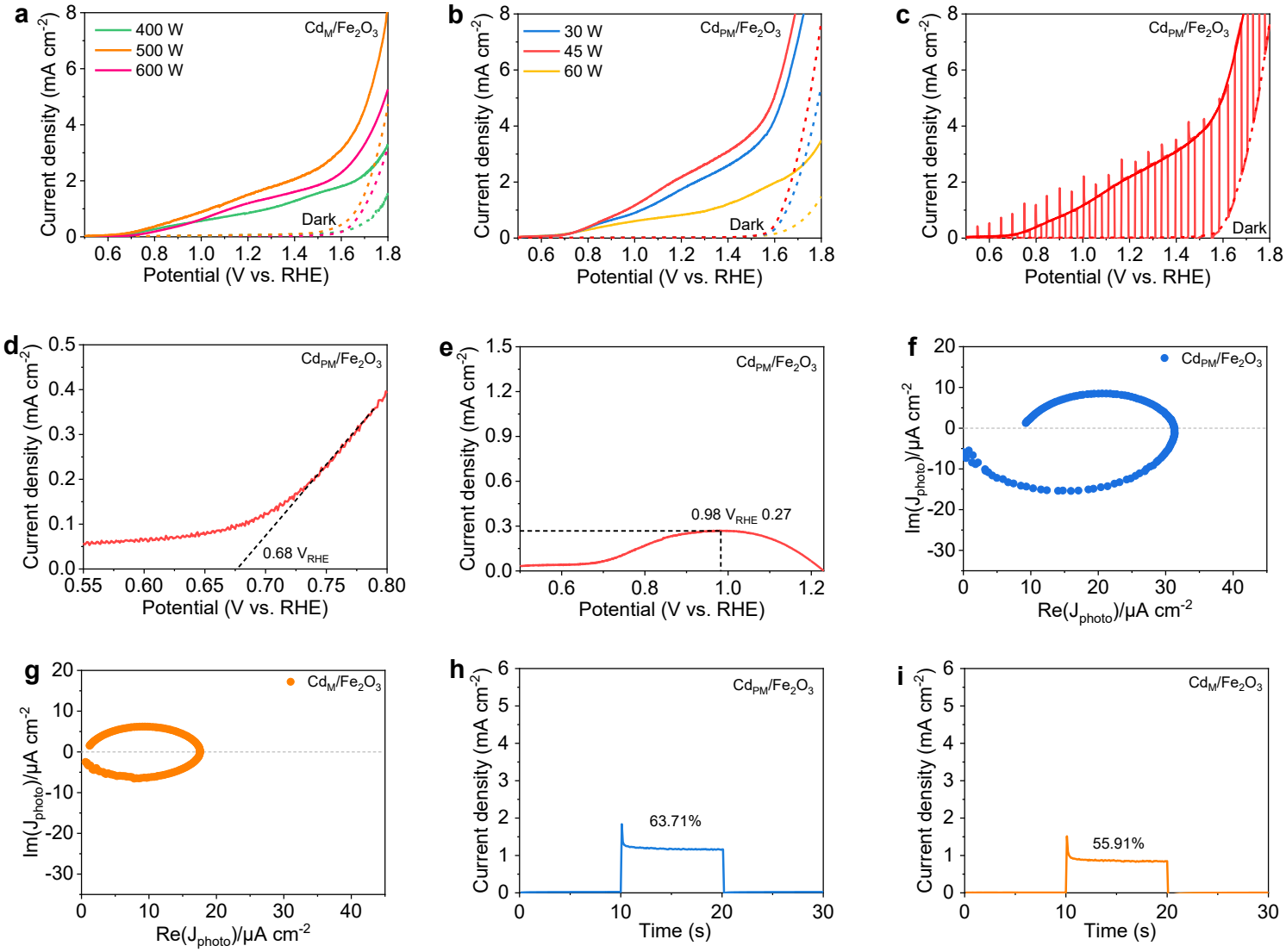

Supplementary Fig.56 Photoelectrochemical performance measurement of Cd$_{PM}$/Fe$_2$O$_3$. a, *J-V* curves of Cd-loaded Fe_2O_3 annealed directly by microwave at various power (400 W, 600 W, and 800 W) without plasma pretreatment. **b,** *J-V* curves of Cd single atoms anchored on Fe_2O_3 via microwave annealing after plasma pretreatment at various powers (30, 45, and 60 W). **c,** Chopped *J-V* curve of Cd$_{PM}$/Fe$_2$O$_3$. **d,** Onset potential of Cd$_{PM}$/Fe$_2$O$_3$. **e,** Applied bias photon-to current efficiency of Cd$_{PM}$/Fe$_2$O$_3$. **f, g,** IMPS responses of Cd$_{PM}$/Fe$_2$O$_3$ and Cd$_M$/Fe$_2$O$_3$ applied at 1 V$_{RHE}$. **h, i,** Transient photocurrent density of Cd$_{PM}$/Fe$_2$O$_3$ and Cd$_M$/Fe$_2$O$_3$. All measurements were performed in 1 M KOH under AM 1.5G illumination (100 mW cm^{-2}).

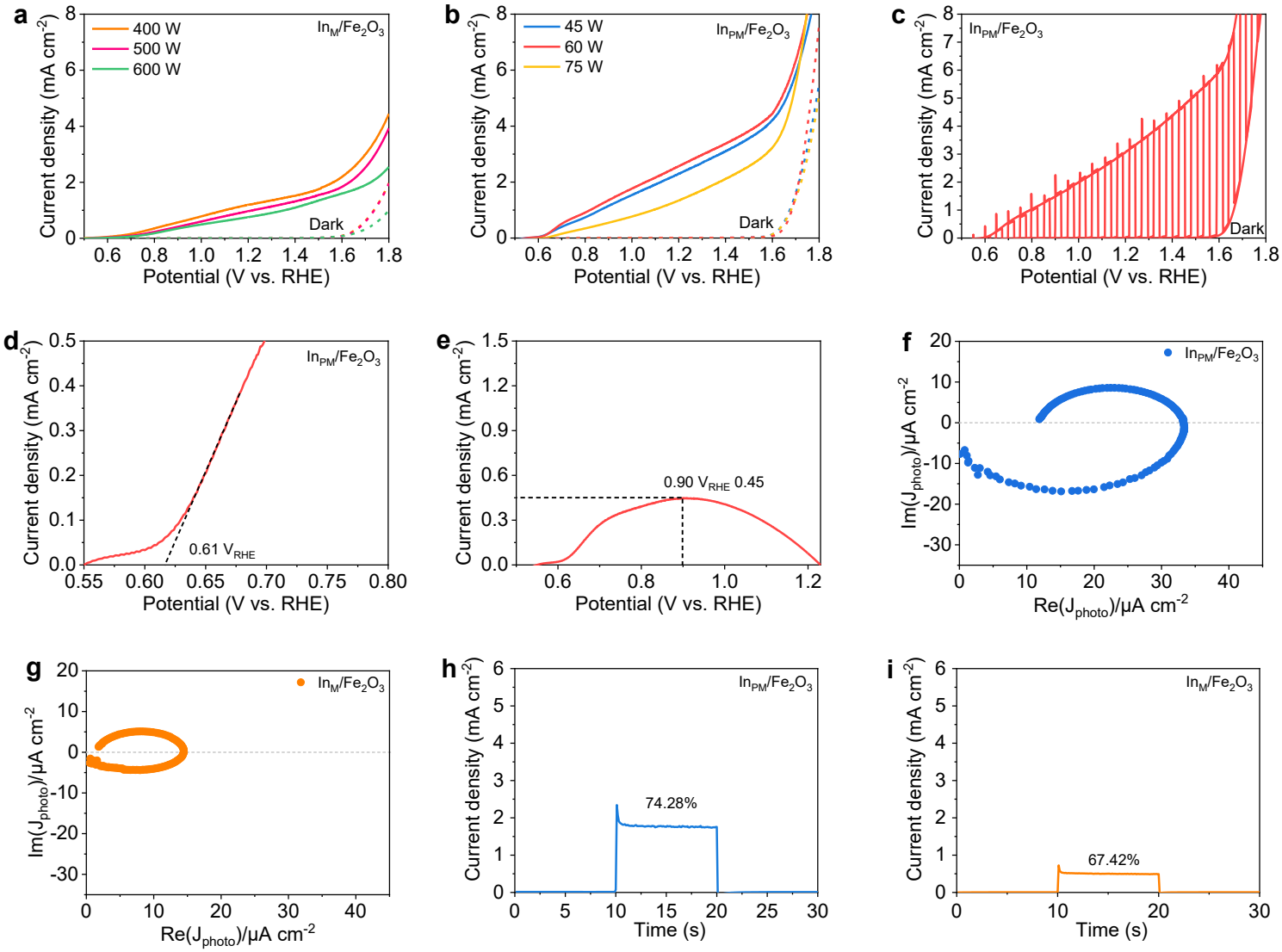

Supplementary Fig.57 Photoelectrochemical performance measurement of In$_{PM}$/Fe$_2$O$_3$. a, *J-V* curves of In-loaded Fe_2O_3 annealed directly by microwave at various power (600 W, 800 W, and 1000 W) without plasma pretreatment. **b,** *J-V* curves of In single atoms anchored on Fe_2O_3 via microwave annealing after plasma pretreatment at various powers (45, 60, and 75 W). **c,** Chopped *J-V* curve of In$_{PM}$/Fe$_2$O$_3$. **d,** Onset potential of In$_{PM}$/Fe$_2$O$_3$. **e,** Applied bias photon-to current efficiency of In$_{PM}$/Fe$_2$O$_3$. **f, g,** IMPS responses of In$_{PM}$/Fe$_2$O$_3$ and In$_M$/Fe$_2$O$_3$ applied at 1 V$_{RHE}$. **h, i,** Transient photocurrent density of In$_{PM}$/Fe$_2$O$_3$ and In$_M$/Fe$_2$O$_3$. All measurements were performed in 1 M KOH under AM 1.5G illumination (100 mW cm^{-2}).

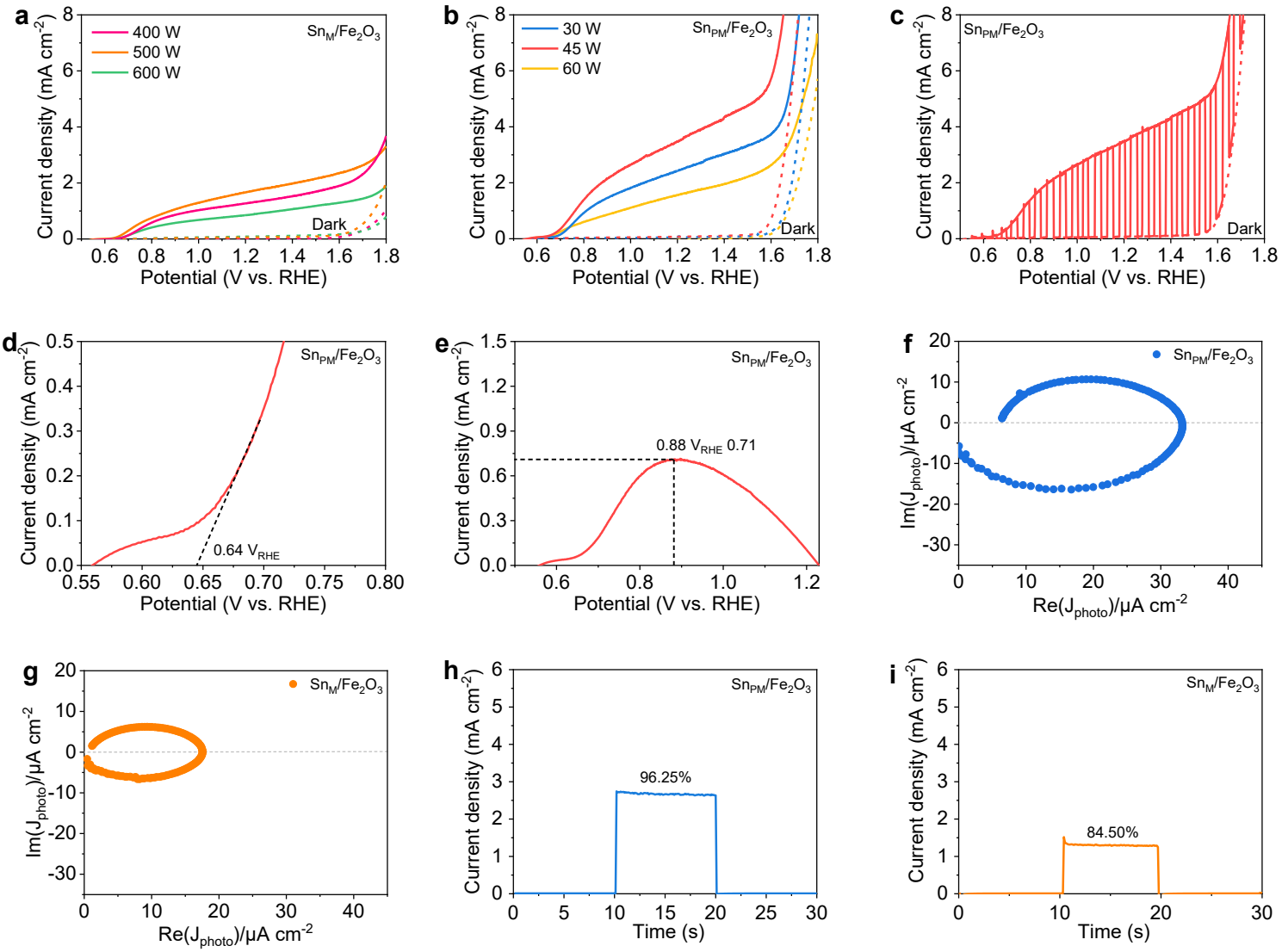

Supplementary Fig.58 Photoelectrochemical performance measurement of Sn_{PM}/Fe_2O_3. a, *J-V* curves of Sn-loaded Fe_2O_3 annealed directly by microwave at various power (400 W, 600 W, and 800 W) without plasma pretreatment. **b,** *J-V* curves of Sn single atoms anchored on Fe_2O_3 via microwave annealing after plasma pretreatment at various powers (30, 45, and 60 W). **c,** Chopped *J-V* curve of Sn_{PM}/Fe_2O_3. **d,** Onset potential of Sn_{PM}/Fe_2O_3. **e,** Applied bias photon-to current efficiency of Sn_{PM}/Fe_2O_3. **f, g,** IMPS responses of Sn_{PM}/Fe_2O_3 and Sn_M/Fe_2O_3 applied at 1 V_{RHE}. **h, i,** Transient photocurrent density of Sn_{PM}/Fe_2O_3 and Sn_M/Fe_2O_3. All measurements were performed in 1 M KOH under AM 1.5G illumination (100 mW cm^{-2}).

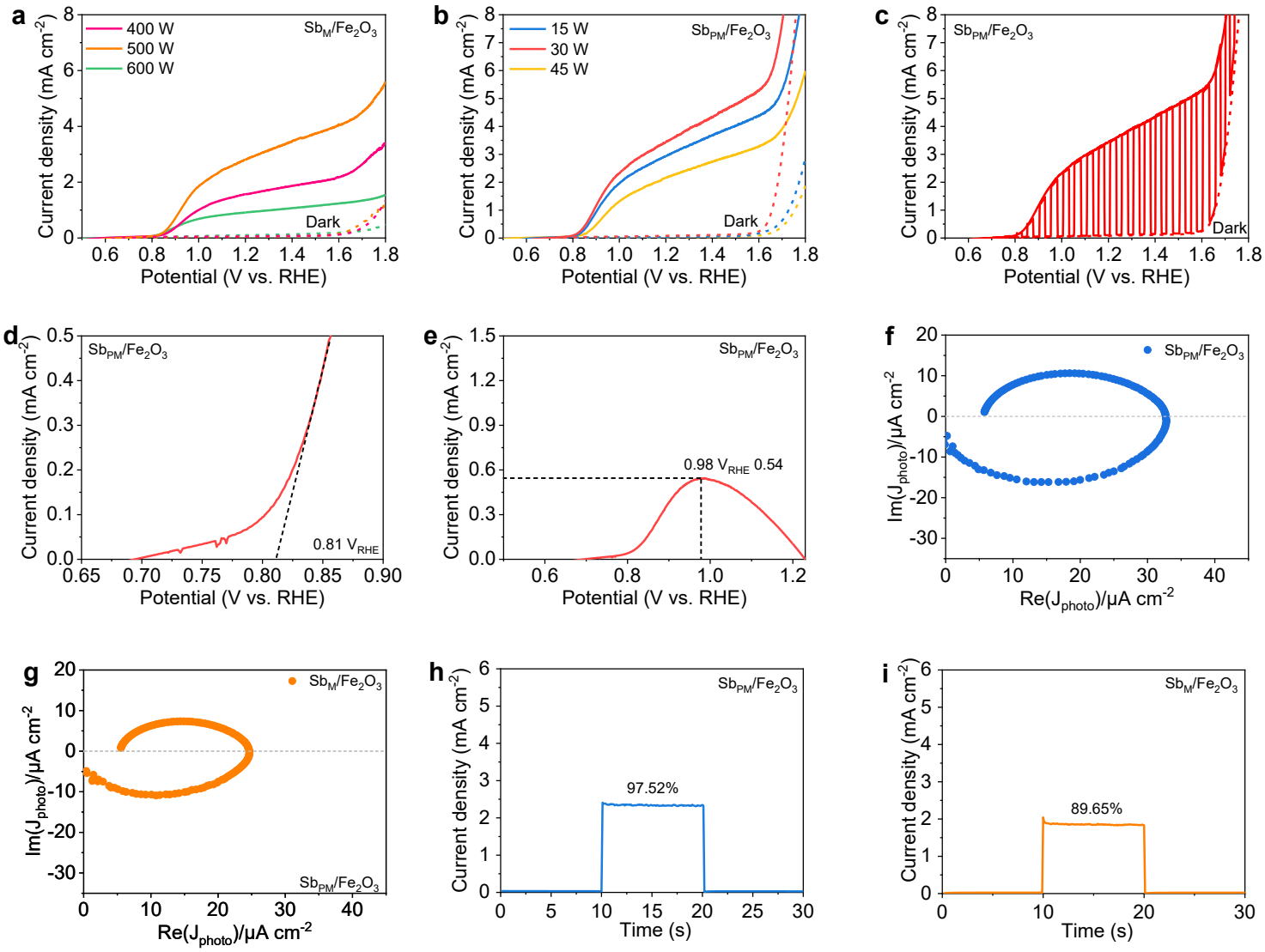

Supplementary Fig.59 Photoelectrochemical performance measurement of Sb_{PM}/Fe_2O_3. a, *J-V* curves of Sb-loaded Fe_2O_3 annealed directly by microwave at various power (600 W, 800 W, and 1000 W) without plasma pretreatment. **b,** *J-V* curves of Sb single atoms anchored on Fe_2O_3 via microwave annealing after plasma pretreatment at various powers (15, 30, and 45 W). **c,** Chopped *J-V* curve of Sb_{PM}/Fe_2O_3. **d,** Onset potential of Sb_{PM}/Fe_2O_3. **e,** Applied bias photon-to current efficiency of Sn_{PM}/Fe_2O_3. **f, g,** IMPS responses of Sb_{PM}/Fe_2O_3 and Sb_M/Fe_2O_3 applied at 1 V_{RHE}. **h, i,** Transient photocurrent density of Sb_{PM}/Fe_2O_3 and Sb_M/Fe_2O_3. All measurements were performed in 1 M KOH under AM 1.5G illumination (100 mW cm^{-2}).

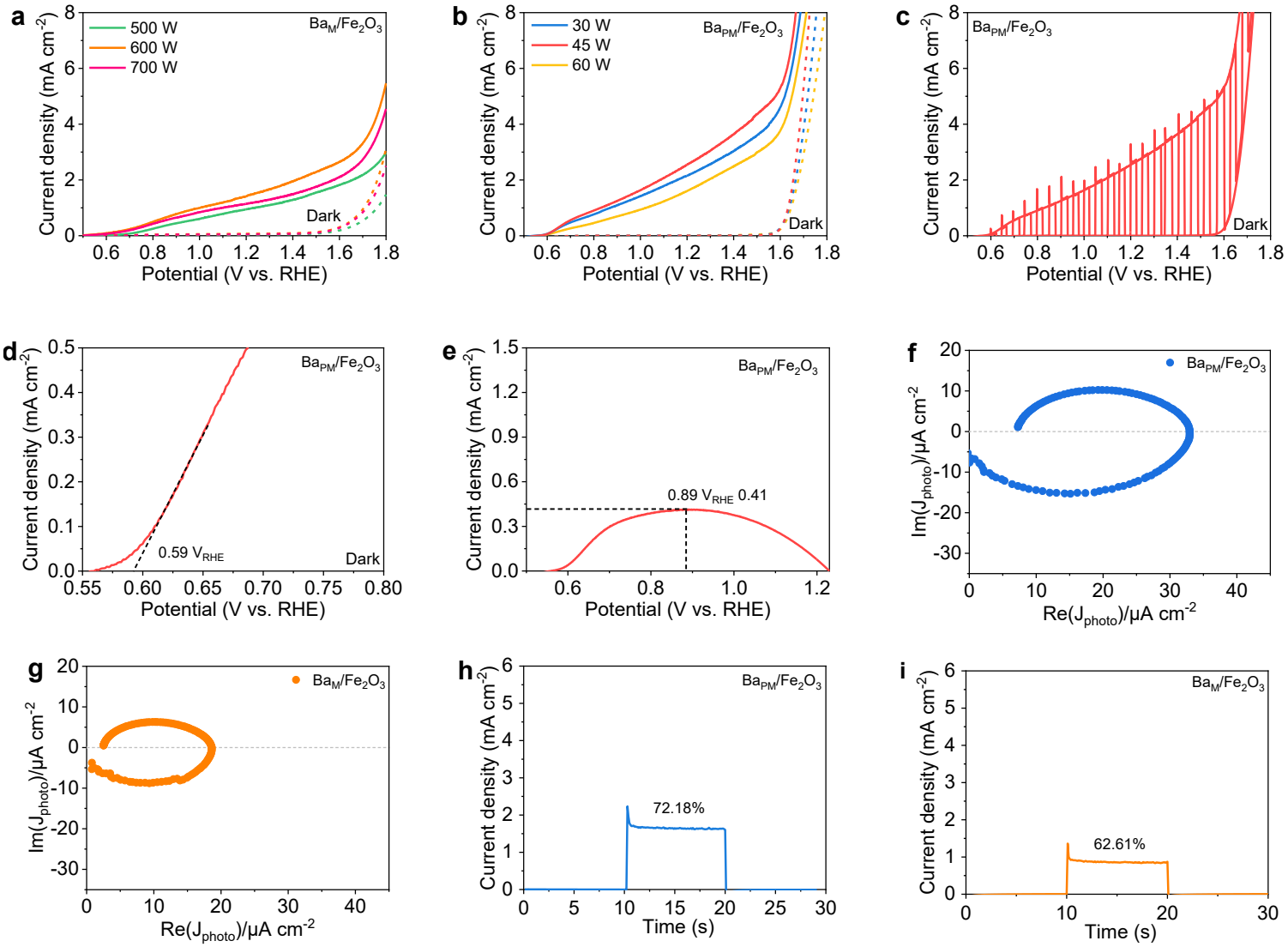

Supplementary Fig.60 Photoelectrochemical performance measurement of Ba$_{PM}$/Fe$_2$O$_3$. a, *J-V* curves of Ba-loaded Fe_2O_3 annealed directly by microwave at various power (800 W, 1000 W, and 1200 W) without plasma pretreatment. **b,** *J-V* curves of Ba single atoms anchored on Fe_2O_3 via microwave annealing after plasma pretreatment at various powers (30, 45, and 60 W). **c,** Chopped *J-V* curve of Ba$_{PM}$/Fe$_2$O$_3$. **d,** Onset potential of Ba$_{PM}$/Fe$_2$O$_3$. **e,** Applied bias photon-to current efficiency of Ba$_{PM}$/Fe$_2$O$_3$. **f, g,** IMPS responses of Ba$_{PM}$/Fe$_2$O$_3$ and Ba$_M$/Fe$_2$O$_3$ applied at 1 V$_{RHE}$. **h, i,** Transient photocurrent density of Ba$_{PM}$/Fe$_2$O$_3$ and Ba$_M$/Fe$_2$O$_3$. All measurements were performed in 1 M KOH under AM 1.5G illumination (100 mW cm^{-2}).

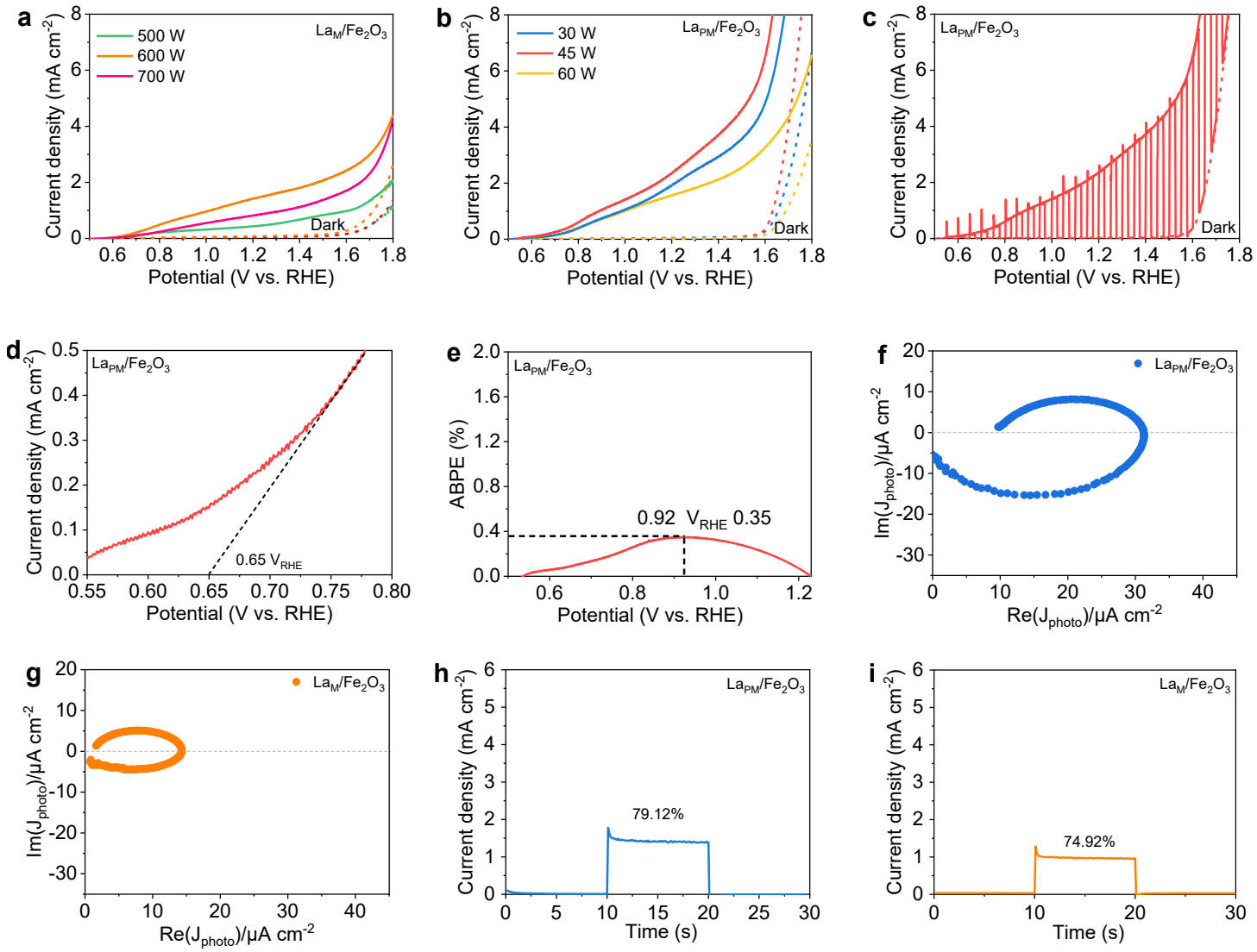

Supplementary Fig.61 Photoelectrochemical performance measurement of La$_{PM}$/Fe$_2$O$_3$. a, *J-V* curves of La-loaded Fe_2O_3 annealed directly by microwave at various power (800 W, 1000 W, and 1200 W) without plasma pretreatment. **b,** *J-V* curves of La single atoms anchored on Fe_2O_3 via microwave annealing after plasma pretreatment at various powers (30, 45, and 60 W). **c,** Chopped *J-V* curve of La$_{PM}$/Fe$_2$O$_3$. **d,** Onset potential of La$_{PM}$/Fe$_2$O$_3$. **e,** Applied bias photon-to current efficiency of La$_{PM}$/Fe$_2$O$_3$. **f, g,** IMPS responses of La$_{PM}$/Fe$_2$O$_3$ and La$_M$/Fe$_2$O$_3$ applied at 1 V$_{RHE}$. **h, i,** Transient photocurrent density of La$_{PM}$/Fe$_2$O$_3$ and La$_M$/Fe$_2$O$_3$. All measurements were performed in 1 M KOH under AM 1.5G illumination (100 mW cm^{-2}).

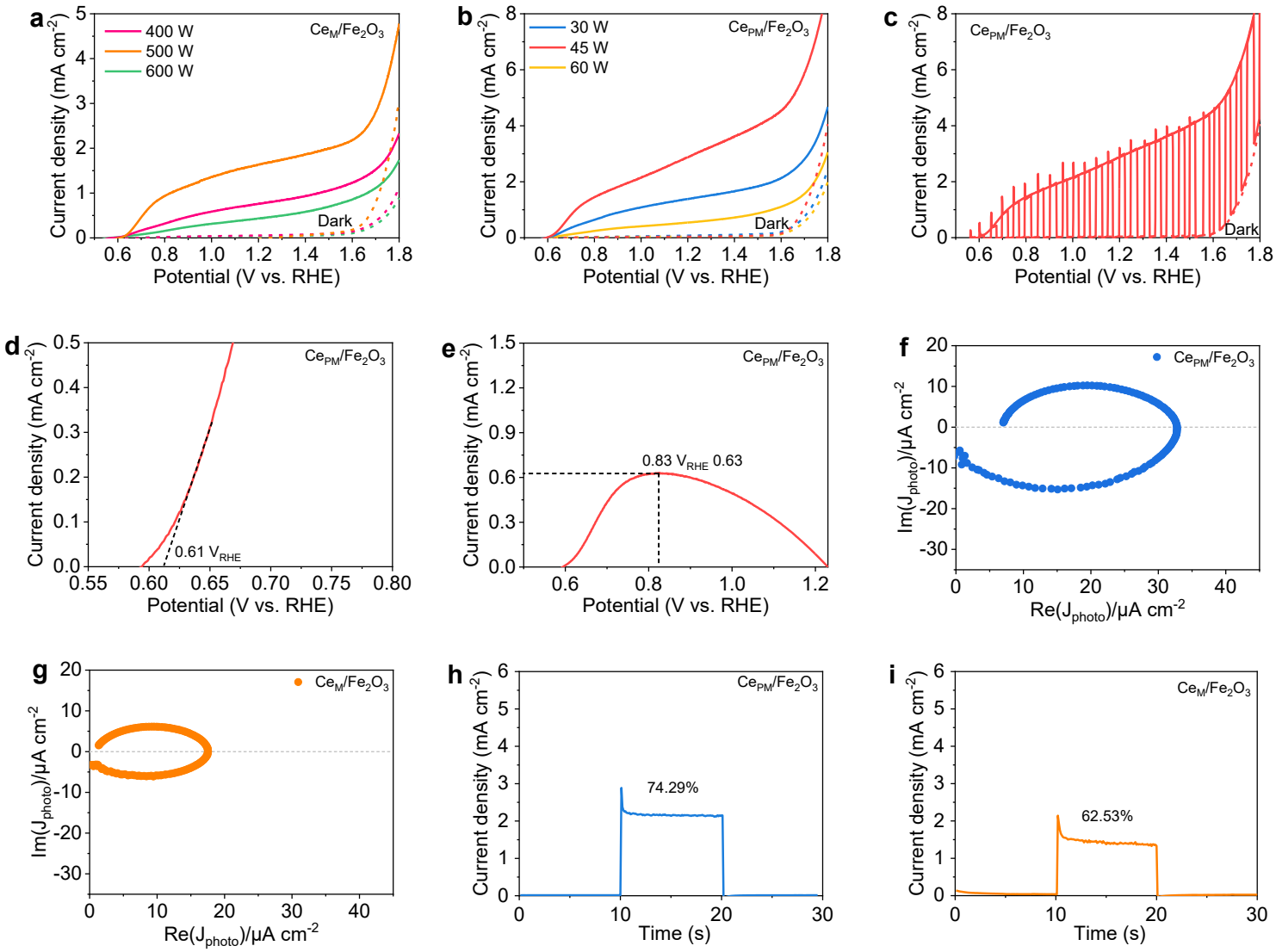

Supplementary Fig.62 Photoelectrochemical performance measurement of Ce$_{PM}$/Fe$_2$O$_3$. a, *J-V* curves of Ce-loaded Fe_2O_3 annealed directly by microwave at various power (600 W, 800 W, and 1000 W) without plasma pretreatment. **b,** *J-V* curves of Ce single atoms anchored on Fe_2O_3 via microwave annealing after plasma pretreatment at various powers (15, 30, and 45 W). **c,** Chopped *J-V* curve of Ce$_{PM}$/Fe$_2$O$_3$. **d,** Onset potential of Ce$_{PM}$/Fe$_2$O$_3$. **e,** Applied bias photon-to current efficiency of Ce$_{PM}$/Fe$_2$O$_3$. **f, g,** IMPS responses of Ce$_{PM}$/Fe$_2$O$_3$ and Ce$_M$/Fe$_2$O$_3$ applied at 1 V$_{RHE}$. **h, i,** Transient photocurrent density of Ce$_{PM}$/Fe$_2$O$_3$ and Ce$_M$/Fe$_2$O$_3$. All measurements were performed in 1 M KOH under AM 1.5G illumination (100 mW cm^{-2}).

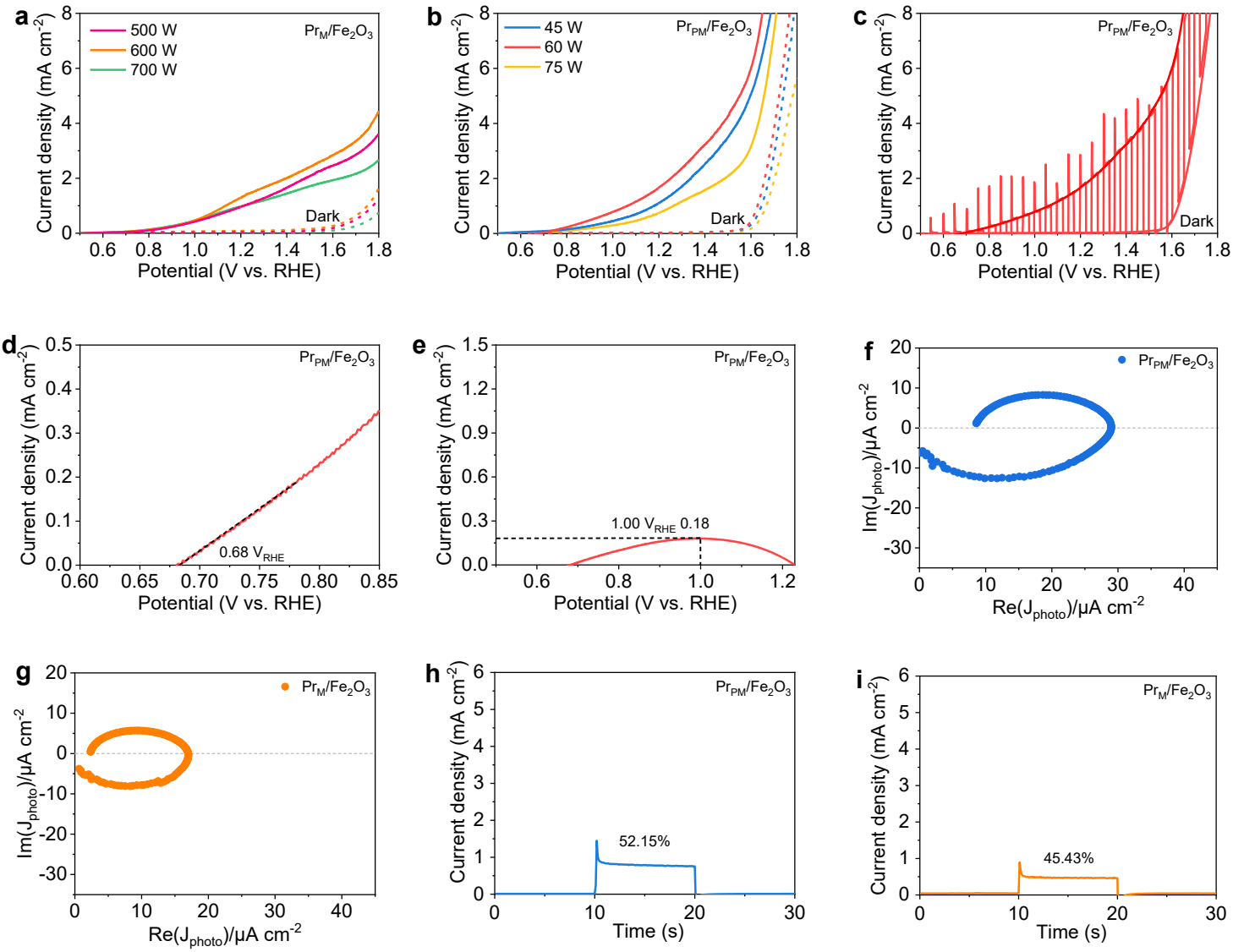

Supplementary Fig.63 Photoelectrochemical performance measurement of Pr$_{PM}$/Fe$_2$O$_3$. a, *J-V* curves of Pr-loaded Fe_2O_3 annealed directly by microwave at various power (800 W, 1000 W, and 1200 W) without plasma pretreatment. **b,** *J-V* curves of Pr single atoms anchored on Fe_2O_3 via microwave annealing after plasma pretreatment at various powers (45, 60, and 75 W). **c,** Chopped *J-V* curve of Pr$_{PM}$/Fe$_2$O$_3$. **d,** Onset potential of Pr$_{PM}$/Fe$_2$O$_3$. **e,** Applied bias photon-to current efficiency of Pr$_{PM}$/Fe$_2$O$_3$. **f, g,** IMPS responses of Pr$_{PM}$/Fe$_2$O$_3$ and Pr$_M$/Fe$_2$O$_3$ applied at 1 V$_{RHE}$. **h, i,** Transient photocurrent density of Pr$_{PM}$/Fe$_2$O$_3$ and Pr$_M$/Fe$_2$O$_3$. All measurements were performed in 1 M KOH under AM 1.5G illumination (100 mW cm^{-2}).

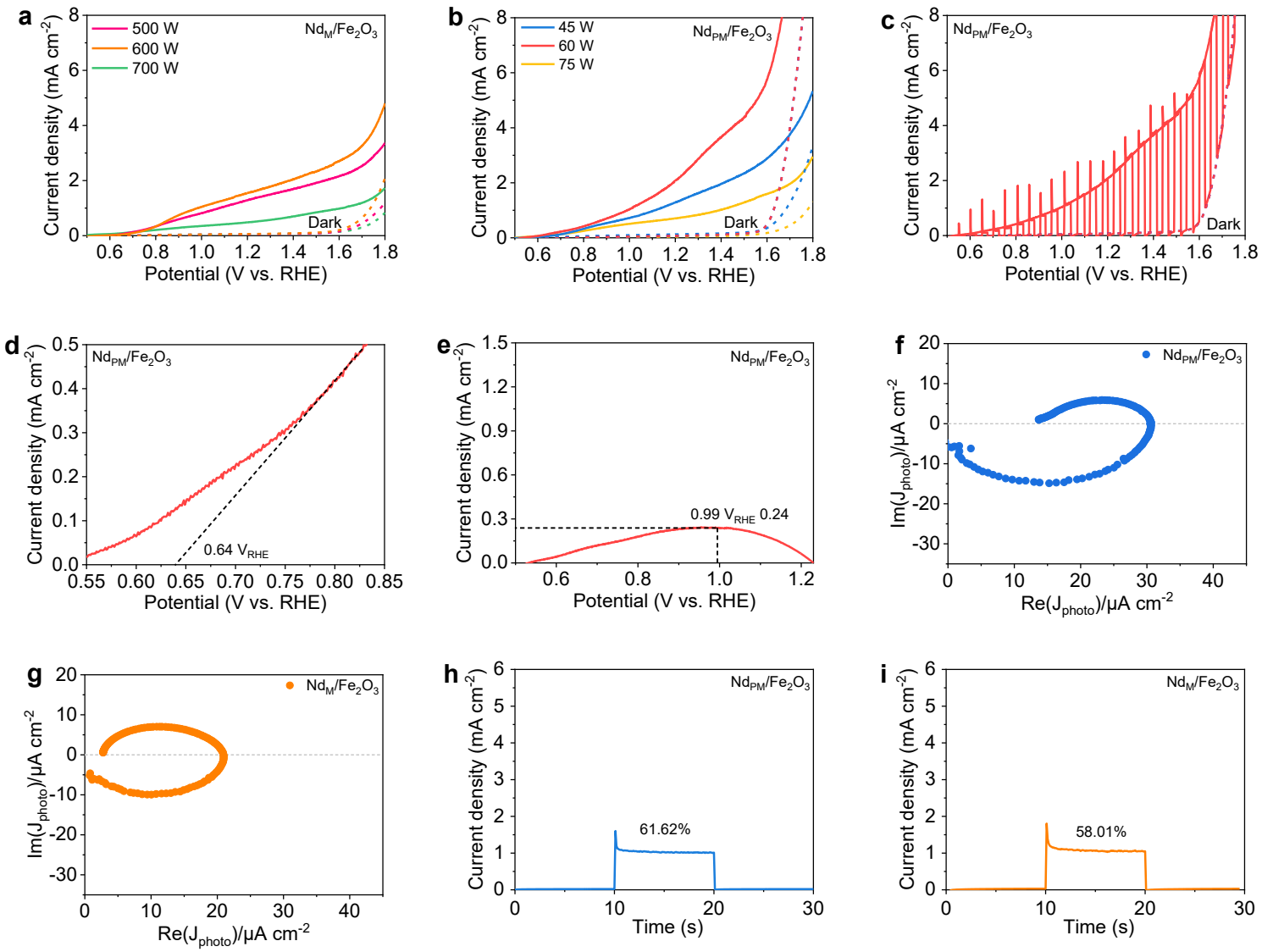

Supplementary Fig.64 Photoelectrochemical performance measurement of Nd$_{PM}$/Fe$_2$O$_3$. a, *J-V* curves of Nd-loaded Fe_2O_3 annealed directly by microwave at various power (600 W, 800 W, and 1000 W) without plasma pretreatment. **b,** *J-V* curves of Nd single atoms anchored on Fe_2O_3 via microwave annealing after plasma pretreatment at various powers (45, 60, and 75 W). **c,** Chopped *J-V* curve of Nd$_{PM}$/Fe$_2$O$_3$. **d,** Onset potential of Nd$_{PM}$/Fe$_2$O$_3$. **e,** Applied bias photon-to current efficiency of Nd$_{PM}$/Fe$_2$O$_3$. **f, g,** IMPS responses of Nd$_{PM}$/Fe$_2$O$_3$ and Nd$_M$/Fe$_2$O$_3$ applied at 1 V$_{RHE}$. **h, i,** Transient photocurrent density of Nd$_{PM}$/Fe$_2$O$_3$ and Nd$_M$/Fe$_2$O$_3$. All measurements were performed in 1 M KOH under AM 1.5G illumination (100 mW cm^{-2}).

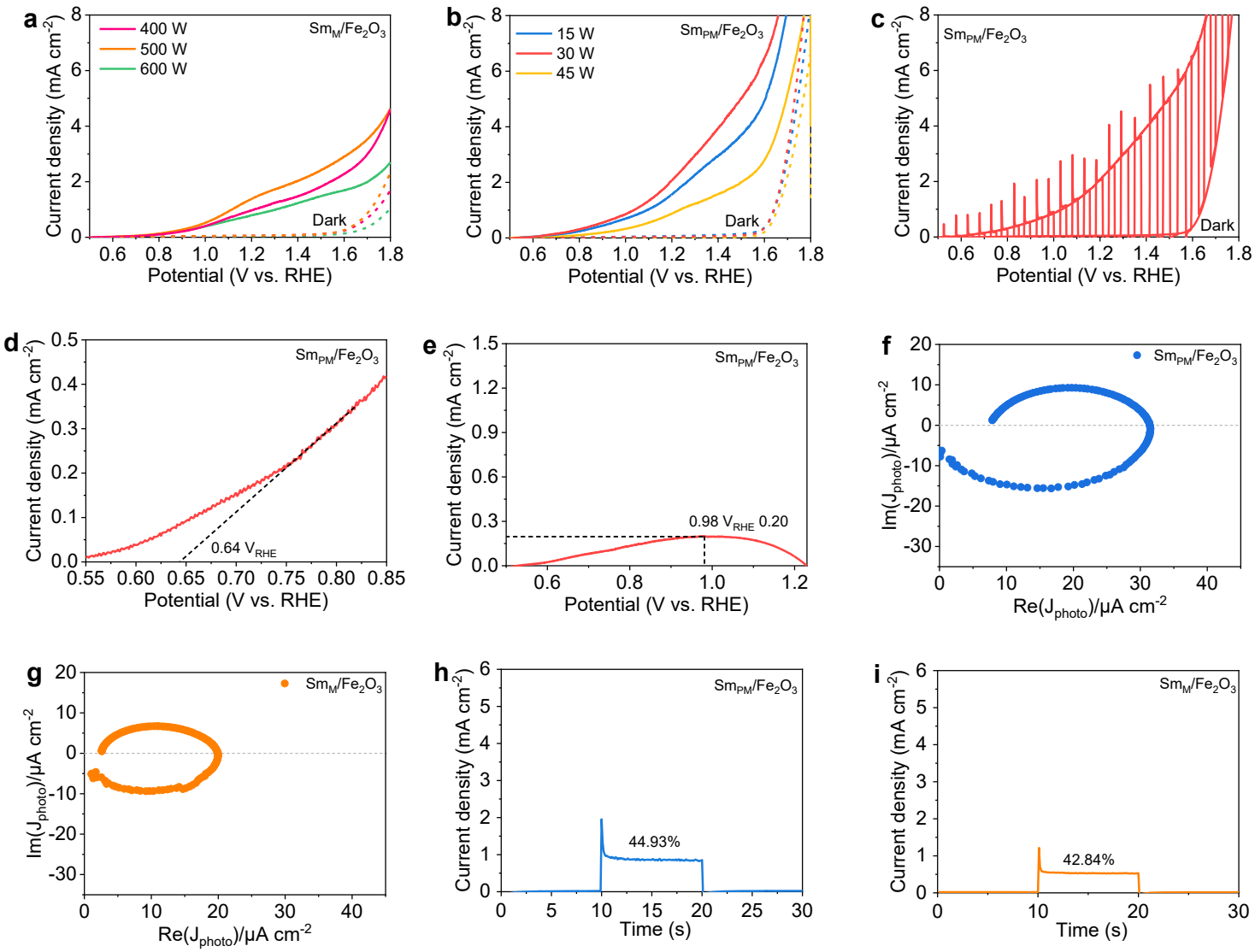

Supplementary Fig.65 Photoelectrochemical performance measurement of Sm$_{PM}$/Fe$_2$O$_3$. a, *J-V* curves of Sm-loaded Fe_2O_3 annealed directly by microwave at various power (400 W, 600 W, and 800 W) without plasma pretreatment. **b,** *J-V* curves of Sm single atoms anchored on Fe_2O_3 via microwave annealing after plasma pretreatment at various powers (15, 30, and 45 W). **c,** Chopped *J-V* curve of Sm$_{PM}$/Fe$_2$O$_3$. **d,** Onset potential of Sm$_{PM}$/Fe$_2$O$_3$. **e,** Applied bias photon-to current efficiency of Sm$_{PM}$/Fe$_2$O$_3$. **f, g,** IMPS responses of Sm$_{PM}$/Fe$_2$O$_3$ and Sm$_M$/Fe$_2$O$_3$ applied at 1 V$_{RHE}$. **h, i,** Transient photocurrent density of Sm$_{PM}$/Fe$_2$O$_3$ and Sm$_M$/Fe$_2$O$_3$. All measurements were performed in 1 M KOH under AM 1.5G illumination (100 mW cm^{-2}).

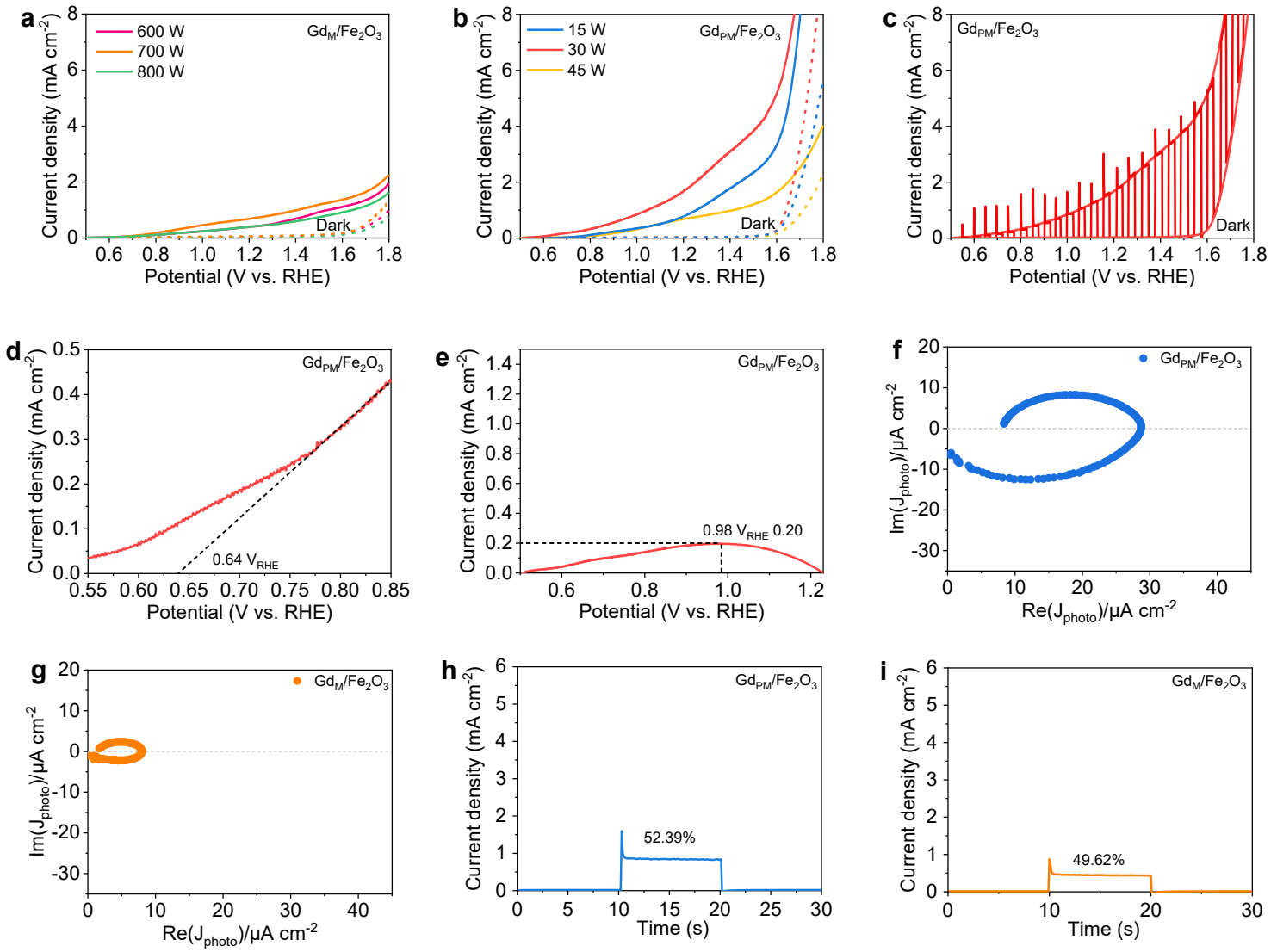

Supplementary Fig.66 Photoelectrochemical performance measurement of Gd$_{PM}$/Fe$_2$O$_3$. a, *J-V* curves of Gd-loaded Fe_2O_3 annealed directly by microwave at various power (800 W, 1000 W, and 1200 W) without plasma pretreatment. **b,** *J-V* curves of Gd single atoms anchored on Fe_2O_3 via microwave annealing after plasma pretreatment at various powers (15, 30, and 45 W). **c,** Chopped *J-V* curve of Gd$_{PM}$/Fe$_2$O$_3$. **d,** Onset potential of Gd$_{PM}$/Fe$_2$O$_3$. **e** Applied bias photon-to current efficiency of Gd$_{PM}$/Fe$_2$O$_3$. **f, g,** IMPS responses of Gd$_{PM}$/Fe$_2$O$_3$ and Gd$_M$/Fe$_2$O$_3$ applied at 1 V$_{RHE}$. **h, i,** Transient photocurrent density of Gd$_{PM}$/Fe$_2$O$_3$ and Gd$_M$/Fe$_2$O$_3$. All measurements were performed in 1 M KOH under AM 1.5G illumination (100 mW cm^{-2}).

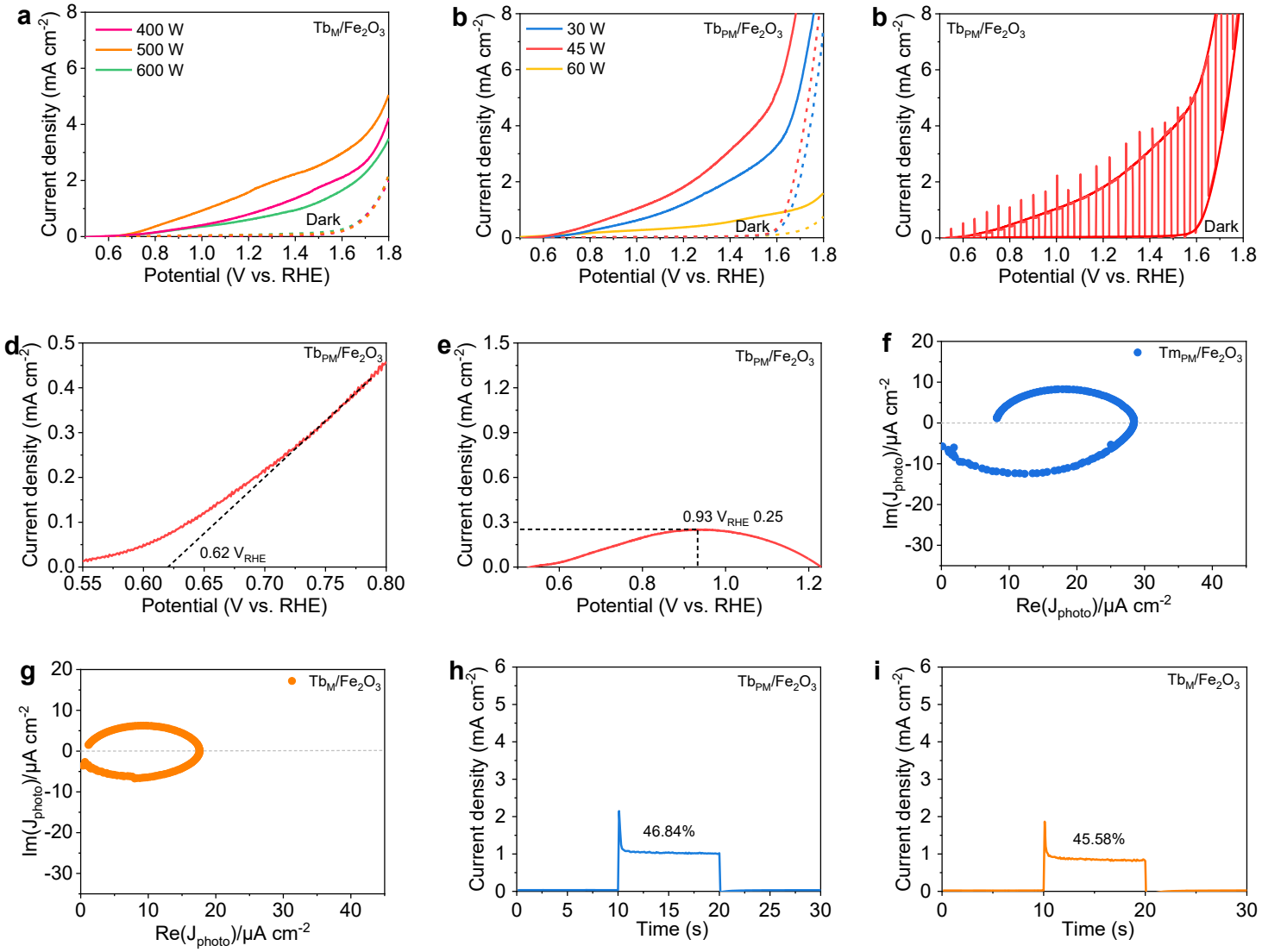

Supplementary Fig.67 Photoelectrochemical performance measurement of Tb_{PM}/Fe_2O_3. a, *J-V* curves of Td-loaded Fe_2O_3 annealed directly by microwave at various power (600 W, 800 W, and 1000 W) without plasma pretreatment. **b,** *J-V* curves of Td single atoms anchored on Fe_2O_3 via microwave annealing after plasma pretreatment at various powers (15, 30, and 45 W). **c,** Chopped *J-V* curve of Td_{PM}/Fe_2O_3. **d,** Onset potential of Td_{PM}/Fe_2O_3. **e,** Applied bias photon-to current efficiency of Td_{PM}/Fe_2O_3. **f, g,** IMPS responses of Td_{PM}/Fe_2O_3 and Td_M/Fe_2O_3 applied at 1 V_{RHE}. **h, i,** Transient photocurrent density of Td_{PM}/Fe_2O_3 and Td_M/Fe_2O_3. All measurements were performed in 1 M KOH under AM 1.5G illumination (100 mW cm^{-2}).

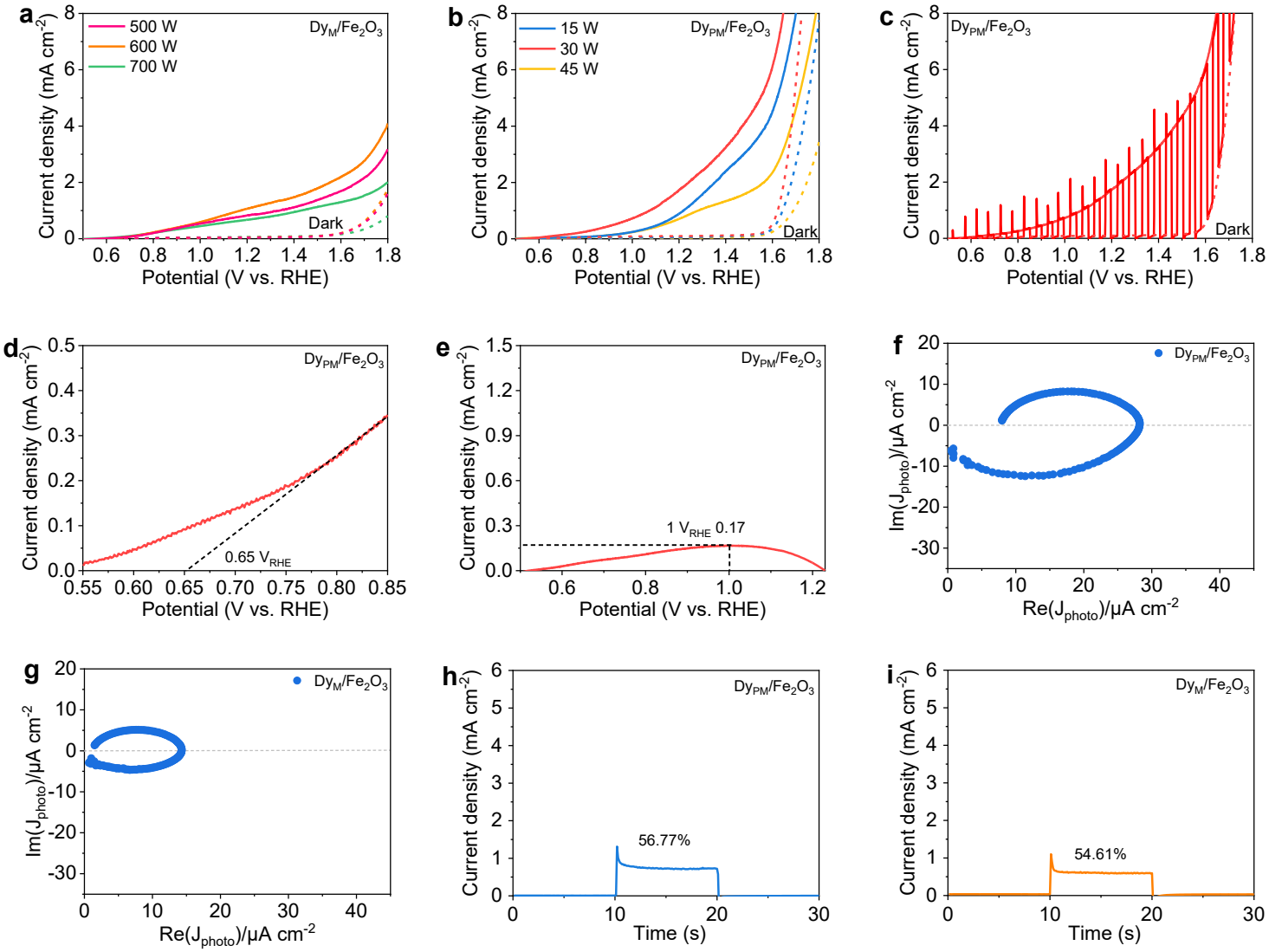

Supplementary Fig.68 Photoelectrochemical performance measurement of Dy$_{PM}$/Fe$_2$O$_3$. a, *J-V* curves of Dy-loaded Fe_2O_3 annealed directly by microwave at various power (600 W, 800 W, and 1000 W) without plasma pretreatment. **b,** *J-V* curves of Dy single atoms anchored on Fe_2O_3 via microwave annealing after plasma pretreatment at various powers (15, 30, and 45 W). **c,** Chopped *J-V* curve of Dy$_{PM}$/Fe$_2$O$_3$. **d,** Onset potential of Dy$_{PM}$/Fe$_2$O$_3$. **e,** Applied bias photon-to current efficiency of Dy$_{PM}$/Fe$_2$O$_3$. **f, g,** IMPS responses of Dy$_{PM}$/Fe$_2$O$_3$ and Dy$_M$/Fe$_2$O$_3$ applied at 1 V$_{RHE}$. **h, i,** Transient photocurrent density of Dy$_{PM}$/Fe$_2$O$_3$ and Dy$_M$/Fe$_2$O$_3$. All measurements were performed in 1 M KOH under AM 1.5G illumination (100 mW cm^{-2}).

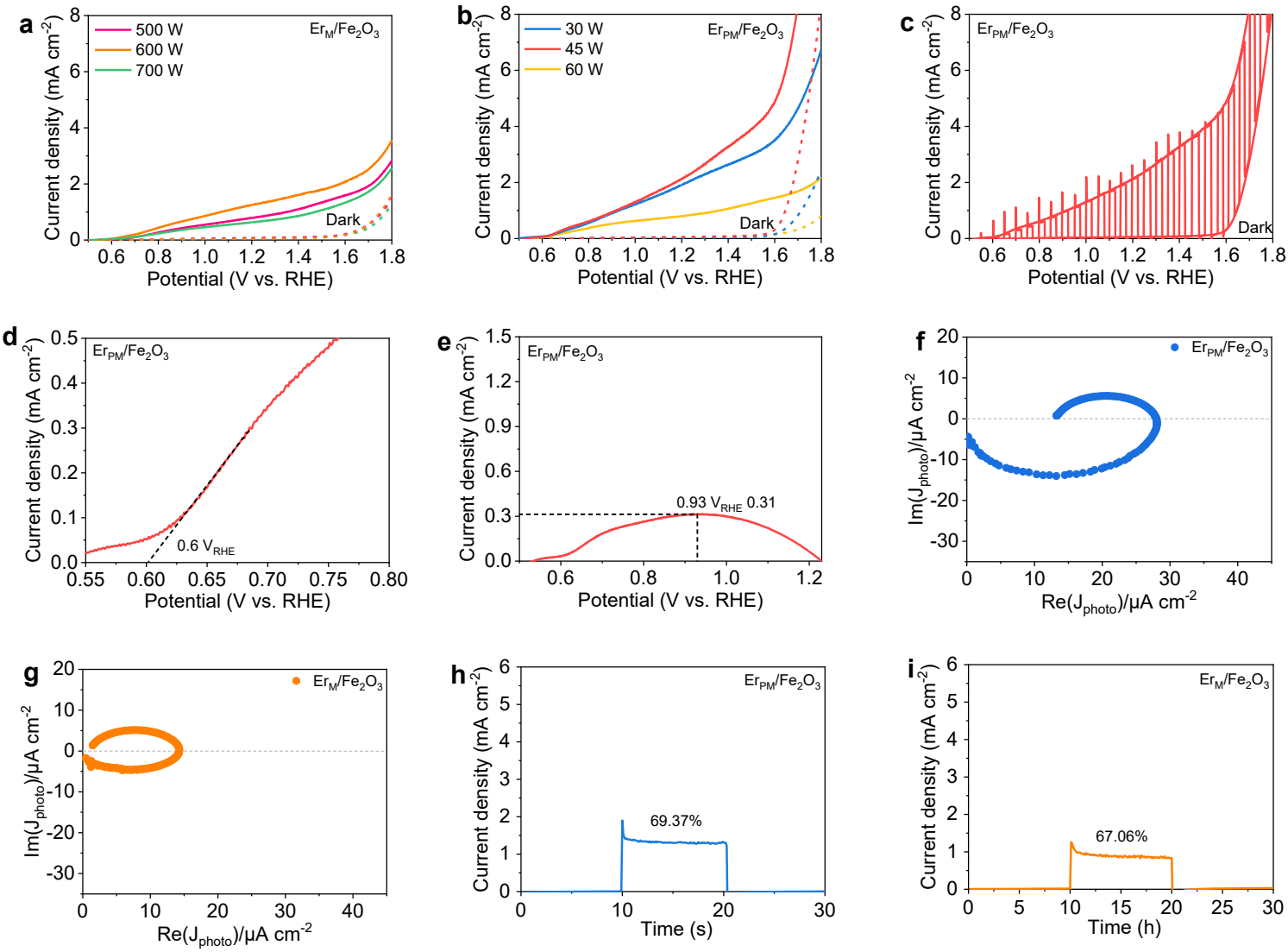

Supplementary Fig.69 Photoelectrochemical performance measurement of Er$_{PM}$/Fe$_2$O$_3$. a, *J-V* curves of Er-loaded Fe_2O_3 annealed directly by microwave at various power (600 W, 800 W, and 1000 W) without plasma pretreatment. **b,** *J-V* curves of Er single atoms anchored on Fe_2O_3 via microwave annealing after plasma pretreatment at various powers (15, 30, and 45 W). **c,** Chopped *J-V* curve of Er$_{PM}$/Fe$_2$O$_3$. **d,** Onset potential of Er$_{PM}$/Fe$_2$O$_3$. **e,** Applied bias photon-to current efficiency of Er$_{PM}$/Fe$_2$O$_3$. **f, g,** IMPS responses of Er$_{PM}$/Fe$_2$O$_3$ and Er$_M$/Fe$_2$O$_3$ applied at 1 V$_{RHE}$. **h, i,** Transient photocurrent density of Er$_{PM}$/Fe$_2$O$_3$ and Er$_M$/Fe$_2$O$_3$. All measurements were performed in 1 M KOH under AM 1.5G illumination (100 mW cm^{-2}).

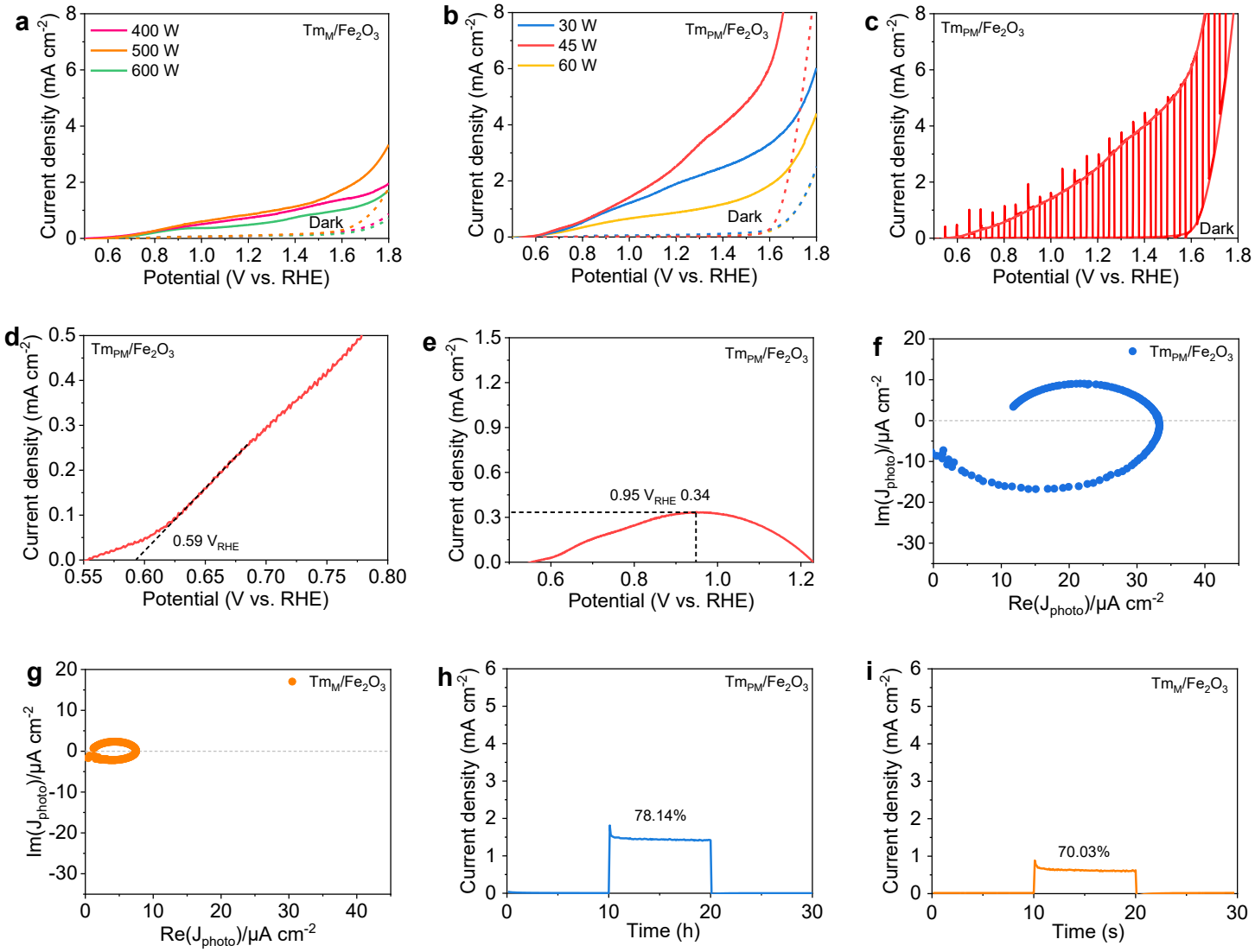

Supplementary Fig.70 Photoelectrochemical performance measurement of Tm$_{PM}$/Fe$_2$O$_3$. a, *J-V* curves of Tm-loaded Fe_2O_3 annealed directly by microwave at various power (600 W, 800 W, and 1000 W) without plasma pretreatment. **b,** *J-V* curves of Tm single atoms anchored on Fe_2O_3 via microwave annealing after plasma pretreatment at various powers (15, 30, and 45 W). **c,** Chopped *J-V* curve of Tm$_{PM}$/Fe$_2$O$_3$. **d,** Onset potential of Tm$_{PM}$/Fe$_2$O$_3$. **e,** Applied bias photon-to current efficiency of Tm$_{PM}$/Fe$_2$O$_3$. **f, g,** IMPS responses of Tm$_{PM}$/Fe$_2$O$_3$ and Tm$_M$/Fe$_2$O$_3$ applied at 1 V$_{RHE}$. **h, i,** Transient photocurrent density of Tm$_{PM}$/Fe$_2$O$_3$ and Tm$_M$/Fe$_2$O$_3$. All measurements were performed in 1 M KOH under AM 1.5G illumination (100 mW cm^{-2}).

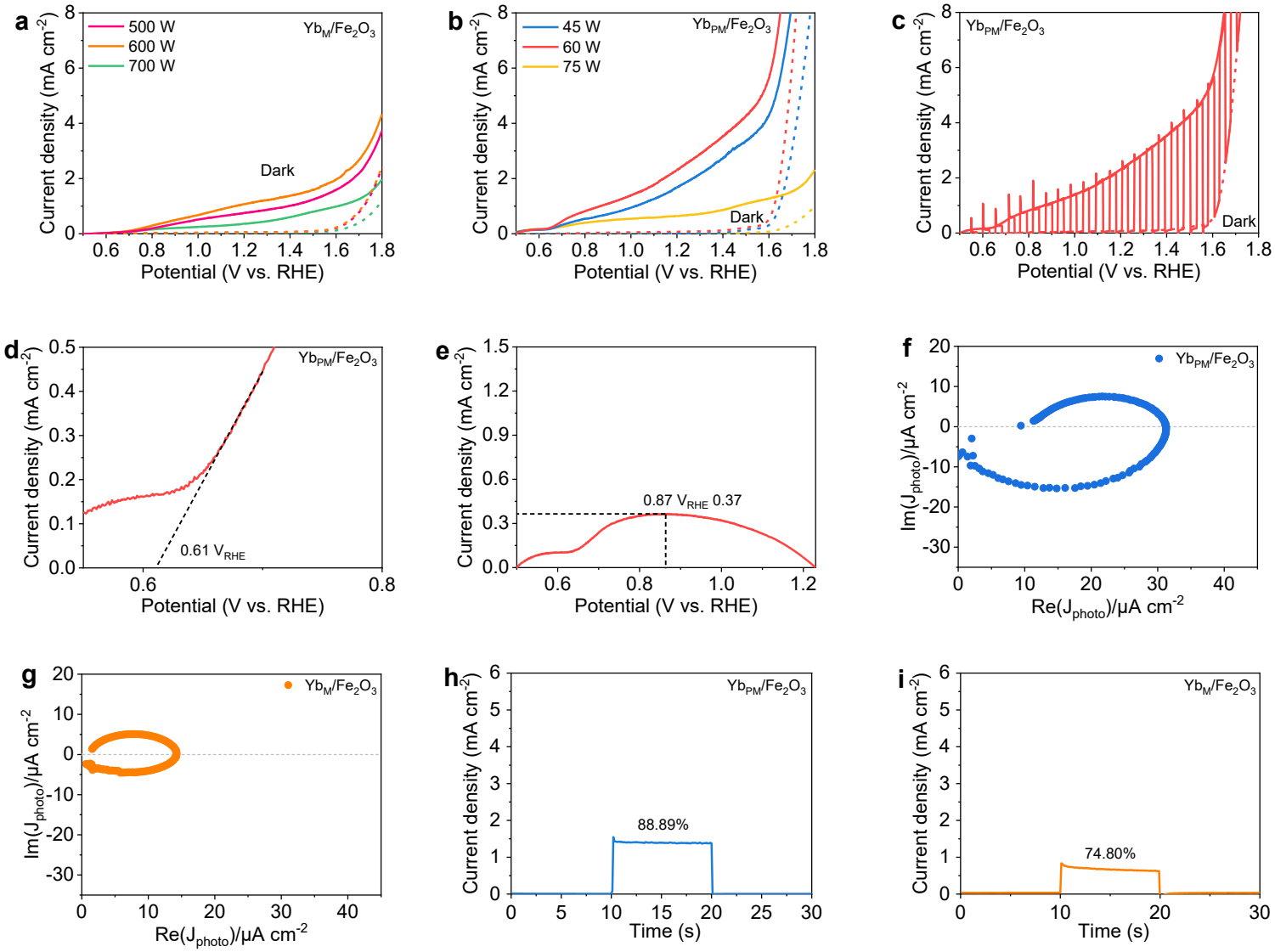

Supplementary Fig.71 Photoelectrochemical performance measurement of Yb_{PM}/Fe_2O_3. a, *J-V* curves of Y-loaded Fe_2O_3 annealed directly by microwave at various power (600 W, 800 W, and 1000 W) without plasma pretreatment. **b,** *J-V* curves of Y single atoms anchored on Fe_2O_3 via microwave annealing after plasma pretreatment at various powers (15, 30, and 45 W). **c,** Chopped *J-V* curve of Y_{PM}/Fe_2O_3. **d,** Onset potential of Y_{PM}/Fe_2O_3. **e,** Applied bias photon-to current efficiency of Y_{PM}/Fe_2O_3. **f, g,** IMPS responses of Y_{PM}/Fe_2O_3 and Y_M/Fe_2O_3 applied at 1 V_{RHE}. **h, i,** Transient photocurrent density of Y_{PM}/Fe_2O_3 and Y_M/Fe_2O_3. All measurements were performed in 1 M KOH under AM 1.5G illumination (100 mW cm^{-2}).

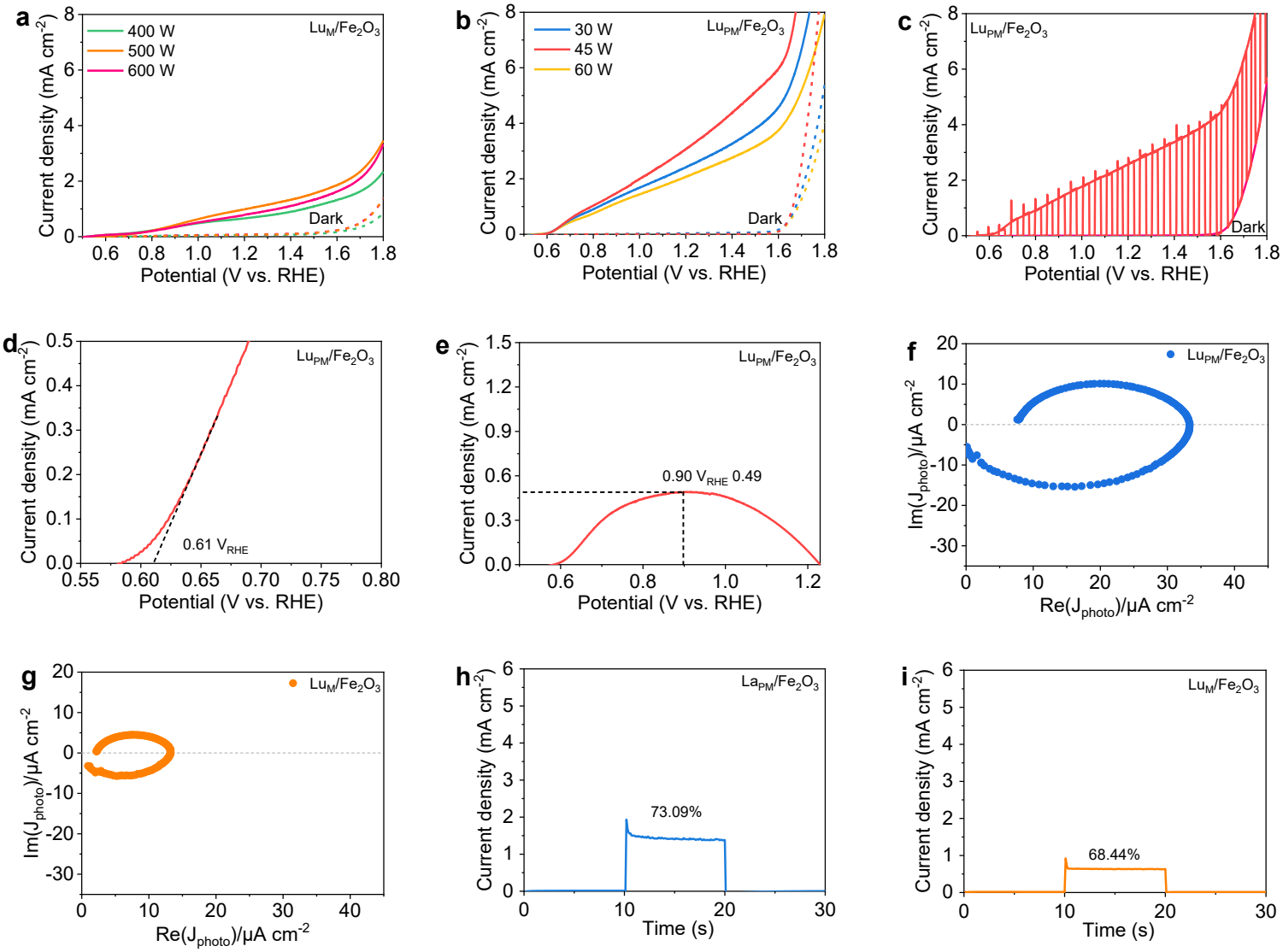

Supplementary Fig.72 Photoelectrochemical performance measurement of Lu$_{PM}$/Fe$_2$O$_3$. a, *J-V* curves of Lu-loaded Fe_2O_3 annealed directly by microwave at various power (600 W, 800 W, and 1000 W) without plasma pretreatment. **b,** *J-V* curves of Lu single atoms anchored on Fe_2O_3 via microwave annealing after plasma pretreatment at various powers (15, 30, and 45 W). **c,** Chopped *J-V* curve of Lu$_{PM}$/Fe$_2$O$_3$. **d,** Onset potential of Lu$_{PM}$/Fe$_2$O$_3$. **e** Applied bias photon-to current efficiency of Lu$_{PM}$/Fe$_2$O$_3$. **f, g,** IMPS responses of Lu$_{PM}$/Fe$_2$O$_3$ and Lu$_M$/Fe$_2$O$_3$ applied at 1 V$_{RHE}$. **h, i,** Transient photocurrent density of Lu$_{PM}$/Fe$_2$O$_3$ and Lu$_M$/Fe$_2$O$_3$. All measurements were performed in 1 M KOH under AM 1.5G illumination (100 mW cm^{-2}).

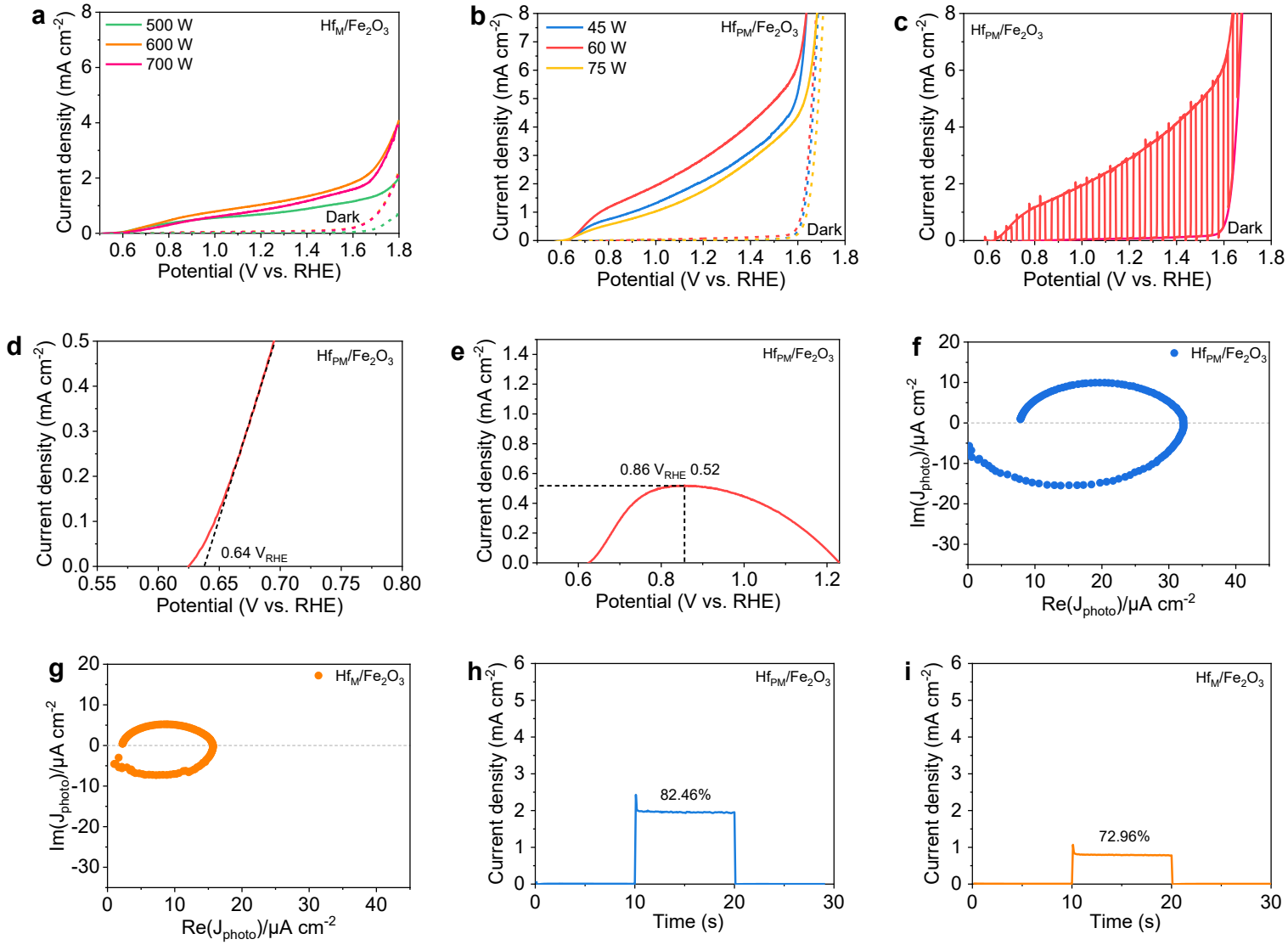

Supplementary Fig.73 Photoelectrochemical performance measurement of Hf$_{PM}$/Fe$_2$O$_3$. a, *J-V* curves of Hf-loaded Fe_2O_3 annealed directly by microwave at various power (600 W, 800 W, and 1000 W) without plasma pretreatment. **b,** *J-V* curves of Hf single atoms anchored on Fe_2O_3 via microwave annealing after plasma pretreatment at various powers (15, 30, and 45 W). **c,** Chopped *J-V* curve of Hf$_{PM}$/Fe$_2$O$_3$. **d,** Onset potential of Hf$_{PM}$/Fe$_2$O$_3$. **e,** Applied bias photon-to current efficiency of Hf$_{PM}$/Fe$_2$O$_3$. **f, g,** IMPS responses of Hf$_{PM}$/Fe$_2$O$_3$ and Hf$_M$/Fe$_2$O$_3$ applied at 1 V$_{RHE}$. **h, i,** Transient photocurrent density of Hf$_{PM}$/Fe$_2$O$_3$ and Hf$_M$/Fe$_2$O$_3$. All measurements were performed in 1 M KOH under AM 1.5G illumination (100 mW cm^{-2}).

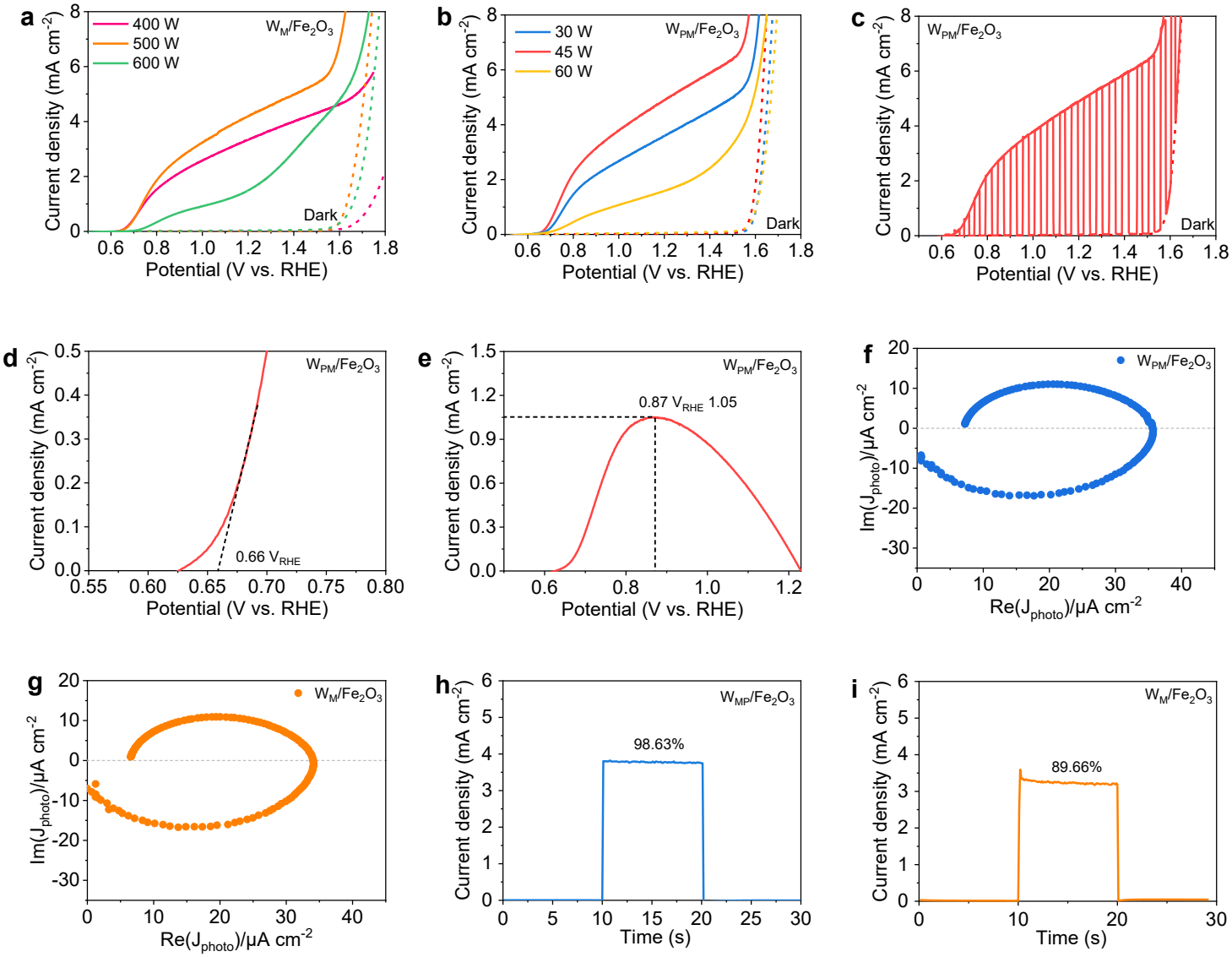

Supplementary Fig.74 Photoelectrochemical performance measurement of W_{PM}/Fe_2O_3. a, *J-V* curves of W-loaded Fe_2O_3 annealed directly by microwave at various power (600 W, 800 W, and 1000 W) without plasma pretreatment. **b,** *J-V* curves of W single atoms anchored on Fe_2O_3 via microwave annealing after plasma pretreatment at various powers (15, 30, and 45 W). **c,** Chopped *J-V* curve of W_{PM}/Fe_2O_3. **d,** Onset potential of W_{PM}/Fe_2O_3. **e,** Applied bias photon-to current efficiency of W_{PM}/Fe_2O_3. **f, g,** IMPS responses of W_{PM}/Fe_2O_3 and W_M/Fe_2O_3 applied at 1 V_{RHE}. **h, i,** Transient photocurrent density of W_{PM}/Fe_2O_3 and W_M/Fe_2O_3. All measurements were performed in 1 M KOH under AM 1.5G illumination (100 mW cm^{-2}).

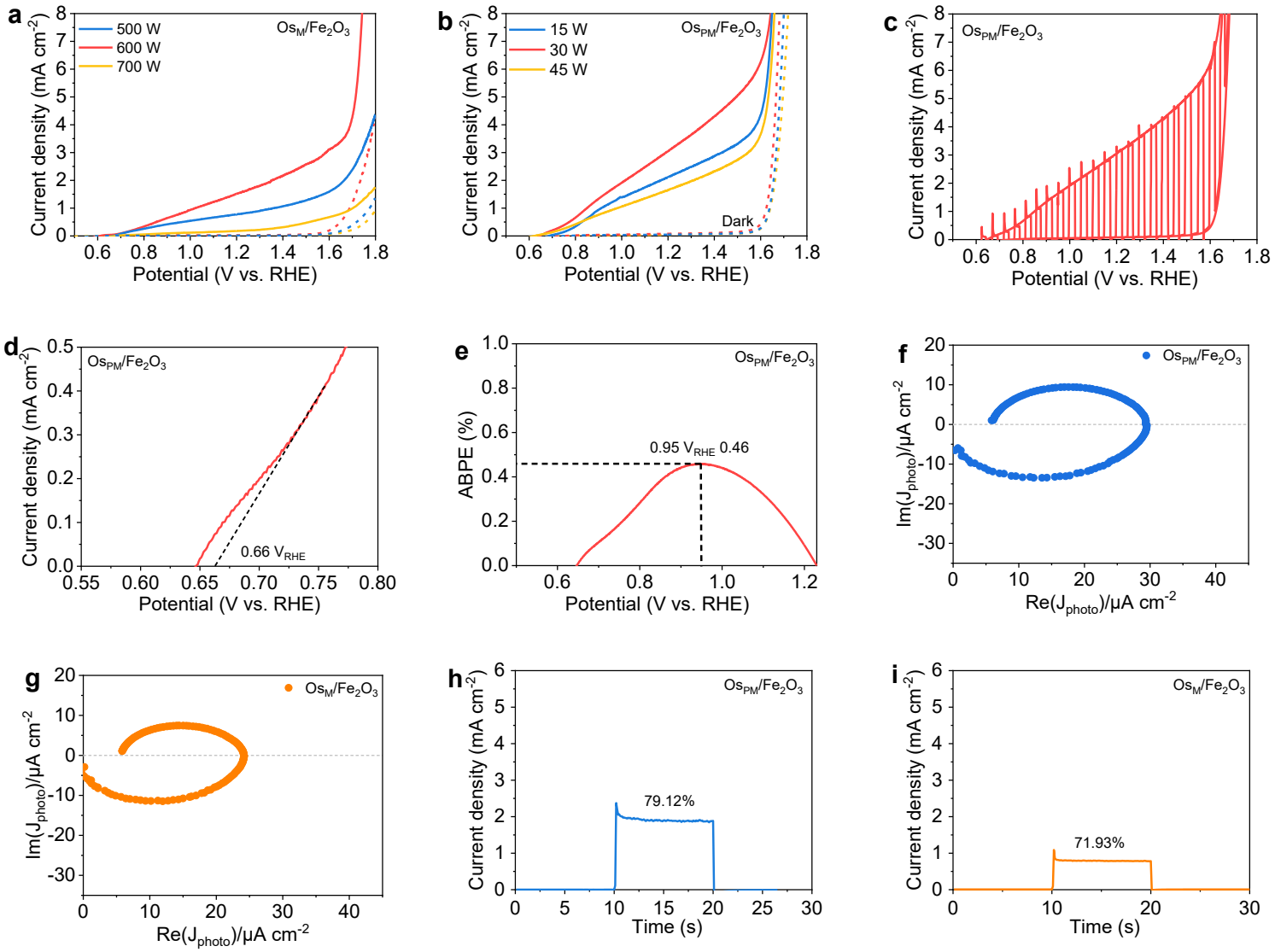

Supplementary Fig.75 Photoelectrochemical performance measurement of Os$_{PM}$/Fe$_2$O$_3$. a, *J-V* curves of Os-loaded Fe_2O_3 annealed directly by microwave at various power (800 W, 1000 W, and 1200 W) without plasma pretreatment. **b,** *J-V* curves of Os single atoms anchored on Fe_2O_3 via microwave annealing after plasma pretreatment at various powers (15, 30, and 45 W). **c,** Chopped *J-V* curve of Os$_{PM}$/Fe$_2$O$_3$. **d,** Onset potential of Os$_{PM}$/Fe$_2$O$_3$. **e,** Applied bias photon-to current efficiency of Os$_{PM}$/Fe$_2$O$_3$. **f, g,** IMPS responses of Os$_{PM}$/Fe$_2$O$_3$ and Os$_M$/Fe$_2$O$_3$ applied at 1 V$_{RHE}$. **h, i,** Transient photocurrent density of Os$_{PM}$/Fe$_2$O$_3$ and Os$_M$/Fe$_2$O$_3$. All measurements were performed in 1 M KOH under AM 1.5G illumination (100 mW cm^{-2}).

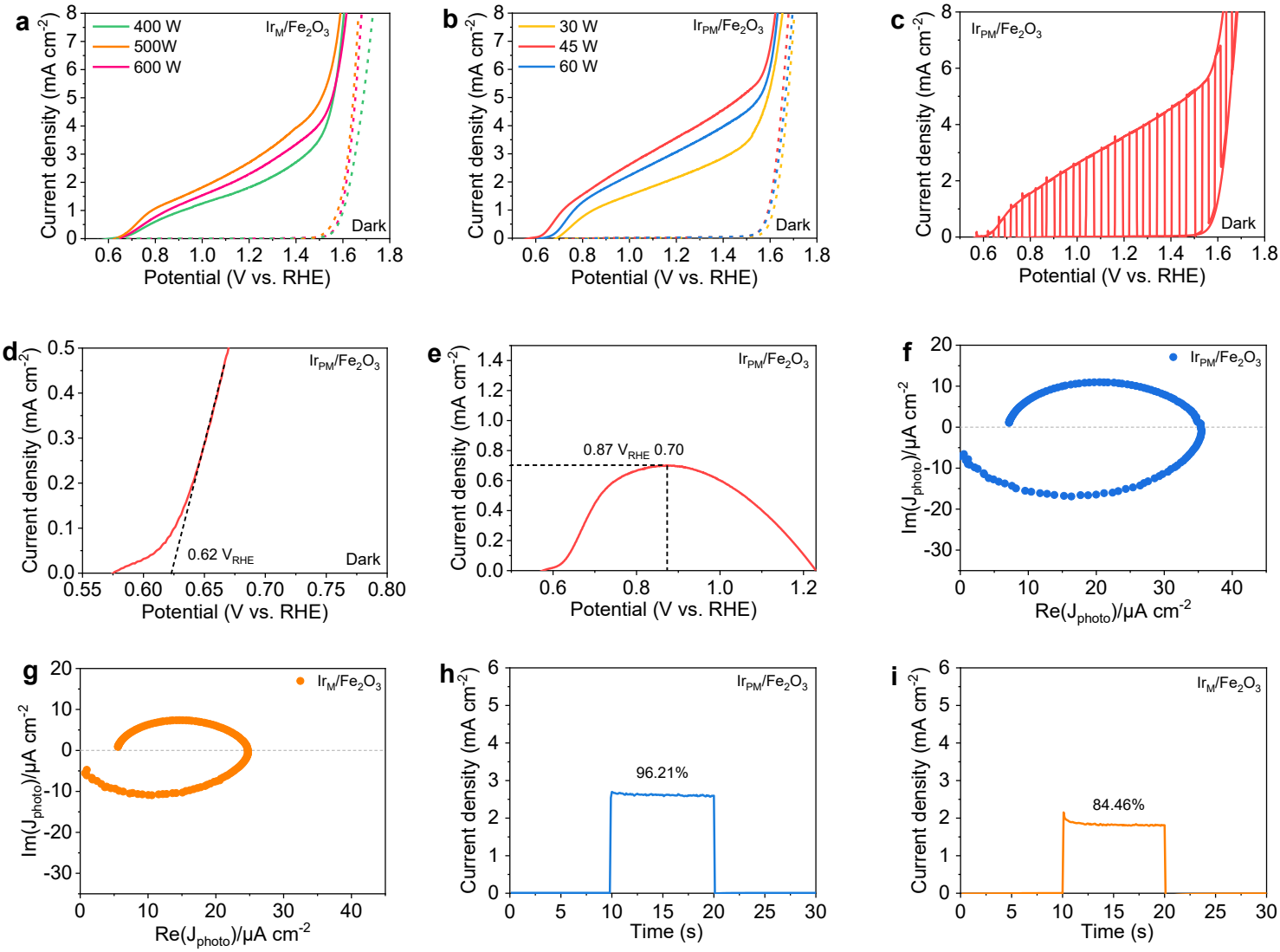

Supplementary Fig.76 Photoelectrochemical performance measurement of Ir_{PM}/Fe_2O_3. a, *J-V* curves of Ir-loaded Fe_2O_3 annealed directly by microwave at various power (400 W, 600 W, and 800 W) without plasma pretreatment. **b,** *J-V* curves of Ir single atoms anchored on Fe_2O_3 via microwave annealing after plasma pretreatment at various powers (30, 45, and 60 W). **c,** Chopped *J-V* curve of Ir_{PM}/Fe_2O_3. **d,** Onset potential of Ir_{PM}/Fe_2O_3. **e,** Applied bias photon-to current efficiency of Ir_{PM}/Fe_2O_3. **f, g,** IMPS responses of Ir_{PM}/Fe_2O_3 and Ir_M/Fe_2O_3 applied at 1 V_{RHE}. **h, i,** Transient photocurrent density of Ir_{PM}/Fe_2O_3 and Ir_M/Fe_2O_3. All measurements were performed in 1 M KOH under AM 1.5G illumination (100 mW cm^{-2}).

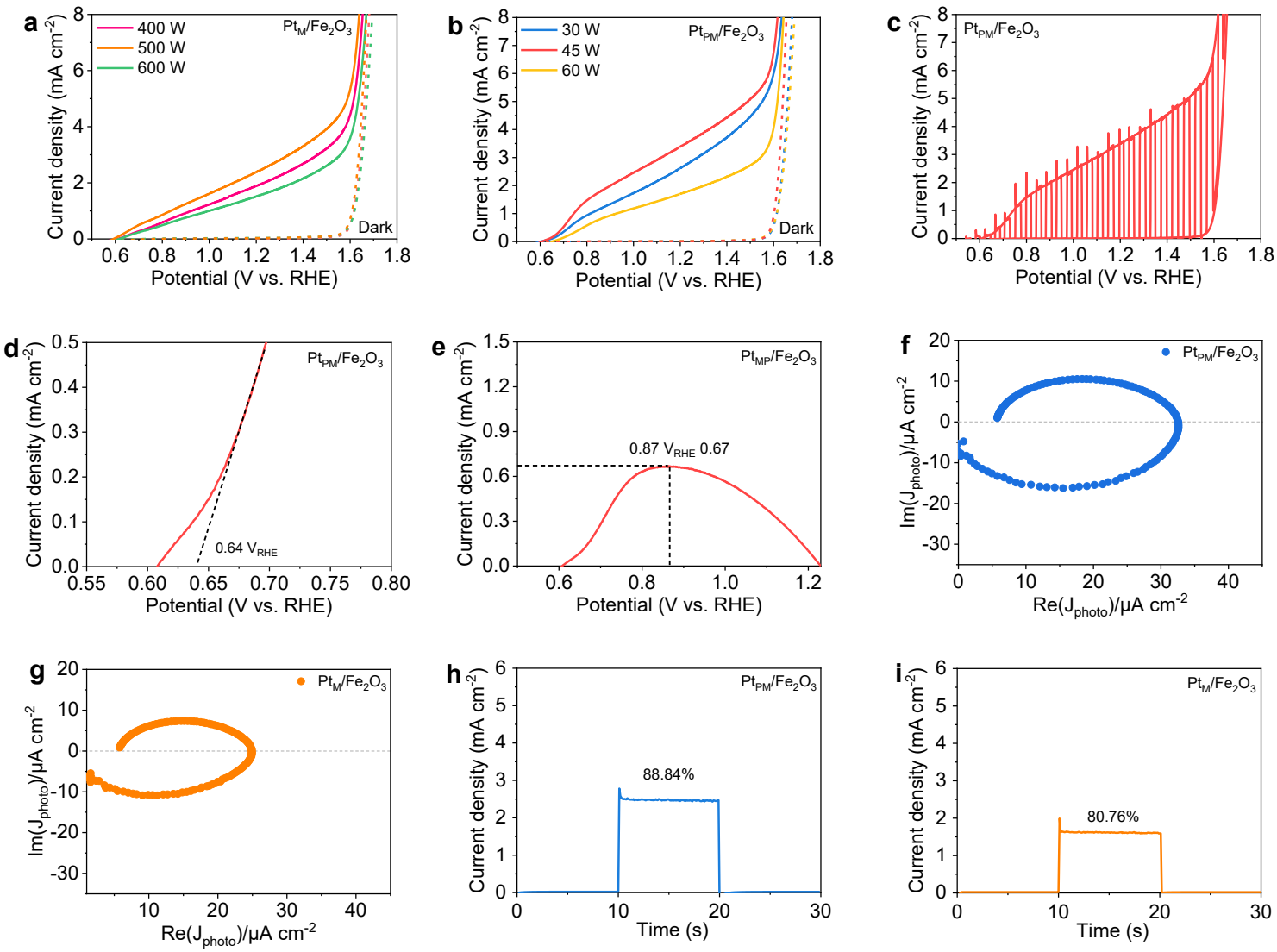

Supplementary Fig.77 Photoelectrochemical performance measurement of Pt$_{PM}$/Fe$_2$O$_3$. a, *J-V* curves of Pt-loaded Fe_2O_3 annealed directly by microwave at various power (600 W, 800 W, and 1000 W) without plasma pretreatment. **b,** *J-V* curves of Pt single atoms anchored on Fe_2O_3 via microwave annealing after plasma pretreatment at various powers (30, 45, and 60 W). **c,** Chopped *J-V* curve of Pt$_{PM}$/Fe$_2$O$_3$. **d,** Onset potential of Pt$_{PM}$/Fe$_2$O$_3$. **e,** Applied bias photon-to current efficiency of Pt$_{PM}$/Fe$_2$O$_3$. **f, g,** IMPS responses of Pt$_{PM}$/Fe$_2$O$_3$ and Pt$_M$/Fe$_2$O$_3$ applied at 1 V$_{RHE}$. **h, i,** Transient photocurrent density of Pt$_{PM}$/Fe$_2$O$_3$ and Pt$_M$/Fe$_2$O$_3$. All measurements were performed in 1 M KOH under AM 1.5G illumination (100 mW cm^{-2}).

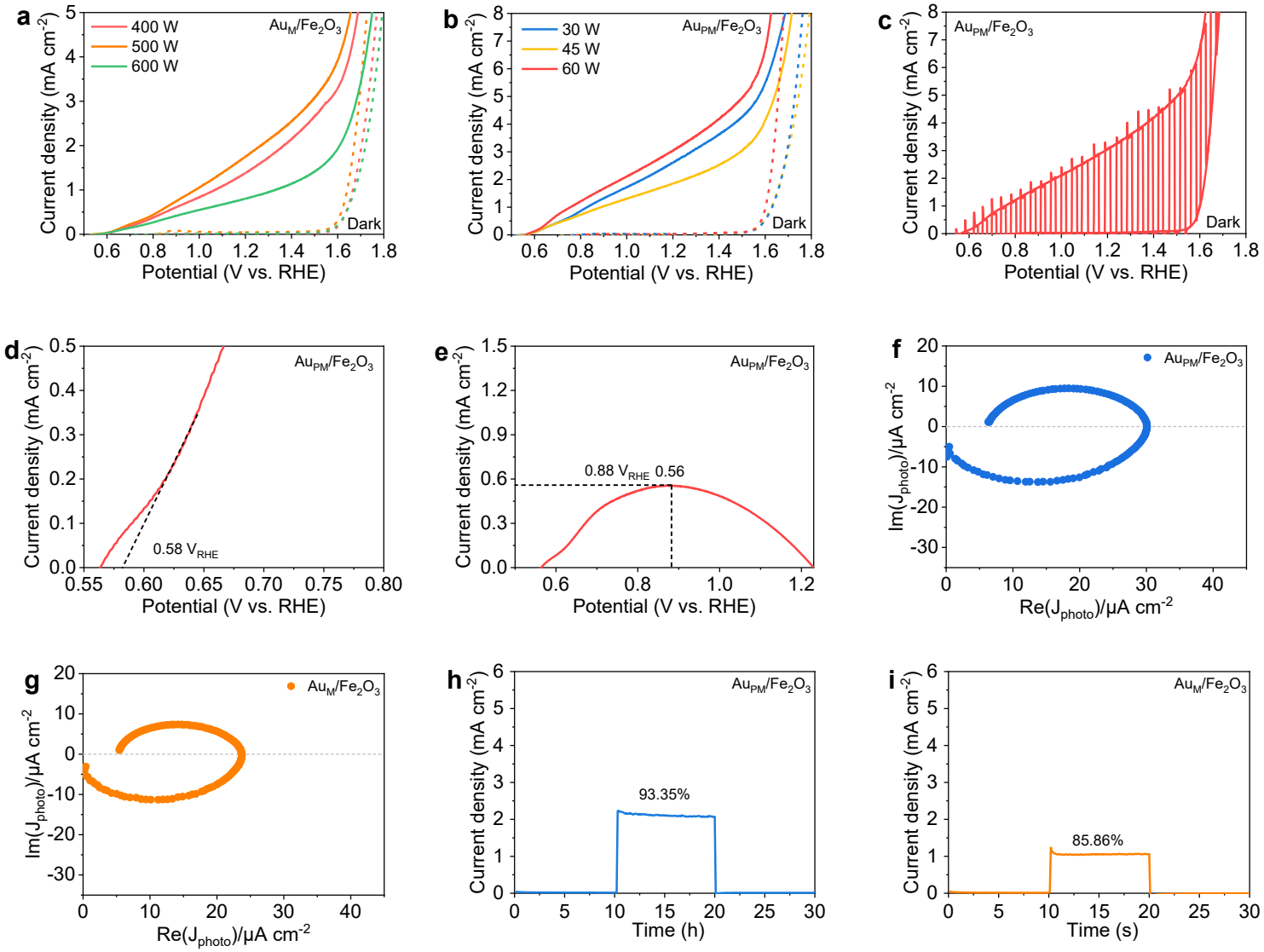

Supplementary Fig.78 Photoelectrochemical performance measurement of Au_{PM}/Fe_2O_3. a, *J-V* curves of Au-loaded Fe_2O_3 annealed directly by microwave at various power (600 W, 800 W, and 1000 W) without plasma pretreatment. **b,** *J-V* curves of Au single atoms anchored on Fe_2O_3 via microwave annealing after plasma pretreatment at various powers (30, 45, and 60 W). **c,** Chopped *J-V* curve of Au_{PM}/Fe_2O_3. **d,** Onset potential of Au_{PM}/Fe_2O_3. **e,** Applied bias photon-to current efficiency of Au_{PM}/Fe_2O_3. **f, g,** IMPS responses of Au_{PM}/Fe_2O_3 and Au_M/Fe_2O_3 applied at 1 V_{RHE}. **h, i,** Transient photocurrent density of Au_{PM}/Fe_2O_3 and Au_M/Fe_2O_3. All measurements were performed in 1 M KOH under AM 1.5G illumination (100 mW cm^{-2}).

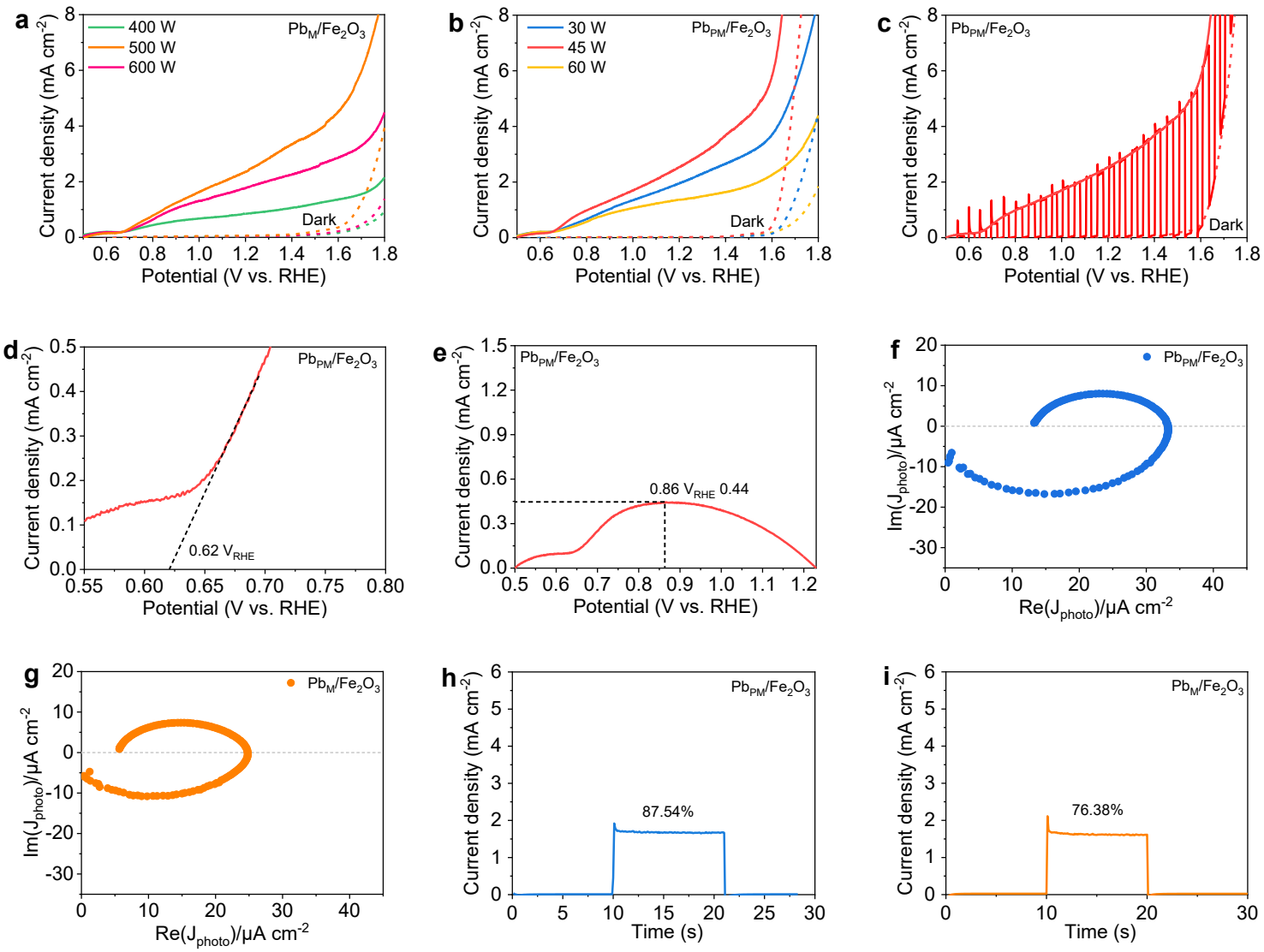

Supplementary Fig.79 Photoelectrochemical performance measurement of Pb_{PM}/Fe_2O_3. a, *J-V* curves of Pb-loaded Fe_2O_3 annealed directly by microwave at various power (600 W, 800 W, and 1000 W) without plasma pretreatment. **b,** *J-V* curves of Au single atoms anchored on Fe_2O_3 via microwave annealing after plasma pretreatment at various powers (30, 45, and 60 W). **c,** Chopped *J-V* curve of Pb_{PM}/Fe_2O_3. **d,** Onset potential of Pb_{PM}/Fe_2O_3. **e,** Applied bias photon-to current efficiency of Pb_{PM}/Fe_2O_3. **f, g,** IMPS responses of Pb_{PM}/Fe_2O_3 and Pb_M/Fe_2O_3 applied at 1 V_{RHE}. **h, i,** Transient photocurrent density of Pb_{PM}/Fe_2O_3 and Pb_M/Fe_2O_3. All measurements were performed in 1 M KOH under AM 1.5G illumination (100 mW cm^{-2}).

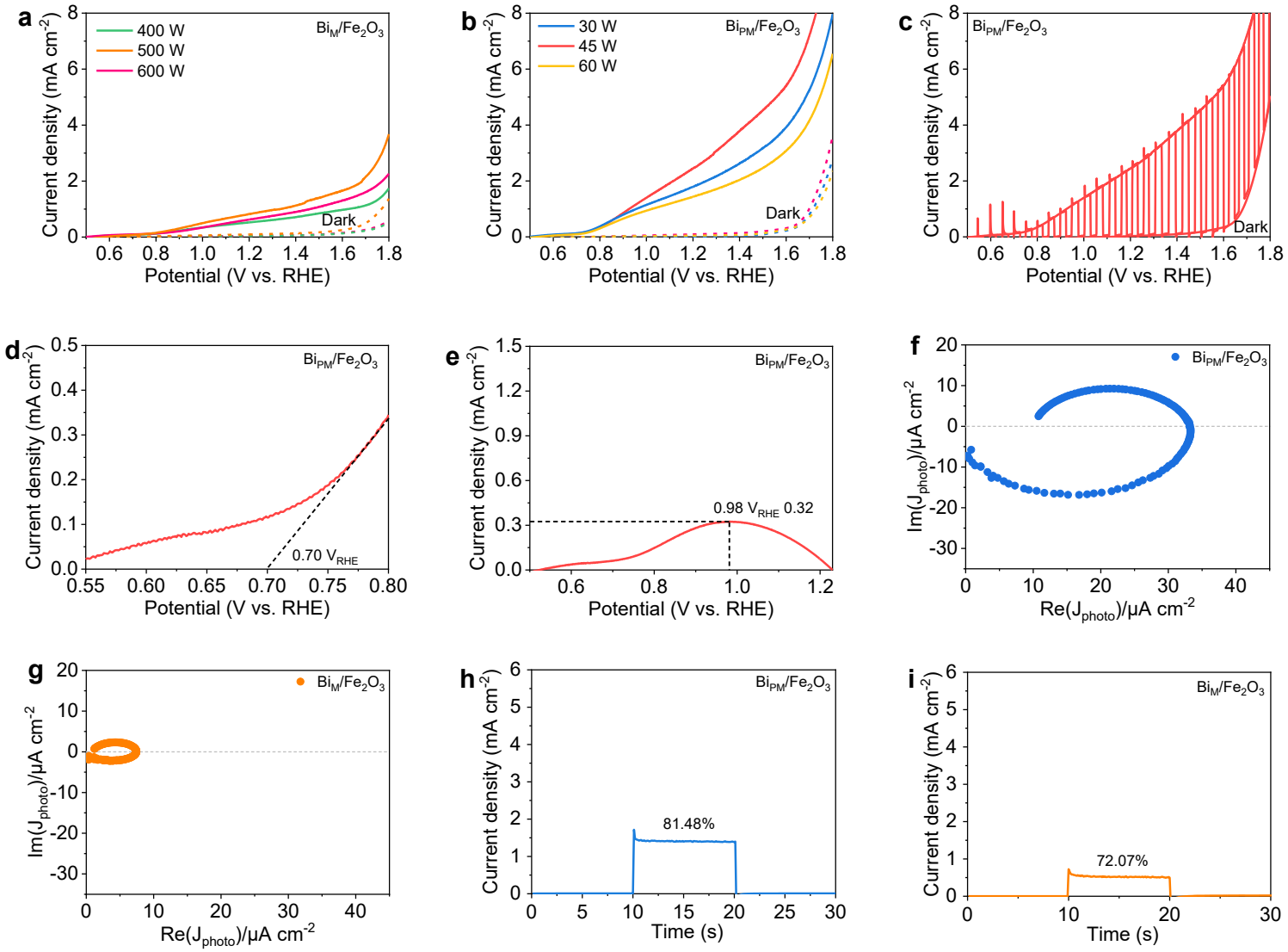

Supplementary Fig.80 Photoelectrochemical performance measurement of Nb$_{PM}$/Fe$_2$O$_3$. a, *J-V* curves of Bi-loaded Fe_2O_3 annealed directly by microwave at various power (600 W, 800 W, and 1000 W) without plasma pretreatment. **b,** *J-V* curves of Bi single atoms anchored on Fe_2O_3 via microwave annealing after plasma pretreatment at various powers (30, 45, and 60 W). **c,** Chopped *J-V* curve of Bi$_{PM}$/Fe$_2$O$_3$. **d,** Onset potential of Bi$_{PM}$/Fe$_2$O$_3$. **e,** Applied bias photon-to current efficiency of Bi$_{PM}$/Fe$_2$O$_3$. **f, g,** IMPS responses of Bi$_{PM}$/Fe$_2$O$_3$ and Bi$_M$/Fe$_2$O$_3$ applied at 1 V$_{RHE}$. **h, i,** Transient photocurrent density of Bi$_{PM}$/Fe$_2$O$_3$ and Bi$_M$/Fe$_2$O$_3$. All measurements were performed in 1 M KOH under AM 1.5G illumination (100 mW cm^{-2}).

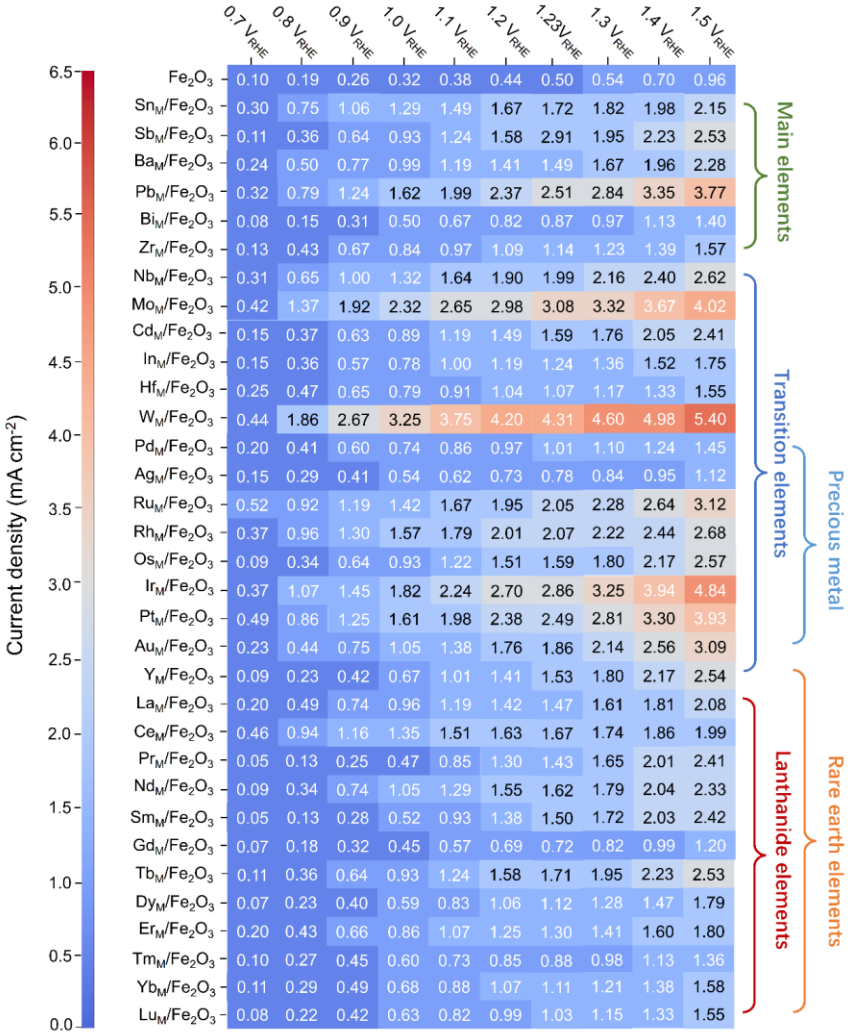

Supplementary Fig.81 The photoelectrochemical performance of 33 photoelectrodes without plasma pretreatment. OER activities of Fe_2O_3 loaded with 33 metallic elements without plasma pretreatment.

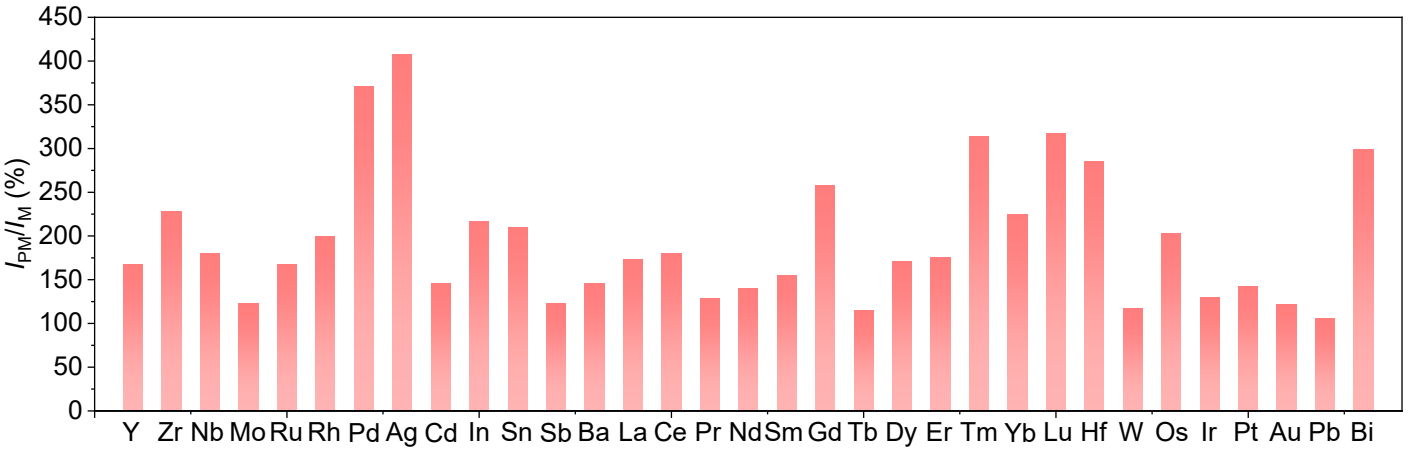

Supplementary Fig.82 Photocurrent density ratio. Photoelectrochemical current density comparison between plasma-microwave and microwave-only methods.

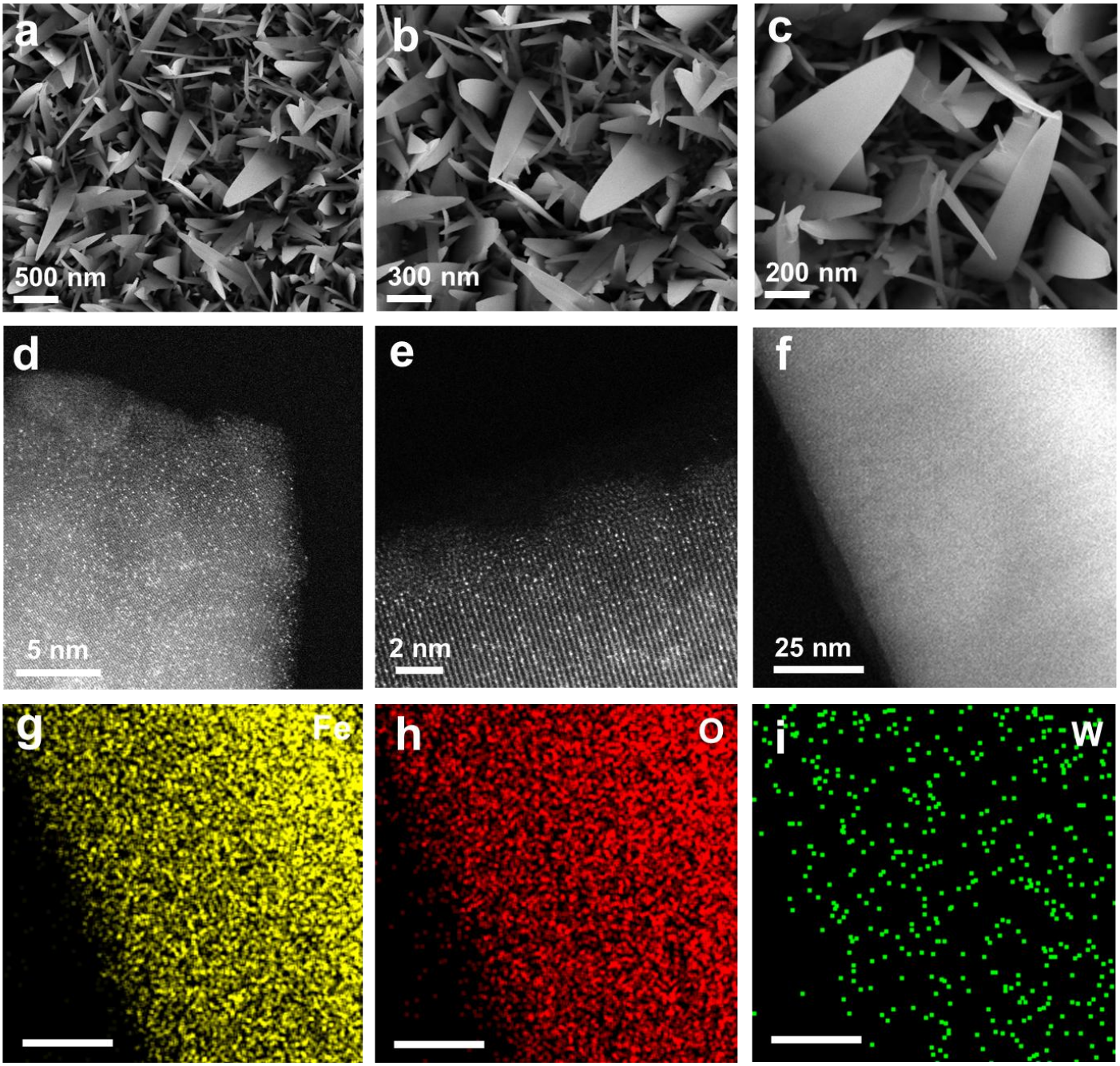

Supplementary Fig. 83 SEM, HAADF-STEM and EDS elemental mappings of W_{PM}/Fe_2O_3. a-c, SEM images of W_{PM}/Fe_2O_3. **d, e,** High resolution HAADF-STEM images of W_{PM}/Fe_2O_3. **f-i,** elemental mappings of W_{PM}/Fe_2O_3.

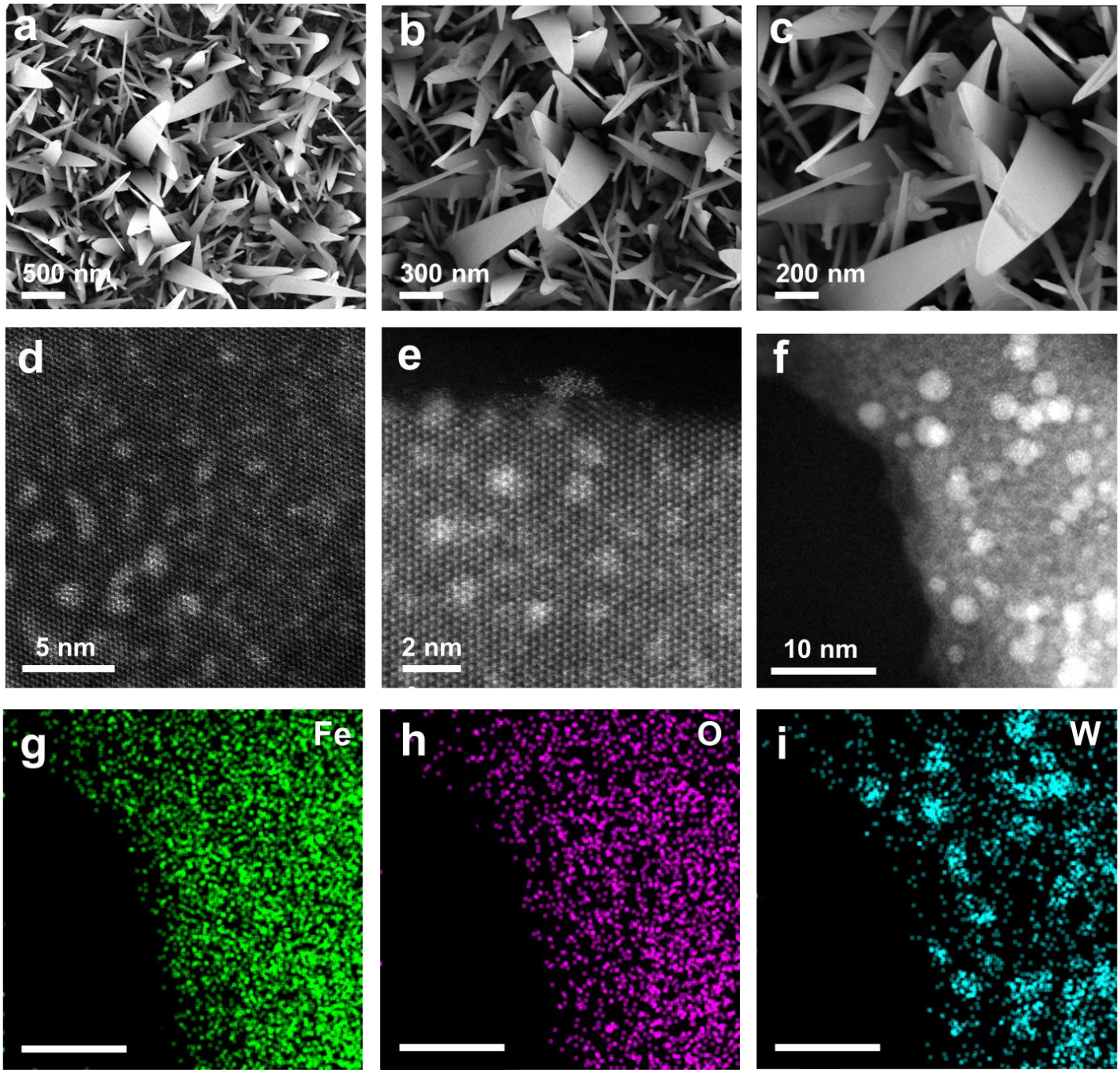

Supplementary Fig. 84 SEM, HAADF-STEM and EDS elemental mappings of W_M/Fe_2O_3. a-c, SEM images of W_M/Fe_2O_3. **d, e,** High resolution HAADF-STEM images of W_M/Fe_2O_3. **f,** elemental mappings of W_M/Fe_2O_3.

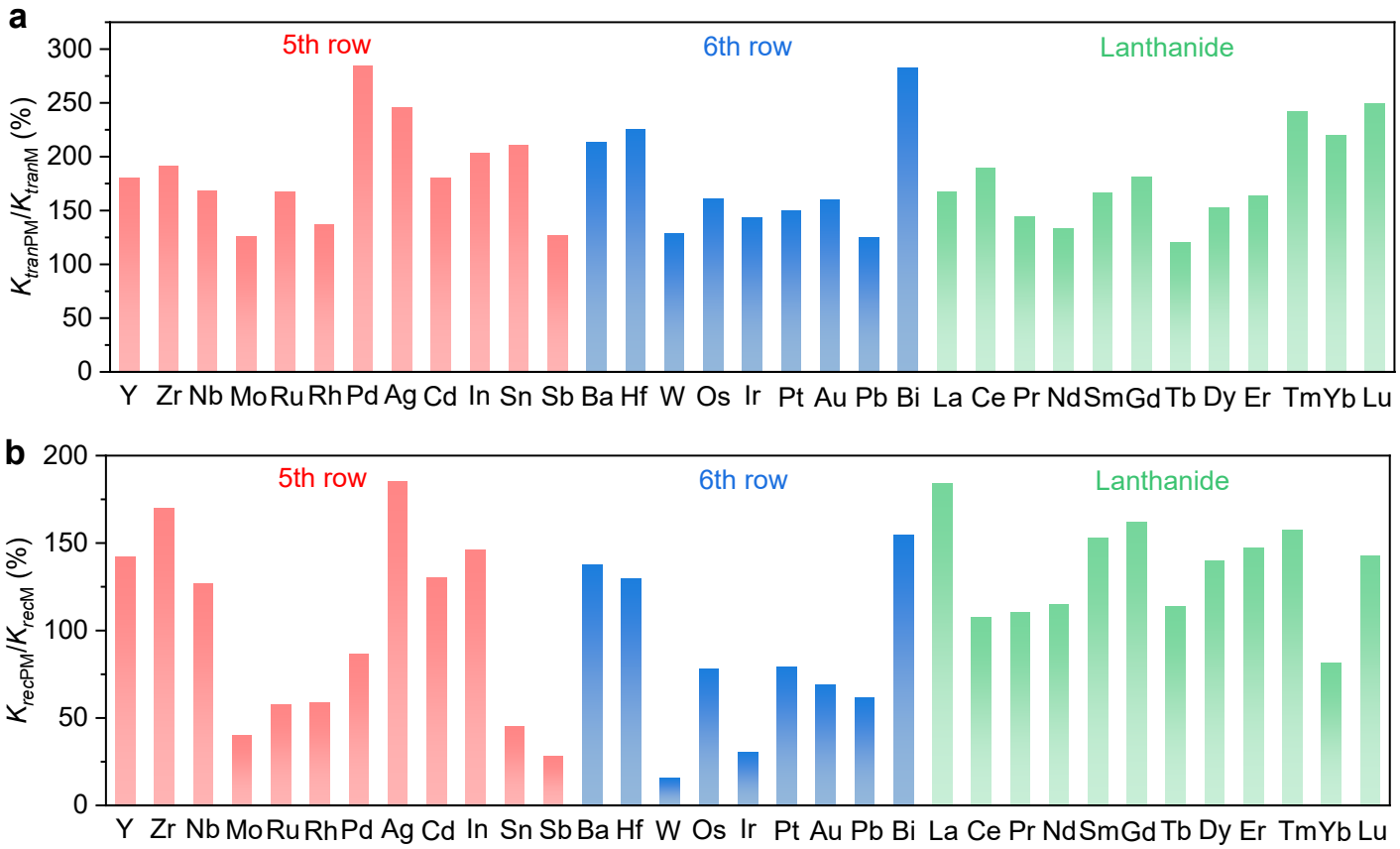

Supplementary Fig. 85 Charge transfer and recombination rate ratios. The charge transfer and recombination rate ratios of plasma-treated and untreated Fe_2O_3 loaded with 33 various metals.

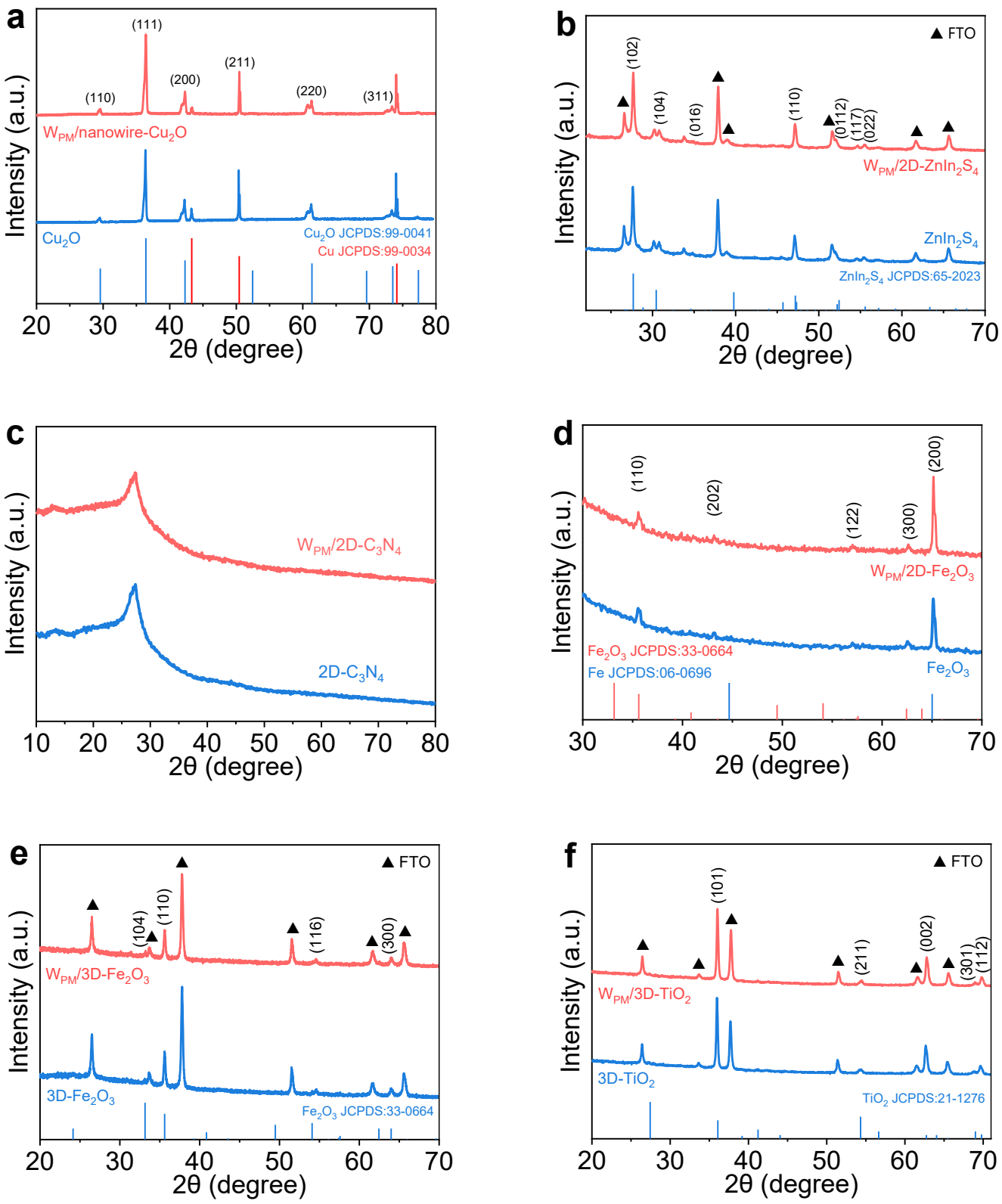

Supplementary Fig. 86 X-ray diffraction (XRD) patterns. a-f, XRD patterns of 1D-Cu_2O, W_{PM}/1D-Cu_2O (**a**), 2D-$ZnIn_2S_4$, W_{PM}/2D-2D-$ZnIn_2S_4$ (**b**), 2D-C_3N_4, W_{PM}/2D-C_3N_4 (**c**), 2D-Fe_2O_3, W_{PM}/2D-Fe_2O_3 (**d**), 3D-Fe_2O_3, W_{PM}/3D-Fe_2O_3 (**e**), 3D-TiO_2 and W_{PM}/3D-TiO_2 (**f**).

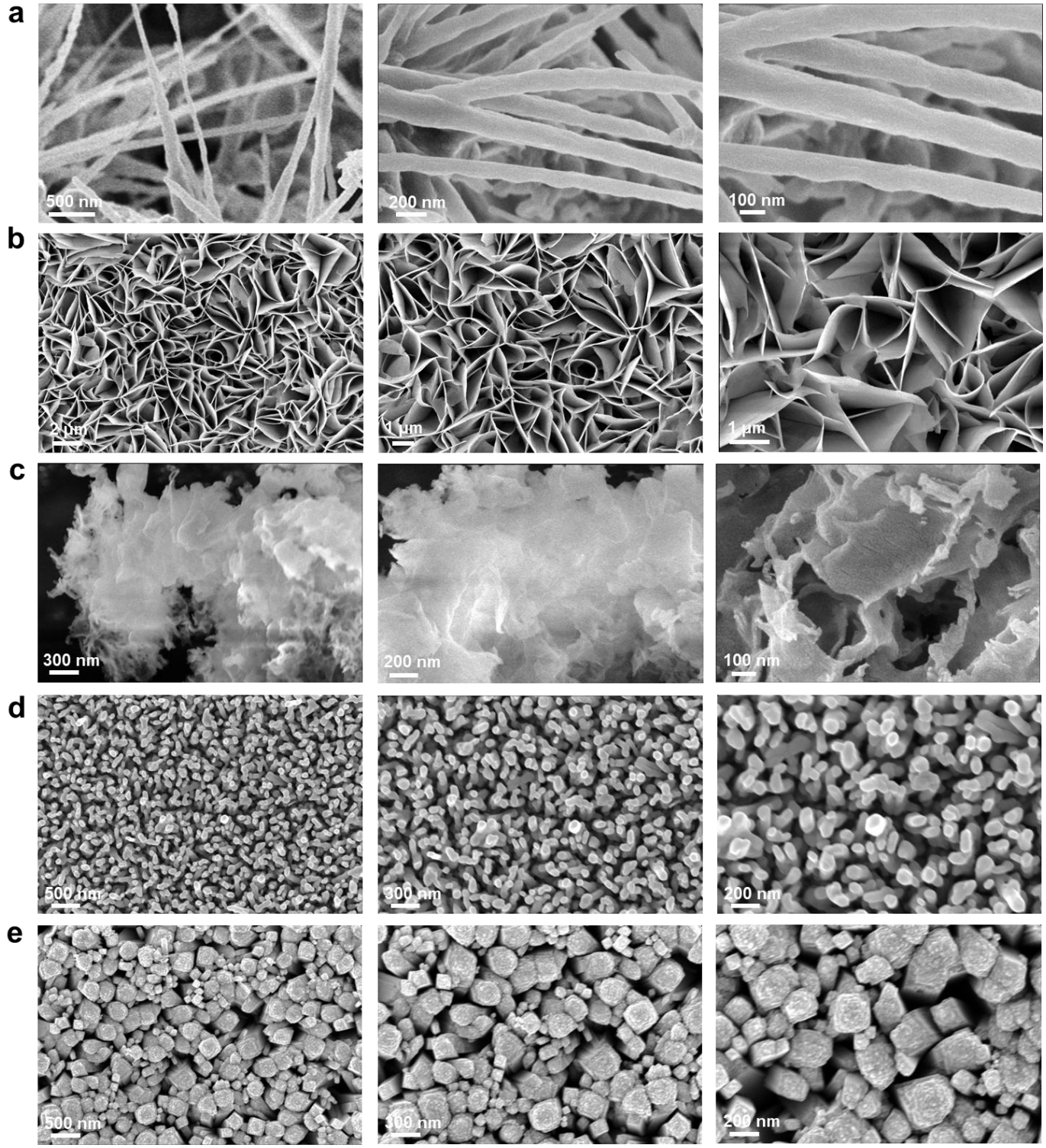

Supplementary Fig. 87 SEM observation. SEM images of 1D-Cu_2O (**a**), 2D-$ZnIn_2S_4$ (**b**), 2D-C_3N_4 (**c**), 3D-Fe_2O_3 (**d**), and 3D-TiO_2 (**e**).

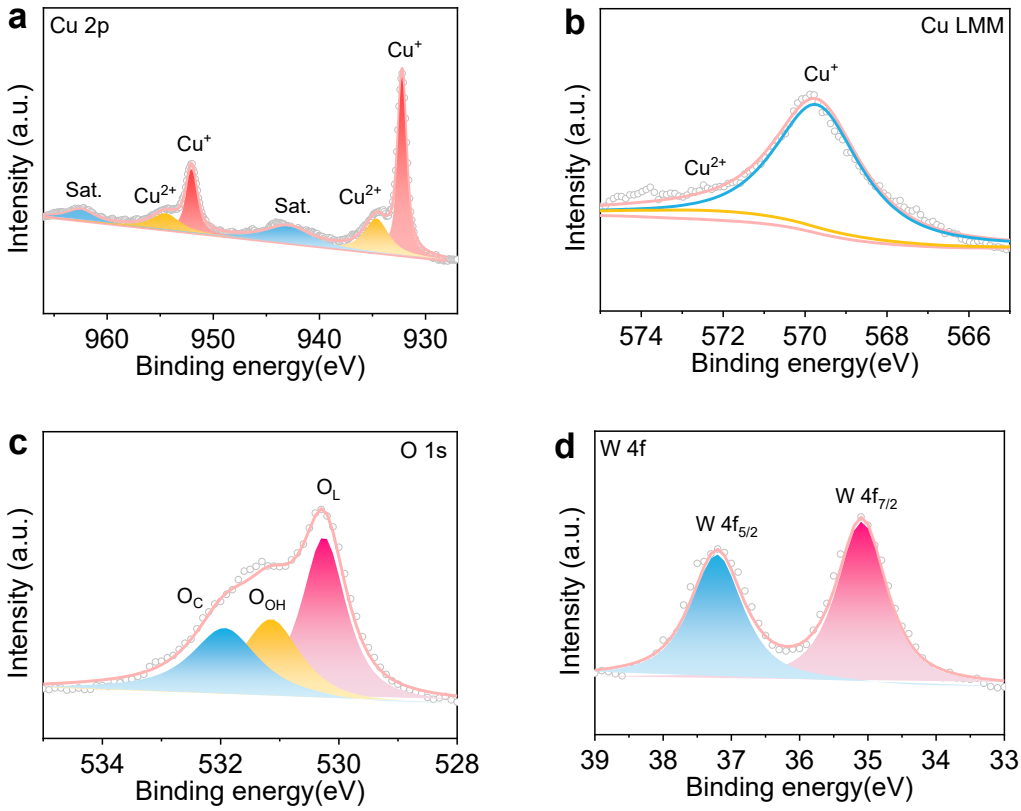

Supplementary Fig. 88 X-ray photoelectron spectroscopy (XPS) characterization of W_{PM}/nanowire-Cu_2O. a, Cu *2p*, **b,** Cu *LMM*, **c,** O *1s*, and **d,** W *4f* XPS spectra for W_{PM}/1D-Cu_2O.

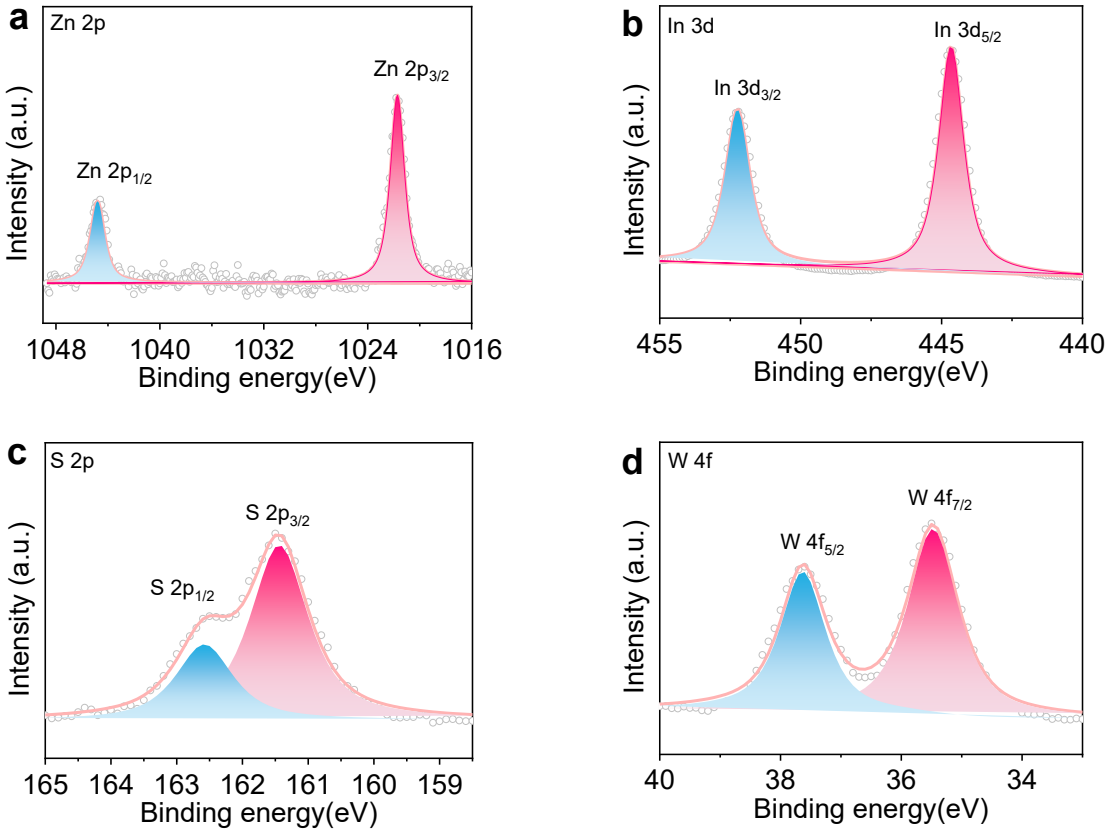

Supplementary Fig. 89 X-ray photoelectron spectroscopy (XPS) characterization of W_{PM}/2D-$ZnIn_2S_4$. **a,** Zn *2p*, **b,** In *3d*, **c,** S *2p,* and **d,** W *4f* XPS spectra for W_{PM}/2D-$ZnIn_2S_4$.

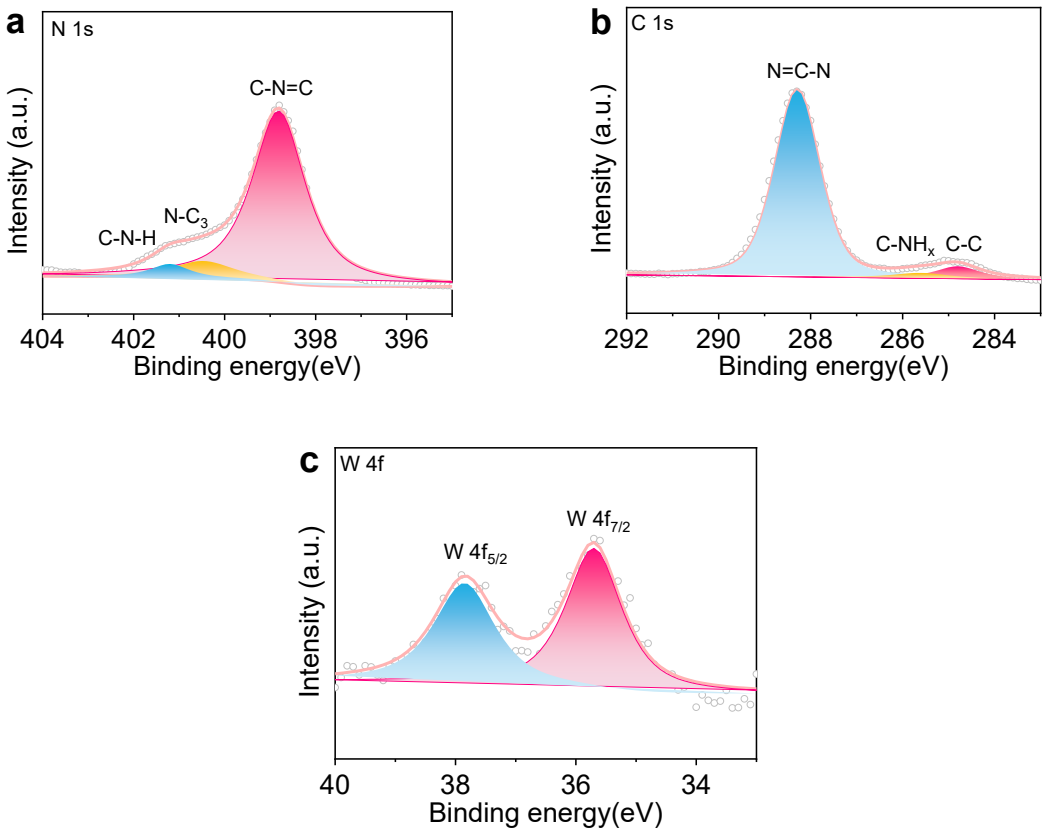

Supplementary Fig. 90 X-ray photoelectron spectroscopy (XPS) characterization of W_{PM}/2D-C_3N_4. a, N *1s* **b,** C *1s*, and **c,** W *4f* XPS spectra for W_{PM}/2D-C_3N_4.

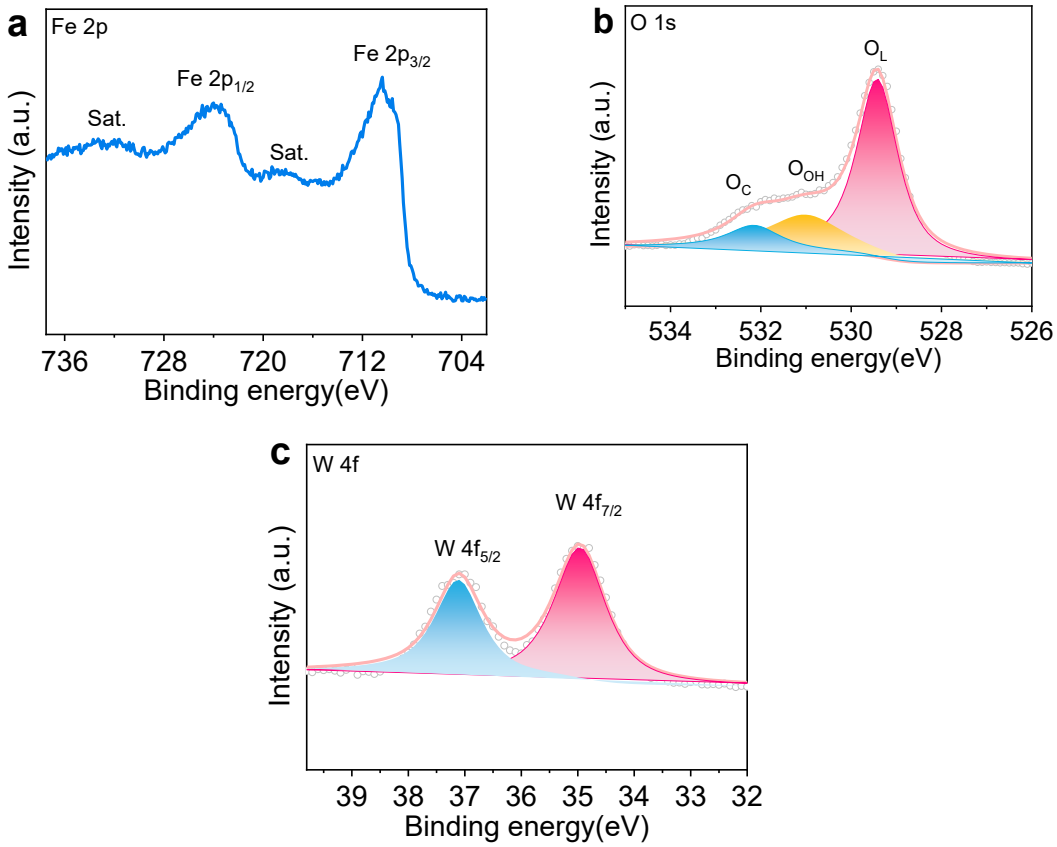

Supplementary Fig. 91 X-ray photoelectron spectroscopy (XPS) characterization of W_{PM}/3D-Fe_2O_3. a, Fe *2p*, **b,** O *1s*, and **c,** W *4f* XPS spectra for W_{PM}/3D-Fe_2O_3.

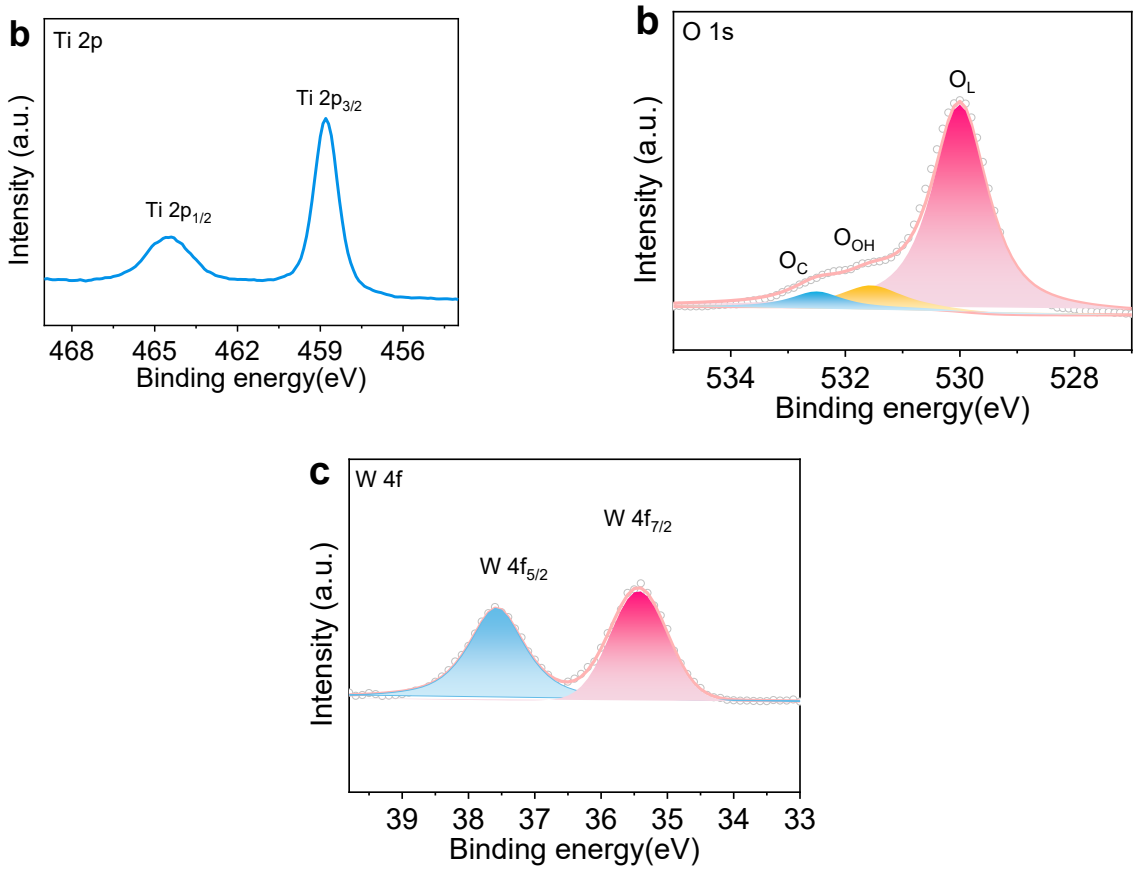

Supplementary Fig. 92 X-ray photoelectron spectroscopy (XPS) characterization of W_{PM}/3D-TiO_2. a, Ti *2p*, **b,** O *1s*, and **c,** W *4f* XPS spectra for W_{PM}/3D-TiO_2.

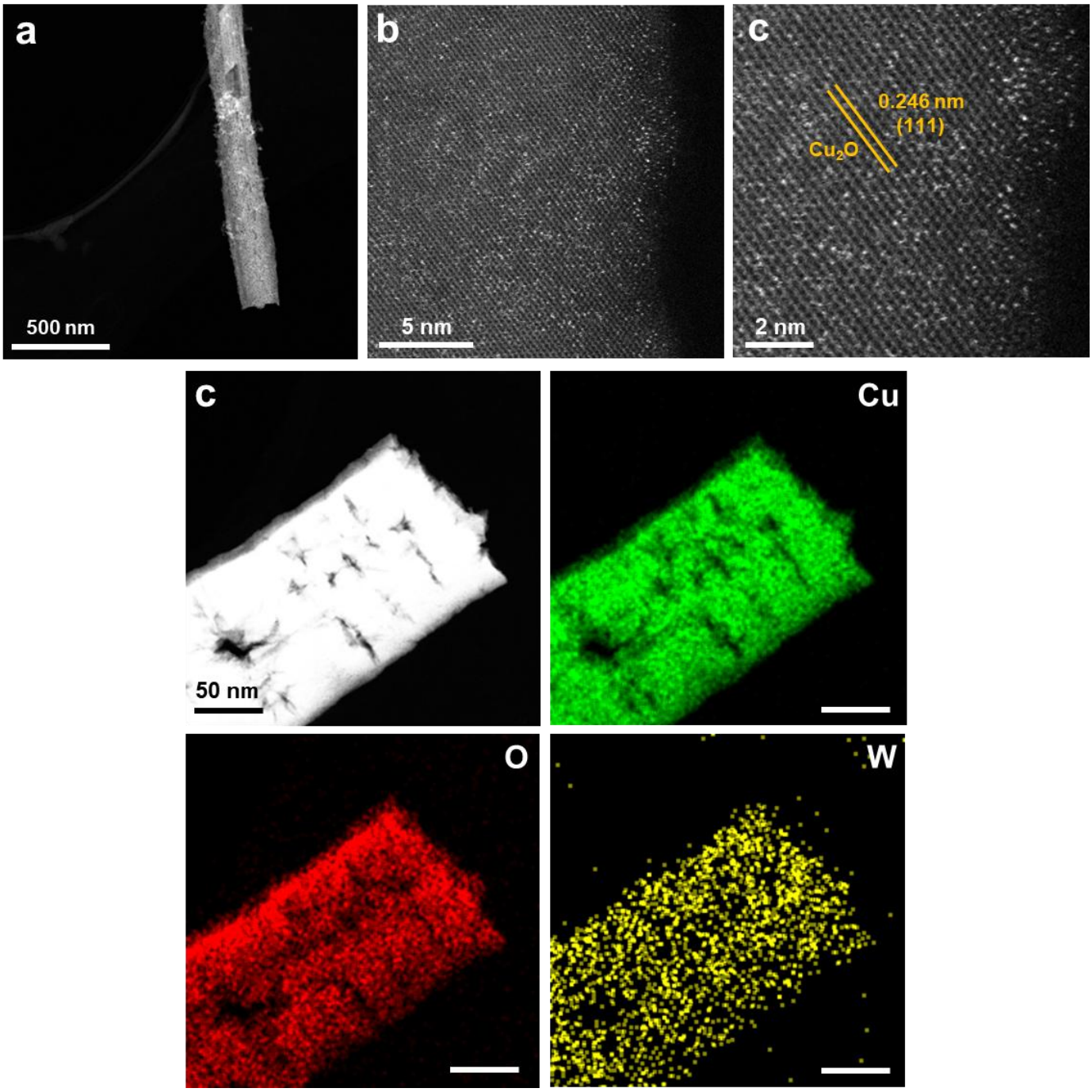

Supplementary Fig. 93 HAADF-STEM and EDS elemental mappings of W/1D-Cu_2O. a-c, HAADF-STEM images and **d,** EDS elemental mappings of W/1D-Cu_2O.

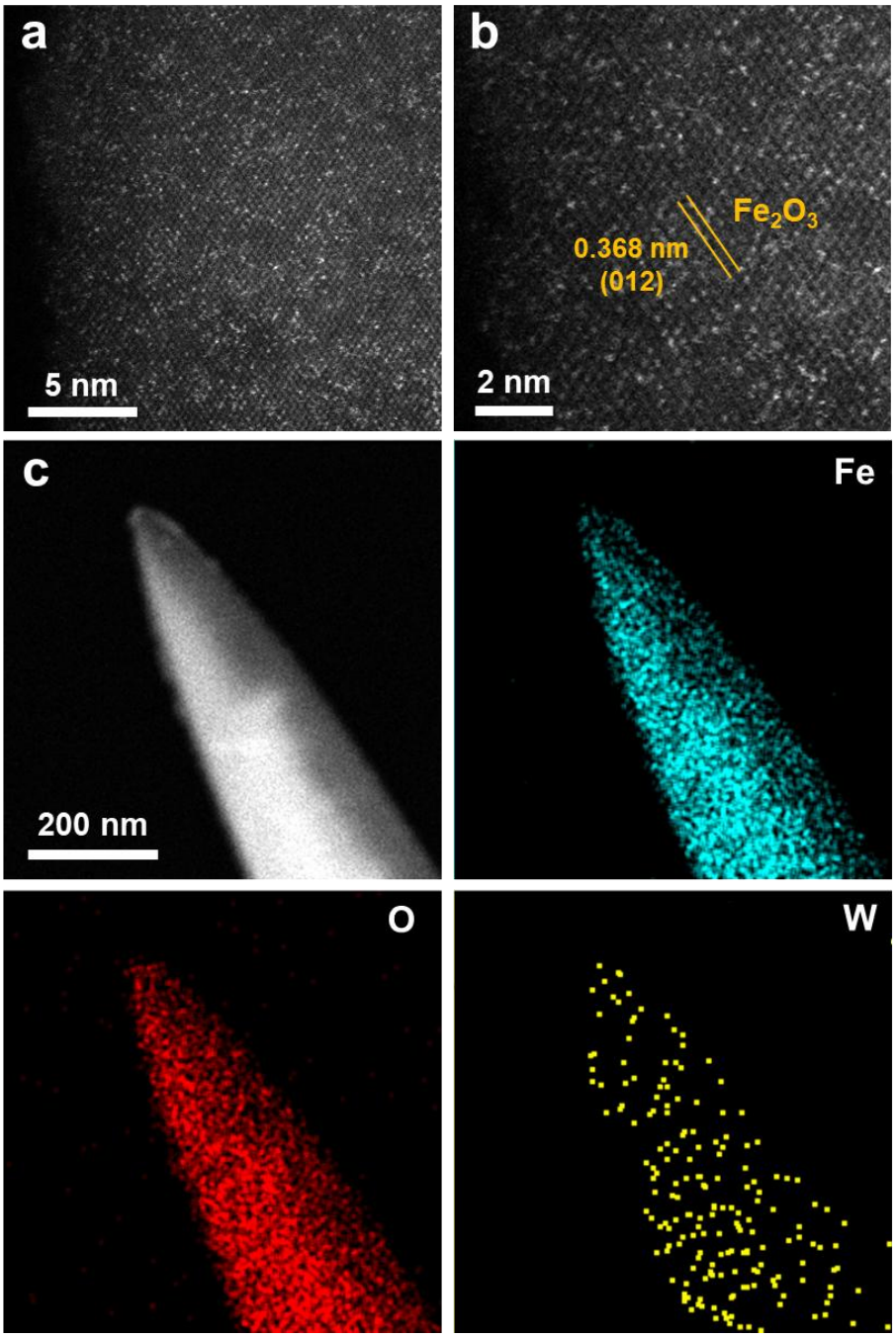

Supplementary Fig. 94 HAADF-STEM and EDS elemental mappings of W/2D-Fe_2O_3. a,b, HAADF-STEM images and **c,** EDS elemental mappings of W/2D-Fe_2O_3.

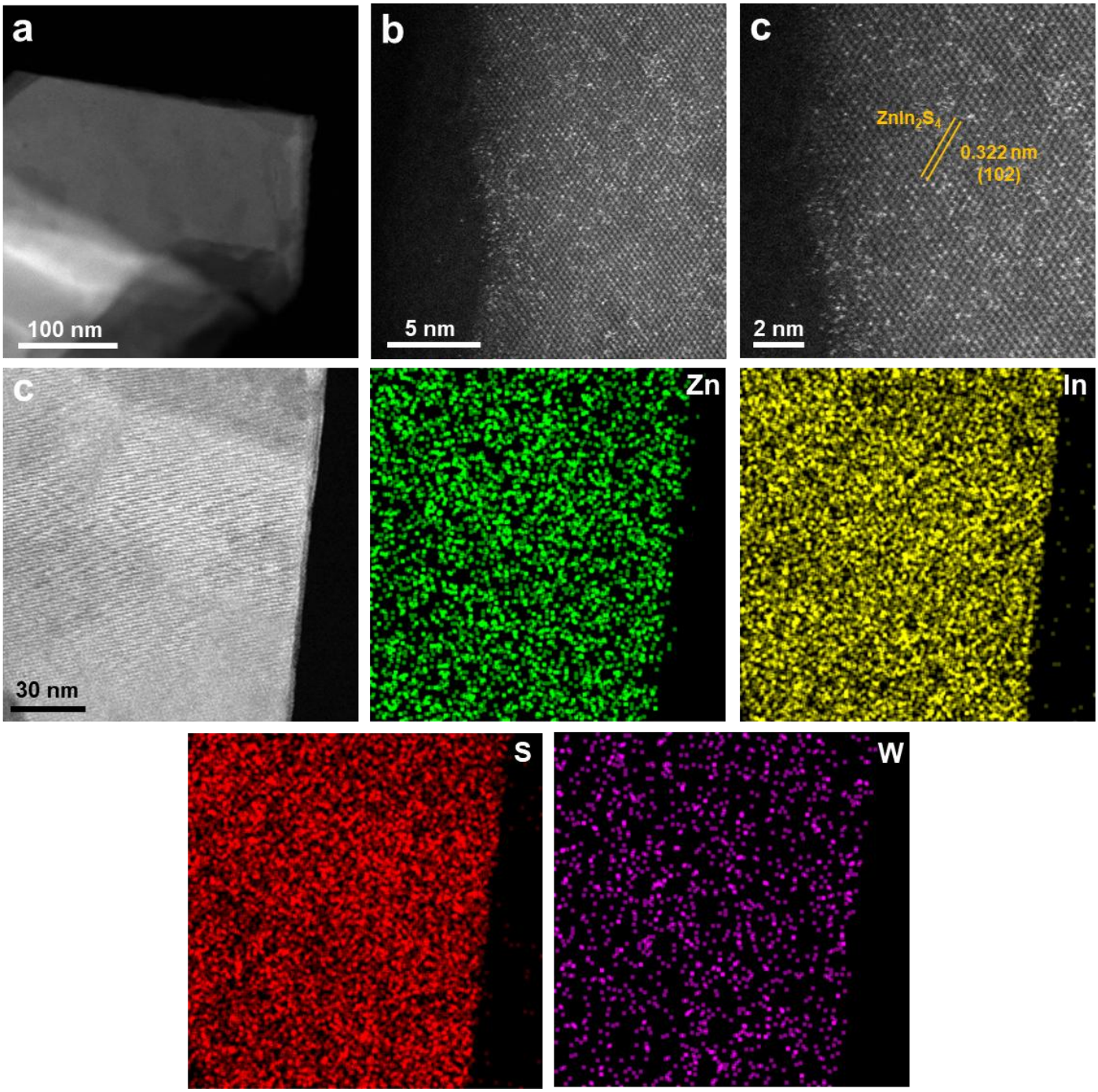

Supplementary Fig. 95 HAADF-STEM and EDS elemental mappings of W/2D-$ZnIn_2S_4$. a,b, HAADF-STEM images and **c,** EDS elemental mappings of W/2D-$ZnIn_2S_4$.

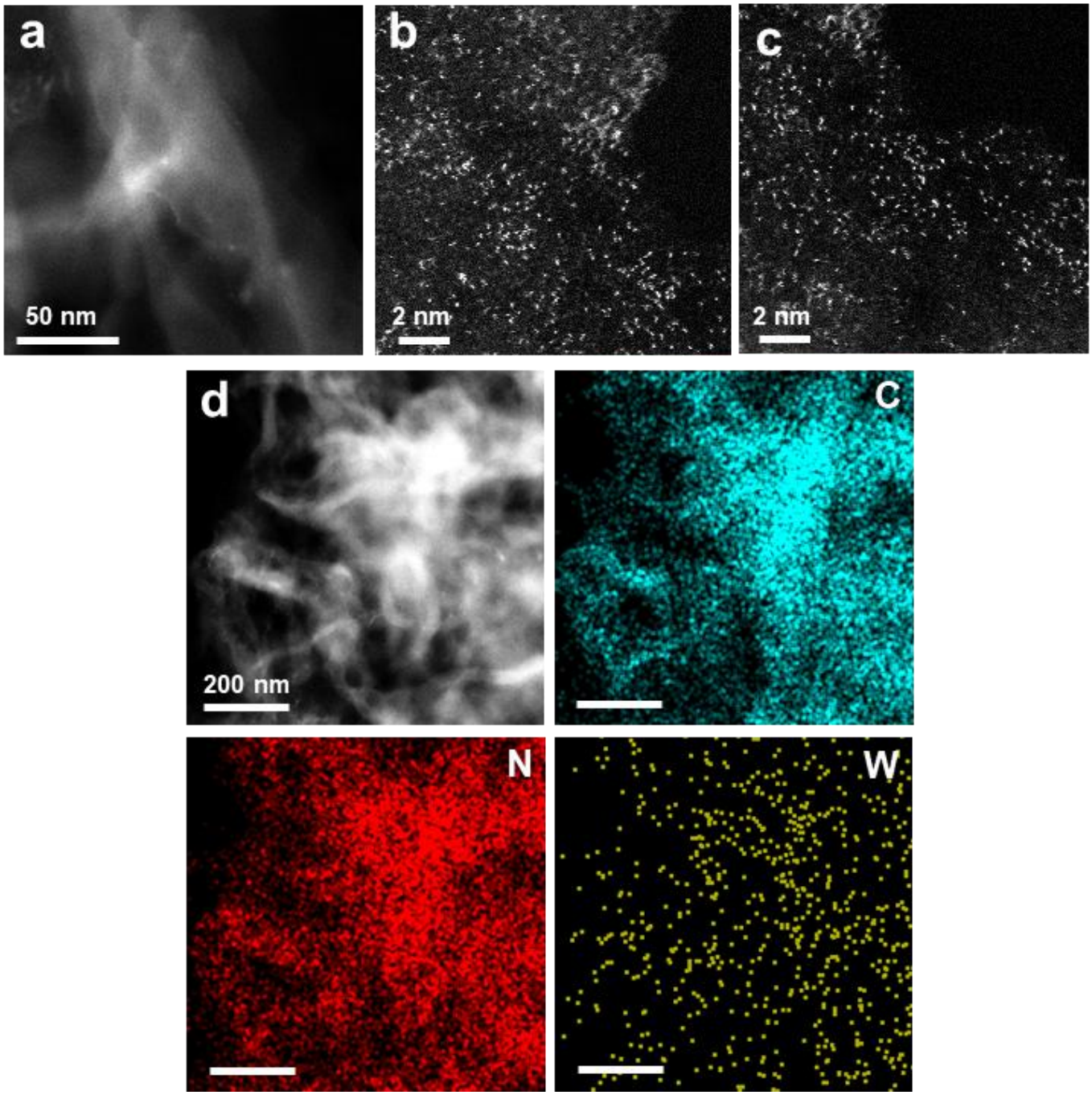

Supplementary Fig. 96 HAADF-STEM and EDS elemental mappings of W/2D-C_3N_4. a,b, HAADF-STEM images and **c,** EDS elemental mappings of W/2D-C_3N_4.

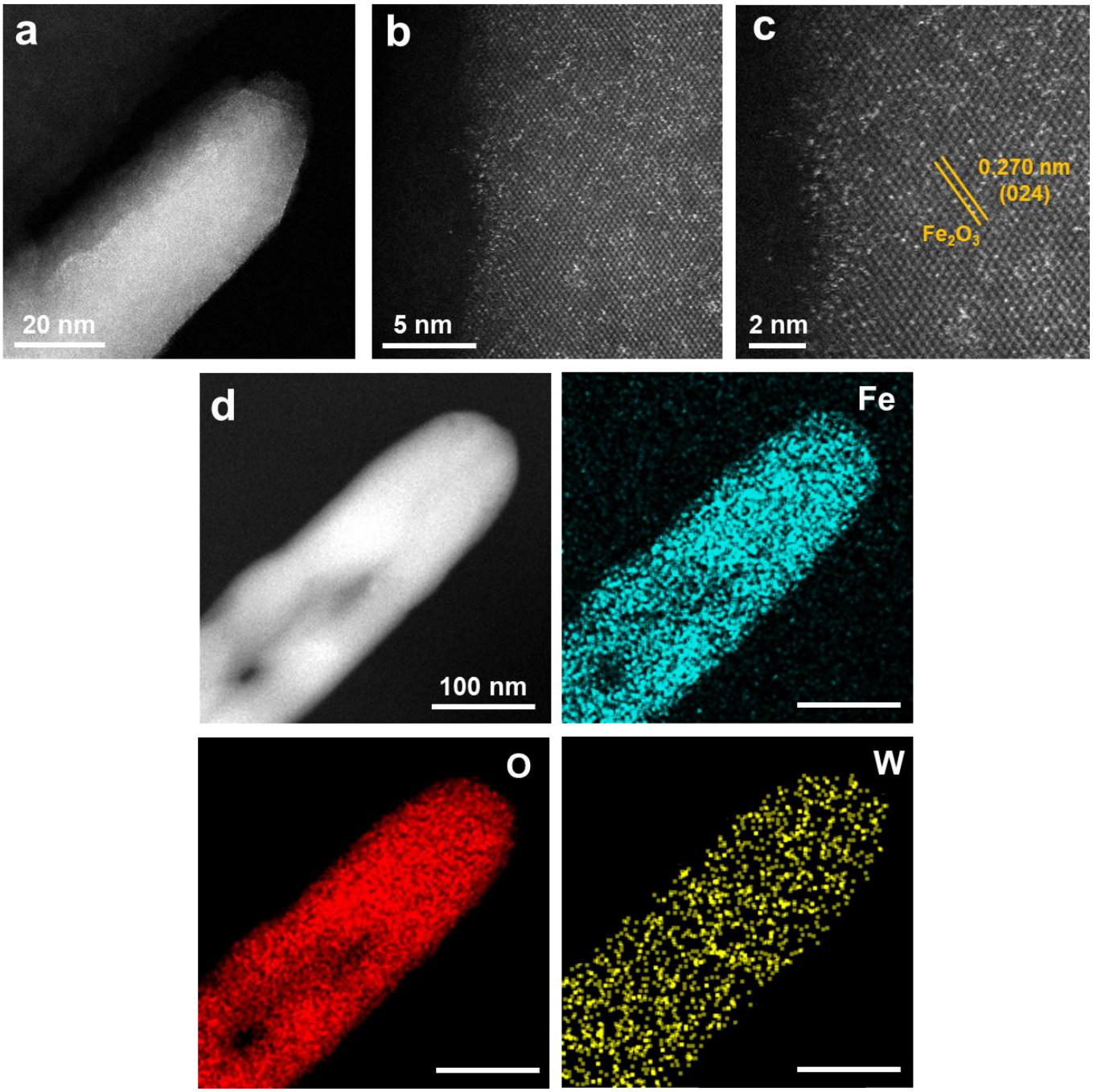

Supplementary Fig. 97 HAADF-STEM and EDS elemental mappings of W/3D-Fe_2O_3. a,b, HAADF-STEM images and **c,** EDS elemental mappings of W/3D-Fe_2O_3.

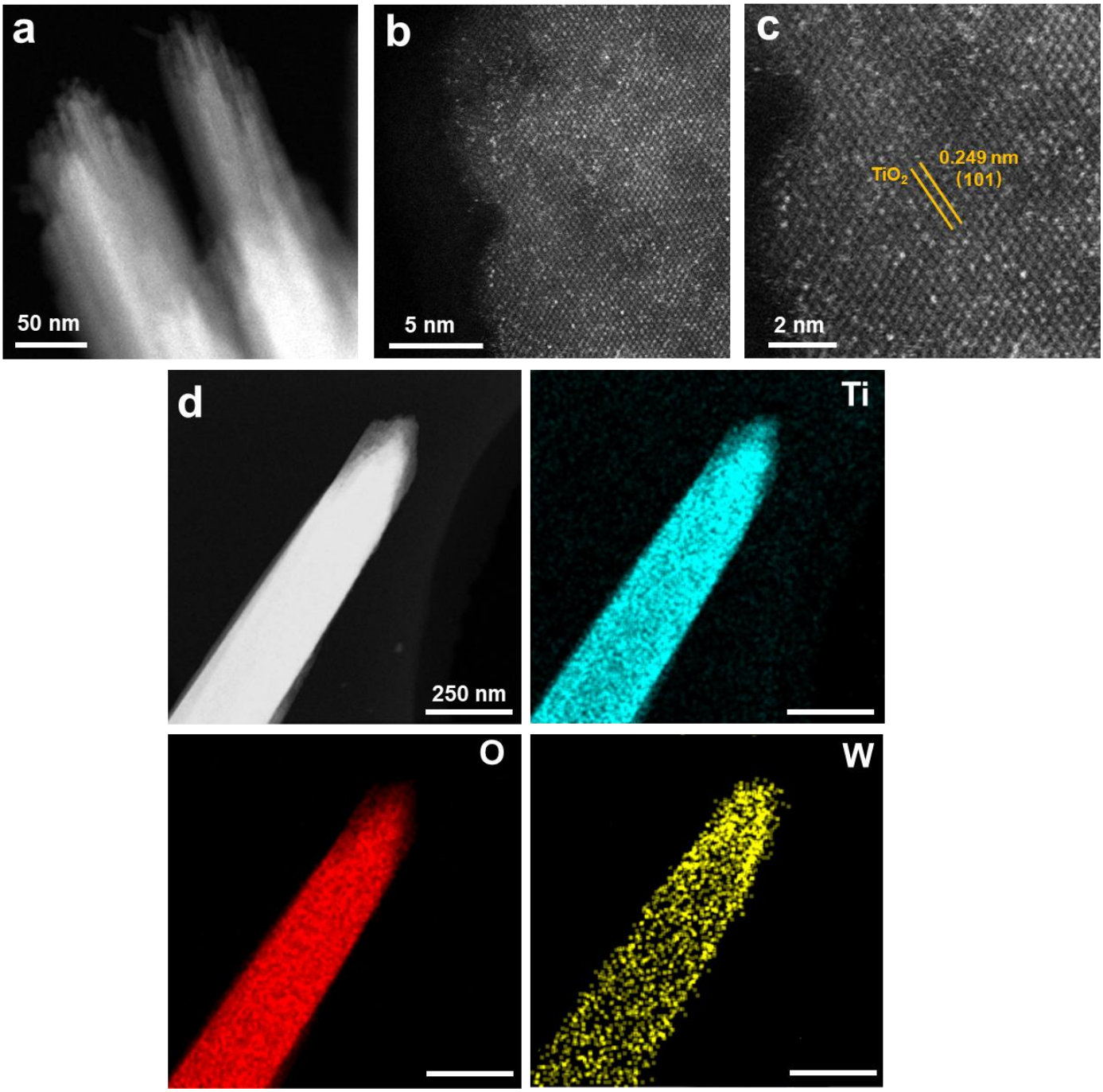

Supplementary Fig. 98 HAADF-STEM and EDS elemental mappings of W/3D-TiO_2. a,b, HAADF-STEM images and **c,** EDS elemental mappings of W/3D-TiO_2.

Supplementary Fig. 99 Industrial-scale production capacity. Schematic representation of kilogram-scale ultra-high single-atom-loaded Fe_2O_3.

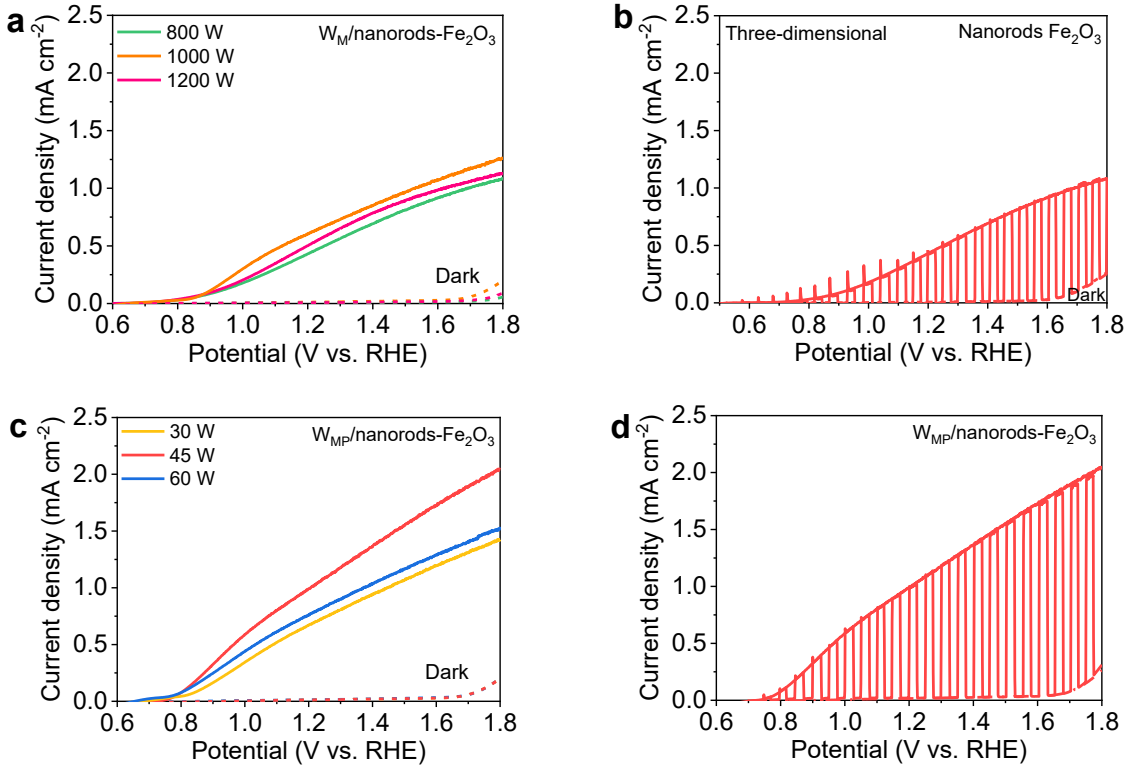

Supplementary Fig. 100 Photoelectrochemical performances of W_M/3D-Fe_2O_3 and W_{PM}/3D-Fe_2O_3. a, *J-V* curves of W_M/nanorods-Fe_2O_3 annealed directly by microwave at various power (800 W, 1000 W, and 1200 W) without plasma pretreatment. **b,** Chopped *J-V* curve of W_M/nanorods Fe_2O_3. **c,** *J-V* curves of W single atoms anchored on nanorods-Fe_2O_3 via microwave annealing after plasma pretreatment at various powers (30, 45, and 60 W). **d,** Chopped *J-V* curve of W_{MP}/nanorods Fe_2O_3. All measurements were performed in 1 M KOH under AM 1.5G illumination (100 mW cm^{-2}).

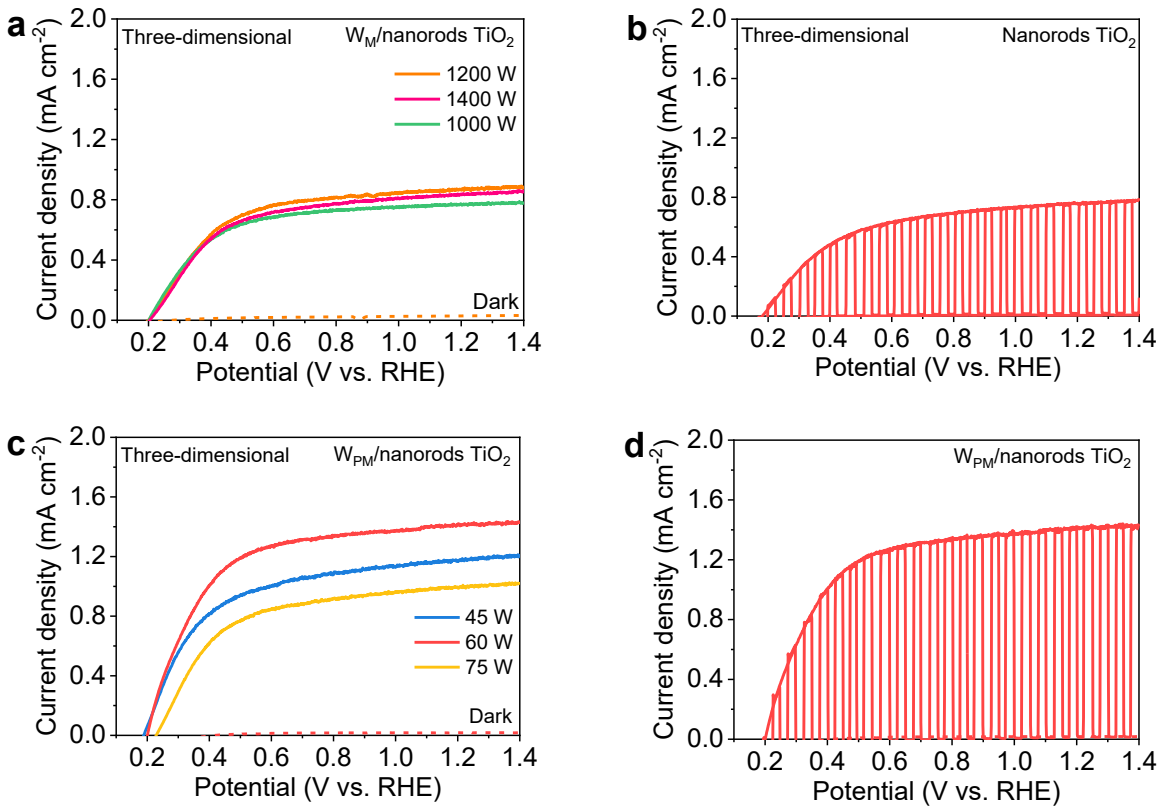

Supplementary Fig. 101 Photoelectrochemical performances of W_M/TiO_2 and W_{PM}/TiO_2. a, *J-V* curves of W_M/nanorods-TiO_2 annealed directly by microwave at various power (1000 W, 1200 W, and 1400 W) without plasma pretreatment. **b,** Chopped *J-V* curve of W_M/nanorods-TiO_2. **c,** *J-V* curves of W single atoms anchored on nanorods-TiO_2 via microwave annealing after plasma pretreatment at various powers (45, 60, and 75 W). **d,** Chopped *J-V* curve of W_{MP}/nanorods TiO_2. All measurements were performed in 1 M KOH under AM 1.5G illumination (100 mW cm^{-2}).

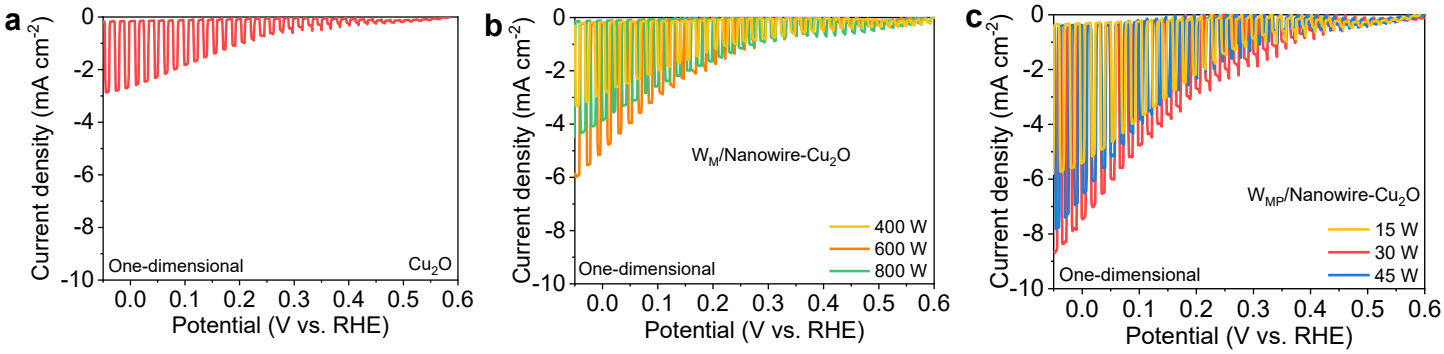

Supplementary Fig. 102 Photoelectrochemical performances of W_M/Cu_2O and W_{PM}/Cu_2O. a, Chopped J-V curve of nanowire-Cu_2O. **b,** Chopped *J-V* curves of W_M/nanowire-Cu_2O annealed directly by microwave at various power (400 W, 600 W, and 800 W) without plasma pretreatment. **c,** *J-V* curves of W single atoms anchored on nanowire Cu_2O via microwave annealing after plasma pretreatment at various powers (15, 30, and 45 W). All measurements were performed in 1 M KOH under AM 1.5G illumination (100 mW cm^{-2}).

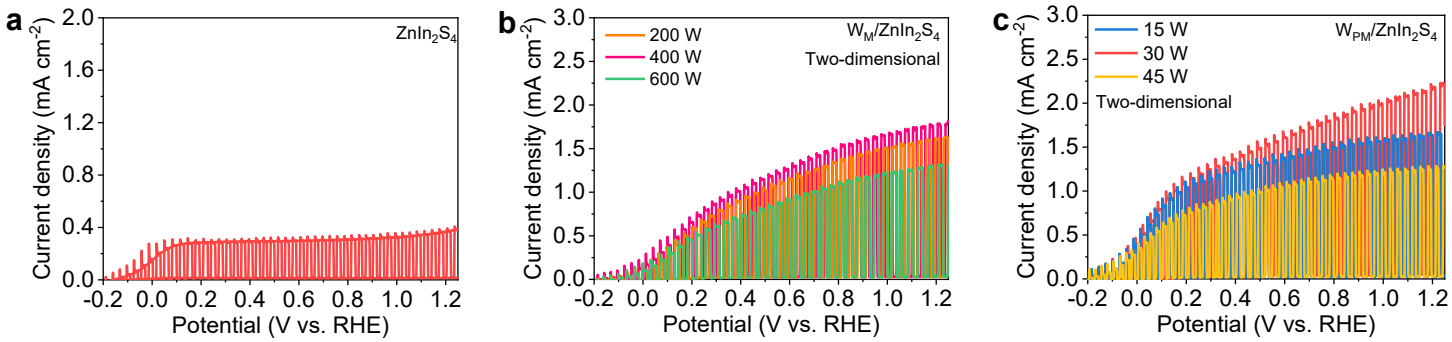

Supplementary Fig. 103 Photoelectrochemical performances of $W_M/ZnIn_2S_4$ and $W_{PM}/ZnIn_2S_4$. a, Chopped *J-V* curve of $ZnIn_2S_4$. **b,** Chopped *J-V* curves of $W_M/ZnIn_2S_4$ annealed directly by microwave at various power (200 W, 400 W, and 600 W) without plasma pretreatment. **c,** *J-V* curves of W single atoms anchored on $ZnIn_2S_4$ via microwave annealing after plasma pretreatment at various powers (15, 30, and 45 W). All measurements were performed in 1 M KOH under AM 1.5G illumination (100 mW cm^{-2}).

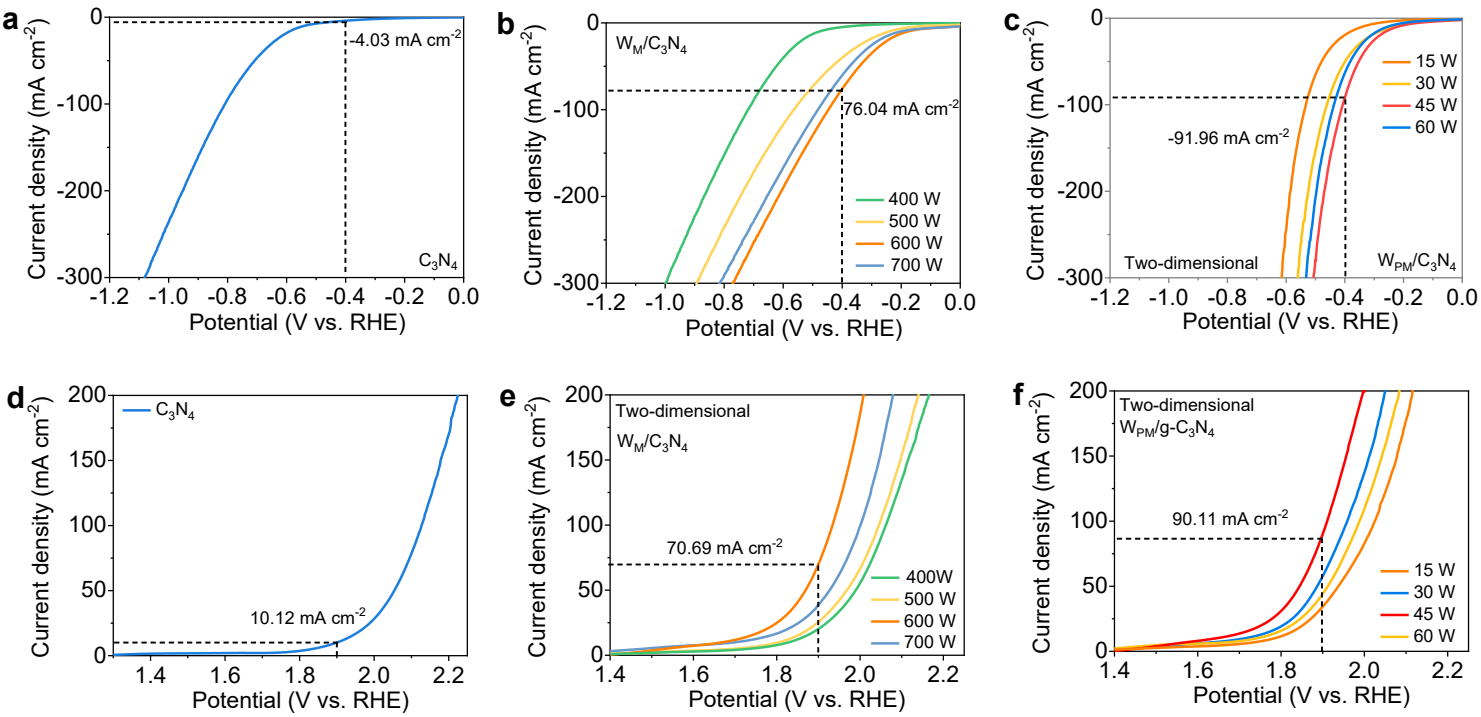

Supplementary Fig. 104 Electrochemical HER and OER performances of W_{PM}/C_3N_4. a, HER performance of C_3N_4 at -0.4 V_{RHE}. **b,** HER *J-V* curves of C_3N_4 annealed directly by microwave at various power (400, 500, 600, and 700 W) without plasma pretreatment. **c,** HER *J-V* curves of W single atoms anchored on C_3N_4 via microwave annealing after plasma pretreatment at various powers (15, 30, 45, and 60 W). **d,** OER performance of C_3N_4 at -0.4 V_{RHE}. **e,** OER *J-V* curves of C_3N_4 annealed directly by microwave at various power (400, 500, 600, and 700 W) without plasma pretreatment. **f,** OER *J-V* curves of W single atoms anchored on C_3N_4 via microwave annealing after plasma pretreatment at various powers (15, 30, 45, and 60 W). All measurements were performed in 0.5 M H_2SO_4.

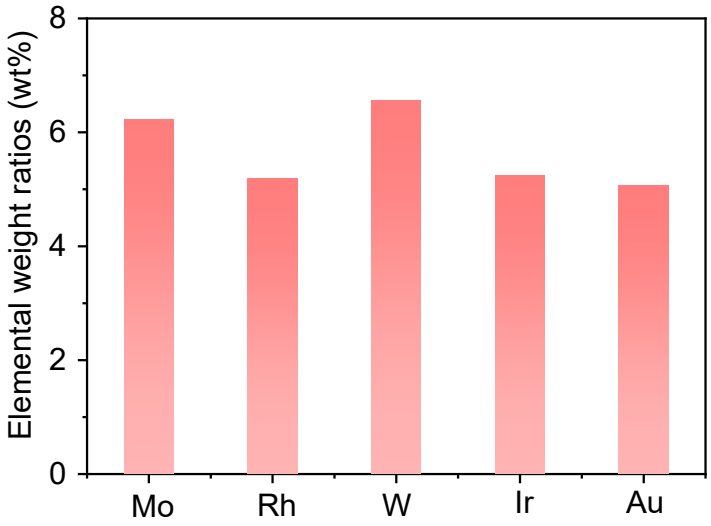

Supplementary Fig. 105 Elemental ratios of the 5-M_{PM}/Fe_2O_3. Surface elemental weight ratios of the 5-M_{PM}/Fe_2O_3 determined by X-ray photoelectron spectroscopy.

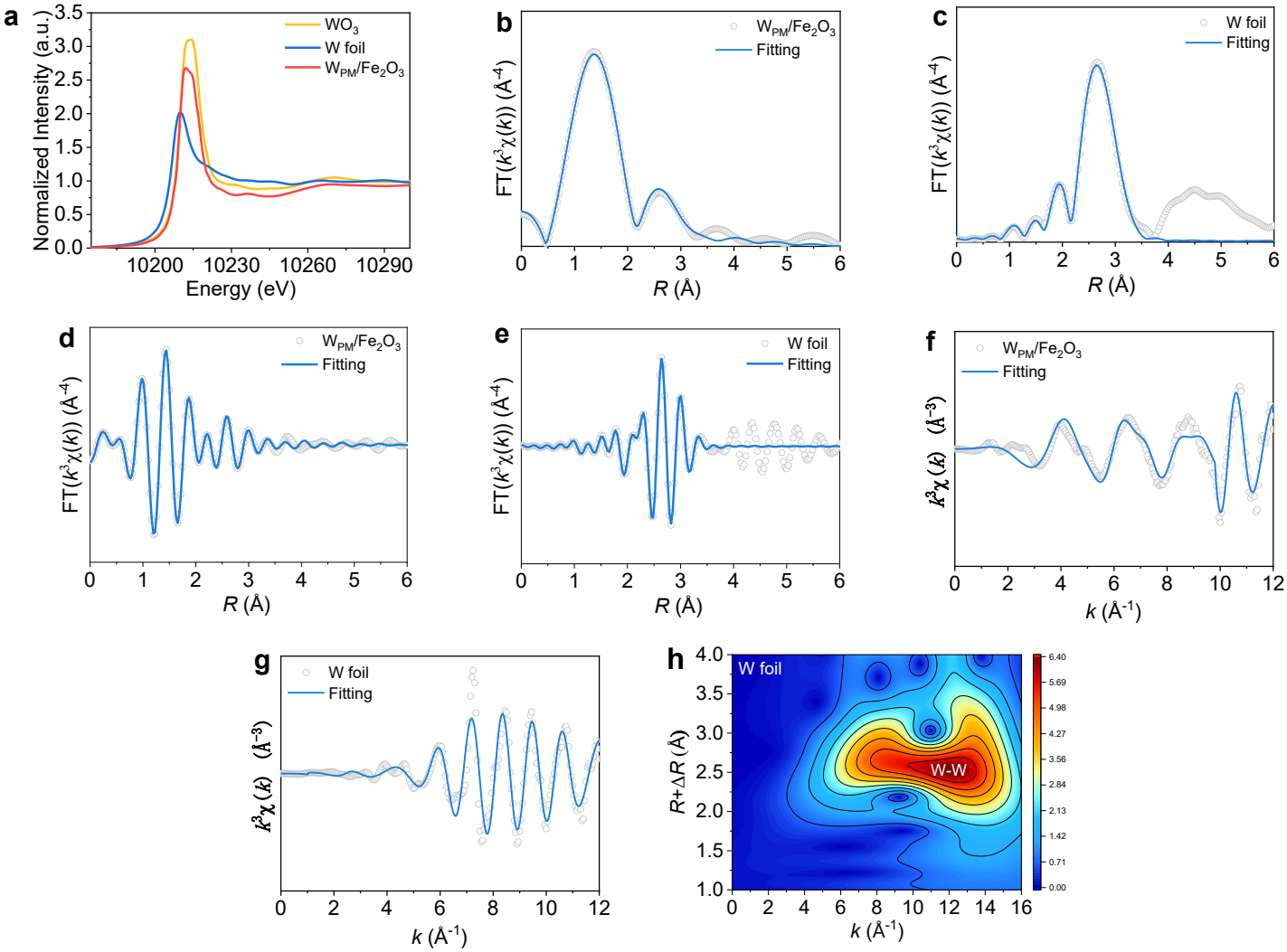

Supplementary Fig. 106 Atom structural characterization of 5-M$_{PM}$/Fe$_2$O$_3$. a, W L_3-edge XANES spectra of 5-M$_{PM}$/Fe$_2$O$_3$, W foil and WO$_3$. **b-e,** W L_3-edge EXAFS data and fit for 5-M$_{PM}$/Fe$_2$O$_3$ and W foil in *R*-space and **f, g,** *k*-space. **h,** WT-EXAFS plot of W foil.

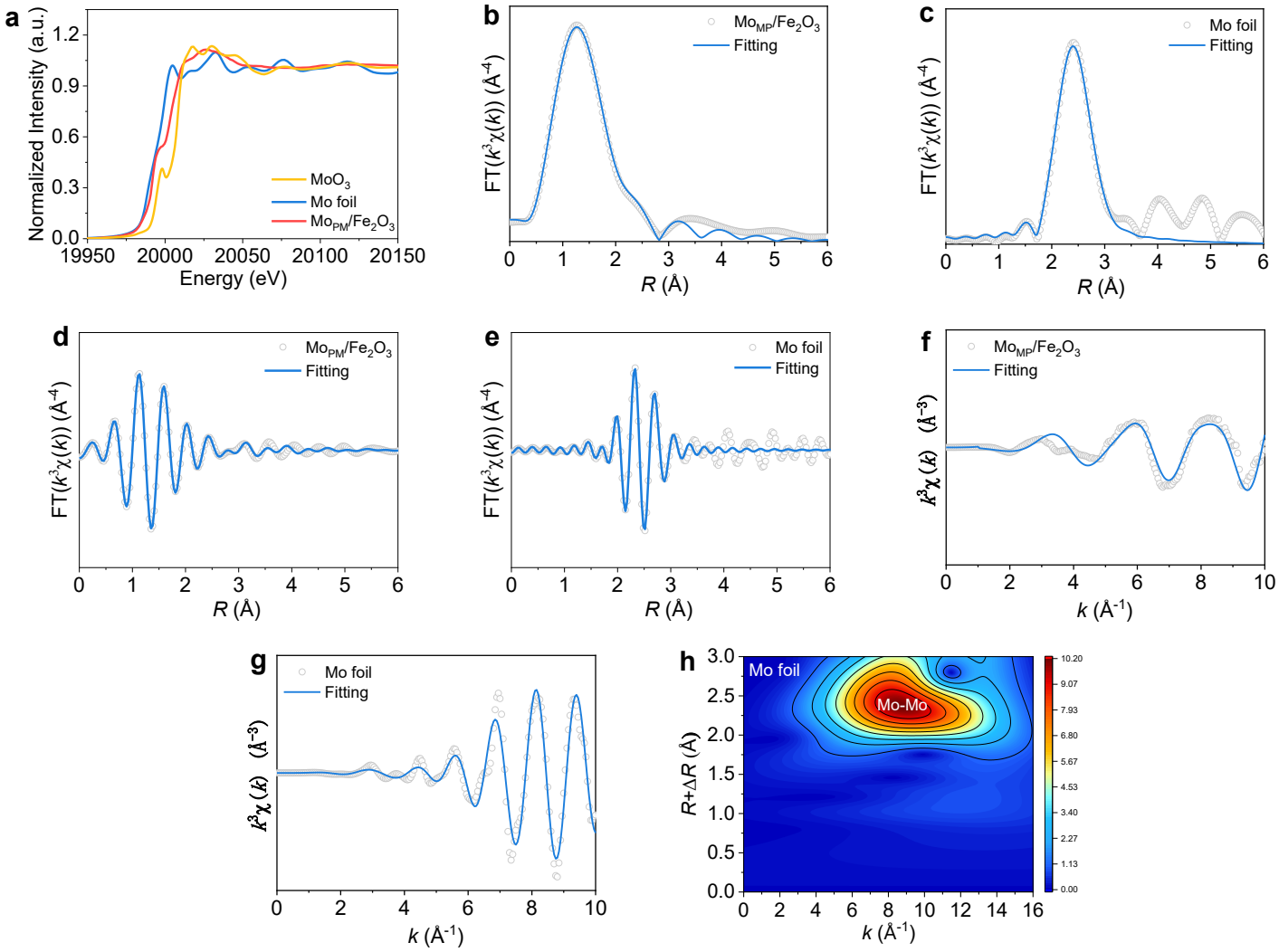

Supplementary Fig. 107 Atom structural characterization of 5-MPM/Fe2O3. a, Mo L_3-edge XANES spectra of 5-M_{PM}/Fe_2O_3, Mo foil and MoO_3. **b-e,** Mo L_3-edge EXAFS data and fit for 5-M_{PM}/Fe_2O_3 and Mo foil in *R*-space and **f, g,** *k*-space. **h,** WT-EXAFS plot of Mo foil.

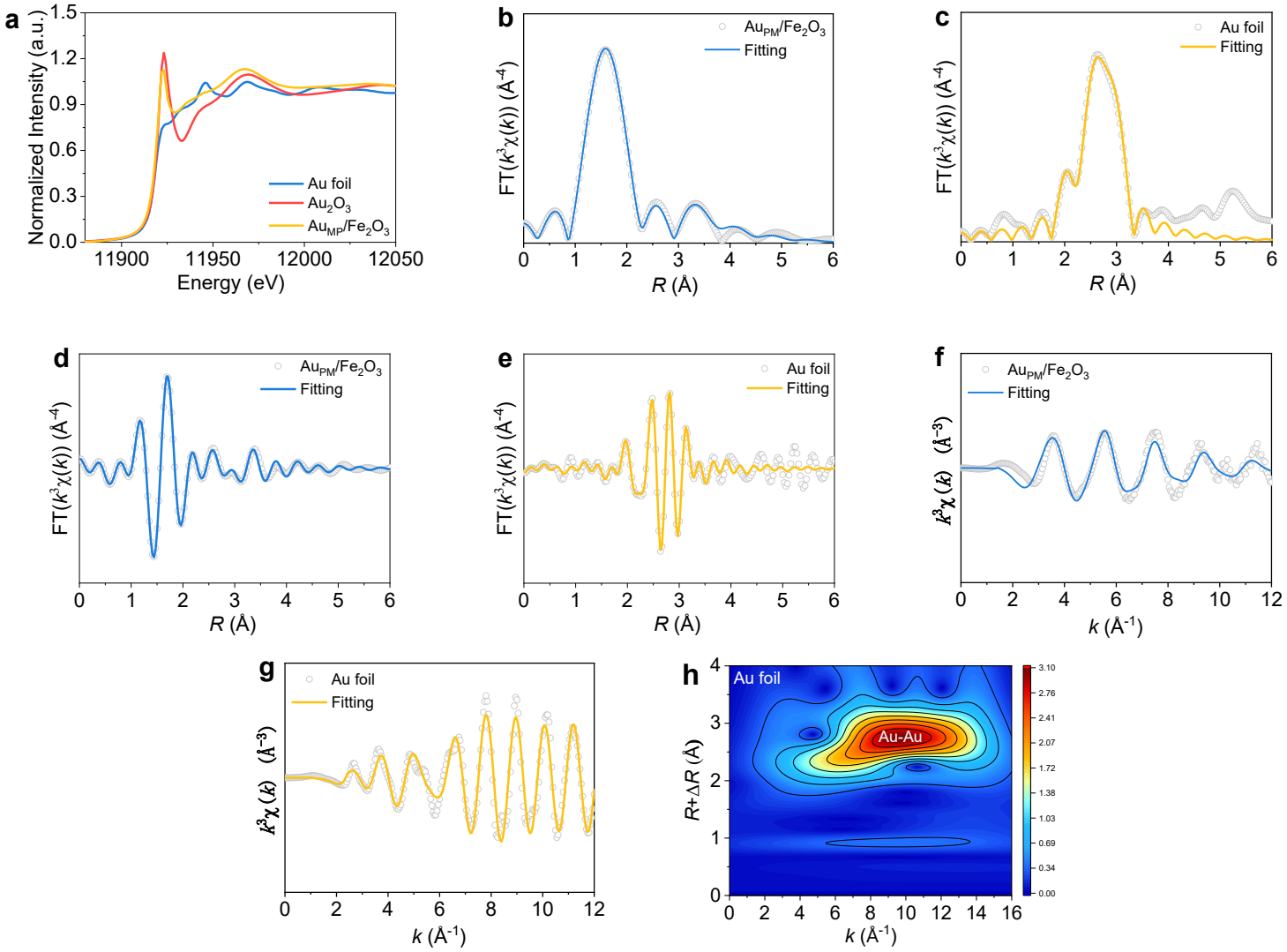

Supplementary Fig. 108 Atom structural characterization of 5-M_{PM}/Fe_2O_3. a, Au *K*-edge XANES spectra of 5-M_{PM}/Fe_2O_3, Au foil and Au_2O_3. **b-e,** Au *K*-edge EXAFS data and fit for 5-M_{PM}/Fe_2O_3 and Au foil in *R*-space and **f, g,** *k*-space. **h,** WT-EXAFS plot of Au foil.

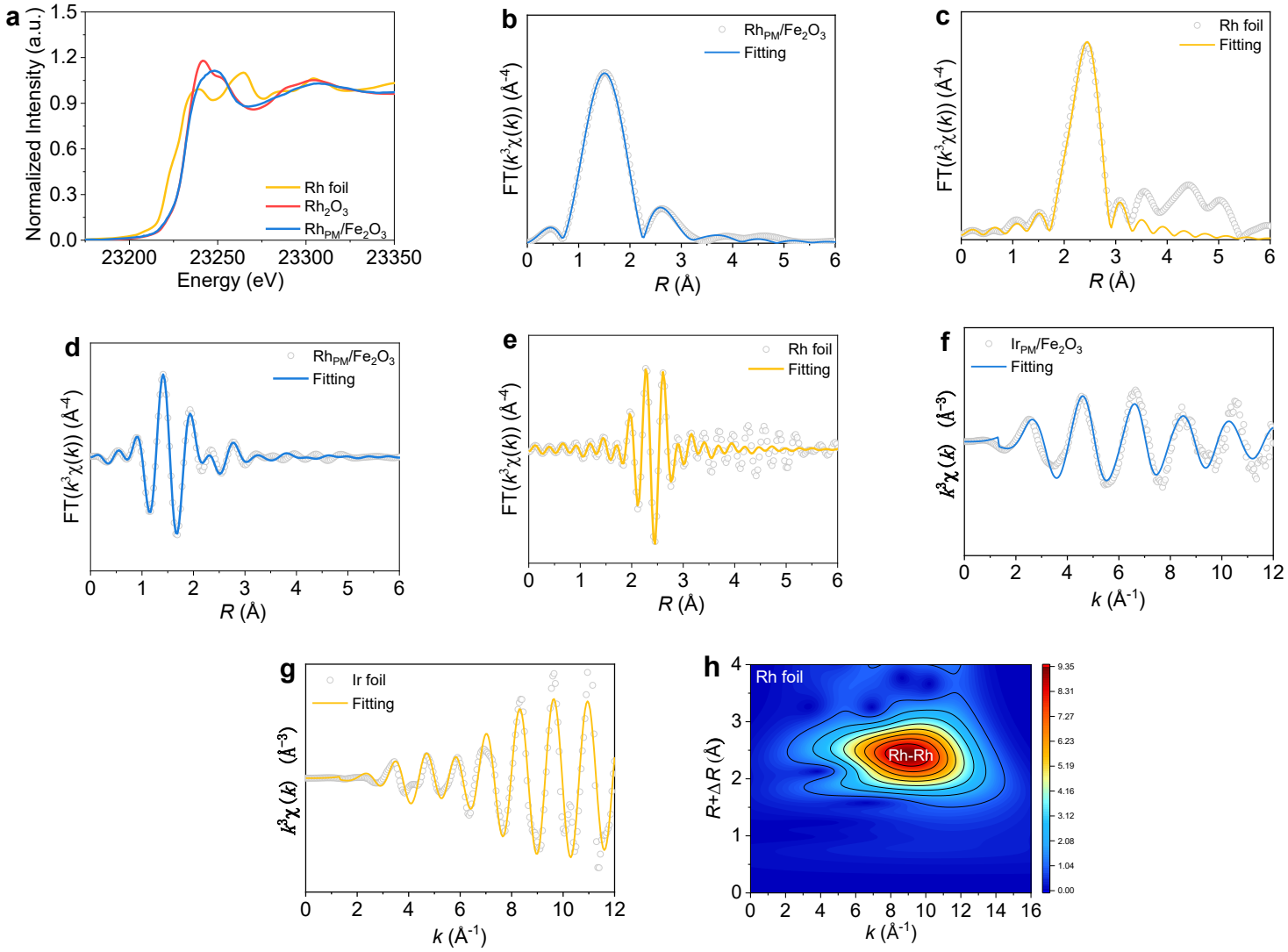

Supplementary Fig. 109 Atom structural characterization of 5-M_{PM}/Fe_2O_3. a, Rh *K*-edge XANES spectra of 5-M_{PM}/Fe_2O_3, Rh foil and Rh_2O_3. **b-e,** Rh *K*-edge EXAFS data and fit for 5-M_{PM}/Fe_2O_3 and Rh foil in *R*-space and **f, g,** *k*-space. **h,** WT-EXAFS plot of Rh foil.

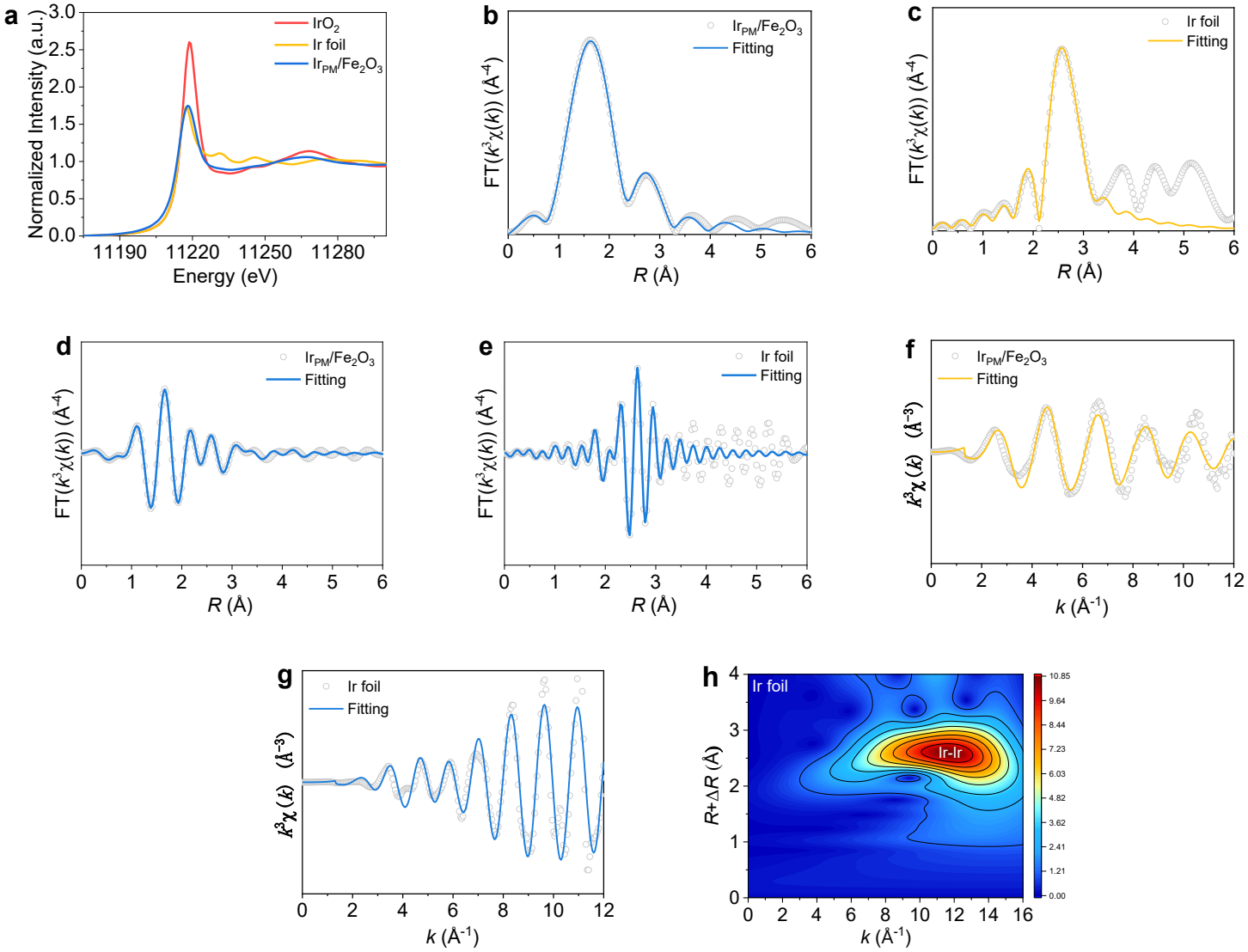

Supplementary Fig. 110 Atom structural characterization of 5-M$_{PM}$/Fe$_2$O$_3$. a, Ir L_3-edge XANES spectra of 5-M$_{PM}$/Fe$_2$O$_3$, Ir foil and Rh$_2$O$_3$. **b-e,** Ir L_3-edge EXAFS data and fit for 5-M$_{PM}$/Fe$_2$O$_3$ and Ir foil in *R*-space and **f, g,** *k*-space. **h,** WT-EXAFS plot of Ir foil.

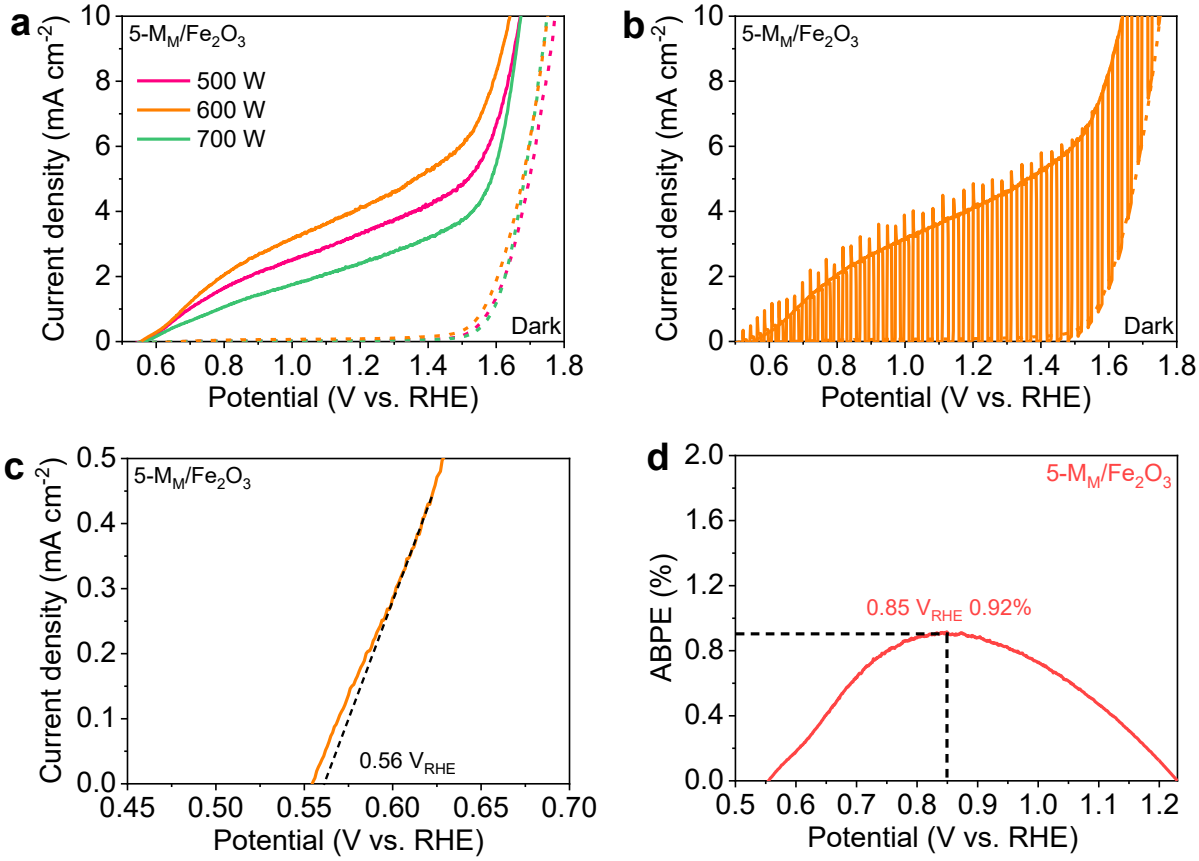

Supplementary Fig. 111 Photoelectrochemical OER performances of 5-M$_M$/Fe$_2$O$_3$. a, *J-V* curves of Fe_2O_3 loaded with five metals (W, Rh, Mo, Ir, and Au) annealed directly by microwave at various power (500 W, 600 W, and 700 W) without plasma pretreatment. **b,** Chopped *J-V* curve of 5-M$_M$/Fe$_2$O$_3$. **c,** Onset potential of 5-M$_M$/Fe$_2$O$_3$. **d,** Applied bias photon-to current efficiency of 5-M$_M$/Fe$_2$O$_3$. All measurements were performed in 1 M KOH under AM 1.5G illumination (100 mW cm^{-2}).

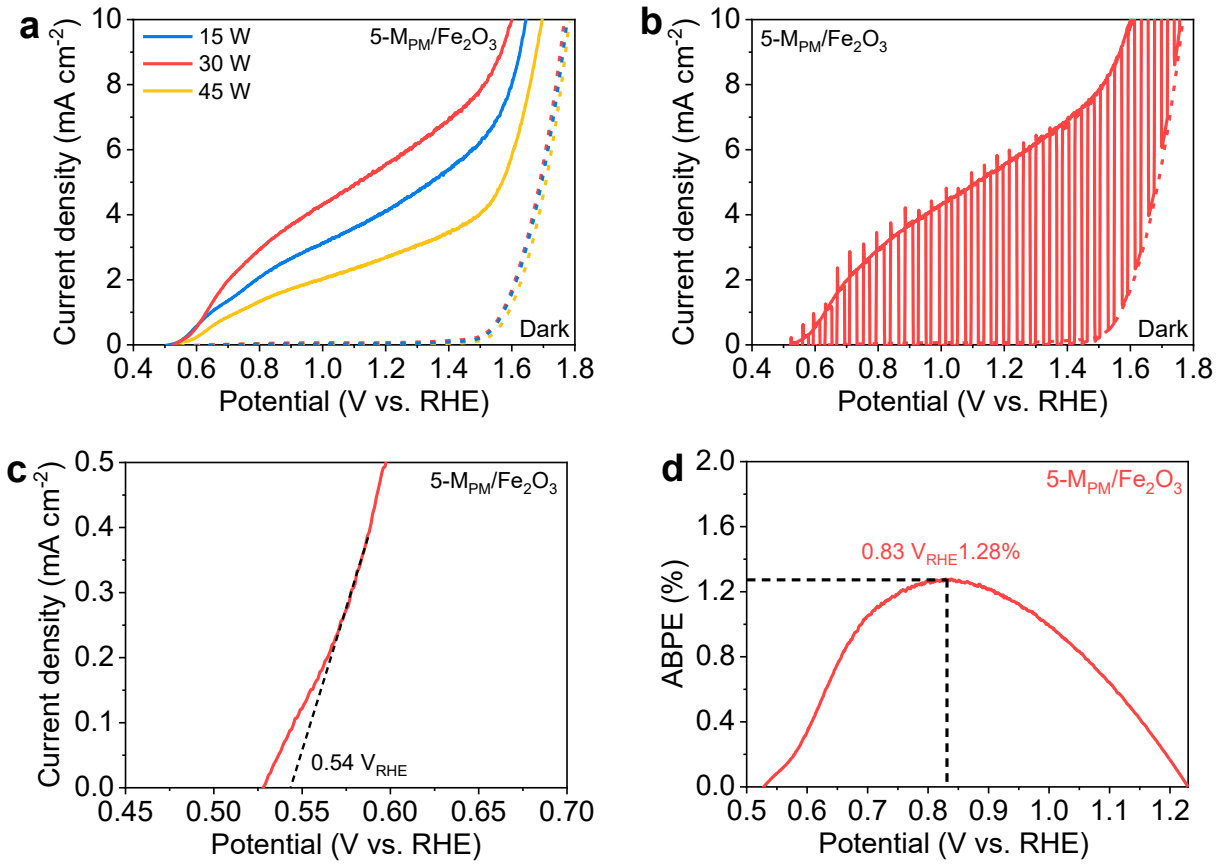

Supplementary Fig. 112 Photoelectrochemical OER performance of 5-M$_{PM}$/Fe$_2$O$_3$. a, *J-V* curves of Fe$_2$O$_3$ loaded with five metals (W, Rh, Mo, Ir, and Au) via microwave annealing after plasma pretreatment at various powers (15, 30, and 45 W). **b,** Chopped *J-V* curve of 5-M$_{PM}$/Fe$_2$O$_3$. **c,** Onset potential of 5-M$_{PM}$/Fe$_2$O$_3$. **d,** Applied bias photon-to current efficiency of 5-M$_{PM}$/Fe$_2$O$_3$. All measurements were performed in 1 M KOH under AM 1.5G illumination (100 mW cm^{-2}).

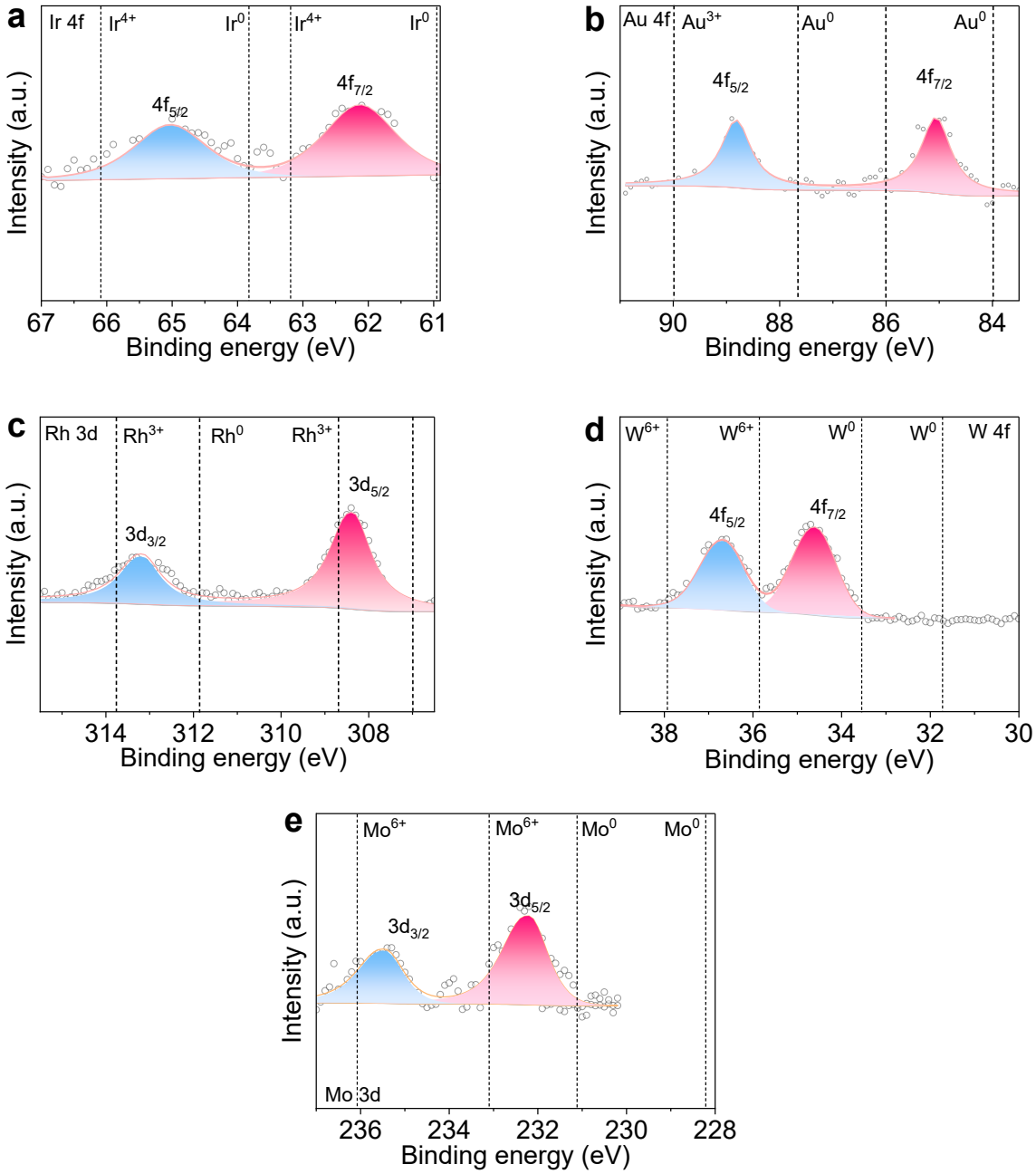

Supplementary Fig. 113 XPS elemental map after stability. XPS spectra of Ir 4f, Au 4f, Rh 3d, W 4f, and Mo 3d for 5-M_{PM}/Fe_2O_3 after stability testing.

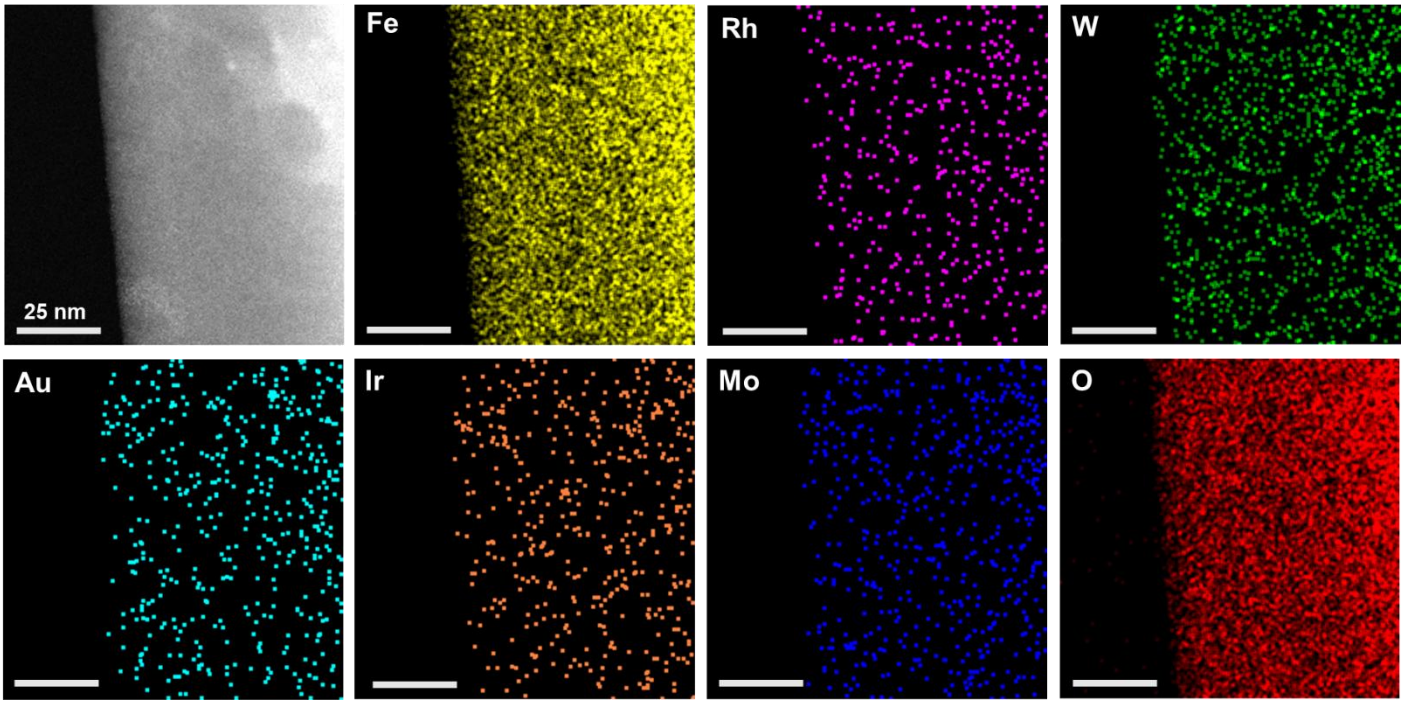

Supplementary Fig. 114 EDS elemental map after stability. EDS elemental mappings of 5-M_{PM}/Fe_2O_3 after stability testing.

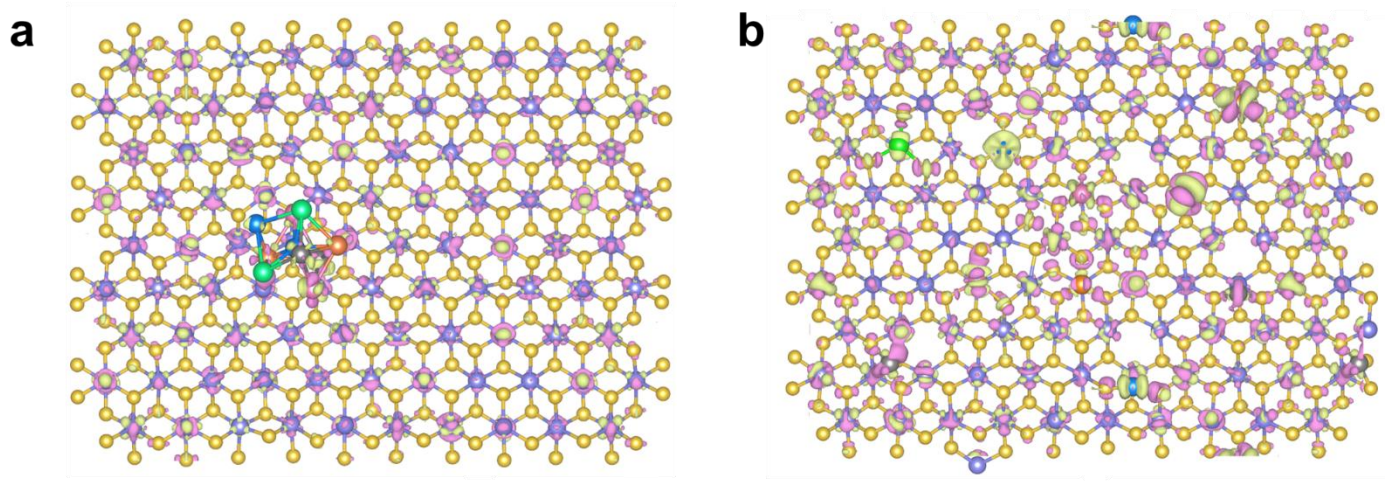

Supplementary Fig. 115 Differential charge density. a,b, Differential charge density of 5-M_M/Fe_2O_3 (a) and 5-M_{PM}/Fe_2O_3 (b).

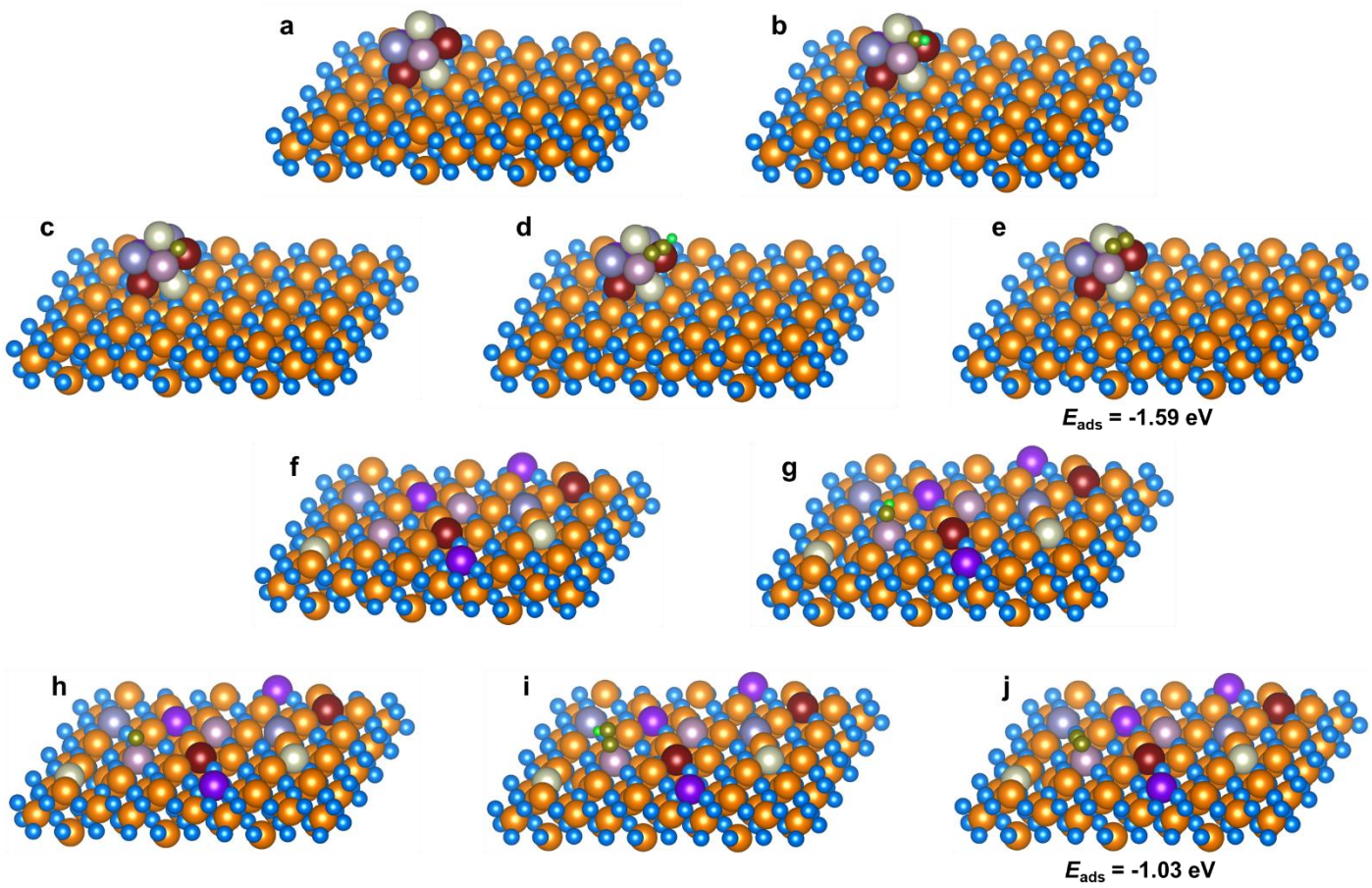

Supplementary Fig. 116 Structure of the key steps and intermediates in OER. (a-e) OER proceeding on the surfaces of 5-M_M/Fe_2O_3 and (f-j) 5-M_{PM}/Fe_2O_3. Here, Fe, O, Mo, Au, Ir, W, Rh and H atoms are represented by orange, pink, grey, purple, red, beige and green, respectively. To distinguish adsorbed oxygen, it is shown in brown.

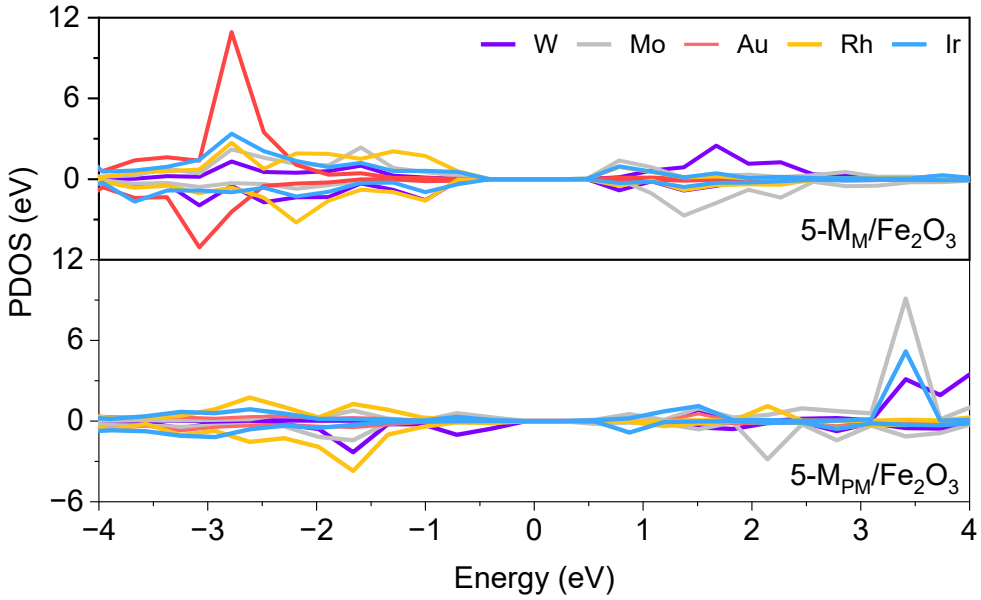

Supplementary Fig. 117 Electronic structures of 5-M_M/Fe_2O_3 and 5-M_{PM}/Fe_2O_3. Projected density of states of 5-M_M/Fe_2O_3 and 5-M_{PM}/Fe_2O_3.

Supplementary Table 1 Comparison between this work and representative reported UHL-SACs.

Catalysts	Metal-atom loadings	Reference
5-M_{PM}/Fe_2O_3	27.69 wt% (7.75 at.%)	This work.
W_{PM}/Fe_2O_3	21.02 wt% (4.13 at.%)	
Pt SAC	11.4 wt%	*Nat. Mater.* **21**, 681-688 (2022).
Ni-N-C	15.3 wt% (3.61 at.%)	*Nat. Chem.* **13**, 887-894 (2021).
Ir-N-C	41.6 wt% (3.8 at.%)	
Pt_1/NC	<25 wt%	*Nat. Nanotechnol.* **17**, 174-181 (2022).
Cu-N-C	0.6 wt%	*Nat. Nanotechnol.* **17**, 403-407 (2022).
Rh SACs/PCN	23 wt%	*Nat. Nanotechnol.* **17**, 174-181 (2022).
Pt/CA-CNF	~0.24 wt%	*Nat. Nanotechnol.* **14**, 851-857 (2019).
SA-Rh/CN	0.92 wt%	*Nat. Nanotechnol.* **15,** 390–397 (2020).
SA-Pd/CN	0.76 wt%	
SA-Pt/CN	0.57 wt%	
A-Ni-NSG	2.8 wt% (0.47 at.%)	*Nat. Energy* **3**, 140-147 (2018).
Cu-SAs/N-G	1.3 wt%	*Nat. Catal.* **1**, 781-786 (2018).
UHD Ni-N-C SACs	23.3 wt%	*Nat. Synth.* **3**, 1427-1438 (2024).
UHD Cu-N-C SACs	26.9 wt%	
UHD Pt-N-C SACs	33.4 wt%	
Ni SACs	20.8 wt%	*Nat. Synth.* **2**, 129-139 (2023).
2000-Pt-N-CNT	7.0 wt%	*Nat. Commun.* **13**, 685 (2022).
Cu-NC SAC	10.5 wt%	*Nat. Commun.* **10**, 1278 (2019).
Ir/meso_S-C	~10 wt% (~0.77 at.%)	*Sci. Adv.* **5**, eaax6322 (2019).

Red denotes single-atom-loaded metal oxides, while blue represents the C/N substrate.

Supplementary Table 2 Surface elemental weight ratios of the UHL-Ir/Fe_2O_3 determined by X-ray photoelectron spectroscopy.

	Ir (at.%)	Fe (at.%)	O (at.%)
UHL-Ir/Fe_2O_3	4.12	36.17	59.71
	Ir (wt%)	Fe (wt%)	O (wt%)
UHL-Ir/Fe_2O_3	21.02 wt%	53.62	25.36

\

Supplementary Table 3 Structural parameters extracted from Ir-L_3 edge $\chi(R)$ space spectra fitting of UHL-Ir/Fe_2O_3.

	S_0^2	shell	CN*	R(Å)	σ^2 (10^{-3} Å^2)	ΔE_0	R factor
Ir foil	0.95	Ir-Ir	12	2.71±0.01	3.5±1.7	9.60±3.88	0.0073
UHL-Ir/Fe_2O_3	0.95	Ir-O	6.2	1.92±0.01	2.3±1.7	-3.35±2.40	0.0087
		Ir-O-Fe	5.2	3.33±0.01	11.0±0.1		

CN: coordination numbers. *R*: bond distance. σ^2: Debye-Waller factors. ΔE_0: the inner potential correction. R factor: goodness of fit.

Supplementary Table 4. Metal precursor salts used in the synthesis of UHL-SACs/Fe_2O_3.

Elements	Atomic numbers	Metal precursors	Solubleness in water
Y	39	$YCl_3·6H_2O$	freely soluble
Zr	40	$ZrCl_4$	very soluble
Nb	41	$NbCl_5$	decomposes
Mo	42	$(NH_4)_6Mo_7O_{24}·4H_2O$	soluble
Ru	44	$RuCl_3$	very soluble
Rh	45	$RhCl_3·xH_2O$	very soluble
Pd	46	$PdCl_2$	soluble
Ag	47	$AgNO_3$	very soluble
Cd	48	$Cd(Ac)_2·2H_2O$	very soluble
In	49	$In(Ac)_3$	soluble
Sn	50	$SnCl_4$	very soluble
Sb	51	$Sb(Ac)_3$	Moderately soluble
Ba	56	$Ba(Ac)_2$	freely soluble
La	57	$La(Ac)_3·xH_2O$	soluble
Ce	58	$(NH_4)_6Ce(SO_4)_5·4H_2O$	soluble
Pr	59	$Pr(Ac)_3·xH_2O$	soluble
Nd	60	$Nd(Ac)_3·xH_2O$	soluble
Sm	62	$Sm(Ac)_3·xH_2O$	soluble
Gd	64	$Gd(Ac)_3·4H_2O$	soluble
Tb	65	$Tb(Ac)_3·6H_2O$	soluble
Dy	66	$Dy(Ac)_3·4H_2O$	soluble
Er	68	$Er(Ac)_3·4H_2O$	soluble
Tm	69	$Tm(Ac)_3·H_2O$	soluble
Yb	70	$Yb(Ac)_3·4H_2O$	soluble

Lu	71	$LuCl_3 \cdot 6H_2O$	soluble
Hf	72	$HfCl_4$	soluble
W	74	$(NH_4)_{10}W_{12}\ O_{41} \cdot xH_2O$	soluble
Ir	77	H_2Cl_6Ir	soluble
Pt	78	$H_2PtCl_6 \cdot 6H_2O$	highly soluble
Au	79	$HAuCl_4 \cdot 3H_2O$	very soluble
Pb	82	$Pb(Ac)_2 \cdot 3H_2O$	freely soluble
Bi	83	$Bi(NO_3)_3$	slightly soluble

Supplementary Table 5 Structural parameters extracted from $\chi(R)$ spatial spectrum fitting of 33 kinds of UHL-SACs/Fe_2O_3 prepared by the plasma-microwave method.

	S_0^2	shell	CN*	R(Å)	σ^2 (10^{-3} Å^2)	ΔE_0	R factor
Y foil	0.95	Y-Y	12.00	3.60±0.01	14.8±3.6	5.03±2.51	0.0131
UHL-Y_{PM}/Fe_2O_3	0.95	Y-O	5.97	2.38±0.01	5.3±1.3	-0.16±0.01	0.0085
Zr foil	0.90	Zr-Zr	8.00	3.19±0.01	7.6±0.3	-8.13±0.42	0.0049
		Zr-Zr	6.00	3.61±0.01	14.6±0.1		
UHL-Zr_{PM}/Fe_2O_3	0.90	Zr-O	5.61	2.17±0.01	7.1±1.0	-0.23±0.01	0.0079
Nb foil	0.90	Nb-Nb	8.00	2.85±0.01	6.5±0.3	4.32±1.03	0.0137
		Nb-Nb	6.00	3.28±0.01	6.8±0.6		
UHL-Nb_{PM}/Fe_2O_3	0.90	Nb-O	5.34	1.99±0.01	13.1±1.5	2.65±0.89	0.0188
Mo foil	0.80	Mo-Mo	8.00	2.72±0.01	2.8±0.2	-6.42±0.74	0.0038
		Mo-Mo	6.00	3.13±0.01	2.2±0.3		
UHL-Mo_{PM}/Fe_2O_3	0.80	Mo-O	5.12	1.75±0.01	12.7±0.5	-8.93±0.93	0.0024
Ru foil	0.84	Ru-Ru	6.00	2.68±0.01	1.7±0.1	-3.17±0.85	0.0080
		Ru-Ru	6.00	2.67±0.01	9.0±2.1		
UHL-Ru_{PM}/Fe_2O_3	0.84	Mo-O	4.82	2.07±0.01	5.1±1.2	5.42±1.24	0.0126
Rh foil	0.82	Rh-Rh	12.00	2.68±0.01	3.6±0.2	-6.03±0.62	0.0087
UHL-Rh_{PM}/Fe_2O_3	0.82	Rh-O	4.57	2.03±0.01	4.1±0.3	-3.63±0.30	0.0011
Pd foil	0.84	Pd-Pd	12.00	2.74±0.01	5.6±0.1	3.85±0.29	0.0030
UHL-Pd_{PM}/Fe_2O_3	0.84	Pd-O	4.20	1.96±0.01	5.5±0.8	-8.54±0.94	0.0145
Ag foil	0.78	Ag-Ag	12.00	2.86±0.01	9.0±0.1	2.52±0.24	0.0028
UHL-Ag_{PM}/Fe_2O_3	0.78	Ag-O	3.10	1.92±0.01	13.7±2.0	9.98±0.01	0.0181
Cd foil	0.80	Cd-Cd	6.00	2.95±0.01	14.7±0.5	-2.66±0.01	0.0014
		Cd-Cd	3.00	3.28±0.01	13.6±1.0		
UHL-Cd_{PM}/Fe_2O_3	0.80	Cd-O	4.1	2.25±0.01	3.5±0.6	-1.03±0.01	0.0052
In foil	0.84	In-In	4.00	3.24±0.01	7.4±0.7	-9.31±0.01	0.0030
		In-In	3.00	3.46±0.01	8.3±0.1		
UHL-In_{PM}/Fe_2O_3	0.84	In-O	3.91	2.17±0.01	10.8±0.2	8.83±0.08	0.0001

Sn foil	0.82	Sn-Sn	4.00	3.00±0.01	8.1±0.8	1.89±0.01	0.0028
UHL-Sn_{PM}/Fe_2O_3	0.82	Sn-O	3.80	2.10±0.01	6.9±0.9	9.16±1.23	0.0021
Sb foil	0.78	Sb-Sb	3.00	2.90±0.01	4.4±0.3	7.02±0.54	0.0192
		Sb-Sb	3.00	3.34±0.01	10.6±2.3		
UHL-Sb_{PM}/Fe_2O_3	0.78	Sb-O	3.72	1.98±0.01	2.0±0.8	9.84±0.01	0.0054
UHL-Ba_{PM}/Fe_2O_3	0.85	Ba-O	7.98	2.87±0.01	4.4±0.9	-8.58±0.43	0.0054
UHL-La_{PM}/Fe_2O_3	0.90	La-O	6.60	2.37±0.01	0.4±0.1	9.92±0.01	0.0046
		La-O	1.30	2.59±0.01	14.3±0.1		
UHL-Ce_{PM}/Fe_2O_3	0.72	Ce-O	7.52	2.56±0.01	14.8±0.1	4.53±0.37	0.0064
UHL-Pr_{PM}/Fe_2O_3	0.80	Pr-O	7.33	2.53±0.01	14.0±1.0	2.86±0.29	0.0037
UHL-Nd_{PM}/Fe_2O_3	0.80	Nd-O	7.20	2.51±0.01	10.8±0.9	4.32±0.24	0.0035
UHL-Sm_{PM}/Fe_2O_3	0.78	Sm-O	7.06	2.42±0.01	4.3±1.4	3.01±0.70	0.0100
Gd foil	0.98	Gd-Gd	6.00	2.95±0.01	9.0±0.1	-9.81±0.01	0.0128
UHL-Gd_{PM}/Fe_2O_3	0.98	Gd-O	6.84	2.47±0.01	0.2±0.1	-9.81±0.01	0.0184
UHL-Tb_{PM}/Fe_2O_3	0.90	Tb-O	6.79	2.28±0.01	14.3±4.2	-9.83±0.01	0.0011
UHL-Dy_{PM}/Fe_2O_3	0.85	Dy-O	6.75	2.27±0.01	9.3±0.8	-8.08±0.68	0.0021
UHL-Er_{PM}/Fe_2O_3	0.78	Er-O	6.71	2.25±0.01	0.8±0.1	-6.85±1.24	0.0105
UHL-Tm_{PM}/Fe_2O_3	0.78	Tm-O	6.43	2.24±0.01	5.9±0.1	-8.20±0.46	0.0010
UHL-Yb_{PM}/Fe_2O_3	0.98	Yb-O	6.21	2.48±0.01	4.1±0.7	9.87±0.01	0.0074
UHL-Lu_{PM}/Fe_2O_3	0.80	Lu-O	6.02	2.26±0.01	8.9±0.9	4.61±0.51	0.0046
UHL-Hf_{PM}/Fe_2O_3	0.81	Hf-O	5.82	2.05±0.01	2.8±1.0	0.78±0.01	0.0038
W foil	0.83	W-W	8.00	2.73±0.01	3.6±0.3	5.09±1.62	0.0082
		W-W	6.00	3.14±0.01	3.8±0.7		
UHL-W_{PM}/Fe_2O_3	0.83	W-O	5.61	2.23±0.01	12.1±0.7	-9.73±0.01	0.0003
UHL-Os_{PM}/Fe_2O_3	0.84	Os-O	5.26	1.96±0.01	14.8±0.1	-6.24±0.01	0.0091
Ir foil	0.95	Ir-Ir	12	2.71±0.01	3.5±1.7	9.60±3.88	0.0073
UHL-Ir/Fe_2O_3	0.95	Ir-O	6.2	1.92±0.01	2.3±1.7	-3.35±2.40	0.0087
		Ir-O-Fe	5.2	3.33±0.01	11.0±0.1		
Pt foil	0.97	Pt-Pt	12.00	2.76±0.01	5.4±0.3	4.73±0.58	0.0040

UHL-Pt_{PM}/Fe_2O_3	0.97	Pt-O	4.10	2.02±0.01	9.3±1.7	9.32±0.94	0.0164
Au foil	0.80	Au-Au	12.00	2.86±0.01	7.6±0.2	4.06±0.39	0.0052
UHL-Au_{PM}/Fe_2O_3	0.80	Au-O	3.92	1.98±0.01	3.3±0.6	9.92±0.01	0.0077
Pb foil	0.81	Pb-Pb	2.00	3.41±0.01	12.4±2.0	-2.75±1.61	0.0029
UHL-Pb_{PM}/Fe_2O_3	0.81	Pb-O	3.73	2.19±0.01	6.5±0.9	-1.73±0.74	0.0150
Bi foil	0.95	Bi-Bi	3.00	3.08±0.01	8.2±0.6	-0.04±0.01	0.0147
		Bi-Bi	2.00	3.69±0.01	12.3±3.5		
UHL-Bi_{PM}/Fe_2O_3	0.95	Bi-O	3.61	2.14±0.01	12.5±0.4	-8.71±0.58	0.0049

CN: coordination numbers; *R*: bond distance; σ^2: Debye-Waller factors; ΔE_0: the inner potential correction. R factor: goodness of fit.

Supplementary Table 6 PEC performance comparisons between this work and typical Fe_2O_3-based photoanodes.

Photoanode	*J* (mA cm^{-2}) @1.23 V_{RHE}	ABPE (%)	Onset potential (V_{RHE})	Reference
5-M_{PM}/Fe_2O_3	**5.70**	**1.2**	**0.54**	**This work**
W_{PM}/Fe_2O_3	**5.04**	**1.05**	**0.66**	
SAs Pt:Fe_2O_3-O_V	3.65	0.68	0.63	Nat. Commun. 14, 2640 (2023).
Ge:Fe_2O_3	3.5	---	0.70	Nat. Commun. 12, 4309 (2021).
NiFe(OH)x/Ta:Fe_2O_3@Fe_2O_3	3.22	0.55	0.55	Nat. Commun. 11, 4622 (2020).
Co-Pi/Ti:Fe_2O_3	3.50	---	0.86	Nat. Commun. 10, 4832 (2019).
$NiFeO_x$/Dual-regrowth Fe_2O_3	1.30	---	0.45	Nat. Commun. 6, 7447 (2015).
Co-Pi/Si:Fe_2O_3	2.70	---	0.82	J. Am. Chem. Soc. 128, 15714 (2006).
Co-Pi/NPs Ag/Fe_2O_3	4.68	0.55	0.70	Adv. Mater. 28, 6405 (2016).
Co-Pi/Zr:Fe_2O_3	2.20	0.23	0.65	Angew. Chem. Int. Ed. 56, 4150 (2017).
FeOOH/Fe_2O_3	1.21	---	0.65	Angew. Chem. Int. Ed. 55, 10854 (2016).
Ti-SiOx/CoPi/Ti:Fe_2O_3	3.19	---	0.80	Angew. Chem. Int. Ed. 55, 9922 (2016).
FeNiOOH/Fe_2TiO_5/Fe_2O_3	2.20	---	0.95	Energy Environ. Sci. 10, 2124 (2017).
Co-Pi/P:Fe_2O_3	3.10	---	0.75	Energy Environ. Sci. 8, 1231 (2015).
FeOOH/SnO_2-SiO_x/Ti:Fe_2O_3	1.54	---	0.64	Adv. Energy Mater. 6, 1501840 (2016).
Fe_2TiO_5/Fe_2O_3/Pt	1.00	---	0.80	Adv. Funct. Mater. 27, 1703527 (2017).
Co-Pi/Co_3O_4/Ti:Fe_2O_3	2.70	0.43	0.64	Adv. Funct. Mater. 29, 1801902 (2019).
Co-Mn/Fe_2O_3	2.09	0.25	0.60	Adv. Funct. Mater. 29, 1904622 (2019).
FeOOH/Fe_2O_3	0.85	---	0.80	Adv Funct Mater. 25, 2686 (2015).
Cobail oxide/Sn:Fe_2O_3	2.20	---	0.80	Nano Lett. 17, 2490 (2017).
Co-Pi/Fe_2O_3@Fe_2TiO_5	2.60	---	0.90	ACS Nano. 9, 5348 (2015).

Supplementary Table 7 PEC performance comparisons between this work and other metal oxide-based photoanodes.

Photoanode	J (mA cm^{-2}) @1.23 V_{RHE}	ABPE (%)	Onset potential (V_{RHE})	Reference
5-M_{PM}/Fe_2O_3	**5.70**	**1.2**	**0.54**	**This work**
W_{PM}/Fe_2O_3	**5.04**	**1.05**	**0.66**	
Vw-WO_3/Co-Pi	4.8	1.2		Nat. Catal. **8**, 229-238 (2025).
WO_3-(PDDA-Aux)$_2$	0.6	0.9		J. Am. Chem. Soc. 142, 21899-21912 (2020).
Y:ZnO NR	0.4	---		Angew. Chem. Int. Ed. 57, 9749-9753 (2018).
Fe_2TiO_5-TiO_2	0.325	0.017		Angew. Chem. Int. Ed. Engl. 59, 8128-8132 (2020).
CuO/WO_3	3.2	---	0.6	Angew. Chem. Int. Ed. 60, 17601(2021).
WO_3 with dual W and O vacancy	2.8	---		Angew. Chem. Int. Ed. 55, 11819-11823 (2016)
WO_3 nanobar	2			Angew. Chem. Int. Ed. 60, 9357-9361 (2021).
Ag@$Ag_3(PO_4)_{1-x}$/ZnO	3.1	---	---	Energy Environ. Sci.,5, 8917-8922 (2012).
m-WO_3 with oxygen vacancy	2.4	---		Adv. Funct. Mater. 32, 2204106 (2022).
In_2S_3-P/WO_3	1.61	0.29		Adv. Energy Mater. 10, 1903951 (2020).
WO_3 porous nanosheet	1.25	---		Adv. Energy Mater. 6, 1600437 (2016).
CoMnO/BBNO/WO_3	3.56	---		Adv. Energy Mater. 8, 1701655 (2018)
Co-Pi/GaN:ZnO	1.19	---		Adv. Energy Mater., 6, 1600864 (2016).
Ni(OH)$_2$/ZIF-8/ZnO/NF	1.95	---		Adv. Energy Mater. 8, 1800101 (2018).
N-TiO_2	1.9	---		Nano Lett. 15, 4692-4698 (2015).

Supplementary Table 8 Surface elemental weight ratios of the various electrodes determined by X-ray photoelectron spectroscopy.

	W (at.%)	Cu (at.%)	O (at.%)	
W_{PM}/1D-Cu_2O	4.02	59.99	35.99	
	W (wt%)	Cu (wt %)	O (wt %)	
W_{PM}/1D-Cu_2O	14.42	74.36	11.23	
	W (at.%)	Zn (at.%)	In (at.%)	S (at.%)
W_{PM}/2D-$ZnIn_2S_4$	3.79	12.74	24.49	58.98
	W (wt%)	Zn (wt%)	In (wt%)	S (wt%)
W_{PM}/2D-$ZnIn_2S_4$	11.18	13.36	45.13	30.34
	W (at.%)	C (at.%)	N (at.%)	
W_{PM}/2D-C_3N_4	3.88	41.19	54.93	
	W (wt%)	C (wt%)	N (wt%)	
W_{PM}/2D-C_3N_4	36.07	25.01	38.92	
	W (at.%)	Fe (at.%)	O (at.%)	
W_{PM}/2D-Fe_2O_3	4.13	34.35	61.52	
	W (wt%)	Fe (wt%)	O (wt%)	
W_{PM}/2D-Fe_2O_3	20.73	52.39	26.88	
	W (at.%)	Fe (at.%)	O (at.%)	
W_{PM}/3D-Fe_2O_3	4.31	36.28	59.41	
	W (wt%)	Fe (wt%)	O (wt%)	
W_{PM}/3D-Fe_2O_3	21.02	53.76	25.22	
	W (at.%)	Ti (at.%)	O (at.%)	
W_{PM}/3D-TiO_2	3.84	30.05	66.11	
	W (wt%)	Ti (wt%)	O (wt%)	
W_{PM}/3D-TiO_2	22.05	44.92	33.03	

Supplementary Table 9 Surface elemental weight ratios of the 5-M_{PM}/Fe_2O_3 electrode determined by X-ray photoelectron spectroscopy.

	Mo (at.%)	Rh (at.%)	W (at.%)	Ir (at.%)	Au (at.%)	Fe (at.%)	O (at.%)
5-M_{PM}/Fe_2O_3	1.75	1.67	1.51	1.44	1.38	37.04	55.21
	Mo (wt%)	Rh (wt%)	W (wt%)	Ir (wt%)	Au (wt%)	Fe (wt%)	O (wt%)
5-M_{PM}/Fe_2O_3	4.08	4.17	6.74	6.72	6.60	50.74	21.57

Supplementary Table 10 Structural parameters extracted from Au-*K* edge, W-L_3 edge, Mo-L_3 edge, Rh-*K* edge and Ir-L_3 edge $\chi(R)$ space spectra fitting of 5-M_{PM}/Fe_2O_3.

	S_0^2	shell	CN*	R(Å)	σ^2 (10^{-3} Å^2)	ΔE_0	R factor
Au foil	0.75	Au-Au	12	2.86±0.01	7.3±0.1	4.54±0.49	0.0039
5-M_{PM}/Fe_2O_3	0.75	Au-O	4.1	1.94±0.01	5.1±1.1	1.25±0.73	0.0036
		Au-O-Fe	2.2	3.61±0.01	13.0±6.4		
Ir foil	0.90	Ir-Ir	12	2.71±0.01	3.5±0.2	9.43±1.07	0.0074
Sample-Ir	0.90	Ir-O	4.1	1.90±0.01	1.6±1.1	-3.15±0.57	0.0039
		Ir-O-Fe	2.0	3.45±0.01	13.7±4.5		
Mo foil	0.75	Mo-Mo	8	2.71±0.01	2.6±0.2	-8.41±0.78	0.0022
		Mo-Mo	6	3.12±0.01	1.4±0.3		
Sample-Mo	0.75	Mo-O	3.6	1.72±0.01	9.4±1.4	9.50±1.56	0.0074
		Mo-O-Fe	1.3	2.79±0.01	14.2±3.5		
Rh foil	0.92	Rh-Rh	12	2.69±0.01	5.0±0.3	6.93±1.43	0.0170
Sample-Rh	0.92	Rh-O	3.6	2.08±0.01	5.2±1.6	7.08±0.89	0.0145
		Rh-O-Fe	1.8	3.50±0.01	14.3±0.1		
W foil	0.80	W-W	8	2.73±0.01	3.8±0.3	4.46±0.70	0.0042
		W-W	6	3.13±0.01	3.8±0.6		
Sample-W	0.80	W-O	4.3	1.72±0.01	2.5±1.2	-3.91±1.11	0.0069
		W-O-Fe	2.1	3.34±0.01	15.0±4.8		

CN: coordination numbers. *R*: bond distance. σ^2: Debye-Waller factors. ΔE_0: the inner potential correction. R factor: goodness of fit.

Supplementary Table 11 The PEC performance of this work is compared with that of C-N-based photoanodes currently reported.

Photoanode	*J* @1.23 V_{RHE}	Stability	Reference
5-M_{PM}/Fe_2O_3	**5.70 mA cm^{-2}**	**500 h**	**This work**
PEDOT/C_3N_4	14.7 μA cm^{-2}	150 s	*ACS Appl. Nano Mater.* 8, 985-996 (2025).
Pt-NCN-CC	~0.21 μA cm^{-2}	24 h	*Int. J. Hydrog. Energy* 48, 29942-29951 (2023).
g-C_3N_4+420-g-C_3N_4	0.16 mA cm^{-2}	400 s	*ChemCatChem* 11, 729 (2019).
V_C and V_N co-doped g-C_3N_4	1.2 μA cm^{-2}	50 s	*Sol. RRL* 3, 1800298 (2019).
SnO_2/g-C_3N_4	42 μA cm^{-2}	80 s	*Appl. Surf. Sci.* 440, 153-161 (2018).
TNTAs/g-C_3N_4	0.86 mA cm^{-2}	10 h	*Nano-Micro Lett.* 10, 37 (2018).
C_{PVP}/g-C_3N_4-60	12.6 μA cm^{-2} at 1.2 V	4000 s	*Chem. Eur. J.* 23, 419 (2017).
Pt/ZnO/g-C_3N_4	30 μA cm^{-2} at 1.12 V_{RHE}	3400 s	*Int. J. Hydrog. Energy* 40, 9080-9087 (2015).
MoS_2/NRGO/CNNS	27.76 μA cm^{-2} at 0.8 V	1400 s	*Adv. Mater.* 25, 6291-6297 (2013).

Supplementary Table 12 Bader charge quantification results for 5-M_M/Fe_2O_3 and 5-M_{PM}/Fe_2O_3.

	5-M_M/Fe_2O_3	5-M_{PM}/Fe_2O_3
Ir	9.22 eV	7.48 eV
Ir	9.18 eV	7.54 eV
W	13.33 eV	12.33 eV
W	13.88 eV	12.57 eV
Mo	13.28 eV	12.46 eV
Mo	13.64 eV	12.30 eV
Au	11.47 eV	10.08 eV
Au	11.51 eV	10.62 eV
Rh	14.76 eV	14.69 eV
Rh	14.73 eV	14.60 eV

Reference

1. Kresse, G. & Furthmüller, J. Efficiency of ab-initio total energy calculations for metals and semiconductors using a plane-wave basis set. *Comput. Mater. Sci.* **6**, 15–50 (1996).
2. Shishkin, M. & Kresse, G. Implementation and performance of the frequency-dependent GW method within the PAW framework. *Phys. Rev. B* **74**, 035101 (2006).
3. Perdew, J. P., Burke, K. & Ernzerhof, M. Generalized gradient approximation made simple. *Phys. Rev. Lett.* **77**, 3865 (1996).
4. Dudarev, S. L., Botton, G. A., Savrasov, S. Y., et al. Electron-energy-loss spectra and the structural stability of nickel oxide: An LSDA+U study. *Phys. Rev. B*, **57**, 1505–1514 (1998).
5. Grimme, S., Antony, J., Ehrlich, S., et al. A consistent and accurate ab initio parametrization of density functional dispersion correction (DFT-D) for the 94 elements H-Pu. *J. Chem. Phys.* **132**, 154104 (2010).
6. Heyd, J., Scuseria, G. E., & Ernzerhof, M. Hybrid functionals based on a screened Coulomb potential. *J. Chem. Phys.* **118**, 8207–8215 (2003).
7. Monkhorst, H. J. & Pack, J. D. Special points for Brillouin-zone integrations. *Phys. Rev. B*, **13**, 5188–5192 (1976).